1-28-2015

HIGH EFFICIENCY AXIAL DIFFRACTION OUTPUT SCHEMES FOR THE A6 RELATIVISTIC MAGNETRON

Christopher Leach

Christopher Joseph Leach
Candidate

Electrical and Computer Engineering
Department

This dissertation is approved, and it is acceptable in quality and form for publication:

Approved by the Dissertation Committee:

Edl Schamiloglu, Chairperson

Mark Gilmore

Christos Christodoulou

Gary Cooper

HIGH EFFICIENCY AXIAL DIFFRACTION OUTPUT SCHEMES FOR THE A6 RELATIVISTIC MAGNETRON

by

CHRISTOPHER JOSEPH LEACH

B.S., Physics, Auburn University, 2006
M. Ed., Secondary Physics Education, Auburn University, 2011

DISSERTATION

Submitted in Partial Fulfillment of the
Requirements for the Degree of

Doctor of Philosophy
Engineering

The University of New Mexico
Albuquerque, New Mexico

December, 2014

DEDICATION

This work is dedicated to every individual and institution that has invested in me or has given me a chance.

ACKNOWLEDGEMENTS

I would like to thank my advising professor, Edl Schamiloglu, for accepting me as his student and for his unwavering support and trust. He has given me a once in a lifetime opportunity, and I have done my best to honor the responsibilities that he has required of me.

This research project was a major endeavor, and was the work of a great number of individuals. Mikhail Fuks and Edl Schamiloglu optimized the MDO's 70%-efficient simulation design and were instrumental in discussion and in cross-checking of results. Jerald Buchenauer provided a wealth of experimental wisdom and wizardry for our systems and diagnostics. Ken Prestwich provided the design for the reconfigured PULSERAD accelerator/pulser and was instrumental in interpreting experimental data and in suggesting future improvements. Marvin Roybal and Mel Pablo constructed the hardware for this reconfiguration. Lee Terry provided machine shop and technical support for the experiments. Rich Compeau provided tireless technical support for the analog electronics design used in the calorimeter. Ralph Kelly welded many of the system's parts. Mark Gilmore helped with discussions regarding grounding and shielding. Fellow student Shawn Soh also contributed to discussion. Two UNM senior design teams made a major contribution to building the calorimeter and the pulsed electromagnet circuit: Chris De La Cruz, Merlyn Bluhm, Ben Schaefer, Chris Stelmar, Edu Sandoval, Joe Perez, Mark Mares, and Carlos Monzon. A whole host of work study employees were instrumental in assisting with these and other aspects of the project: Jeremy McConaha, Chad Roybal, Mike Padilla, Matt Dill, Tyler Jordan, and others.

Thank you to the Air Force Research Lab at Kirtland AFB, particularly Peter Mardhal and Tim Flemming. Peter was my AFRL/USRA Scholars internship mentor and helped with ICEPIC modelling and interpretation of data for the MDO, the rodded metamaterial-like cathode, and other projects. He was instrumental in providing additional funds that were required to manufacture the MDO. I would also like to thank Andrey Andreev of Raytheon-Ktech for help in the investigation of the rodded metamaterial-like cathode.

Above all, I would like to thank Sarita Prasad, director of the laboratory. She has overseen every step of this project and has ultimately been the one to double-check, sign off on, and take responsibility for a great many aspects of it. She has taken part in and has arranged important high-level theoretical and technical discussions. She was present for every late night of data taking, while also doing the same for other students' projects. In times when my strength faltered, she picked me up.

This research was supported by a variety of contracts and grants. I would like to thank AFOSR Grant FA9550-11-1-0200, ONR Grant N00014-13-1-0565, Raytheon University Research Project #2012-UNI-00022, and AFOSR DURIP Grant AF2386-12-13027, the latter of which supported the manufacture of the MDO.

HIGH EFFICIENCY AXIAL DIFFRACTION OUTPUT SCHEMES FOR THE A6 RELATIVISTIC MAGNETRON

By

Christopher Joseph Leach

B.S., PHYSICS, AUBURN UNIVERSITY, 2006
M. ED., SECONDARY PHYSICS EDUCATION, AUBURN UNIVERSITY, 2011

PH.D., ENGINEERING, UNIVERSITY OF NEW MEXICO, 2014

ABSTRACT

High-power microwave research strives for compact and highly efficient vacuum diode-driven sources. MAGIC particle-in-cell (PIC) computer simulations have shown that the performance of the well-known A6 relativistic magnetron with radial power extraction through one or more of its cavities can be improved by instead using axial power extraction through a mode-converting horn antenna, resulting in improved efficiency (30% improved to 70%) and greater output power handling capability (sub-gigawatt improved to multi-gigawatt) without breakdown. In addition, axial extraction results in a more compact profile that is compatible with mounting permanent magnets, which eliminate the need for bulky pulsed electromagnets or cryo-magnets and greatly enhance system efficiency.

To this end, a variety of technologies were simulated and tested in experiment, the latter which required the design, construction, testing, and calibration of new diagnostics, pulsed power systems, and hardware, such as the complex A6 magnetron with diffraction output horn antenna (MDO). The primary goal of the experiments was to verify simulated 70% efficiency and greater than 1 GW of output power from the MDO. A less expensive

"compact MDO" variant, essentially an A6 magnetron with a flat-plate mode converter and π-mode strap was also simulated. Although both the MDO and the compact MDO are compatible with permanent magnets fitted around their exteriors, an effective configuration was simulated for the compact MDO, promising reduced size and increased efficiency of the total microwave system. In addition, both versions of the MDO were susceptible to bombardment of leakage electrons on their output windows; cathode endcaps were developed and tested to mitigate this issue. Finally, to further improve output power, a rodded metamaterial-like cathode that showed improved power in other relativistic magnetrons was also considered by simulation in an A6 magnetron with radial extraction.

TABLE OF CONTENTS

LIST OF FIGURES

CHAPTER 1 INTRODUCTION

This introduction will cover the history of the magnetron, its basic operation, as well as providing a brief explanation and history of axial diffraction output schemes used in relativistic (applied voltages of ~511 kV) magnetrons. A more developed theory of axial extraction scheme operation will be covered in Chapter 2.

1.1 Magnetron history and basic operation

Like many important discoveries, the discovery of the magnetron, a device with perpendicular E-field and B-field (cross-fields), came by accident. The magnetron was born of General Electric's desire to not pay royalties to Lee De Forest for use of his famous vacuum triode. It was figured in 1920 by Albert Hull that by varying the axial magnetic field between a thermionic-emission coaxial diode structure, the amount of current reaching the outer conductor could be controlled. What was eventually noticed in 1924 by independent research by Czechoslovakian August Zacek and German Erich Habann was that the magnetron could produce an oscillation between 100 MHz to 1 GHz when the device was operating in the Hull cutoff regime, where the magnetic field was strong enough to prevent current flow to the outer anode.

Following up, British physicists Harry Boot and John Randall added resonant cavities to the anode by 1940, improving power output beyond that of even the Nazi Germany klystrons [1, 2]. It is thought by some that the power and compactness brought by this cavity magnetron had a larger effect on the outcome of WWII than the atomic bomb [3], providing superior radar and early-warning detection. The technology was even used

as a trading chip to coax the United States to enter the war on Britain's behalf. Still though, the magnetron was not without its problems at this time; it suffered from poor frequency stability that was eventually resolved post-war via strapping and the advent of the rising sun magnetron variant [4].

With the advent of pulsed power by the Englishman Charlie Martin [5], application of high voltages and currents to the magnetron (and other microwave tube devices) was only a matter of time. Several groups, including MIT, produced a number of "high power" magnetrons that were capable of megawatts of power, including the A6. The MIT A6 has become a modern standard for basic research and is well studied in experiment and replicated in computer simulation [6-10]. It is also used as the basis for this dissertation work. The A6 magnetron and a solid and transparent cathode, the latter which was developed at UNM [11, 12], are shown in Figure 1.1.1. The transparent cathode allows the first order azimuthal wave electric field to go to zero on-axis, thereby having a much stronger value near the radius of electron emission, leading to more rapid spoke formation than for the case of using a traditional solid cathode.

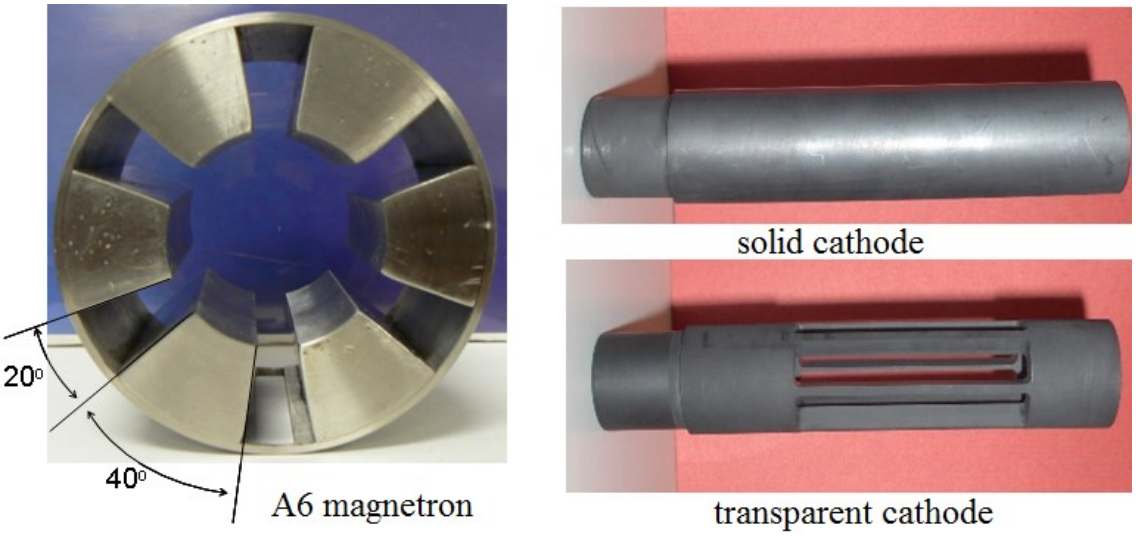

Figure 1.1.1. A6 magnetron anode (left) and solid and transparent cathodes (right).

1.2 Basic magnetron operation

The magnetron is a "cross-field device," meaning that the applied magnetic and electric field vectors are orthogonal to each other. In this case, a magnetic field is applied down the axis of the magnetron's coaxial structure, and the applied voltage creates electric field lines in the radial direction. A single-particle analysis of a single-species (electron) plasma in crossed electric and magnetic fields indicates that the electrons undergo a cyclotron-motion guiding-center drift in the **E x B** (azimuthal) direction with a speed $|\boldsymbol{E}|/|\boldsymbol{B}|$. This velocity is perturbed by the space charge effects of the dense electron beam, by diamagnetic plasma drifts caused by a variation in electron density, and by radial variation of the electric field [3]. The anode of the magnetron, its embedded cavities, and the cathode are capable of supporting a variety of electromagnetic modes with phase velocities in the azimuthal direction with magnitude less than *c*, and thus the anode is often called a "slow wave structure." When a sizeable fraction of the electrons have velocity magnitude equal to a

mode that was seeded by shot noise or a priming effect, inverse Landau damping occurs and electron potential energy is transferred to electromagnetic energy of its synchronous mode. This mode instability grows with a characteristic growth rate, then typically reaches saturation.

These modes are described by the number, n, of 2π variations that the RF fields see in one complete revolution around the anode block structure. To account for the phase shift between adjacent resonators, this number n is multiplied by the fractional angular displacement of N total cavities, $\Delta\theta = 2\pi/N$ to obtain $n\Delta\theta = 2\pi n/N$. For a magnetron mode that completes 3 RF cycles in one revolution around a magnetron with 6 cavities, this mode is the π-mode, which is a common operating mode. Another commonly-used mode is the 2π-mode, which would completed 6 RF cycles around a 6-cavity magnetron. These electromagnetic modes all occur along a characteristic ω vs. k dispersion relation curve, *e.g.* one for the A6 relativistic magnetron [3, 6]. Here ω is the radian frequency and k is the wavenumber. In a dispersion relation, the phase velocity of a mode can be obtained by taking the derivative of the dispersion curve with respect to wavenumber, k.

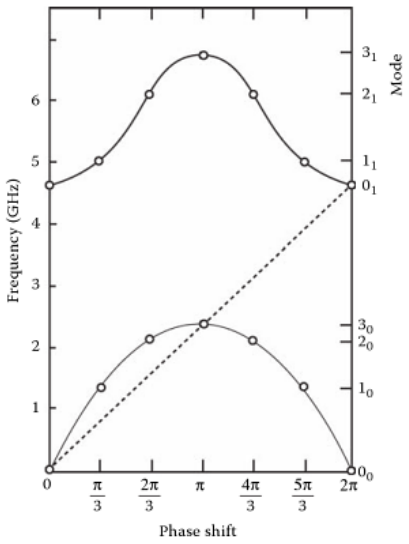

Figure 1.2.1. Dispersion relation for the A6 relativistic magnetron [3, 6].

The anode slow wave structure must be physically tuned and built to produce modes with phase velocity that match a range of **E** x **B** velocities that do not necessitate the use of magnetic and electric fields that result in shorting of the device. To avoid shorting, it is necessary to provide a sufficiently high insulating magnetic field, the value that satisfies the Hull cutoff condition [13], .

$$B^* = \frac{mc}{ed_e}(\gamma^2 - 1)^{\frac{1}{2}}, \tag{1.2.1}$$

$$d_e = \frac{r_a^2 - r_c^2}{2r_a} \tag{1.2.2}$$

where d_e, Equation 1.2.2, is the magnetron cylindrical geometry effective gap, *m* and *e* are the electron mass and charge, respectively, r_a is the anode radius, and r_c is the cathode radius. The relativistic factor, γ, is given in Equation 1.2.3.

$$\gamma = 1 + \frac{eV}{mc^2} = 1 + \frac{V(\text{kV})}{0.511} \tag{1.2.3}$$

If a magnetron is designed properly, then there are values of electric and magnetic field which satisfy the Hull Cutoff condition and also produce an **E** x **B** velocity that is synchronous with electromagnetic modes supported by the structure. This is known as the Buneman-Hartree condition, Equation 1.2.4, where ω_n is the operating frequency in radians per second and B_z is the applied axial magnetic field [13].

$$\frac{eV}{mc^2} = \frac{eB_z\omega_n}{mc^2 n} r_a d_e - 1 + \sqrt{1 - \left(\frac{r_a\omega_n}{cn}\right)^2} \tag{1.2.4}$$

For large currents or for long cathodes, such as used in the magnetron with diffraction output (MDO), this synchronous condition becomes relaxed due to the presence of Bφ (induced by I_z) along the magnetron's interaction space, Equation 1.2.5.

$$\frac{eV}{mc^2} = \frac{eB_z\omega_n}{mc^2 n} r_a d_e - 1 + \sqrt{\left[1 + b_\varphi^2\right]\left[1 - \left(\frac{r_n\omega_n}{cn}\right)^2\right]}, \tag{1.2.5}$$

where

$$b_{\varphi} = \frac{I_z(\mathrm{kA})}{8.5} \ln\left(\frac{r_a}{r_c}\right) \tag{1.2.6}$$

There is a region in voltage vs. magnetic field space that satisfies the Hull cutoff and Buneman-Hartree conditions that is represented in a general form in Figure 1.2.2 and for an A6 magnetron operating in the 2π-mode in Figure 1.2.3.

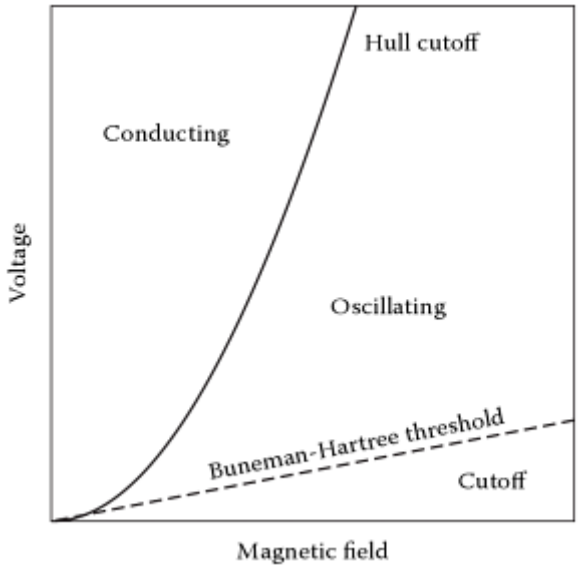

Figure 1.2.2. General representation of the Hull cutoff and Buneman-Hartree curves enclosing a region of operating space for a magnetron [3].

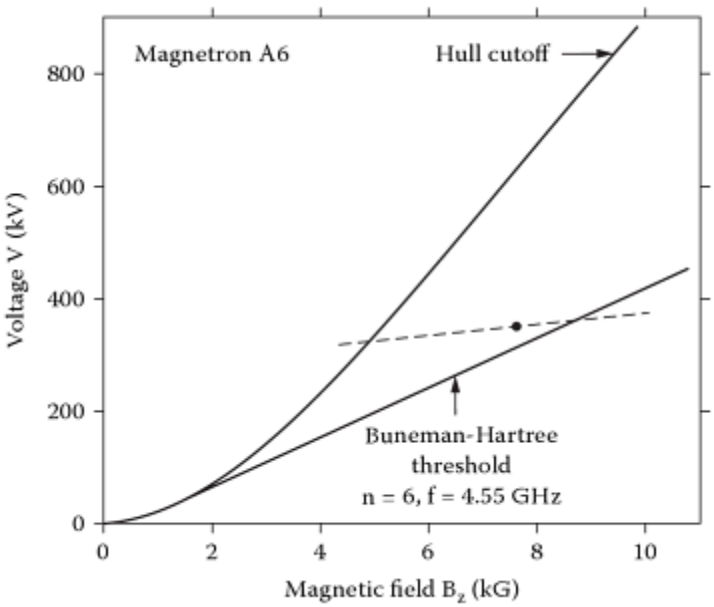

Figure 1.2.3. A6 magnetron Buneman-Hartree diagram [6].

There are some important general equations that relate current to voltage, Equation 1.2.7, and power to applied voltage, Equation 1.2.8. Note that the factor *K* is the perveance of the beam, a way of describing the self-field or space charge fields that the electrons exert on one another in the dense beam. This first relation is reminiscent of a non-relativistic Child-Langmuir diode. Both equations are oddly enough governed by space-charge effects, not by magnetic field, which suggests that space charge is the predominant limiter for current transport across the anode-cathode (A-K) gap [3].

$$I \approx KV^{3/2}, V < 500 \text{ kV} \tag{1.2.7}$$

$$P \approx \eta KV^{5/2}, V < 500 \text{ kV}. \tag{1.2.8}$$

Lastly, it is important to note that for magnetrons, mode competition can be an issue. Mode competition is movement of RF energy from the desired mode of operation to an undesired mode. This occurs due to the close frequency-proximity of adjacent modes that is caused by the close placement of a large number of small cavities in an anode that is large enough for high power extraction. The cavities must be closely spaced to provide low-impedance operation, and small cavities are needed for high mode frequencies [4]. As an example, frequency spacing from the π-mode to adjacent modes can be as little as 2%. However, using techniques such as strapping, where alternate vanes are connected with a conductive wire, or using a rising-sun-geometry, where alternate cavities have different heights, this spacing can be increased to 10%.

1.3 History of axial diffraction output in relativistic magnetrons

While most relativistic magnetrons extract power through a slot located in one or more cavities (radial extraction), axial extraction employs a horn antenna or multiple waveguides to excite output modes that travel in the direction that is downstream of the pulsed power systems used to power the device. Axial extraction in a relativistic magnetron was first tested in Russia in the late 1970's [14, 15], as part of the dissertation work of Mikhail Fuks, who is now the senior scientist for UNM's Pulsed Power, Beams, and Microwaves Laboratory. He later optimized the design of this device to achieve 70% efficient axial extraction that was experimentally tested in this dissertation.

The efficiency of this original X-band design did not exceed 12%-13% due to extraction of the desired mode from shallow cavities that were extended to a radius less

than the cutoff requirement, Figure 1.3.1. It did, however, output 4 GW of power in experiment.

The concept of a relativistic magnetron with axial extraction did not see appreciable design improvement until it was re-visited by Daimon and Jiang at the Nagaoka University of Technology in Japan in 2007 [16, 17]. It was there that the cavities in the horn antenna were deepened, such that extraction from a radius greater than the cutoff frequency of the desired output microwave mode could occur, a process discovered as several parameters were optimized in MAGIC (an FDTD simulation code) to produce up to 37% efficiency, Figure 1.3.2. Subsequent work was performed by Fuks and Schamiloglu to improve upon this using MAGIC to produce over 1 GW at 70% efficiency when radiating in the TE_{21} circular mode [18], Figure 1.3.3. Other unique and effective schemes to excite axially-directed modes have since been developed [19, 20].

Figure 1.3.1. Photograph of an early relativistic magnetron with diffraction output (MDO) [14].

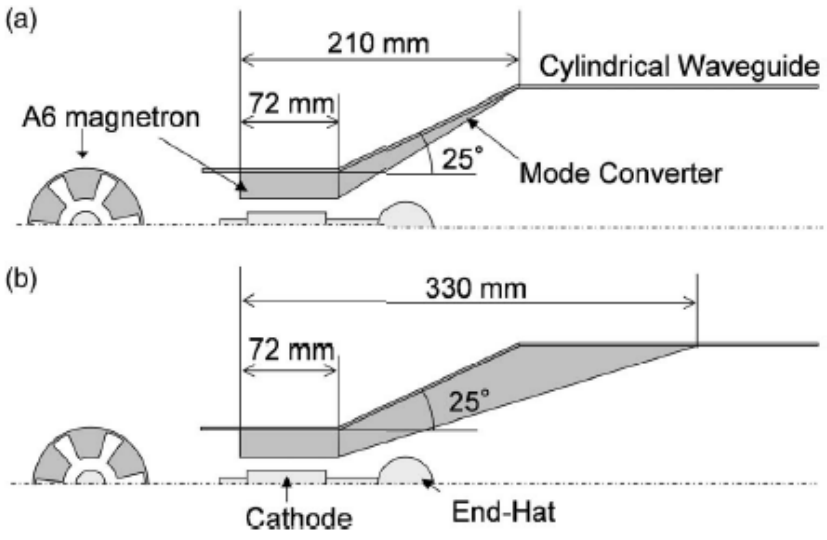

Figure 1.3.2. Geometry of early Russian MDO (top) compared to an improved Japanese design (bottom) [16].

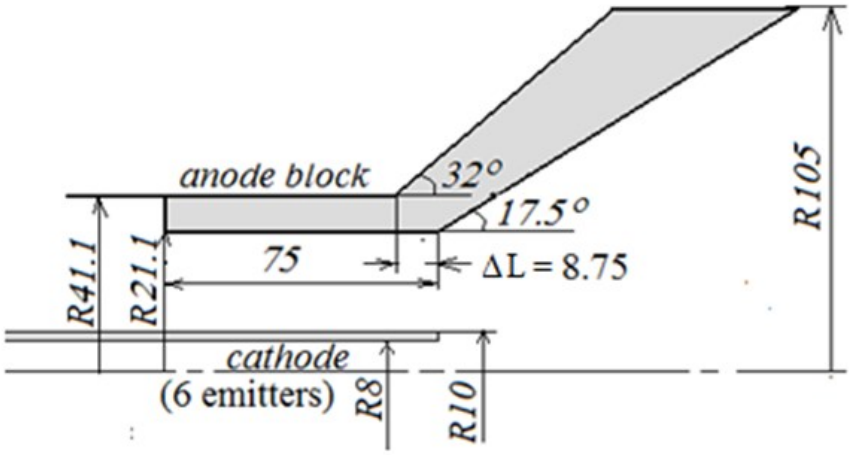

Figure 1.3.3. MDO, as optimized by Fuks and Schamiloglu for 70% electronic efficiency in simulations [18].

The remainder of this dissertation is organized as follows. Chapter 2 discusses the theory of operation and design challenges of the MDO and the compact MDO. Chapter 3 presents as a comprehensive overview of the computational codes used and simulation results for the MDO, compact MDO, a variety of cathode endcaps, a rodded metamaterial-like cathode, UNM's recently-reconfigured PULSERAD electron accelerator firing into an MDO load, and the newly-constructed PULSERAD pulsed electromagnet circuit. Chapter 4 details the experiment overview, and Chapter 5 displays the experimental results. Conclusions and recommendation for future work are summarized in Chapter 6.

CHAPTER 2 THE MDO AND COMPACT MDO

This chapter discusses the basic theory of the operation and challenges of the MDO and its smaller compact variant.

2.1 The MDO

At its heart, the diffractive output method of axial extraction is based upon simple diffraction and then superposition of magnetron cavity fields onto a horn antenna to excite an output mode. One advantage of using a horn antenna is that it presents a much larger aperture than the thin slots used in radial extraction so that it can handle significantly more power output due to its breakdown resistance. Compared to radial extraction hardware, the MDO is much more compact and might benefit from a smaller-diameter pulsed electromagnet that is not limited in design due to a radial extraction slot waveguide that would interfere. (It is also compatible with a permanent magnet design.) In addition, when a properly-selected horn antenna is matched to an A6 magnetron, it behaves as a weakly-irregular waveguide open resonator, which benefits from superb mode selection that is most supportive of the lowest-order longitudinal modes. Equation 2.1.1 shows that the Q-factor for such an irregular waveguide open resonator is highest when the axial variation of the mode is lowest, s = 1 [18, 21]. L is the resonator length. As magnetrons are designed to have an axial length no greater than λ/2 to eliminate higher-order longitudinal modes, this behavior means that this axial length can be relaxed, *e.g.* [22], to achieve other benefits.

$$Q \approx Q_{diff} = (8\pi/s)(L/\lambda)^2 \tag{2.1.1}$$

Another advantage of using a horn antenna for extraction is that the device preserves symmetric loading of all of the magnetron's cavities, meaning that any operating mode in the magnetron can be used as an output mode. For example, it was found that not only could the π-mode be used to output a circular TE_{31} mode, but the 4π/3-mode could also be used to output a TE_{21} mode [18], Figure 2.1.1 and Figure 2.1.2. This is not the case in a magnetron with radial extraction that has some of its cavities loaded and some unloaded. Such a situation demands the use of non-degenerate axial operating modes, such as the π-mode or 2π-mode. Use of degenerate operating modes can be destructive to a magnetron, as power is transferred into unloaded sub-modes that are not extracted. However, in an MDO this is not a problem.

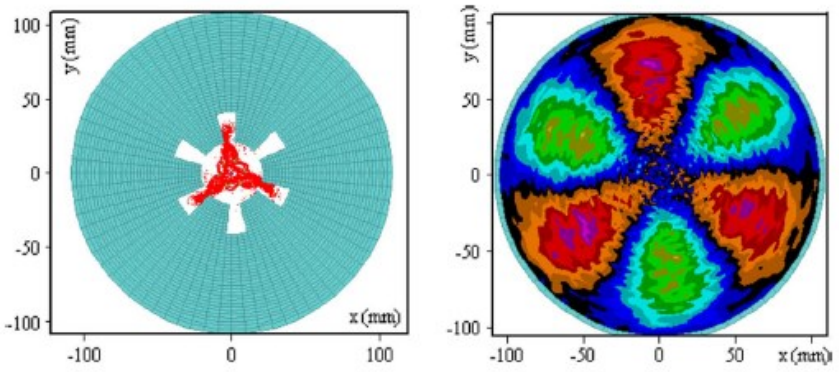

Figure 2.1.1. Electron particle plot in an A6 MDO illustrating the π-mode (left) used to excite the TE_{31} mode (Eφ, right).

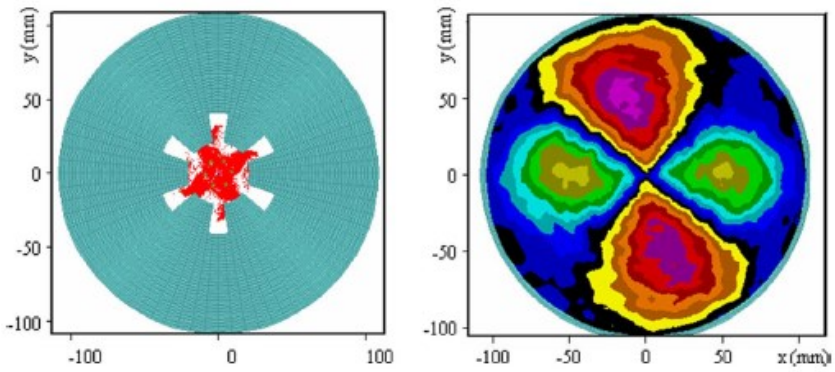

Figure 2.1.2. Electron particle plot in an A6 MDO illustrating the 4π/3-mode (left) used to excite TE_{21} mode (Eφ, right).

If the π-mode is chosen as the operating mode in the MDO through reduction of the cathode radius to ~1 cm [6, 23, 24], it is possible to suppress the expression of some of its cavity fields in the horn antenna so that a TE_{01} or Gaussian-like circular TE_{11} mode is output [23], Figure 2.1.3. Not shown is that two pairs of diametrically-opposed cavities may also be expressed in the horn to produce a TE_{11} microwave beam, with greater power and efficiency than if only one pair of cavities is used, see Chapter 3.2.3. The effect of suppressing some cavities on non-degenerate modes has not been studied in this dissertation.

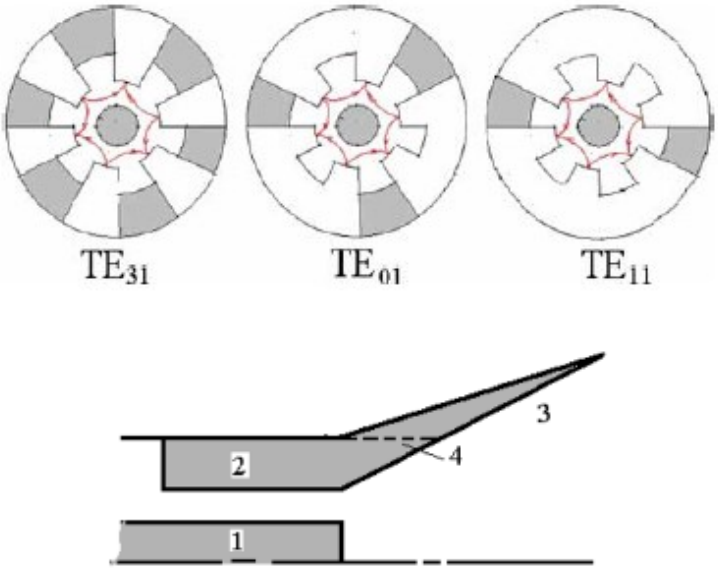

Figure 2.1.3. Selected expression of MDO cavities to excite a variety of modes. (1) cathode, (2) anode, (3) horn antenna, and (4) extension of the interaction-space cavity to an output waveguide radius that is cut-off to the radiated frequency.

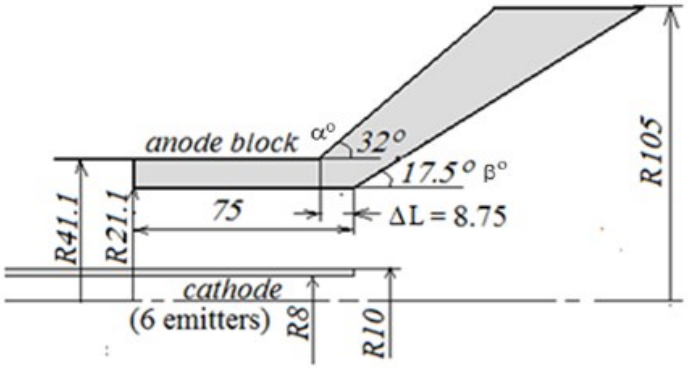

Figure 2.1.4. Schematic of UNM's 70% efficient MDO.

For UNM's 70% efficient design [18], shown in Figure 2.1.4, a number of changes were made to improve upon previous work (the 37% efficient design of Daimon and Jiang

[16]). Some of these were alteration of horn angles α° and β°, Figure 2.1.5, elongation of anode block length, addition of a ΔL section to the anode block's inner surface, Figure 2.1.6, elongation of the cathode, and use of a transparent cathode clocked to the correct angle, Figure 2.1.7.

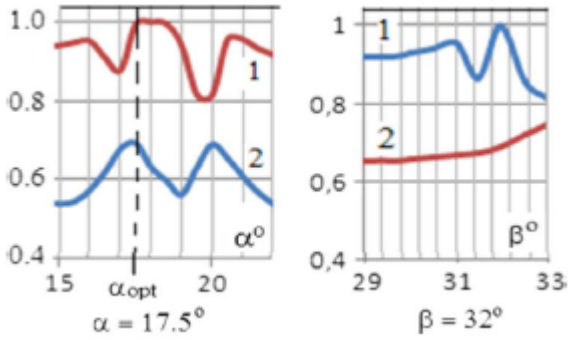

Figure 2.1.5. Dependence of MDO power P/P_{max} (1) and efficiency η_e (2) on horn angles α° and β°.

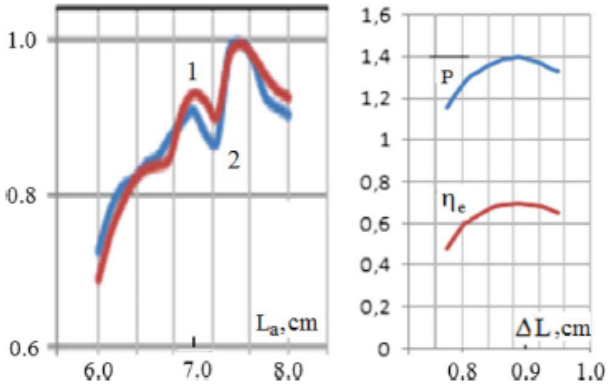

Figure 2.1.6. (Left) Power P/P_{max} (1) and efficiency $\eta/\eta_{e\ max}$ (2) as a function of MDO cavity length. (Right) Power (GW) and η_e as a function of ΔL.

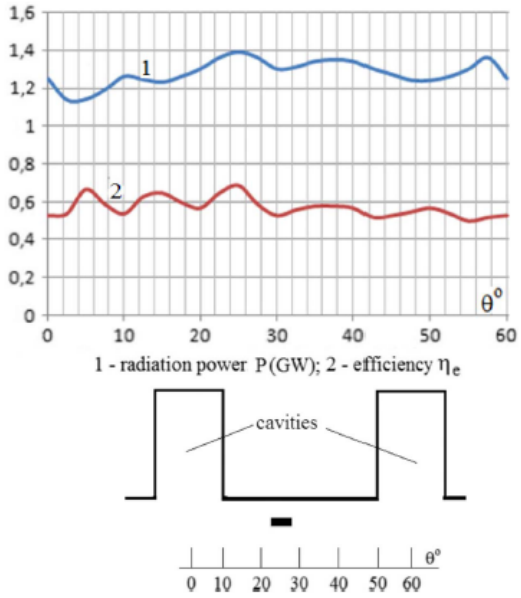

Figure 2.1.7. Power (GW, 1) and efficiency η_e (2) as a function of transparent cathode clocking angle with $B_z = 0.38$ T, anode length 7.5 cm, $\Delta L = 0.875$ cm, $\alpha = 17.5°$, and $\beta = 32°$.

It is important to note that the use of a longer cathode resulted in powerful and efficient RF generation over a wider range of applied magnetic fields due to the relaxation of the synchronous condition [18], Figure 2.1.8. Recall that the drift velocity of electrons must match the phase velocity of the magnetron mode, $v_{e\theta} = v_{ph}$, which is difficult due to their differing dependencies on r. The drift velocity and phase velocity are given in Equation 2.1.2, where $n = p + mN$ is the azimuthal index of a synchronous spatial harmonic, p is the operating wave's azimuthal index of the fundamental harmonic, and m is the harmonic number. However, with substantial azimuthal magnetic field the magnetic field seen by the electrons changes, Equation 2.1.3. Substituting the latter equation into the former one, it is straightforward to see that the $1/r$ dependency of $v_{e\theta}$ is relaxed slightly,

Equation 2.1.4. It is for this reason that the MDO can be better tuned by controlling the cathode length and that the longer cathode causes the MDO to operate effectively over a wider range of magnetic fields.

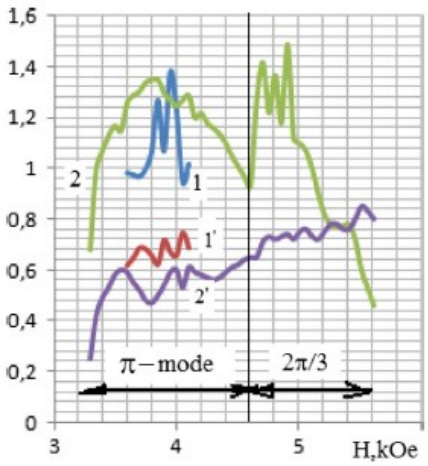

Figure 2.1.8 Power (1, 2) and efficiency (1', 2') for a short cathode ($L_{cathode} = L_{anode}$) and long cathode ($L_{cathode} = 1.4L_{anode}$), respectively, with an applied voltage of 400 kV.

$$v_{e\theta} = \frac{1}{r}\frac{cU}{H_{0z}\ln(R_a/R_c)}, \quad v_{ph} = \frac{\omega r}{n} \tag{2.1.2}$$

$$H_0 = \sqrt{H_{0z}^2 + H_{0\theta}^2} \tag{2.1.3}$$

$$v_{e\theta} = \frac{cUr}{[r^2+(2I_z/cH_{0z})^2]H_{0z}\ln(R_a/R_c)}. \tag{2.1.4}$$

2.1.1 Challenges of the MDO experimental verification

The fundamental challenge with realizing the 70% efficient MDO in experiment, aside from the manufacture of the complicated design, was the lack of realistic modeling of the confining magnetic field or emission from surfaces in the original simulation work, and the need for implementation of an effective magnetic field to prevent single-surface electron multipactor on the dielectric microwave output window. Using the analysis done at the University of Michigan [25], RF fields in excess of 115 kV/m and magnetic field present in the MDO would present conditions for multipactor. The magnetic field was originally modeled as being perfectly uniform in the magnetron interaction space between the cathode and anode and along the cathode's extended length downstream, yet very quickly diverged beyond that point [18]. Any magnetic field realizable with an electromagnet or permanent magnet fails to satisfy both of these conditions at the same time; there is always some compromise between the two. In addition, the more uniform the magnetic field is along the extended cathode's length, the more the leakage current is tapered down and curtailed, and the efficiency is increased. Although simulations at UNM on the A6 suggest that there is meaningful reduction of leakage current even for magnetic field non-uniformities of up to 16% for a cathode extension of 2.5 cm [26], reports from AFRL and our own in-house simulations demonstrated a sizeable reduction in the MDO's power and efficiency with a non-uniform magnetic field in the interaction space [22].

In addition to this problem, with a realistic Helmholtz magnetic field profile, leakage current constrained to magnetic field lines would not drift as expected to the outside walls. Instead, space charge and reduced electric and magnetic fields in the horn antenna allowed for the drift of electrons toward the axis of the MDO, where it would hit

the dielectric output window. Only cathodes that emit leakage electrons at a radius greater than 1 cm, preferably ~2 cm, in the presence of a bucking-coil configuration could successfully protect the window, as was likely concluded by the National University of Defense Technology, China [27]. They employed a flared, conical endcap and reverse bucking coil to deal with the problem of electron window impact. Curiously, they only modeled emission from a narrow region under the anode and did not include emission from their conical endcap, despite the presence of fields that exceed the explosive emission threshold for any polished metal surface.

Replacement of the artificial magnetic field in UNM's MDO simulation work with a bucking coil proved to be futile as well, because the design allowed for leakage current to escape at a small radius. This resulted in electron impact on the output window.

Reduction of leakage current that was provided by an extended cathode in a uniform magnetic field, [18], also did not occur as expected due to the field being highly non-uniform. The strongly non-uniform magnetic field was also not advantageous because it reduced the region of synchronous interaction of electrons with the operating mode. Lastly, some of the leakage current that would quickly diverge to the wall would redirect to the axis and strike the output window, Figure 2.1.9. It was postulated that some combination of magnetic mirroring and repulsive magnetic scalar potential effect caused this.

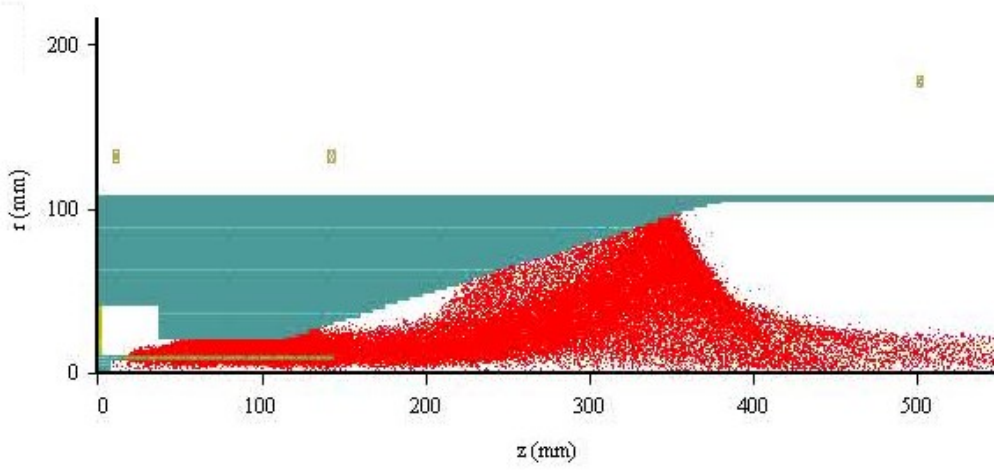

Figure 2.1.9 Electron particle plot (red) of an MDO with reverse (bucking) coil configuration.

2.1.1.1 Endcap

Simulations and experiments were performed on cathode endcap technology at UNM with the aim of protecting the output window of the MDO from electron bombardment [26]. An alternative technology to the bucking coil is the cathode endcap, which could potentially eliminate leakage current altogether. Experimental work on an MDO by Daimon and Jiang at the Nagaoka University of Technology in Japan made use of an extended cathode with a large spherical carbon endcap in the presence of a Helmholtz field [16]. Their work did not document leakage current diagnostics or report of possible effects of this current. Replication of this work in MAGIC with realistic emission thresholds of up to 300 kV/cm showed emission from this spherical endcap would occur and strike the output window. Others have also experimented with endcaps in radial-extraction relativistic magnetrons, and claimed that leakage current could be reduced but not entirely eliminated [28].

To decrease this leakage electron current several approaches and their combinations have been used: 1) the cross section of the electron beam is enlarged [28, 29] to decrease the space-charge-limited flow by using different endcaps on the cathode edge; 2) non-emitting endcaps are placed on the cathode edge that is often used in non-relativistic magnetrons [4]; 3) special cathode materials that have high threshold for explosive electron emission are used in conjunction with polished endcaps [30]; 5) different coatings are used on the cathode [30, 31].

The ideal solution to the window breakdown problem would be to completely suppress electron leakage current. The initial approach was to extend the cathode along a uniform axial magnetic field and use endcaps on the cathode edge covered by a thin dielectric. Applying a thin layer of dielectric reduces surface fields by about a factor of the dielectric constant, ε_r, as shown in Figure 2.1.10 [4]. Earlier experiments [32, 33] confirmed the ability of dielectric coatings to suppress emission. However, special care would have to be given to reduce the triple-point electric field where metal meets dielectric and vacuum [34, 35], such that surface flashover of the dielectric could be avoided [36, 37].

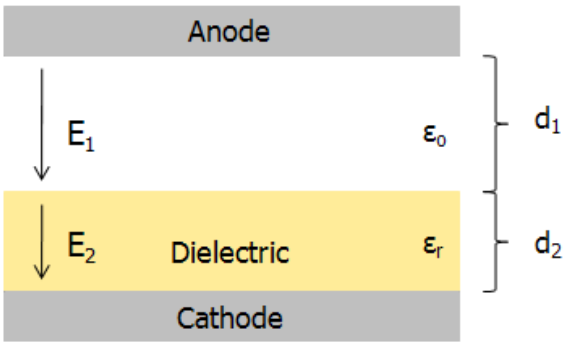

Figure 2.1.10. The electric field strength on the cathode surface is $1/\varepsilon_r$ of that with no dielectric coating.

2.1.1.2 Magnetic endcap (magcap)

The case was also considered where the annular electron flow leaving the magnetron interaction space at a large radius is not completely suppressed by a smaller-radius cathode endcap. A cathode endcap constructed of a permanent magnet with a magnetization vector aligned to the pulsed background magnetic field would create fields shaped such that electrons are pinched down to the cathode surface, preventing them from traveling further downstream and reaching the vacuum window.

Also, if annular electron leakage current emitted from the endcap with dielectric coating is not completely avoided, then a permanent magnet placed inside the endcap gives the possibility to deposit this flow significantly closer to the cathode edge than for the case without the permanent magnet to avoid electron bombardment of the vacuum window. Magnetic field lines for such a situation in the MDO are shown in Figure 2.1.11. On the circumferential surface of the magnetized endcap, the total magnetic field is nearly absent;

therefore, electrons that are born along the dielectric coating following a surface breakdown will flow toward the horn antenna following the electric field between the endcap (5) and horn antenna (2). Such an approach to reducing the path of leakage electrons from the cathode to the electron dump does not prohibit us from providing a uniform magnetic field in the interaction space, unlike the case when two coils with oppositely directed magnet fields are used, as in [27].

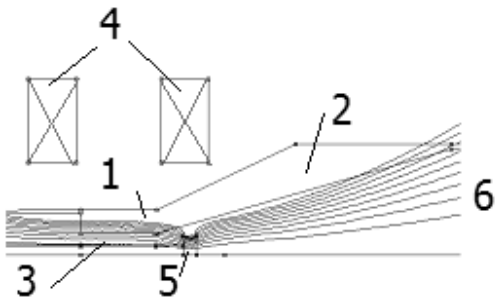

Figure 2.1.11. FEMM magnetic field solution to an MDO with a magnetized endcap at the cathode edge: 1.- anode block; 2.- horn antenna (diffraction output); 3.- cathode; 4.- Helmholtz coils creating a uniform magnetic field in the interaction space; 5.- magnetic endcap with dielectric coating; 6. – magnetic field lines.

Neodymium magnets have a conductivity of no greater than 9.1×10^5 S/m with relative permeability 1.05 H/m. The magnetic diffusion time of the pulsed magnetic field through this permanent magnet is less than that for stainless steel. As a result, the field lines in Figure 2.1.11 have time to fully penetrate the metal and provide electrons with a properly constrained path. Additionally, since the permanent magnet is aligned with the field produced by the pulsed magnetic system, it is not possible to de-magnetize it.

2.2 The compact MDO

A more compact variant of the MDO, hereon in referred to as the "compact magnetron" or "compact MDO," was conceived upon realization that the A6 magnetron could excite a TE_{11} mode in a circular waveguide that matches the outer radius of the A6 anode (4.11 cm) using the π-mode of operation in much the same way as can be done in the MDO. The bulk of the concept and initial optimization was done by Fuks and Prasad [38]. At the frequency of operation, ~2.5 GHz, the excited TE_{11} output mode is not cut-off. However, without the large optimized mode converter/horn antenna section of the MDO, microwave generation should be less powerful and less efficient. Another advantage of exciting output modes into a 4.11 cm radius is that non-TE_{11} modes that might be excited due to mode competition are cut-off, meaning that a sufficiently long extraction waveguide would attenuate and reflect unwanted modes from radiation [39]. The compact magnetron enjoyed side-grade optimization that can be seen later in this dissertation.

The advantages of the compact magnetron did not end at its ability to directly produce a Gaussian beam using a small size package; it was much cheaper to produce and could benefit from the insulating magnetic field profile of either a solenoid or permanent magnet [40], which would dump leakage current quickly to the walls of the device, thereby protecting the dielectric output window from damage. A comparison of size between the MDO and compact magnetron is seen in Figure 2.2.1 and Figure 2.2.2, which represents a potential 8-fold reduction in volume [41].

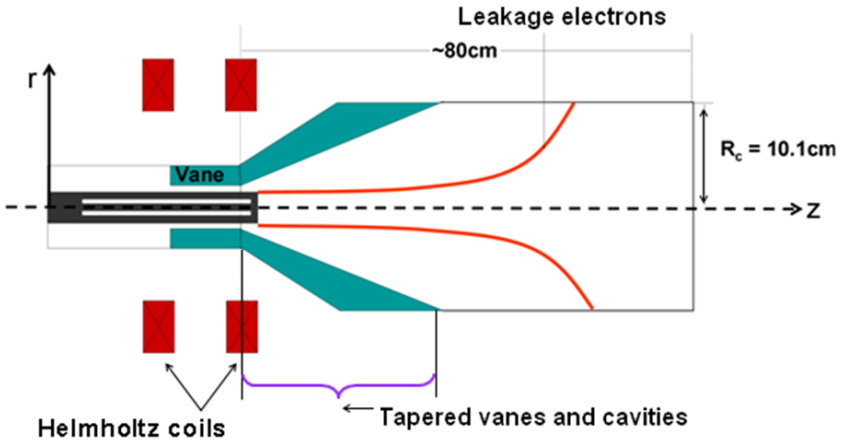

Figure 2.2.1. Schematic of the volume of experimental MDO system.

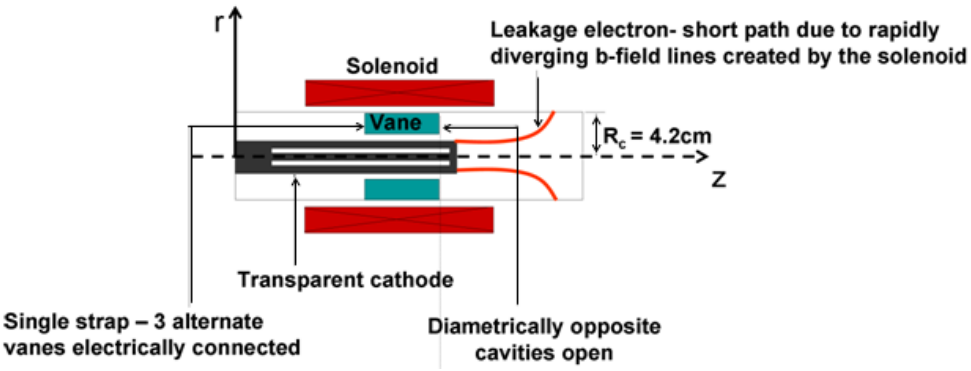

Figure 2.2.2. Schematic of the volume of the experimental compact magnetron system.

The desired TE_{11} output mode is linearly symmetric. Intuition would warrant that the arrangement of resonator cavity fields that are allowed to excite the desired mode in the downstream waveguide would share this line of symmetry, similar to [23]. This forces the requirement that the mode converter plate used to accomplish this would need to be used on a magnetron with a number, *N*, of vanes/cavities to be effective, where *N* is,

$$N = 2(2s + 1), \tag{2.2.1}$$

and where *s* is a positive integer. To achieve mode conversion between the π-mode in the magnetron interaction space to a TE_{11} output mode, only the cavity fields that align to the instantaneous polarization of the TE_{11} mode should be expressed. Alternatively, cavity fields that counter this should be repressed. This is done using a flat metal plate that features holes that are congruent with the cavity resonator slots (or slightly larger). Due to the φ-direction of the cavity fields, this imposes further limitations on the mode converter design, as these fields must add constructively or deconstructively in both the direction collinear and perpendicular to the TE_{11} mode's line of symmetry located in the φ-r plane. As such, the location of the mode converter openings must be symmetric to this line of symmetry so that the cavity field components that are perpendicular to this line may cancel. In a similar way, the placement of the mode converter openings must be symmetric to the line perpendicular to the output mode's line of symmetry.

The design permutations for a magnetron with 6 cavities ($s = 1$), 10 cavities ($s = 2$), and 14 cavities ($s = 3$) is $2s$. Configurations for these are seen in Figure 2.2.3, Figure 2.2.4, and Figure 2.2.5, [38]. In these figures, the dark grey signifies the location of the magnetron vanes, the light grey signifies the location of cavity fields that are suppressed by the mode converter, the white slots signify cavities and other areas that are not suppressed by the mode converter, and the red arrows represent the instantaneous polarization of the operating π-mode cavity fields. It is to be expected that the mode conversion efficiency would be greater for designs with a greater number of mode converter holes. The change

of loaded Q-factor with increasing number of mode converter holes is not an issue, due to it being a non-degenerate mode.

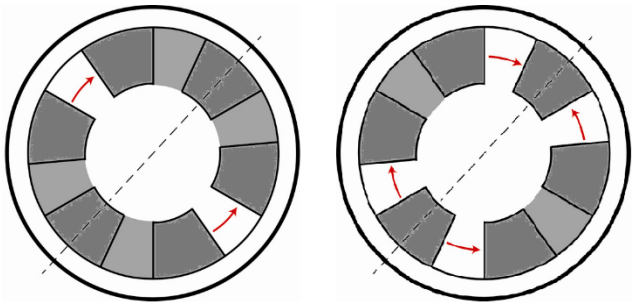

Figure 2.2.3. Design permutations for a magnetron with 6 cavities (s = 1).

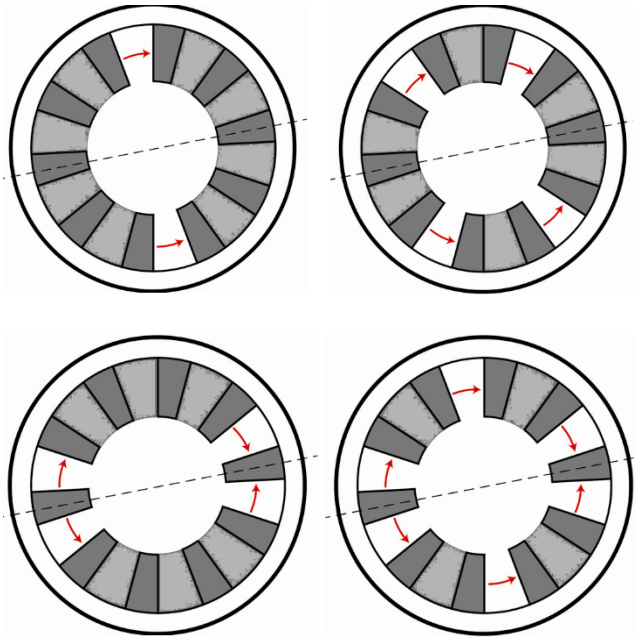

Figure 2.2.4. Design permutations for a magnetron with 10 cavities (s = 2).

One of the major advantages of using a TE_{11} output mode (that is not cut off for the standard A6 magnetron cavity radius of 4.11 cm) is that a complicated horn antenna mode

converter that tapers to a much larger radius is not necessary. Instead, an inexpensive, easy-to-machine flat metal plate can be used. However, if this plate is directly attached to the downstream side of the magnetron's anode block, vanes that are located to either side of a cavity that is blocked off by the mode converter would be effectively strapped to the 2π-mode. This is problematic to the π-mode of operation, which relies upon oppositely-polarized perturbed RF potentials across alternate vanes. Subsequent work explored slightly separating this mode converter and attachment of it to the anode block to alternate vanes, so that it would function as a π-mode strap, see for example Figure 2.2.6 for a magnetron with 6 cavities [38].

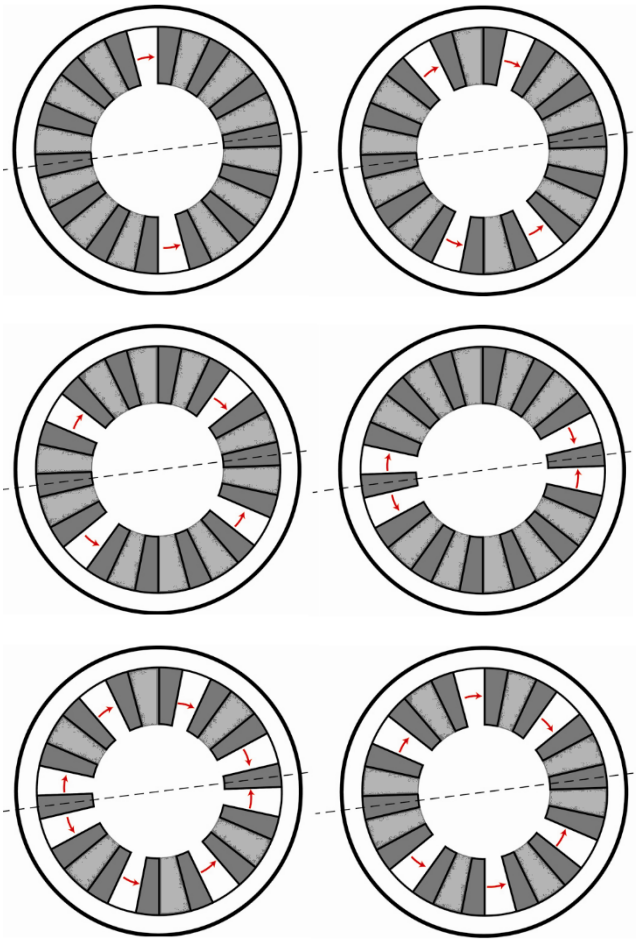

Figure 2.2.5. Design permutations for a magnetron with 10 cavities ($s = 3$).

The case was explored when the symmetry of the mode converter hole placement was broken, to test the design intuition. To that end, a magnetron with 6 and 4 cavities was considered, Figure 2.2.7 [38]. This would test both the conditions for symmetry and if the number of magnetron cavities must adhere to Equation 2.2.1, i.e. it might be possible for effective operation in a magnetron with even number of cavities. It is wholly expected that if the symmetry of the mode converter is broken, that the fields of the TE_{11} mode would be malformed, and it is possible that the symmetry of the operating π-mode would be affected.

Such a malformed mode might propagate a clean TE_{11} mode after a long-enough section of circular waveguide because the TE_{11} mode is not cut off and because the spurious modes that compose the malformed field pattern might be cut off, e.g. the TE_{21} or TE_{31} mode. The evanescent decay of these other modes might necessitate the use of a very long output waveguide, which would attenuate the output power and increase the size of the system. The possible deformation of the π-mode, the malformed generated TE_{11} mode, and a long output waveguide present several detriments to efficient generation of RF power with an asymmetric mode converter. This might exclude the use of such a mode converter in a magnetron with missing cavities [42] or with a rising-sun geometry.

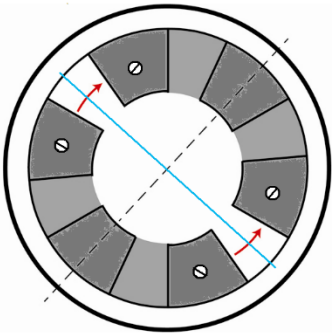

Figure 2.2.6. A mode converter on a 6-cavity magnetron that is functioning as a π-mode strap. This is attached via screws to alternate vanes. The blue line indicates that the mode converter is separated into two conductors.

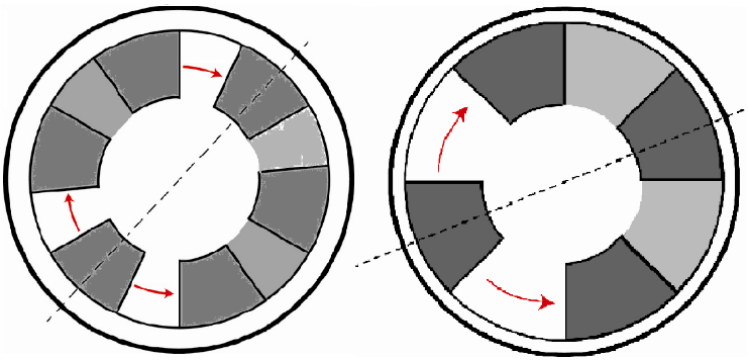

Figure 2.2.7. A 6- (left) and 4-cavity (right) magnetron with asymmetric mode converter.

As a final note on the compact MDO, an effective (500 MW) simulation design employed a single π-mode strap that electrically connected alternate vanes on the upstream side of the A6 anode block and a mode converter, as in the right side of Figure 2.2.3, directly connects to the downstream side of the anode block. Traditionally, a strap is a metal wire that traces a circle around an end of a magnetron anode block that is used to enforce the π-mode by electrically connecting alternate vanes and by supplying extra capacitance to adjacent vanes [4]. It accomplishes this by lowering the frequency of the π-mode and raising the frequency of any other mode. In a magnetron, these frequencies are usually close to one another due to the close-spacing of modes and the large size of resonators. The dynamics of how these frequencies are separated are simple: each resonator cavity in the magnetron behaves like a parallel RLC resonator with frequency $1/\sqrt{LC}$. For the π-mode, alternately-connected vanes are at the same RF voltage and hence see no current flow; at the same time, the strap connecting the two adds capacitance in parallel to the resonators because it passes over vanes of opposite RF voltage polarity. The combined effect is such that the resonator inductance does not change, the capacitance increases, and

the resonant frequency is reduced. For all other operating modes that are not π-mode, there is current flow in the straps, which leads to a parallel inductance that reduces the resonator inductance. At the same time, there is also a slightly raised value of capacitance. The net effect is that the resonant frequency of these modes increases.

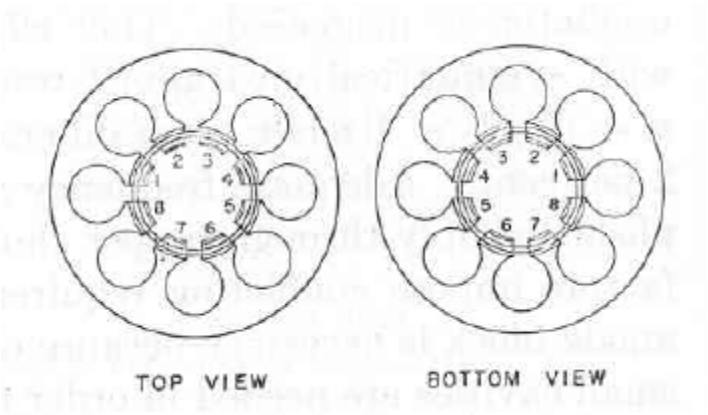

Figure 2.2.8. Illustration of a double strap configuration [4].

.

Typically for an A6 with cathode radius of 1.58 cm, the operating mode is the 2π-mode, and for smaller radii of 1-1.2 cm, the A6 favors the π-mode [6]. Recall that the compact MDO relies on the π-mode for generation of a TE_{11} output mode. As such, it was found that a single upstream strap could force a π-mode with a larger 1.58 cm cathode and lead to more powerful microwave generation than an unstrapped compact MDO of smaller radius. One thing to note about the strap design used: the separation of the strap from the vanes of opposite electrical polarity is comparable to the separation of anode-block vanes of opposite polarity. This separation avoids electrical breakdown in vacuum. However, there is still the risk of a two-surface multipactor between the strap and the anode block.

2.2.1 Challenges of the compact MDO design

A chief issue with the compact MDO is that non-desired fields in the interaction space are in close proximity to the downstream circular waveguide, leading to the excitation of undesired TE_{11}-like modes with wrong polarity that account for some 10% of the total radiated power from the source. We refer to these undesired polarities as "rotated modes." These excitation fields likely leak out of the narrow gap between the cathode and anode and stand in contrast to the desired mode-excitation fields that diffract out of the slots cut into the mode converter. Another source of the "rotated modes" is likely impurity in the π-mode, which is evident in asymmetric MAGIC electron particle plots. Should this source be considered for radar applications, the rotated mode should be eliminated as much as possible to reduce radar signal processing load and complexity. One final challenge of the compact MDO is that, similar to the MDO, the compact MDO requires protection of the output window from electron bombardment. However, the compact MDO's smaller outer diameter allows the use of a solenoid or permanent magnet, which has a rapidly divergent magnetic field that favors electron deposition upstream of the dielectric window and which is explored later in this dissertation.

CHAPTER 3 SIMULATIONS

3.1 Overview of computational codes

A variety of computational codes were used in this dissertation work. These range from particle-in-cell (PIC) finite-difference-time-domain codes (FDTD) such as MAGIC [43] and ICEPIC [44], to finite-element-method (FEM) codes such as FEMM [45] and HFSS [46], to other codes such as TopSpice [47], which is used to model and solve circuits. Use of these codes in the modern age is necessary since analytical solutions are not usually feasible for complicated geometries or circuits.

3.1.1 FDTD – MAGIC and ICEPIC

FDTD is a simple and powerful method of solving the temporal evolution of electromagnetic fields, accounting for space charge effects and charged particle currents. The concept of FDTD simulation began with a 1966 paper by Yee that proposed a numerical solution method to Maxwell's equations via a Cartesian gridding system that deconstructed electric fields and magnetic fields into set components [48, 49]. In his "Yee cell," Figure 3.1.1, electric field loops are staggered in location and time from magnetic field loops, and Ampere's Law and Faraday's Law are used to take advantage of the interlinking of these loops to solve for both fields across alternating time steps. The maximum allowable time step that does not result in numerical instability is known as the Courant limit, $\Delta t = \Delta x/(\sqrt{3}\sqrt{\mu\varepsilon})$ for 3D, which prevents field information from propagating faster than the speed of light in a given medium. After the availability of computers many years later, researchers unearthed Yee's paper and introduced changes to

the basic FDTD algorithm to include charged particles, currents, the "perfectly matched boundary layer" (PML), and other needed additions. FDTD is now one of the most popular computational techniques for electromagnetics.

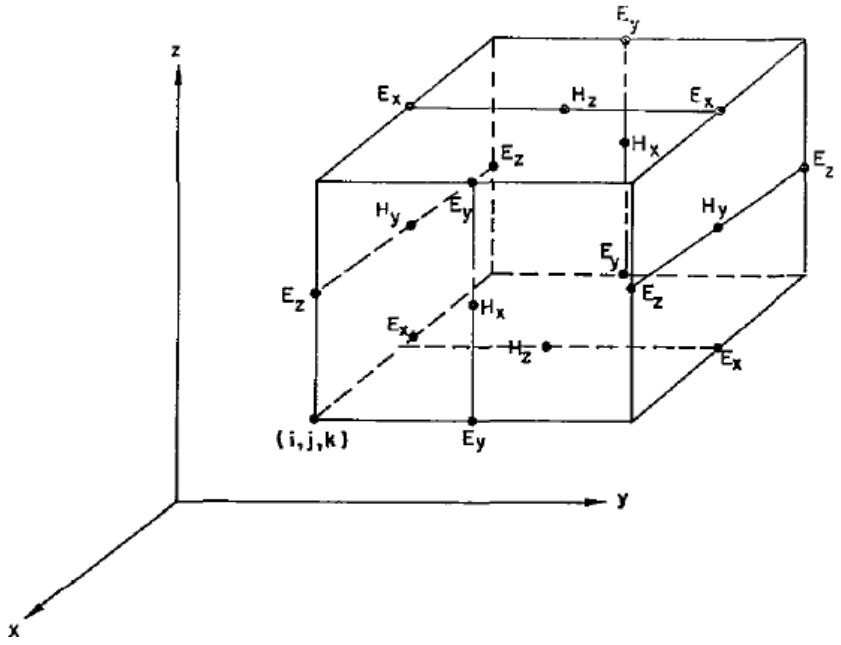

Figure 3.1.1. Cartesian Yee cell [48].

Both MAGIC and ICEPIC are FDTD codes. MAGIC was developed to deal with relativistic beam physics in high power microwave devices in 1995. MAGIC harkened the coming of age of FDTD in HPM research after introduction of a numerical damping factor designed to reduce high-frequency simulation noise that was problematic to relativistic simulations. Tuning of this numerical damping factor to match MAGIC's results to known experimental data led to validation of the MAGIC code, as it was able to successfully predict new experimental results.

Other codes soon followed, such as ICEPIC, the Air Force Research Laboratory's custom-developed workhorse code that dynamically rebalances calculation load across an array of processing nodes, allowing large-scale/fine-resolution jobs to be executed in very little time, especially when run on a supercomputing cluster. Paired with APPSPACK, a nonlinear optimization algorithm that is a part of DAKOTA [50, 51], ICEPIC can automatically optimize HPM source designs across daunting multidimensional parameter spaces. APPSPACK was used in optimization of the conical cathode endcap for the MDO, which required the delicate balancing of Helmholtz coil and bucking coil locations and currents, as well as conical endcap dimensions and placement to seek maximum power/efficiency yet minimizing the amount of current intercepting the vacuum window.

3.1.2 FEM – FEMM and HFSS

The Finite Element Method (FEM) is another popular and powerful tool to solve electromagnetic eigenvalue problems in the frequency domain. The inner workings of the FEM methodology lies in solving a governing differential equation across a geometrical space that is completed by a proper set of boundary conditions. To account for the complexity of modern problems and the real objects that are contained in them, the problem space is subdivided into smaller finite elements that are bound by nodes or edges, depending on the dimension of the problem space. Solutions to spatial locations not on nodes/edges are approximated by a chosen polynomial weighting function; higher order weighting functions will result in more accurate solutions, but add complexity to the computation.

To arrive at a solution, a technique very similar to the calculus of variations is employed, where an error function is extremized (minimized). This is accomplished by reducing the numerous node/edge equations into an integro-differential function through either minimizing a functional that represents the total energy of the system or through using a weighted-residual technique, such as the Galerkin method. Either method results in a series of linear equations that can be computationally solved, provided that the solutions convergence.

Two FEM programs were used in this dissertation work: FEMM (Finite Element Method Magnetics) and HFSS (originally High Frequency Structural Simulator). FEMM, a freeware, allowed for the rapid prototyping of electromagnet coils and permanent magnets considered for use in the MDO and compact magnetron. HFSS was used to prototype a directional coupler intended to be mounted on the output circular waveguide to be used with both sources, but production of these never commenced due the decision to instead use a calorimeter and S-band waveguide as power diagnostics.

3.2 Simulation results

In this section is detailed the computational results from a variety of codes and programs for the following topics: magnetic insulation of electrons from the MDO's dielectric output window, cathode endcaps that suppress leakage electrons, MDO operation with a spherical endcap, optimization of the compact MDO (including use of permanent magnet for insulation), a rodded meta-material-like cathode that favors the π-mode, and the pulsed electromagnet system used on the PULSERAD accelerator.

3.2.1 Magnetic insulation – MAGIC

MAGIC was used to explore numerous candidate technologies that would prevent the deposition of leakage electrons from striking the dielectric output window of the MDO and compact magnetron. Without endloss leakage current suppression, greater than 1 kA of current can impact the dielectric output window, resulting in the previously mentioned problems. UNM's optimized 70% efficiency in the MDO using MAGIC employed an unrealistic magnetic field profile that was 100% uniform along the cathode length and quickly diverged to a very low value just past the downstream end of the cathode [18]. For experimental verification of the MDO source, a realistic magnetic field solution had to be developed. The first avenue of investigation was simulating the actual electron behavior in a number of pulsed electromagnetic coil configurations, and the second was on complete prevention of leakage current using endcaps.

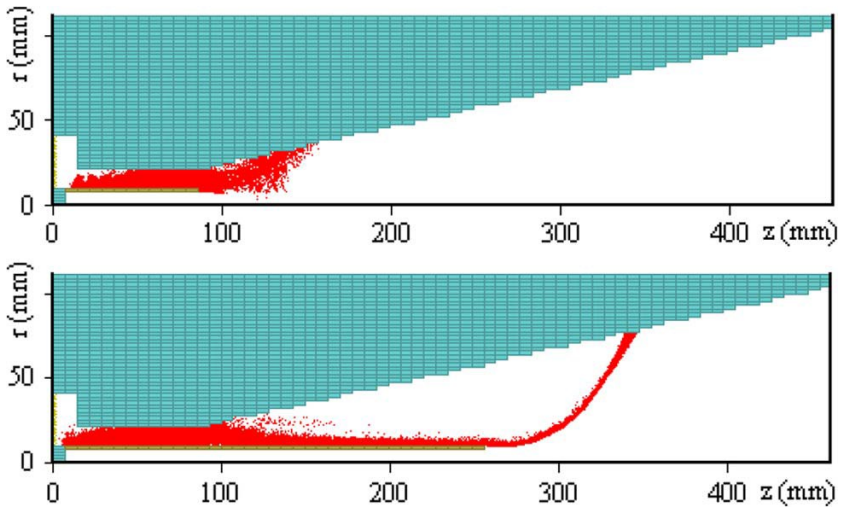

Figure 3.2.1. Electron particle plots depicting the magnetic field profile used in UNM's 70% efficiency optimization of the MDO [18].

The natural starting point for investigation was modeling the Helmholtz coil pair already in use for UNM's radial-extraction A6. The results were surprising, Figure 3.2.2, as the downstream leakage beam does not constrain itself to the magnetic field lines established by the Helmholtz coil pair shown. The magnetic field generated by the Helmholtz coil should have deposited the leakage beam much sooner and prevented impingement of the beam on the dielectric window entirely. The confinement failure is likely the result of the magnetic field dropping below the needed value where space charge effects overpower the magnetic field. The electric field in the horn antenna and further downstream also quickly falls off, as there is no coaxial structure there to support high fields. Modulation of the beam by the output microwave field can be seen in the beam striations in the right-hand side of Figure 3.2.2.

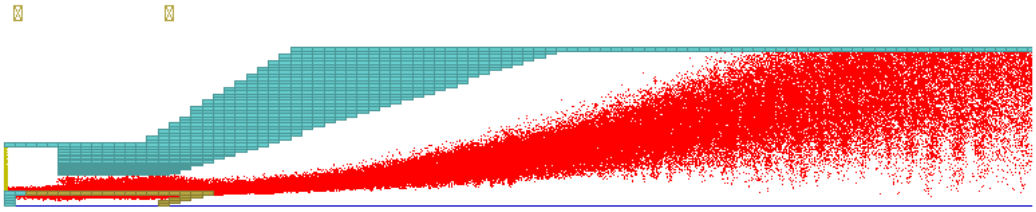

Figure 3.2.2. MAGIC results showing the divergence of the electron beam (red) from the anticipated following of the magnetic field profile.

Moreover, simulated attempts to contain the leakage electron beam were unsuccessful with any bucking coil (reverse downstream coil) configuration. A typical result of these attempts is shown in Figure 3.2.3. This was equally surprising, and it was eventually concluded that magnetic scalar potential effects were responsible for electron

trajectories that would otherwise dump to the anode wall, turning electrons down to the axis and drifting into the window. After consideration, use of an exotic coil design was abandoned, and another technology was explored: the cathode endcap.

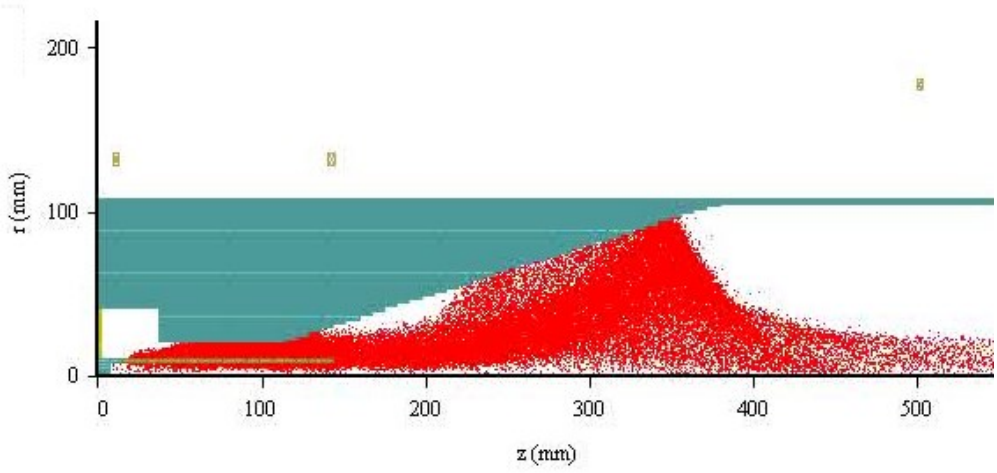

Figure 3.2.3. A downstream reverse (bucking) coil configuration failed to deposit electrons on the anode, resulting in electron impact on the simulated output window along the axis.

3.2.2 Endcap, magcap – FEMM, MAGIC, and ICEPIC

With coil configuration solutions not meeting expectations, completely eliminating the leakage beam seemed to be the only solution, although this has never been achieved previously in a relativistic system.

Computer simulations using the particle-in-cell (PIC) code MAGIC [26] indicate (Figure 3.2.4) that, in comparison with a short cathode, the thickness of the electron hub drifting downstream along the uniform axial magnetic field is significantly less for the extended cathode. This behavior persists up to a 2.5% non-uniformity in axial field that was

produced by a Helmholtz coil pair. With a cathode extension of 2.5 cm, simulations show this behavior persists weakly even up to a 16% non-uniformity in the axial field, where uniformity is measured along the length of the extension. This reduction in electron cloud thickness is caused by two factors: i) the axial electric field $-E_z$ of the electron space charge that fills the interaction space and the azimuthal magnetic field H_θ of the axial cathode current that provides negative radial drift (to $-r$) of electrons leaving the interaction space, $v_r \sim -E_z H_\theta$; ii) the radial electric field E_r along the extended cathode gradually decreases, which reduces the height of the electron trajectories that determine the thickness of the electron hub. For the short cathode the electric field $E_r(z)$ downstream of the anode block is absent, resulting in a thicker flow of leakage electrons moving along the magnetic field, which in turn reduces the negative radial drift.

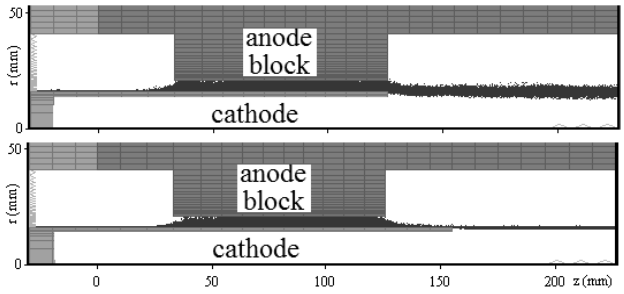

Figure 3.2.4. Electron trajectories in the magnetron with short (top) and extended (bottom) cathodes (from PIC simulations).

The advantage of using a cathode that extends beyond the anode block was readily apparent in these simulations. Even though it did not completely eliminate the leakage current, it did increase the fraction of emitted electrons that would lose energy to the

microwave field. With the goal of eliminating the leakage current to zero, this elongated cathode feature was retained and a cylindrical endcap with radius larger than the inner anode surface was added.

Knowing full well that emission from the endcap's surface would be a problem, the use of a dielectric coating on metal surfaces to suppress emission in previous work provided new inspiration to the problem. It is possible to coat a cylindrical endcap with dielectric and to nest the triple point in an area of low electric field just above the lowered radius of the leakage electron cloud that the extended cathode provided, Figure 3.2.5.

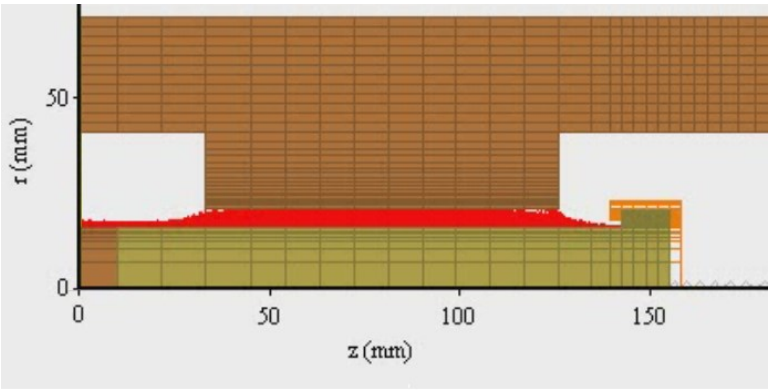

Figure 3.2.5. Cathode endcap with dielectric coating (orange) and nested triple point.

3.2.2.1 Spherical endcap - ICEPIC

This dielectric-coated endcap scheme can be directly translated into the compact magnetron; however, the tapered shape of the downstream section of the MDO anode creates a situation where a cylindrical endcap would pass too close to the anode, causing high electric field. A spherical endcap would be more suitable. Because modeling of the

surface fields on a spherical endcap requires a finer 3D mesh, ICEPIC was chosen because of its powerful multiprocessor capabilities. Figure 3.2.6 below shows the surface fields (as visualized using VisIt) for a spherical endcap of radius 2 cm that has its center located ~2.5 cm from the end of the MDO's interaction space when the applied voltage is 350 kV. The fields shown barely exceed 300 kV/cm, which is at the explosive emission threshold for well-polished stainless steel, indicating that this could be a viable solution to suppress leakage current. As such, it was tested in MAGIC for viability, Figure 3.2.7, and was employed in the MDO experiments, Figure 3.2.8.

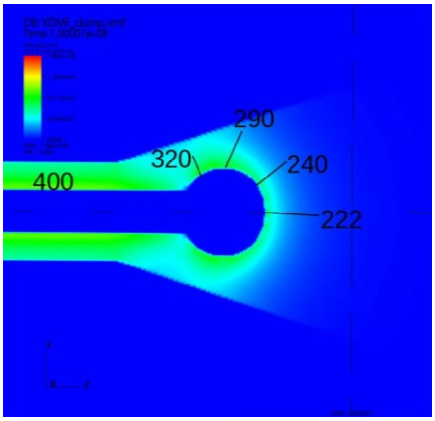

Figure 3.2.6. ICEPIC "cold" solution to cathode and spherical cathode endcap fields with an applied voltage of 350 kV.

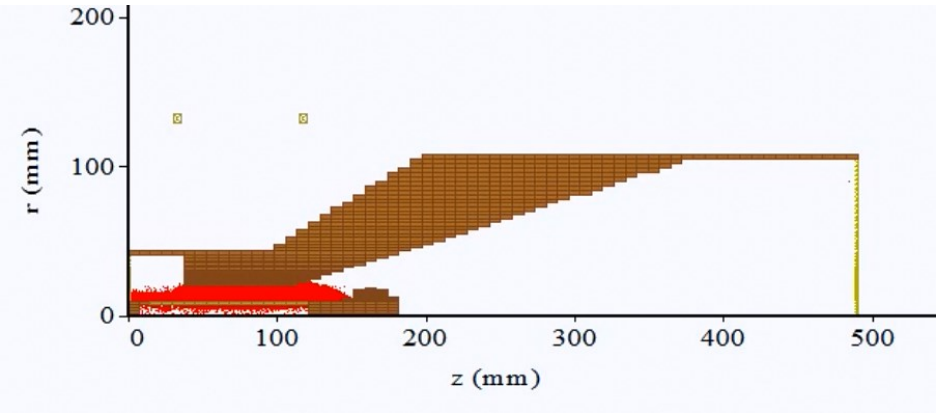

Figure 3.2.7. MAGIC electron (in red) particle plot of an MDO with non-emitting spherical cathode endcap.

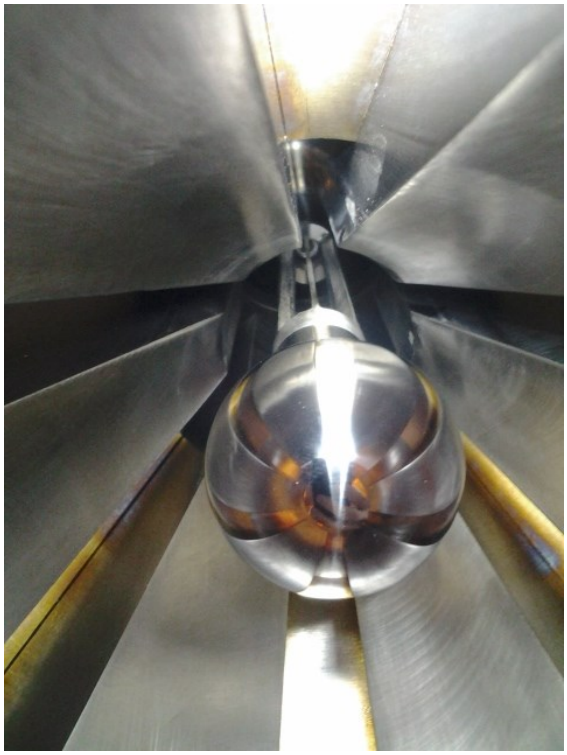

Figure 3.2.8. Photograph of the polished stainless-steel spherical endcap used in MDO experiments that was based on the MAGIC designs.

3.2.2.2 Magcap - FEMM

FEMM also allowed rapid calculations that were predictive in improving the cathode endcap design through the incorporation of permanent magnets. If annular electron leakage current from the endcap with dielectric coating is not completely suppressed, then a permanent magnet placed within the endcap gives the possibility to deposit this flow significantly closer to the cathode edge than without the permanent magnet to avoid electron bombardment of the vacuum window. Magnetic field lines for such a situation in the MDO are shown in Figure 3.2.9. On the circumferential surface of the magnetized endcap, the total magnetic field is practically absent; therefore, electrons that are born along the dielectric coating following a surface breakdown will flow toward the horn antenna following the electric field between the endcap (5) and horn antenna (2). Such an approach to reducing the path of leakage electrons from the cathode to the electron dump does not prohibit us from providing a uniform magnetic field in the interaction space, unlike the case when two coils with oppositely directed magnet fields are used, as in [27].

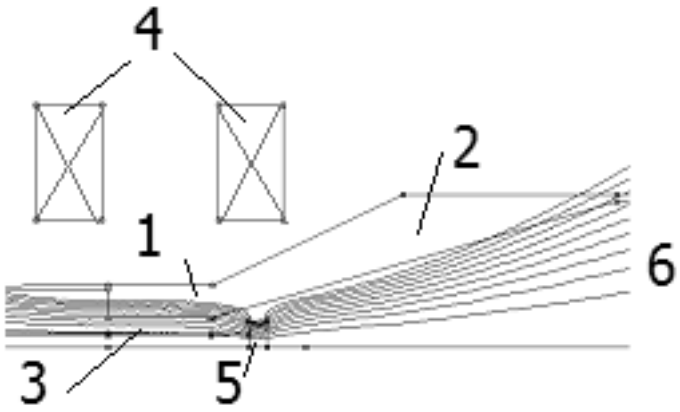

Figure 3.2.9. MDO with a magnetized endcap at the cathode edge: 1. anode block; 2. horn antenna (diffraction output); 3. cathode; 4. Helmholtz coils creating a uniform magnetic field in the interaction space; 5. magnetic endcap with dielectric coating; 6. magnetic field lines.

Neodymium magnets have a conductivity of no greater than 9.1×10^5 S/m with relative permeability 1.05 H/m. This supports a magnetic diffusion time of the pulsed magnetic field that is less than that of stainless steel. As a result, the field lines in Figure 3.2.9 have time to fully penetrate the metal and provide electrons with a properly constrained path. Additionally, since the permanent magnet is aligned with the field produced by the pulsed magnetic system, it is not possible to de-magnetize it. One potential disadvantage of using a magnetic endcap is that if the upstream side of the endcap should emit, the electric and magnetic fields would roughly share collinear paths to the anode, completely disrupting magnetic insulation and causing a short in the diode.

3.2.3 MDO operation with a spherical endcap

MAGIC simulations were performed for an MDO with a transparent cathode, a spherical endcap, and with a Helmholtz coil pair providing magnetic insulation, Figure 3.2.10. Due to physical constraints, the spacing between the Helmholtz coil pair was slightly reduced. This was the first serious attempt to simulate the MDO under real experimental conditions. A magnetic field scan was performed with power extracted from 6, 4, and 2 cavities and with a 4 ns risetime, 30 ns flattop 350 kV driving pulse (voltage dynamically enforced by the CIRCUIT command), Figure 3.2.11 and Figure 3.2.12.

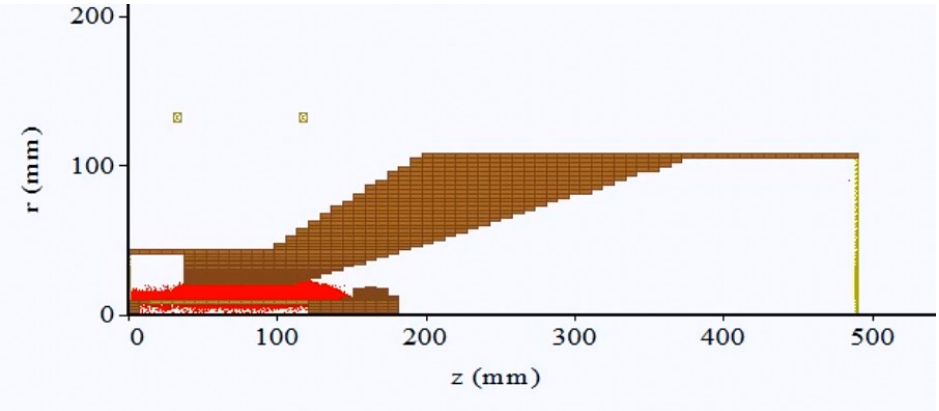

Figure 3.2.10. MAGIC MDO simulation with transparent cathode, spherical endcap, and modified Helmholtz coil pair.

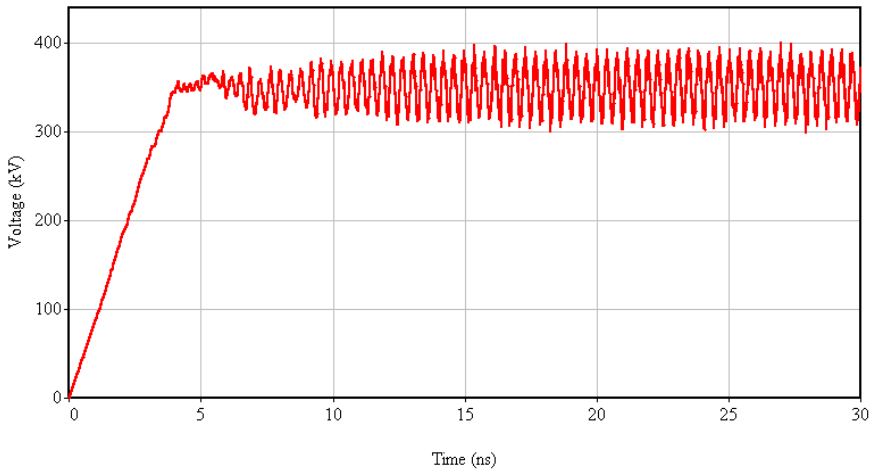

Figure 3.2.11. MAGIC 3D CIRCUIT command enforcing a 350 kV pulse and suppressing natural voltage reflections.

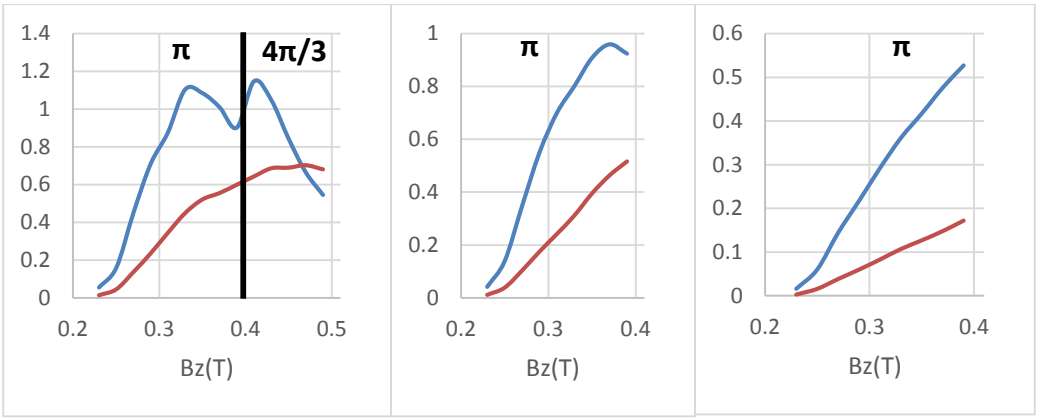

Figure 3.2.12. MAGIC simulation results for MDO power (GW, blue) and efficiency (red) for 6-cavity extraction (left), 4-cavity extraction (middle), and 2-cavity extraction (right). Also shown is the operating mode.

After preliminary experimental data for the MDO with spherical endcap was obtained, there was difficulty in interpreting the behavior of the device that stemmed from

the impedance mismatch of the 20 Ω transmission line to the 60-100 Ω MDO. The 20 Ω design was optimized for an A6 magnetron with radial extraction. Initially in experiments, a voltage would be launched down the pulser's 20 Ω transmission line such that when the MDO reached current and power saturation it would see 350 kV. This was accomplished by altering the pulser's Marx-bank charging voltage. For example, at 0.43 T and 350 kV, simulations indicate that the MDO should behave as an 83 Ω load. Equation 3.2.1 states that only 217 kV would be needed on the transmission line to deliver this 350 kV pulse.

$$V_0 = V_L/(1 + (Z_L - Z_0)/(Z_L + Z_0)), \tag{3.2.1}$$

where V_0 is the voltage incident on the load from the transmission line, V_L is the voltage on the load, Z_0 is the transmission line impedance, and Z_L is the load impedance.

Because the experiment's voltage probes were numerically integrated after data acquisition, it was not possible to in real time determine which shots were in an acceptable voltage range and which were not. Initially, the self-integrated current signal from the Rowgoski coil diagnostic was used as a measure of shot accuracy and consistency by comparing to the simulation data since early power diagnostics were neither accurate nor immediate. However, the current waveforms obtained in experiment did not match what was observed in simulations and did not appear to reach saturation until halfway through the applied 30 ns voltage pulse.

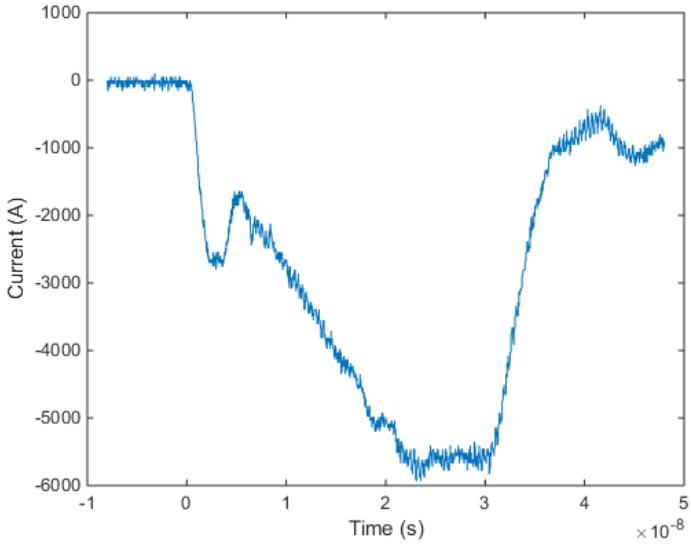

Figure 3.2.13. MDO current pulse obtained in experiment.

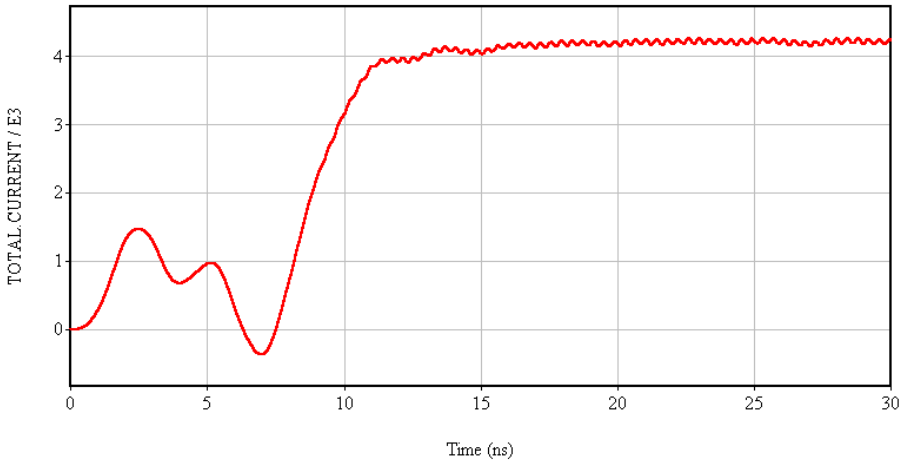

Figure 3.2.14. MAGIC 3D (with CIRCUIT command) current pulse does not match experimental data seen in Figure 3.2.13.

This was troubling, but a number of simulation steps helped to understand what occurred in experiment. A 2D MAGIC simulation of the 20 Ω transmission line and oil-

vacuum interface was performed, Figure 3.2.15. It was discovered that the 4 ns risetime, 30 ns flattop voltage pulse would see a slight bump on the leading edge of the wave, Figure 3.2.17. This voltage bump would further be enhanced when the voltage wave hits the MDO before the current turns on because it has near-infinite impedance and would nearly double the voltage delivered by the 20 Ω transmission line for a short period of time.

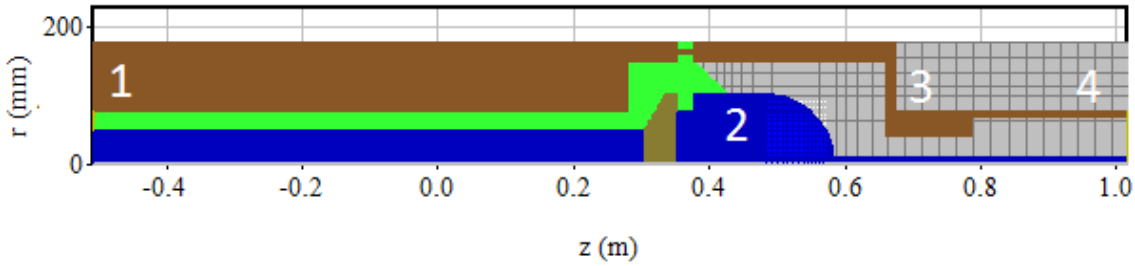

Figure 3.2.15. MAGIC 2D representation of the 20 Ω transmission line used to feed the MDO load: (1) 20 Ω oil-insulated line voltage input, (2) 20 Ω oil-vacuum interface, (3) marked location of MAGIC 3D's MDO file, and (4) marked voltage-measurement location of 80 Ω outlet port "load."

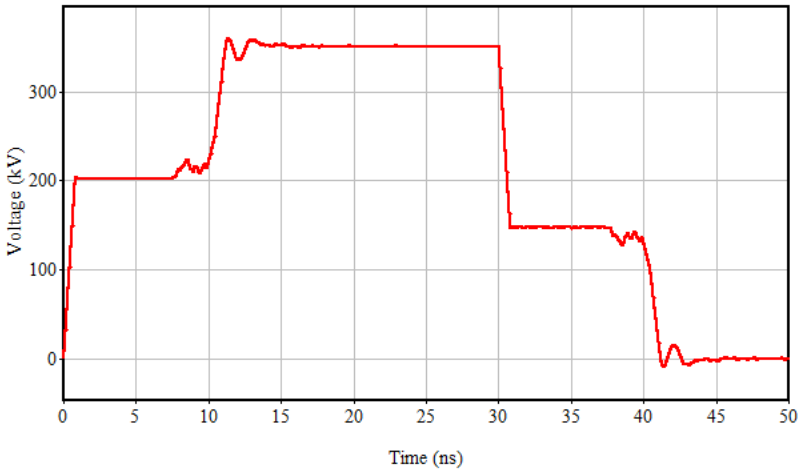

Figure 3.2.16. MAGIC 2D voltage measurement at location 1 of Figure 3.2.15.

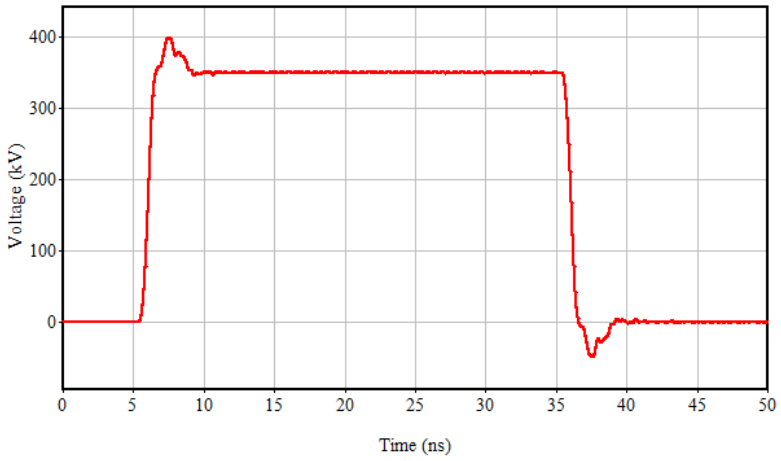

Figure 3.2.17. MAGIC 2D voltage measurement at location 3 of Figure 3.2.15.

To fully render the dynamic changes to the voltage wave seen by the MDO, it was necessary to remove the CIRCUIT command from the MAGIC 3D input file, input the MAGIC 2D modified voltage wave seen in Figure 3.2.17, and modify the inlet port to 20 Ω. This allowed the simulations to better inform the experiments which relied on a 20 Ω

input transmission line and which needed an output power of ~500 MW that would not breakdown the air just outside of the antenna. To do this, the simulated inlet voltage was reduced to 200 kV to provide 520 MW and 72% efficiency at 0.51 T. These parameters would provide excellent conditions for experimental verification of 70% efficiency using the calorimeter. Over a range of magnetic fields that spanned 0.37-0.51 T, the π-mode and 4π/3-mode were generated in similar trends to the original optimization simulations, Figure 3.2.18 and Table 1.

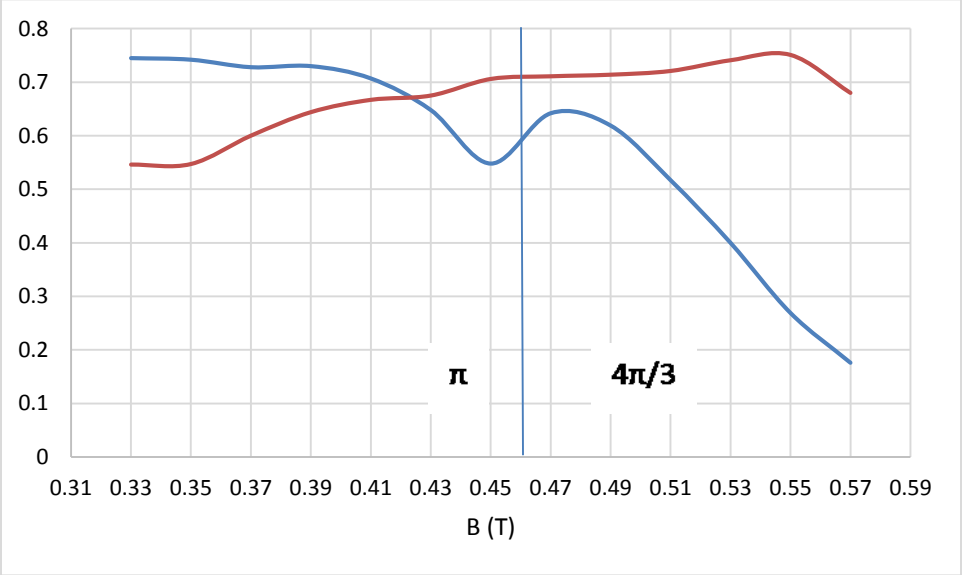

Figure 3.2.18. MAGIC 3D MDO power (GW, blue) and efficiency (red) with modified voltage pulse (Figure 3.2.17) launched from a 20 Ω inlet port with the CIRCUIT command turned off.

Table 1. MAGIC 3D results for MDO with modified 200 kV voltage pulse launched into a 20 Ω inlet port and with the CIRCUIT command disabled.

B (T)	V (kV)	I (kA)	Z (Ω)	P (GW)	η (%)	F (GHz)	Mode
0.33	313	4.29	69.6	0.745	54.6	2.5	π
0.35	320	4.05	77.1	0.742	54.7	2.38	π
0.37	328	3.59	87.5	0.728	60	2.38, 2.53	π
0.39	334	3.37	97.5	0.73	64.4	2.38	π
0.41	341	3.04	107.5	0.707	66.7	2.38	π
0.43	347	2.67	127.2	0.648	67.5	2.35	π
0.45	357	2.13	163.4	0.548	70.6	2.35	π
0.47	350	2.58	135.5	0.642	71.1	2.58	4π/3
0.49	356	2.32	151	0.619	71.4	2.55	4π/3
0.51	360	1.93	187.5	0.517	72.1	2.55	4π/3
0.53	375	1.45	251.1	0.400	74.1	2.55	4π/3
0.55	386	0.96	424.8	0.269	75.1	2.525	4π/3
0.57	387	0.65	560	0.176	68	2.5	4π/3

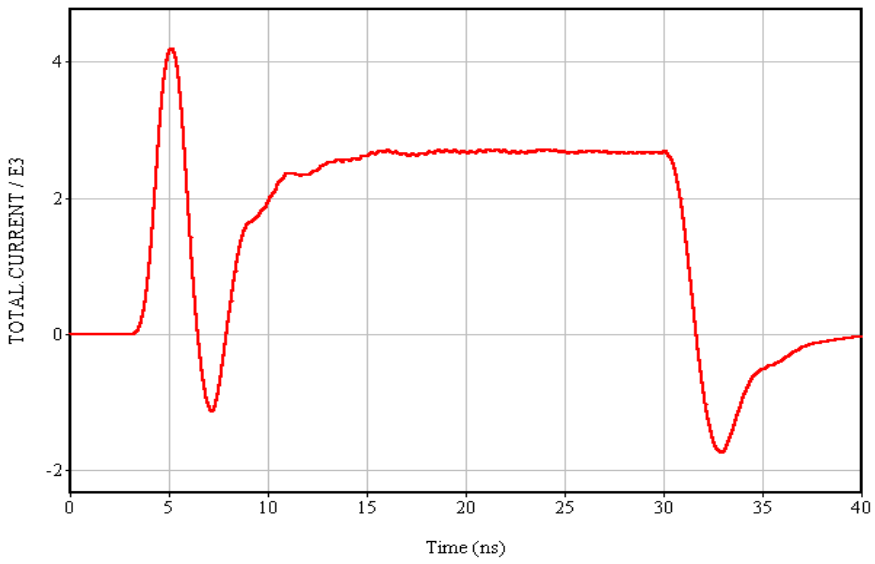

Figure 3.2.19. MAGIC 3D (without CIRCUIT command) current pulse more resembles experimental data.

Although the current pulse shape was also a closer match to experiment, values in experiment were still off by ~1 kA compared with computer simulation results. To account for this, extra emission surfaces were added to the end of the cathode and on select regions of the cathode endcap. Although these later simulations did not match the microwave power produced in experiment, the current pulse shape and amplitude did match, Figure 3.2.20 and Figure 3.2.21.

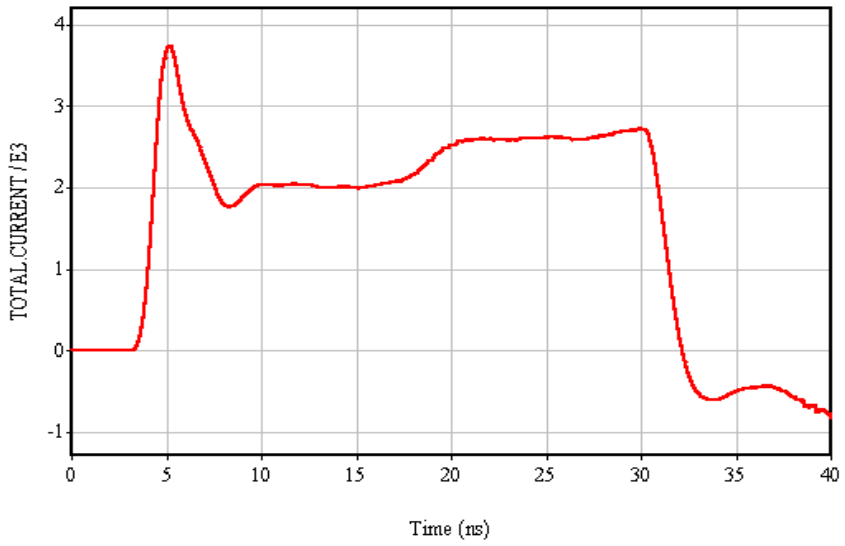

Figure 3.2.20. When emission on select surfaces of the cathode endcap is turned on, the current pulse shape and magnitude closely resemble experimental data.

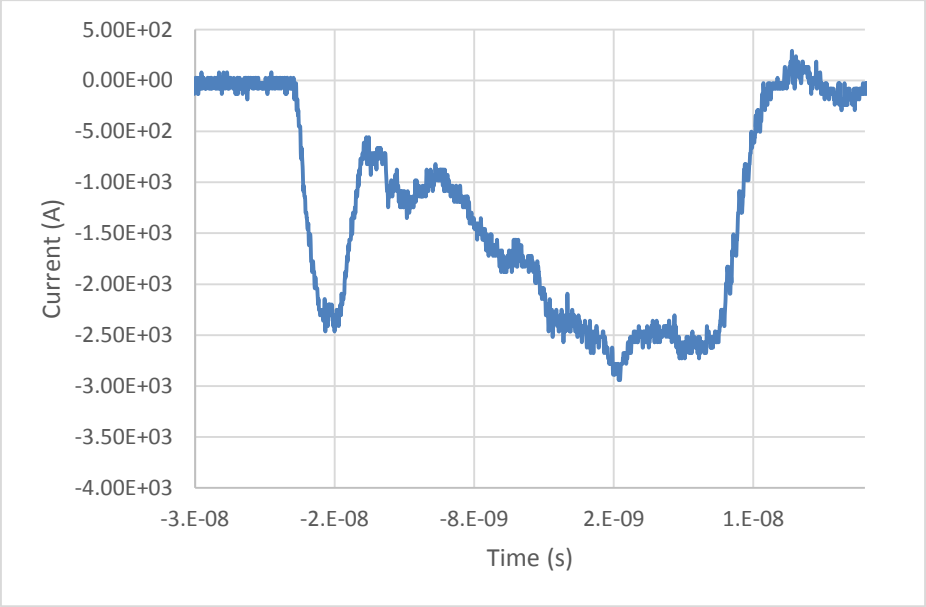

Figure 3.2.21. Experimental MDO current pulse at 0.51 T and a 20 Ω feed voltage of 200 kV.

Another attractive feature of modifying the original MDO MAGIC input file to include a 20 Ω inlet port is that the diameter of the inner conductor (cathode) is large for a short portion near the inlet port, Figure 3.2.22; this allows the interception of upstream leakage current before it would hit the inlet port and prevents loss of energy from the simulation system in a way that does not occur in experiment. Because the input current is calculated by the integral of $\boldsymbol{S} * d\boldsymbol{A}$ divided by the inlet voltage, where $\boldsymbol{S}$ in the Poynting vector of power flow and $d\boldsymbol{A}$ is a differential area of the simulation inlet port, and because impact on the inlet port by electrons would lower the input power calculated at the port, removing the impact of the beam on the inlet port resulted in more accurate current measurement. This current measurement is also a better match for the current diagnostics in the experiment, a self-integrating Rogowski coil loop that effectively measures $\boldsymbol{J} * \mathrm{d}\boldsymbol{A}$ in its interior, where $\boldsymbol{J}$ is the current density in the cathode and vacuum region and where $d\boldsymbol{A}$ is a differential portion of the area enclosed by the coil. This might not be immediately intuitive since the value of current measured by the Rogowski is the current flowing along the cathode minus the upstream leakage current that deposits on a cathode-potential dome just upstream of the coil. However, the simulation will automatically calculate this current difference since the upstream leakage current electrons merge back into the larger-diameter 20 Ω hub on the cathode shank, thereby reducing the total current seen by the simulated system.

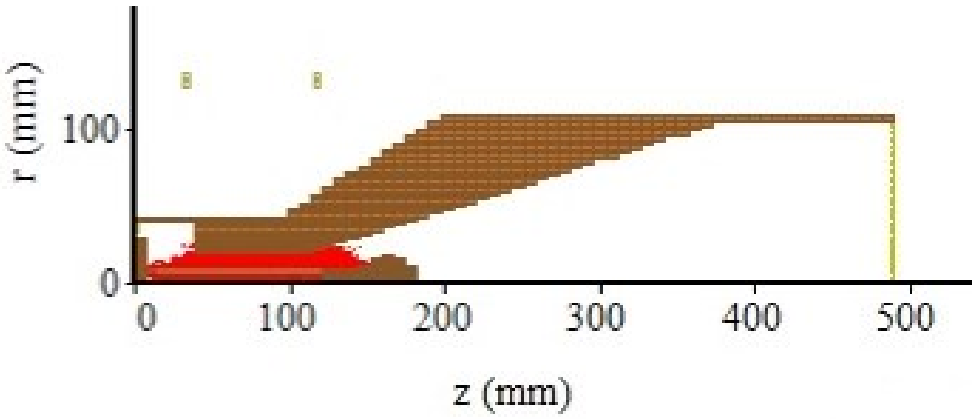

Figure 3.2.22. Modified MAGIC MDO geometry that includes a 20 Ω inlet port that has a large inner diameter and is short in the z-direction. This also serves to intercept upstream leakage current.

3.2.4 Compact magnetron – MAGIC

To demonstrate the efficacy of a compact magnetron with Gaussian radiation pattern, computer simulations of this new configuration were performed using MAGIC [38, 43], with the goal of demonstrating effective conversion of the operating π-mode to an output TE_{11} mode. For the PIC simulations and in planned experiments, the selected anode block was the A6 magnetron [6]. A transparent cathode was chosen for fast establishment of the π-mode and higher mode saturation power than the solid cathode [12, 52]. To facilitate comparison, a transparent cathode of radius $R_c = 1.45$ cm provides a much faster start of oscillations than a solid cathode of radius $Rc \leq 1$ cm with power saturating after 30 ns for the π-mode. To match the voltage pulse planned to be used in experiments, a 30 ns voltage pulse with rise time 4 ns was applied. The solid cathode was an untenable solution due to the slow RF rise time it produces. However, cathodes with radius greater than 1 cm in the

A6 magnetron have a propensity to operate in the 2π-mode, which is undesirable. As such, a strapping system had to be devised to fix the mode of operation to the π-mode, as can be seen in Figure 3.2.23 (top) [38].

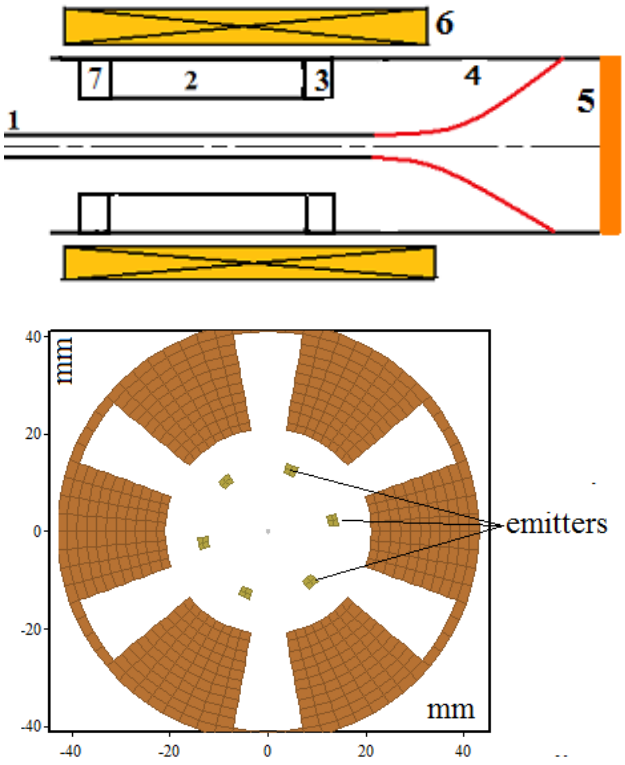

Figure 3.2.23. An *r-z* plane schematic of the compact magnetron (top) with (1) transparent cathode, (2) anode block, (3) mode converter, (4) output waveguide, (5) dielectric window, (6) solenoid electromagnet, (7) and π-mode strap. An r-φ cross section of the compact MDO (bottom).

Simulations were performed with the transparent cathode strips clocked as seen in Figure 3.2.23 (bottom), which is the optimal clocking for power and efficiency for a standard A6 magnetron with radial extraction operating the 2π-mode [11, 52]. This is for

the case where the applied magnetic field is coming out of the page and where the electron cloud **E** x **B** drift is counter-clockwise. No effort was made to ascertain if this clocking position was best for the compact MDO operating in the in π-mode.

As per previous discussion in Chapter 2, the simulated design of the mode converter was as a thin metal plate with either 2 or 4 holes that were congruent to the resonator cavity shapes. This was directly attached to the anode block. It was necessary to enforce the π-mode with a thin-band strap on the upstream side of the anode block with the 1.45 cm radius transparent cathode. As such, with a mode converter with 4 holes, an applied magnetic field of 0.57 T, and voltage of 350 kV, the compact MDO can be seen operating in the π-mode and generating a TE_{11} output mode with a power of 520 MW and a frequency of 2.44 GHz, Figure 3.2.24 and Figure 3.2.25 (left). Some asymmetry in the π-mode and TE_{11} output mode can be seen in Figure 3.2.24. As also mentioned in Chapter 2, the direct connection of the mode converter to the anode block is likely the cause of this asymmetry.

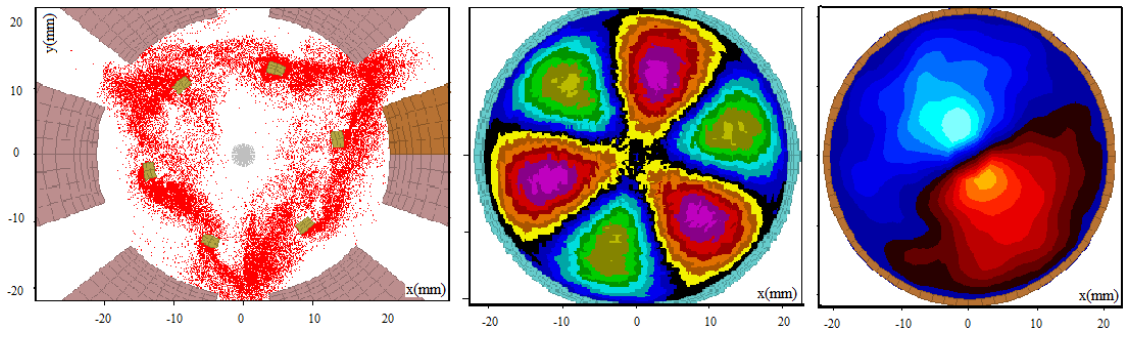

Figure 3.2.24. Operation of the compact MDO in the π-mode (left and center) with a TE_{11} output mode (E_φ right) at an applied magnetic field of 0.57 T and voltage of 350 kV.

Strap thickness and distance from the anode block had little effect on the performance of the source. For example, the thickness of the straps was varied between 5–17.5 mm, and the length of the stubs mounting the strap was varied between 5–10 mm. However, addition of a second strap slightly reduced the power, Figure 3.2.25 (right).

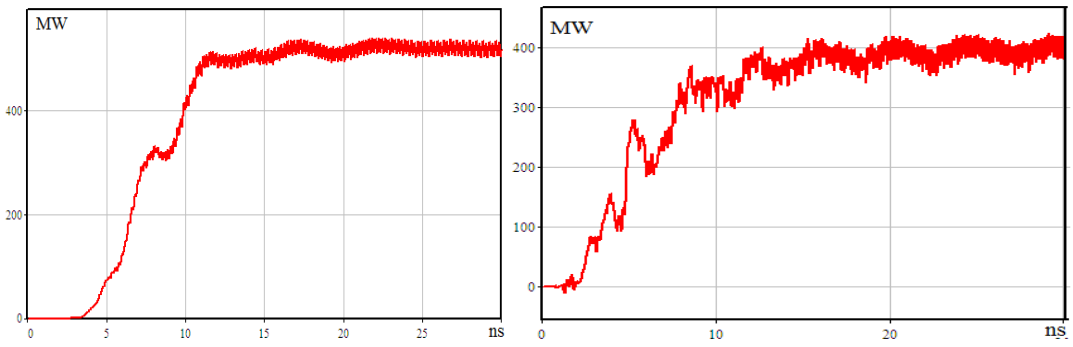

Figure 3.2.25. Output power of the compact MDO vs. time (ns) at an applied magnetic field of 0.57 T and voltage of 350 kV with single strap (left) and double strap (right).

At this voltage and magnetic field, anode current for the device was ~13 kA, and the leakage current was ~3.3 kA, Figure 3.2.26 [38], resulting in an electronic conversion efficiency $\eta_e \approx 14\%$ and a total efficiency is $\eta \approx 12$ %.

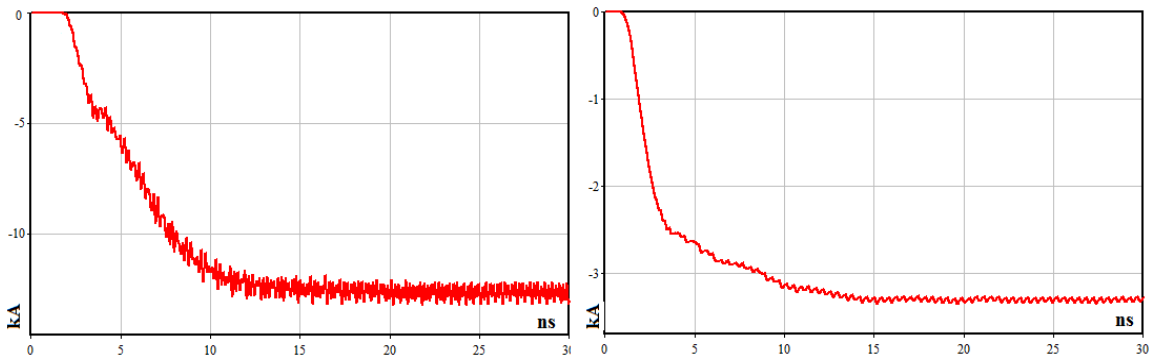

Figure 3.2.26. Anode (left) and leakage current (right) vs. time (ns) in the compact MDO with an applied magnetic field of 0.57 T and voltage of 350 kV.

As predicted in Chapter 2, use of a mode converter with only 2 holes resulted in reduced output power and efficiency, Figure 3.2.27, in the TE_{11} mode [38]. However, it was not possible to generate the π-mode when such a mode converter was directly attached to the anode block. Operation in the π-mode was observed in simulations for separation distances between 1.8-3.6 mm. When the 2-hole mode converter was instead attached as a π-mode strap, as in Figure 2.2.6, there was little change in the output power compared to Figure 3.2.27. The general behavior of the directly-connected, separated, and strap-connected mode converters strongly suggests that the directly-connected design does enforce 4 of the 6 cavities to the 2π-mode and that this effect is enough to be detrimental to the performance of the source.

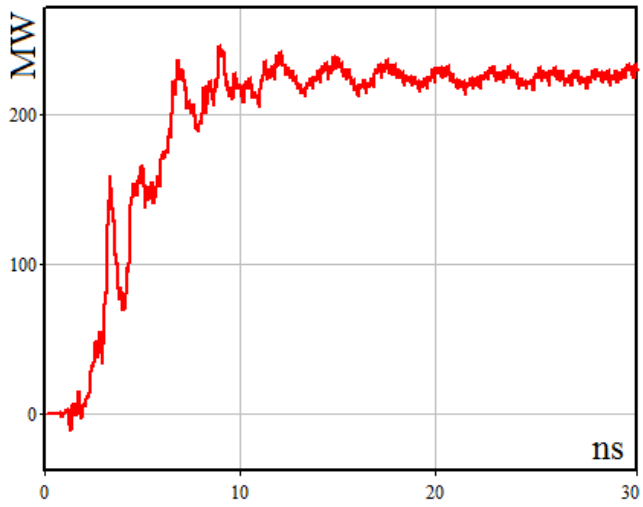

Figure 3.2.27. Output power of the compact MDO vs. time (ns) with a 2-hole mode converter that was separated 1.8 mm from the anode block.

These results verify that is possible to generate the TE_{11} mode from the π-mode with such a mode converter, provided that the radius of the cavities exceeds the cutoff of that mode at the operating frequency. Although the efficiency is less than that of the full-size MDO, the compact MDO is less complicated and thus much easier to construct. However, radiation of ~500 MW in experiment from a circular antenna aperture of equal radius to the outer cavity radius (4.11 cm) will likely result in air breakdown. Attachment of a conical horn antenna that is tapered to a larger radius would be necessary.

It was interesting to note that tuning the phase velocity of the outlet port in MAGIC created a reflection coefficient of the incident outgoing RF power with the outlet port of magnitude $\rho = \left[\left(\nu - \nu_{port}\right)/\left(\nu + \nu_{port}\right)\right]^2 = 0.05$ (where ρ is the reflection coefficient of the incident RF wave, ν is the phase velocity of the incident wave, and ν_{port} is the user-

defined matched phase velocity of the outlet port) and caused an increase in output power, Figure 3.2.28 (left), over that seen in Figure 3.2.25 (left) [38].

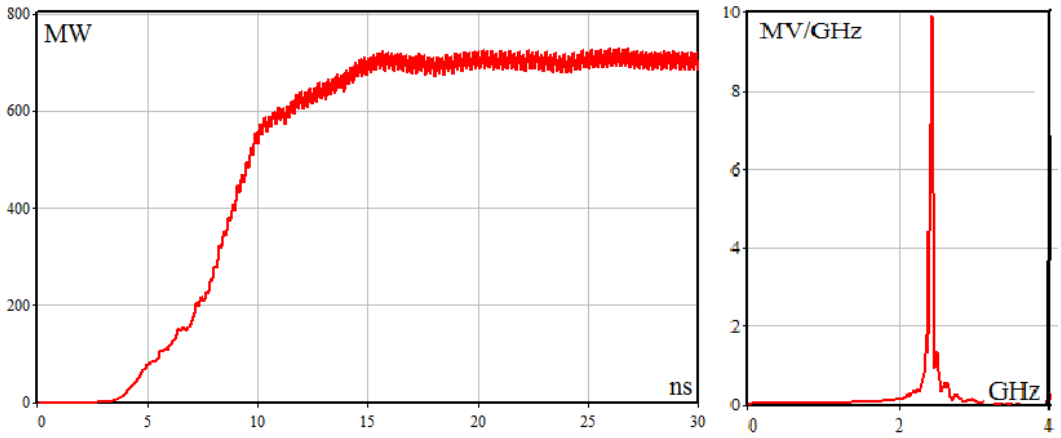

Figure 3.2.28. Output power (left) of the compact MDO vs. time (ns) and spectrum (right) when the reflection coefficient on the outlet boundary is tuned to 0.05 by adjustment of the boundary's phase velocity.

To provide a holistic analysis of the efficacy of the compact magnetron, it was necessary to study the impact of asymmetric excitation of the downstream circular waveguide. It was found that with a 3-hole mode converter (Figure 2.2.7 (left)), there was low efficiency of mode conversion using an asymmetric converter, Figure 3.2.29 (left), and its fast Fourier transform (FFT) spectrum indicates the presence of multiple frequencies, Figure 3.2.29 (right) [38]. Moreover, the case was simulated where the mode converter is used in a magnetron with N number of cavities that does not conform to Equation 2.2.1. A 4-cavity magnetron that employed a 2-hole mode converter generated very low power, Figure 3.2.30.

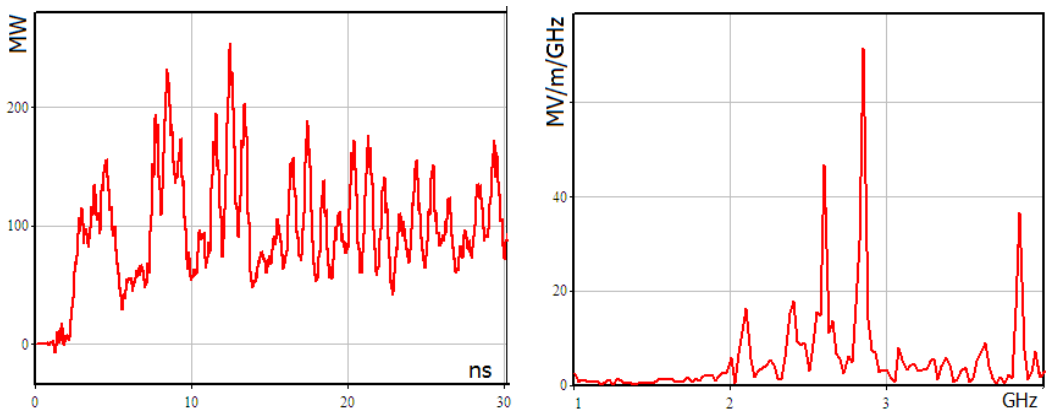

Figure 3.2.29. Output power (left) of the compact MDO vs. time (ns) and spectrum (right) with an asymmetric 3-hole mode converter.

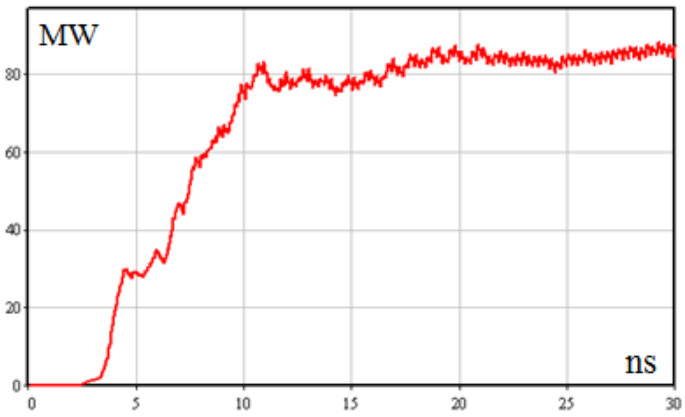

Figure 3.2.30. Output power of a 4-cavity compact MDO vs time (ns) with a 2-hole mode converter.

In concluding the preliminary PIC simulation study of the compact magnetron, it was found that a mode converter consisting of a thin conducting plate with a symmetric pattern of 2 or 4 diametrically opposed cavity openings affixed to an A6 magnetron with an upstream π-mode-enforcing strap that is connected to alternating vanes and with a

transparent cathode of radius 1.45 cm was capable of generating over 500 MW in the TE_{11} circular waveguide mode with efficiency of 14%. The compact magnetron was also capable of generating the π-mode and sufficient microwave output power over a wide range of magnetic fields with voltage fixed at 350 kV, Figure 3.2.31 and Figure 3.2.32. It was indeed possible to demonstrate the original concept, resulting in a compact MDO (including its magnetic field coils) with a Gaussian radiation pattern and minimal expenditure of energy to create the necessary uniform magnetic field. Since the output waveguide supports only the lowest order mode, this compact MDO will be simple to implement in experiments.

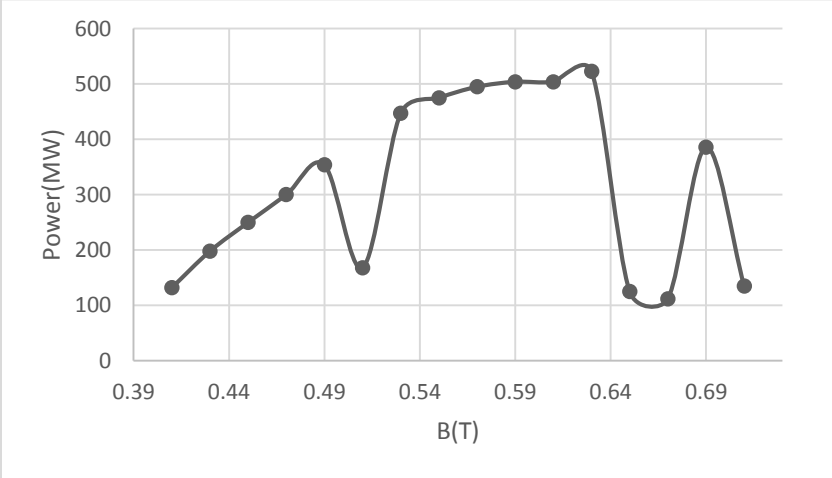

Figure 3.2.31. Output microwave power as a function of applied magnetic field for the compact MDO.

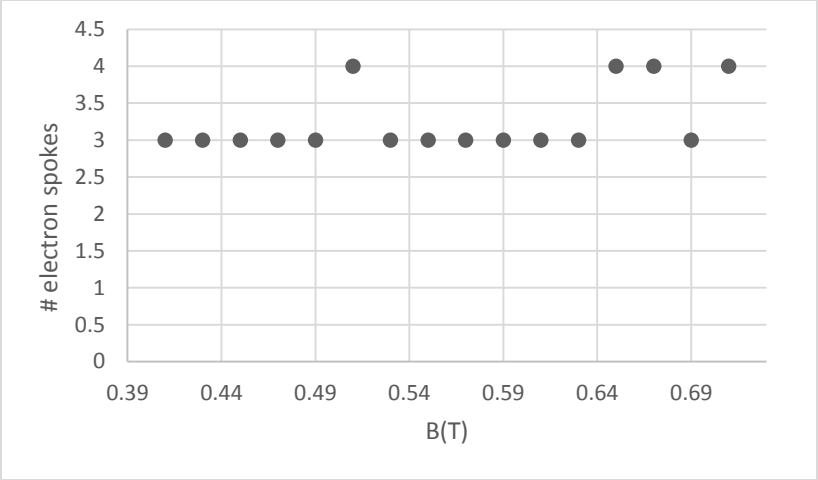

Figure 3.2.32. Operating mode as a function of applied magnetic field for the compact MDO.

3.2.4.1 Compact magnetron mode purification – MAGIC eigenmode solver

While the compact magnetron designed using the PIC code might be satisfactory for some applications, it did not look like a suitable candidate for a short pulse radar due to the presence of a rotating TE_{11} mode that contained 10% of the power in the non-rotating mode. This mode became apparent when the electric field of the non-rotating mode is zero magnitude during the electric field polarity flip that occurs each RF cycle for the TE_{11} mode. This can be seen in Figure 3.2.33 where the normal polarity of the non-rotating mode is shown left, and the rotated quasi-TE_{11} mode is shown right. One unfortunate reality of the undesired mode was that it was also TE_{11}, meaning that an elongated output waveguide had no chance in cutting off its propagation.

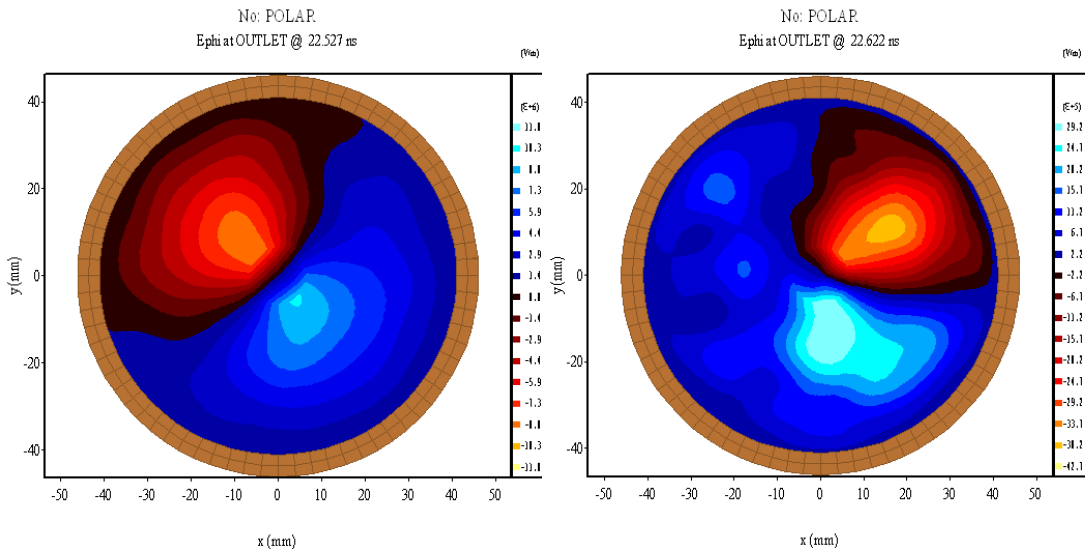

Figure 3.2.33. E_φ of TE_{11} mode at peak RF field (left) and smaller E_φ attributed to the TE_{11} mode rotation (right).

Upon closer inspection of the π-mode electron spoke pattern, there were also signs of mode competition; the spectrum was not entirely clean. One explanation is that the compact magnetron is an axially asymmetric device with its upstream strap edifying the π-mode and its downstream mode that strap two pairs of adjacent vanes to one another, doing something else altogether. The π-mode strap will lock in the π-mode on the upstream side of the magnetron at one frequency and the downstream strap will do the same for the π-mode at another frequency.

MAGIC's eigenmode solver was employed to study the effects of varying strap and mode converter geometries on the purity of π-mode generation. The cold-test eigenmode solver could converge on a solution much faster than a hot-test with particles. The 1 cm cathode radius was chosen because of the ability to support both modes - the 2π-mode

converged at 3.74 GHz and π-mode converged at 2.58 GHz. It should be noted that in the following eigenmode tests, parameters such as cathode clocking, cathode radius, and other geometries were systematically altered. The results shown are a small number of representative samples that display the best results. This might appear as an overly-liberal study as a result. As a starting reference point, the standard A6 with a transparent cathode of radius 1 cm was first tested for 2π-mode (Figure 3.2.34, top) and π-mode (Figure 3.2.34, bottom), operation.

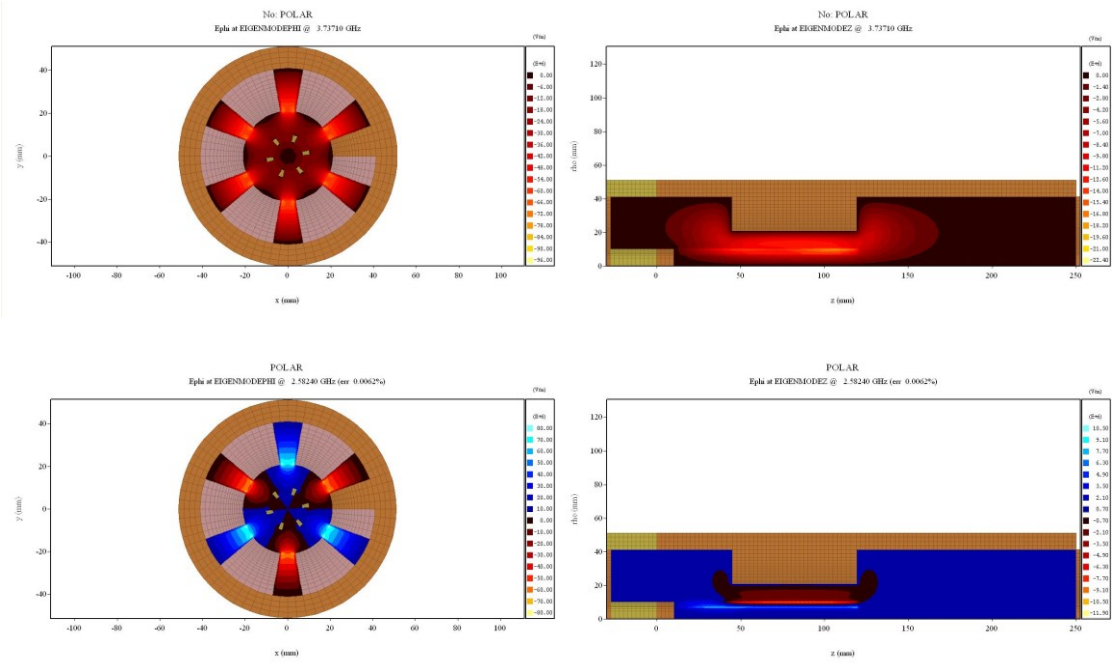

Figure 3.2.34. MAGIC eigenmode solutions to an A6 magnetron with transparent cathode with radius 1 cm in the 2π-mode (E_φ top) and π-mode (E_z bottom).

The original compact magnetron design converged from various seed frequencies to the π-mode covering several frequencies ranging from 2.79 GHz through 3.31 GHz. This

illustrates the robust character of the compact magnetron to lock-in the π-mode under a variety of conditions and easily explains why the compact magnetron generates the π-mode across a very large span of magnetic fields, Figure 3.2.31 and Figure 3.2.32. As expected, the π-mode is not symmetric (Figure 3.2.35, left), and there appears to be axial over-moding (Figure 3.2.35, right). This indicates that the upstream strap and downstream mode converter are influencing their respective sides as predicted.

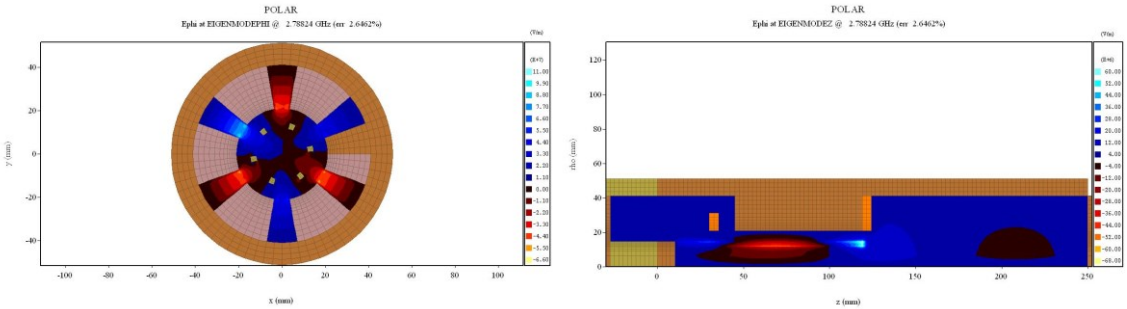

Figure 3.2.35. MAGIC eigenmode solutions to compact MDO (π-mode). E_φ left and E_z right.

To persuade the downstream side of the magnetron to behave like the strapped upstream side, the mode converter was attached to alternating vanes to emulate a π-mode strap. While this resulted in a more symmetric π-mode (Figure 3.2.36, left), the magnetron was still axially over-moded (Figure 3.2.36, right), albeit to a lesser degree. The band over which seeded frequencies converged to the π-mode also decreased to the range 2.79 GHz through 3.00 GHz. Thus, this variant seemed less frequency stable than the original compact magnetron. Hot test results of this configuration did not perform well.

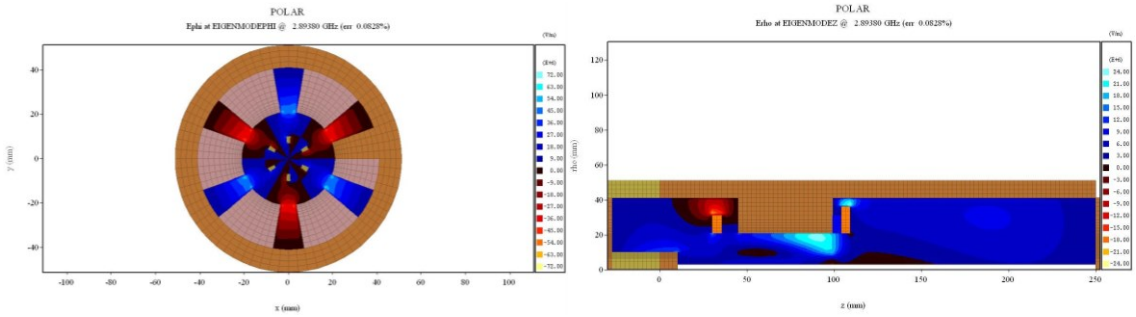

Figure 3.2.36. MAGIC eigenmode solution to a compact MDO with the downstream mode converter attached as a π-mode strap, to alternate vanes, while operating in the π-mode. E_φ left and E_z right.

Finally, the ill effects of the strap and converter are minimized by eliminating the strap and separating the mode converter from the anode block. The result is a more symmetric π-mode (Figure 3.2.37, left) and no axial over-moding (Figure 3.2.37, right). The π-mode converges to only one value, increasing from the original A6's 2.58 GHz to 2.66 GHz. This shift is likely due to the capacitive effects introduced by the close proximity of the downstream vanes to the mode converter.

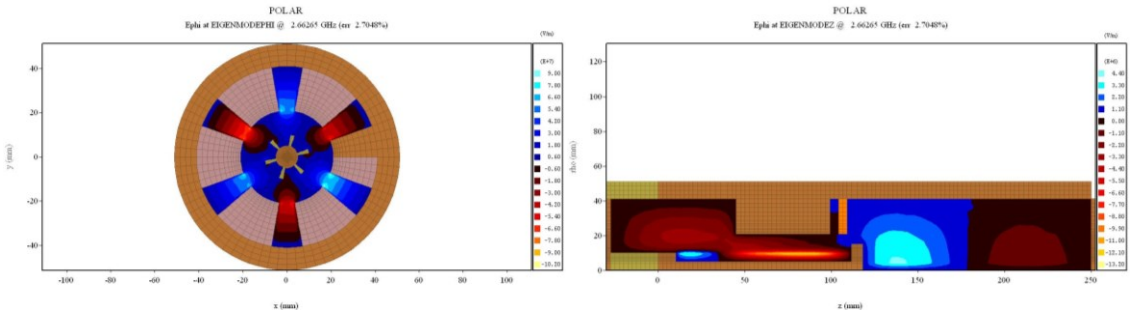

Figure 3.2.37. MAGIC eigenmode solution to a compact MDO with strap removed and with mode converter unattached operating in the π-mode. E_φ left and E_z right.

With the strap removed and mode converter detached, a MAGIC hot test indicated a reduction in power of the rotating mode from 10% of the non-rotating mode down to 4%. Clarity of the π-mode electron spoke mode was also noticed, Figure 3.2.38. The final simulation configuration is shown in Figure 3.2.39.

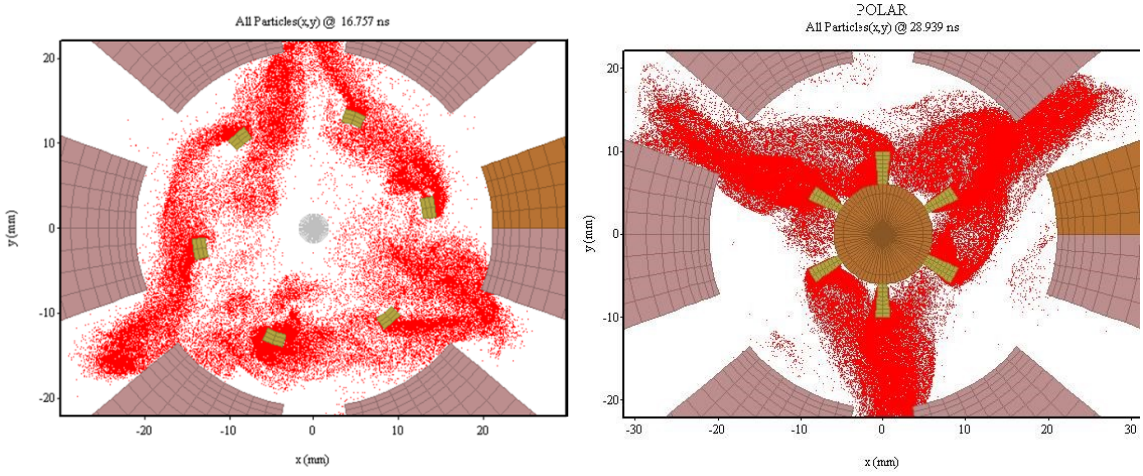

Figure 3.2.38. MAGIC hot test of original compact MDO (left) to optimized design (right).

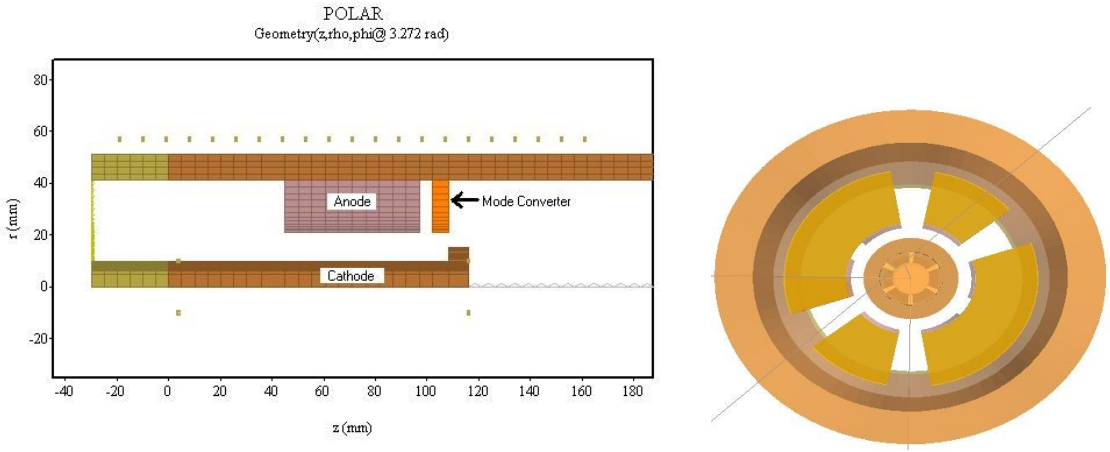

Figure 3.2.39. MAGIC simulation configuration of compact MDO optimized for mode clarity.

Given the low grid resolution available to single-cpu MAGIC simulations, further optimization will need to be carried out in experiment. For example, there might be noticeable effects of small changes in distance between the anode block and mode converter, where there is a fine trade off between negative capacitive effects upon mode of operation, probability of arcing, and more effective diffraction of cavity fields between mode converter holes.

3.2.4.2 Compact magnetron with permanent magnet – FEMM and MAGIC

Replacing the pulsed solenoid electromagnet around the compact magnetron with a permanent magnet would both compensate for the low efficiency of the compact magnetron by adding to the total system efficiency and further reduce total system size considerably. This has been recently explored by other groups [53]. Investigations to this end began using the FEMM solver (a FEM code), Figure 3.2.40. The goal was to craft a

permanent magnet system that provided a sufficient field, greater than 0.53 T, with greater than 95% magnetic field uniformity in the A6's electron interaction space, yet diverged to the outer walls as quickly as possible for ideal deposition of axial-leakage electrons. FEMM showed that a simple hollow cylinder of neodymium iron boron with permeability μ_r of 1.1 and coercivity of $9x10^5$ A/m was able to achieve all of these, except for the 95% uniformity. Only 94.3% field uniformity was achieved at a radius of 1.5 cm along the length of the anode block. Introduction of upstream and downstream neodymium magnets embedded in the cathode increased this to 95.3% uniformity and provided a surprisingly greater number of axial electron paths that both increased efficiency by pinching leakage currents down to the cathode and protected the dielectric window by rapidly dumping electrons that passed the endcap to the outer wall of the device, Figure 3.2.40. Interaction space field strength (Figure 3.2.41, top) as a function of magnet thickness, t (cm), is illustrated in Figure 3.2.41, bottom.

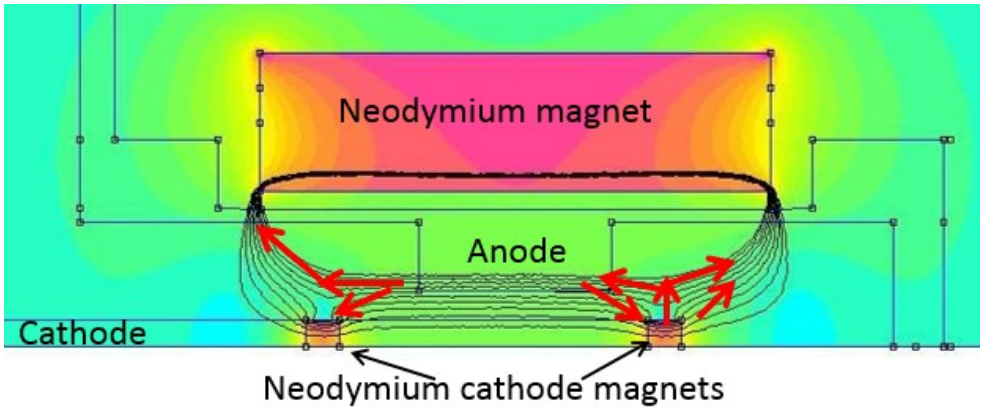

Figure 3.2.40. Compact MDO with permanent magnets.

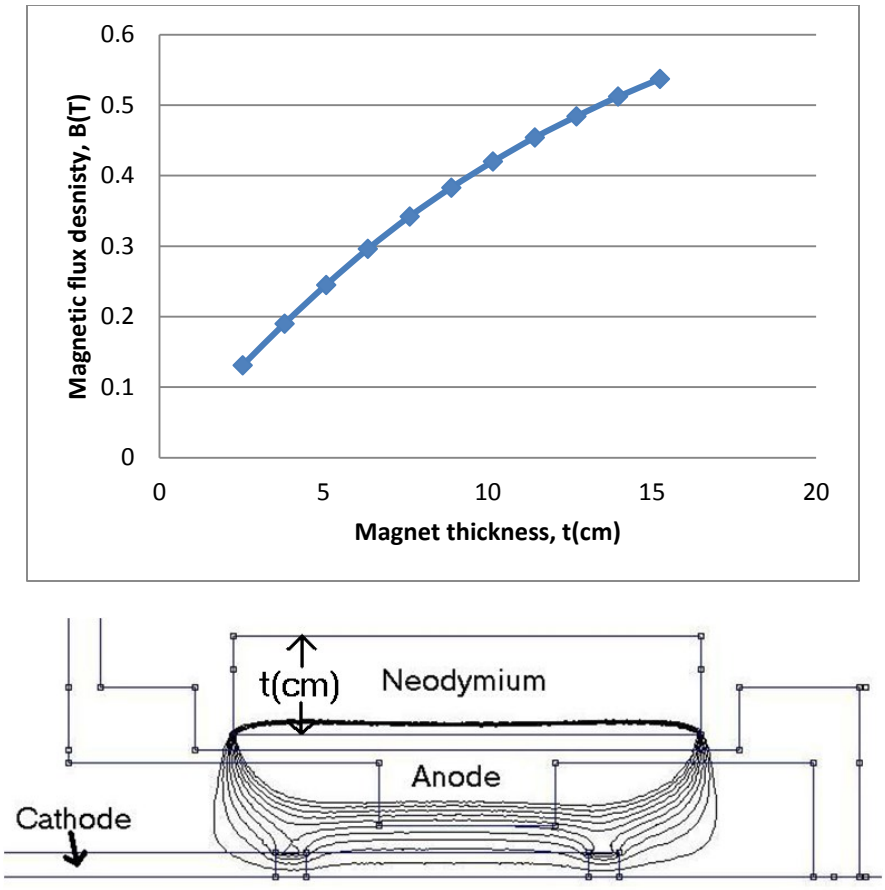

Figure 3.2.41. Magnetic field in the compact MDO's interaction space as a function of the thickness of the permanent magnets.

Eventually, the findings in FEMM had to be translated to a PIC simulation in MAGIC. At the time of this writing, MAGIC was not capable of modeling magnetic materials directly, but there is a good approximate method. For a material with magnetic polarization vector M, it is possible to closely approximate the fields around a permanent magnet by ascribing current loops with area vectors that are aligned to M on the surface of the desired material. The current density (A/m) needed in each current loop array is simply $J_s = M \times n$, where *Js* is the surface current density, *M* is the magnetization vector, and *n* is

the vector normal to the magnet's surface. For a coercivity of $9x10^5$ A/m, an axially-directed *M* vector field, and the annular cylinder magnet, the current density needed in MAGIC is $9x10^5$ A/m. A comparison between the magnetic field in the interaction space for FEMM and MAGIC is given in Figure 3.2.42.

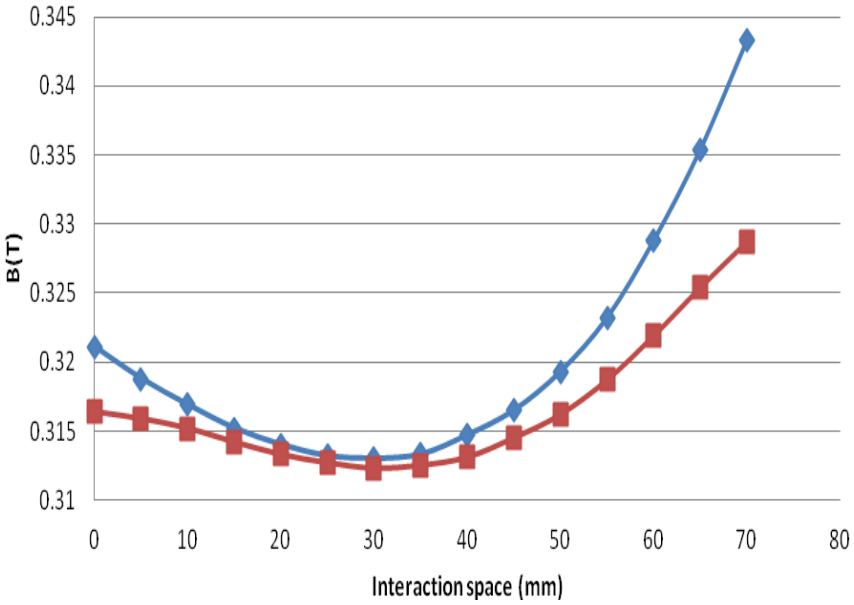

Figure 3.2.42. FEMM (blue) and MAGIC (red) magnetic field profile in the interaction space of the compact MDO.

An image of a hot test in MAGIC (Figure 3.2.43) shows that the favorable electron trajectories are present. Also, performance of the compact magnetron with permanent magnets in MAGIC was comparable with compact magnetron performance with a Helmholtz coil pair or solenoid, Figure 3.2.44 through Figure 3.2.48.

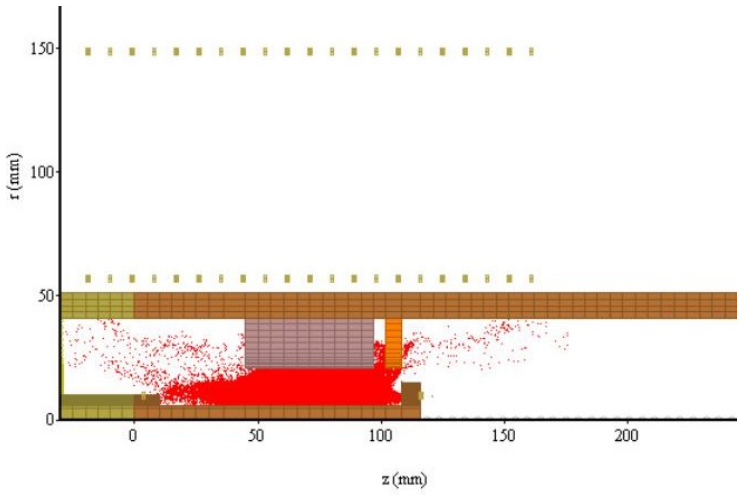

Figure 3.2.43. MAGIC hot test of compact MDO with coil-approximation of permanent magnets in the r-z plane.

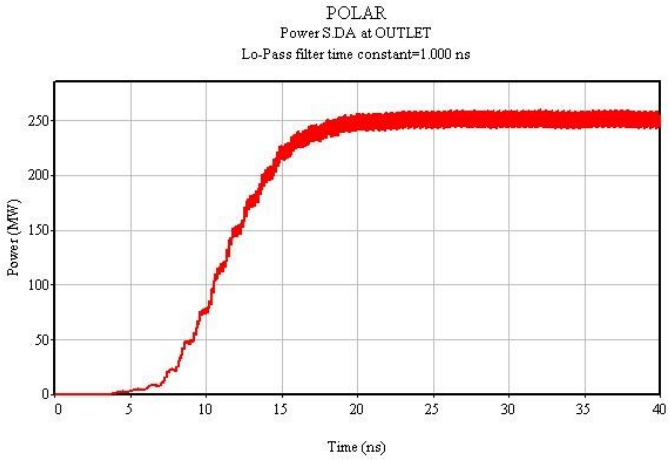

Figure 3.2.44. Simulated output power vs. time (ns) of the compact MDO with permanent magnet.

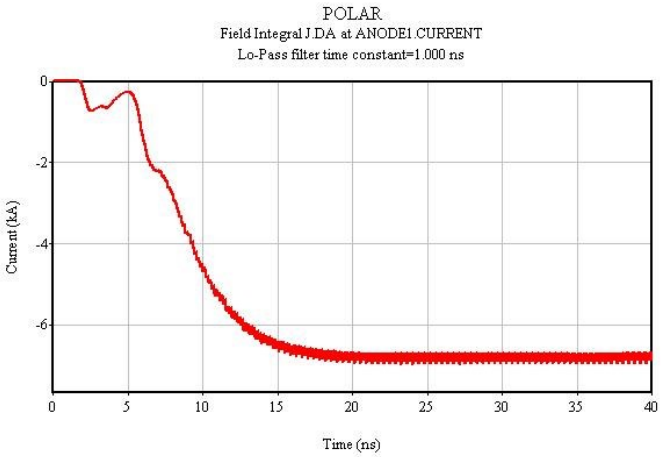

Figure 3.2.45. Anode current vs. time (ns) in compact MDO with permanent magnet.

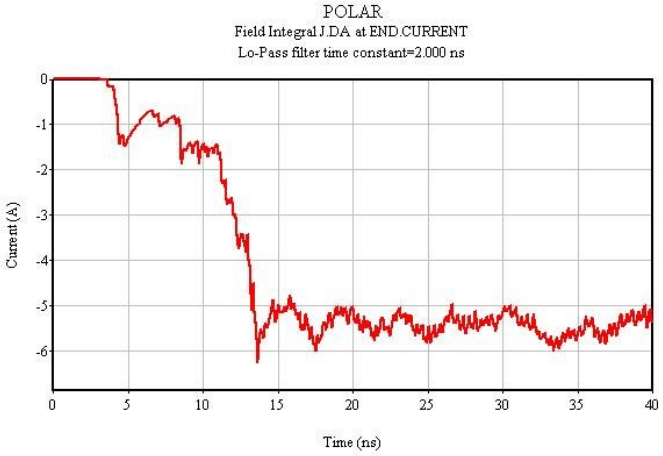

Figure 3.2.46. Leakage current (less than 6 A) vs. time (ns) in compact MDO with permanent magnet.

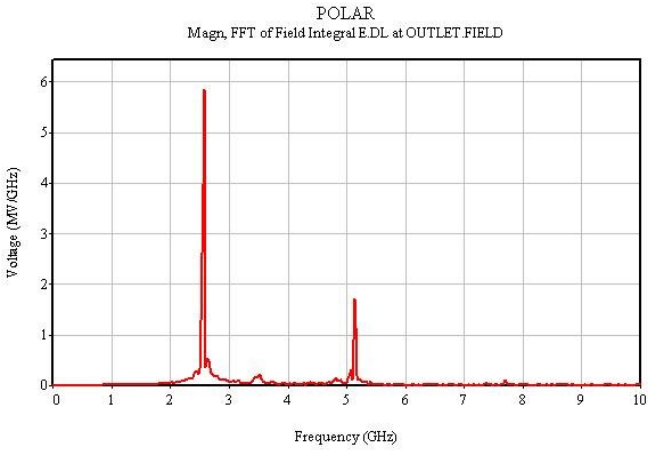

Figure 3.2.47. FFT of the output of the compact MDO with permanent magnet.

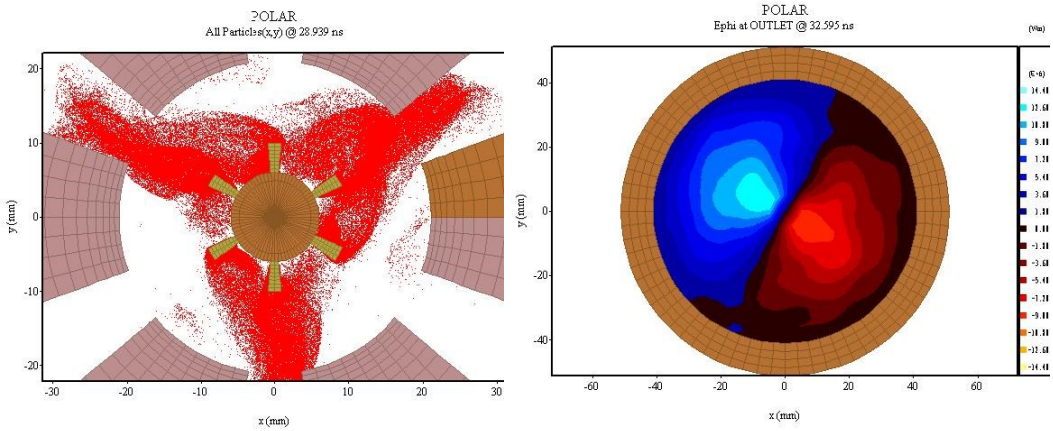

Figure 3.2.48. π-mode (left) and TE_{11} microwave output mode (E_φ right) in a compact magnetron with permanent magnet.

Attempts were made to create a magnetic circuit using high permeability metals to increase the effectiveness of the permanent magnet design, but were unsuccessful; these metals always detracted from the field present in the magnetron. However, there are methods to do this properly that should be investigated in the future.

3.2.5 Rodded cathode – ICEPIC

In an effort to extend the success of a finely rodded cathode in a conventional magnetron by Andreev and Hendricks [54], the University of New Mexico's Pulsed Power, Beams, and Microwaves Laboratory has, under the auspices of Raytheon-Ktech support, performed a comprehensive parameter scan of a rodded cathode operating in a relativistic MIT A6 magnetron using ICEPIC [55]. At the heart of the concept of the rodded cathode is the hypothesis that (i) the periodic sub-wavelength structure of the rodded cathode's rod spacing interacts with the operating mode for positive effect (acting as a metamaterial-like medium), and (ii) that as in other experiments [56], the presence of the fine rods might contribute to an increase in the space-charge-limited current emitted from the cathode, thereby increasing anode current and, concomitantly, microwave output power.

This dissertation sub-project was aimed at studying rodded (metamaterial-like) cathode operation in a relativistic A6 magnetron and finding such topology of the rodded cathode that would allow the A6 magnetron to operate more efficiently and at a higher level of output microwave power compared with an A6 magnetron equipped with the standard cylindrical solid and the transparent cathodes of the same outer diameter. Numerical simulations of the virtual model (VM) of the A6 magnetron equipped with different cathodes (solid, transparent, and rodded) were performed using supercomputer clusters provided by AFRL, HPM Division, KAFB, NM.

Figure 3.2.49. Schematic of a rodded cathode.

The main challenge of these simulations was determining the optimal number and topology of the single cathode rods within the 3D cylindrical space determined by the outer cathode diameter. The rodded cathode used in this research represents a set of longitudinally oriented rods (periodic lattice of single rods, Figure 3.2.49), which may be considered as the rodded medium characterized by the outer radius of the lattice, R_{out}, and the lattice parameter or distance between the adjacent rods, a. Both the number of rods and the topology of the cathode determine magnetron operation, and this is why the same A6 magnetron operates differently with the solid, transparent, and rodded cathodes having the same outer diameter. As such, presented below is a summary of the comprehensive parameter scan of the rodded cathode, starting with a study of the solid and transparent cathode to provide a baseline of performance for the A6 and to validate the ICEPIC model.

3.2.5.1 Simulation setup

In each simulation run, the confining magnetic field was set to 0.6 Tesla, which is a common value in experiments and simulations performed by other groups. This ensured proper validation of our ICEPIC model by easy reference and increased physical intuition of how changes in the model or inclusion of various structures might behave. For example, the anode and cathode endcaps employed in other works [6, 28, 52, 57] were easily integrated into the ICEPIC model.

The geometry consisted of a cathode 1.58 cm in radius, a surrounding anode with inner radius 2.11 cm and 20-degree-wide resonating cavities of outer radius 4.11 cm. In one of the resonating cavities, a slot was tapered into an appropriately-sized waveguide for the frequencies of extraction to remove microwave power from the device. Due to the presence of operating modes with frequencies at or below 2 GHz with some configurations of the rodded cathode, it was necessary to alter the output power extraction port located in one of the A6's cavities so as to avoid reflections due to cut-off. The 10 degree extraction slot that tapered into an S-band waveguide, as is seen on the UNM A6 experimental setup, is changed to taper into a larger R-band waveguide located at the same radial distance as the old S-band waveguide, Figure 3.2.50 and Figure 3.2.51. Simulation gridding convergence was tested and grid size settled to 0.5 mm. The wave absorbing boundary, emission model, and output perfectly-matched layer (PML), and all output diagnostics were also all tested to be valid.

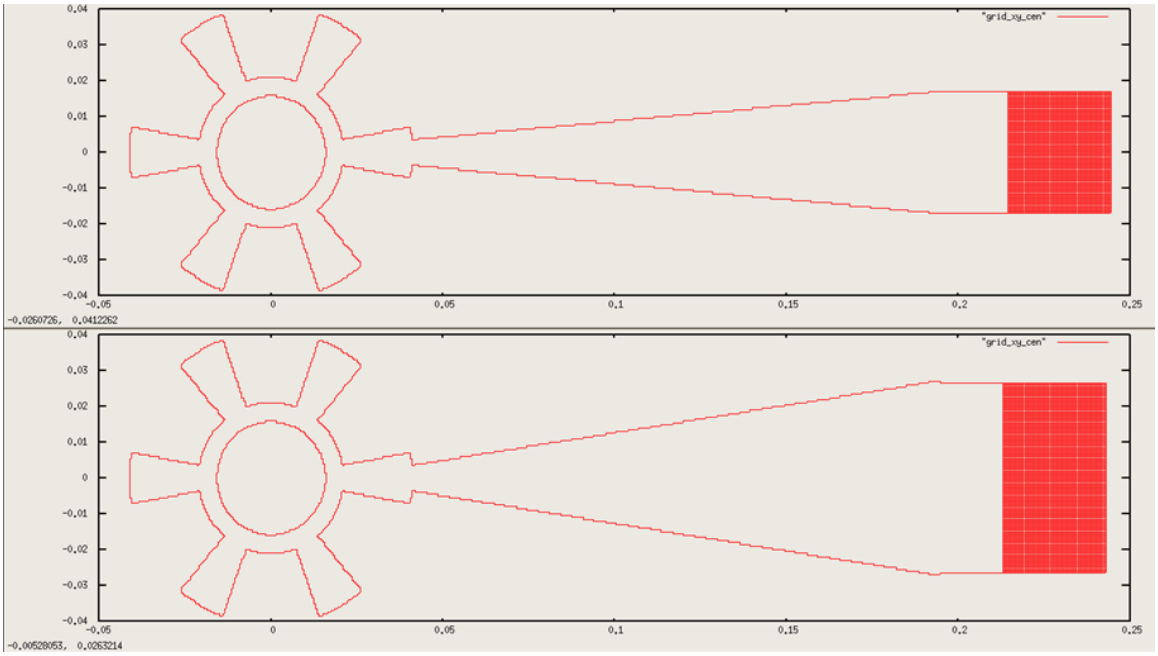

Figure 3.2.50. (Top) x-y plane cross section of A6 magnetron with UNM-style S-band extraction, (bottom) A6 magnetron with larger R-band extraction.

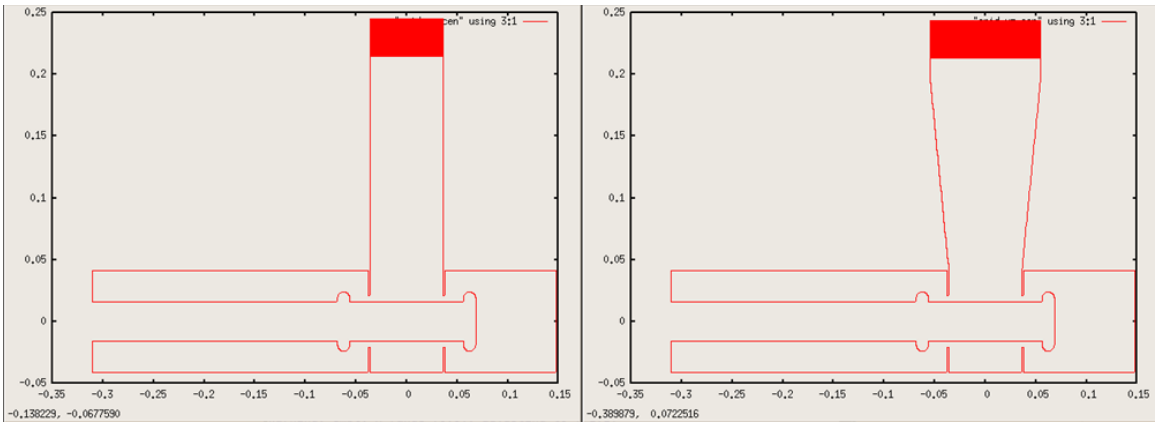

Figure 3.2.51. (Left) x-z plane cross section of A6 magnetron with UNM-style S-band extraction. (Right) A6 with larger R-band extraction.

3.2.5.2 Solid and transparent cathode

The A6 with solid and transparent cathode was run to validate our ICEPIC model, so that trustworthy results on the metamaterial-like rodded cathode could be obtained. The solid cathode is a solid conducting cylindrical electron-emitting structure, and the transparent cathode consists of 6 thin 10-degree-wide strips that are equally spaced at the same outer diameter of the solid cathode, Figure 3.2.52 and Figure 3.2.53. To this end, the results for the solid and transparent cathode matched expected trends.

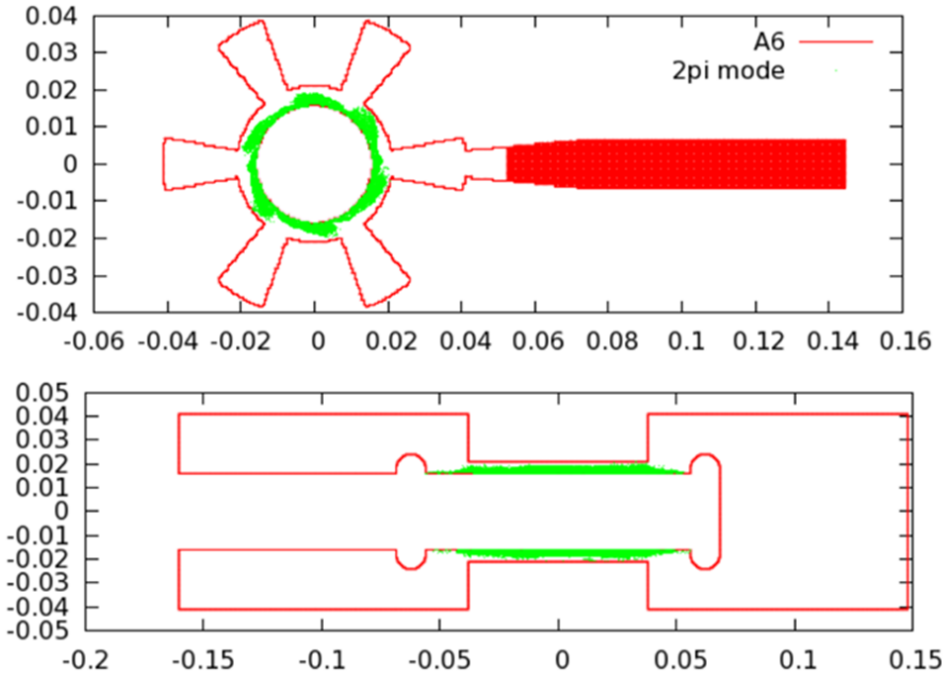

Figure 3.2.52. 2π-mode generation using a solid cathode.

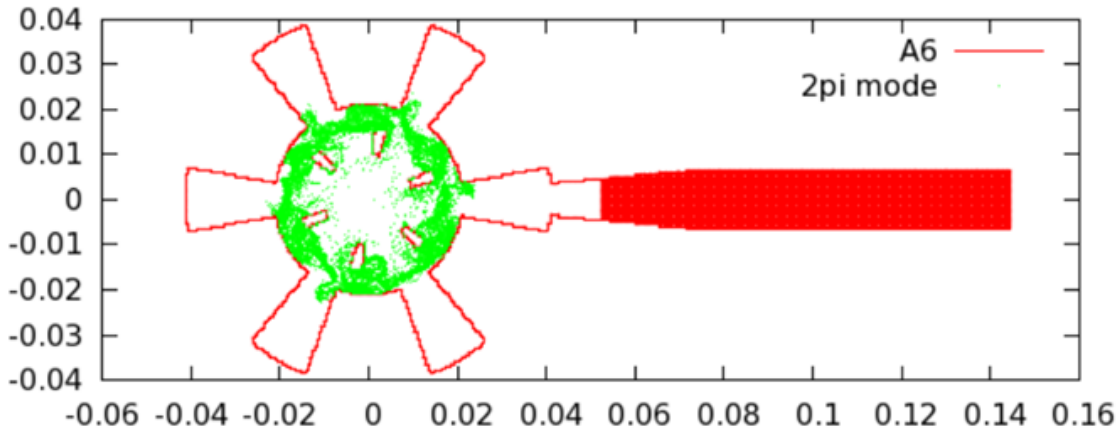

Figure 3.2.53. 2π-mode generation using a transparent cathode.

For 0.6 T magnetic field and 350 kV voltage, the literature suggests the dominant mode to be the 2π-mode, which is characterized by 6 electron spokes for both the solid and transparent cathode, as can be seen in Figure 3.2.52 and Figure 3.2.53. For the transparent cathode, the initial growth rate is much faster because it emits in 6 locations that seed the 2π-mode and that produce a much higher initial growth rate of the beam/microwave instability. This results are higher power, faster rate of the desired microwave mode with reduction in competition from other unwanted modes, better efficiency, and ultimately higher microwave output power for the transparent cathode over the solid cathode [12]. These are our expected trends. What follows in this section are the results of the solid (AK voltage in Figure 3.2.54, anode and leakage currents in Figure 3.2.55, output microwave power in Figure 3.2.56, and time-frequency spectrogram of electric field oscillations in one of the resonators in Figure 3.2.57) and transparent (AK voltage in Figure 3.2.58, anode and leakage currents in Figure 3.2.59, output microwave power in Figure 3.2.60, and time-frequency spectrogram of electric field oscillations in one of the resonators in

Figure 3.2.61) cathodes to illustrate this. The particle plots showing electron spoke distribution in the solid and transparent cathode magnetrons are shown in Figure 3.2.62 (top, bottom), respectively.

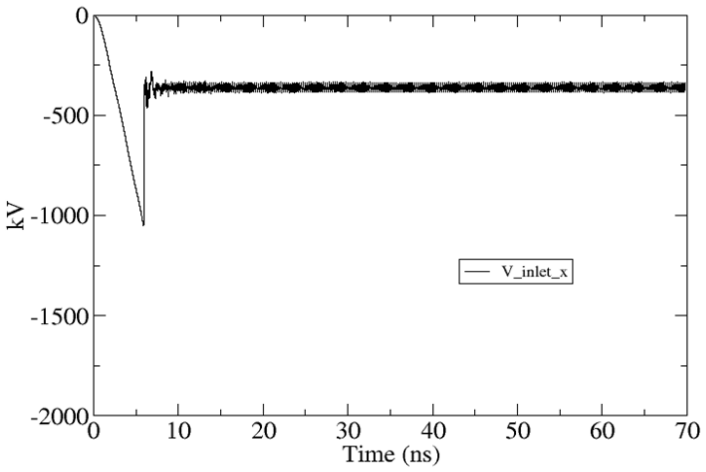

Figure 3.2.54. Applied DC voltage waveform of 350 kV for a solid cathode.

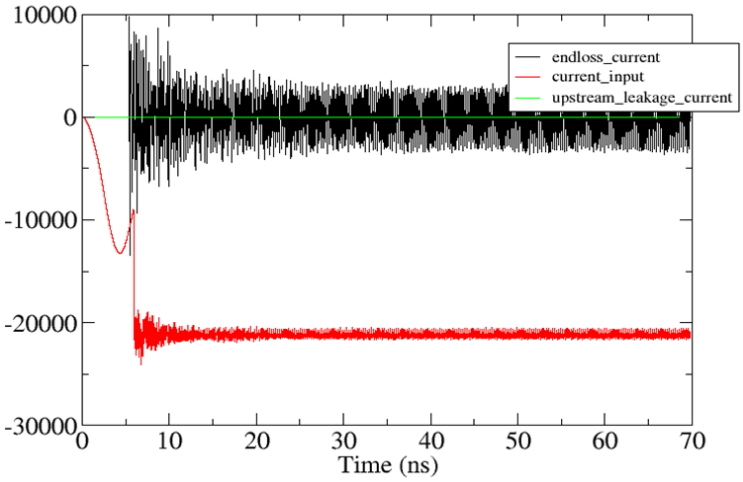

Figure 3.2.55. Electron current to the anode (anode current) shown in red for a solid cathode.

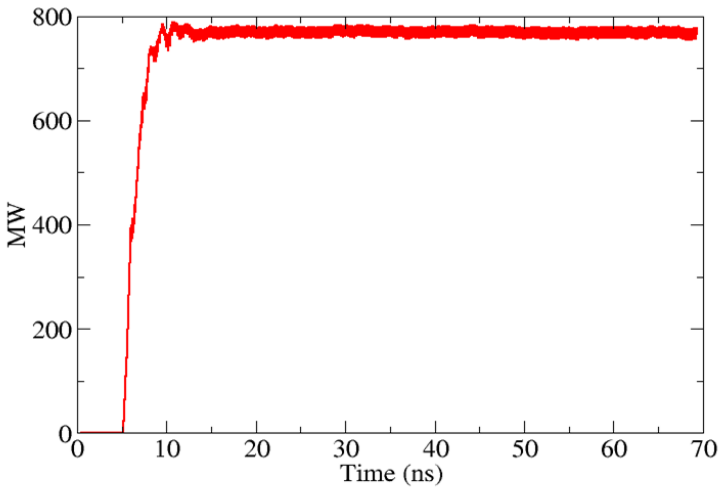

Figure 3.2.56. Microwave output power for a solid cathode.

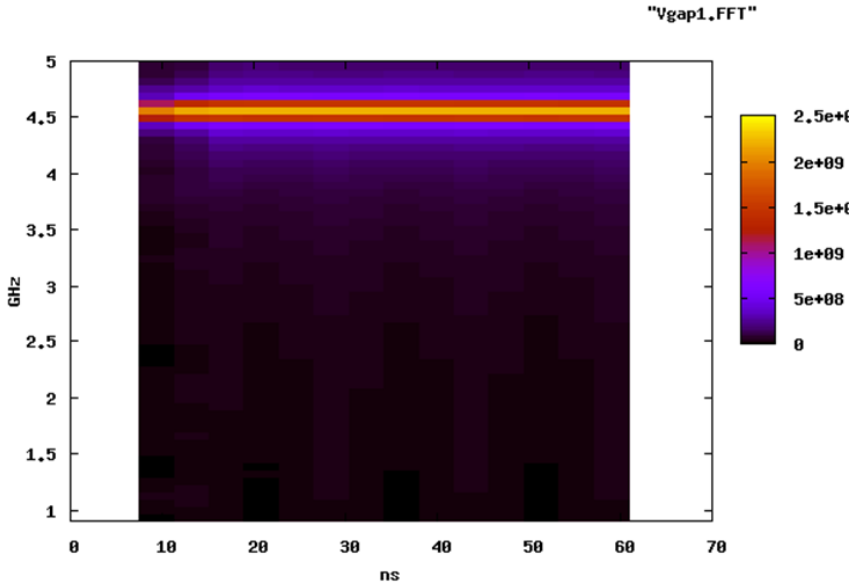

Figure 3.2.57. Time-frequency analysis (TFA) showing time variation of frequencies generated for a solid cathode.

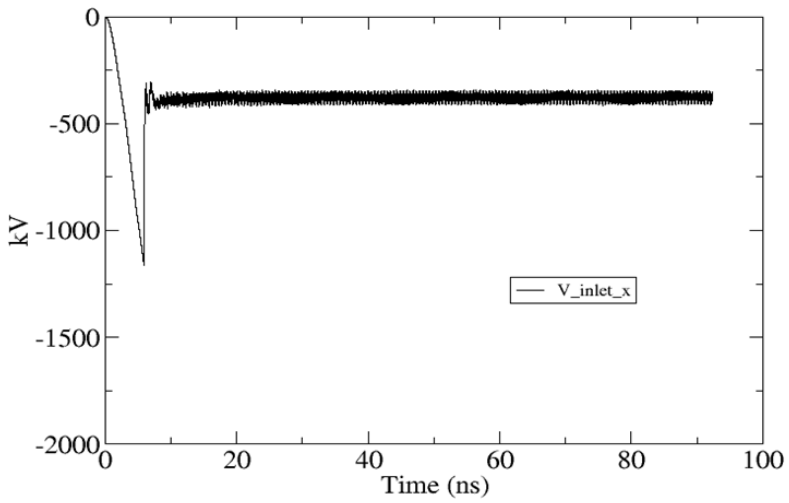

Figure 3.2.58. Applied DC voltage waveform of 350 kV for a transparent cathode.

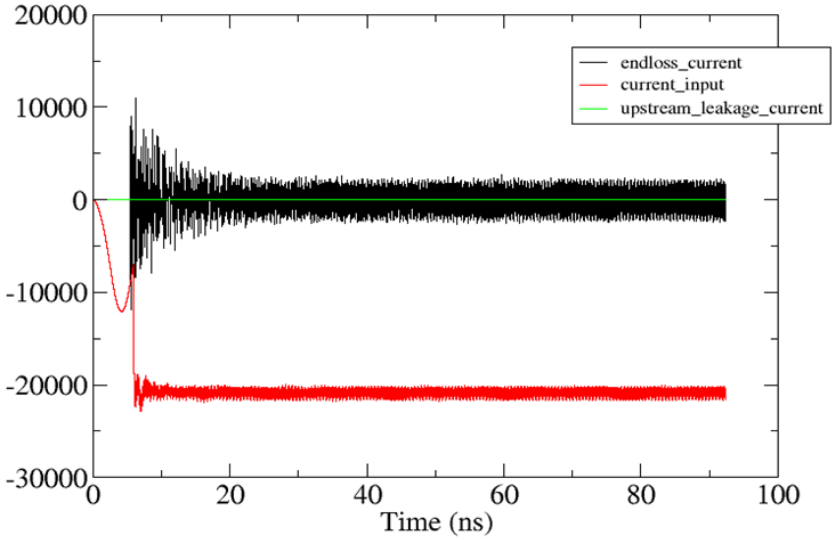

Figure 3.2.59. Anode current (red) for a transparent cathode.

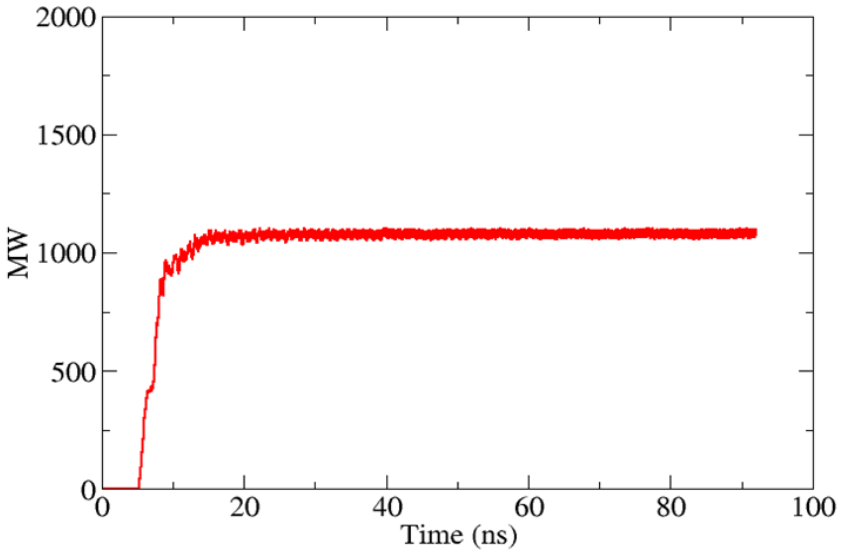

Figure 3.2.60. Microwave output power for a transparent cathode.

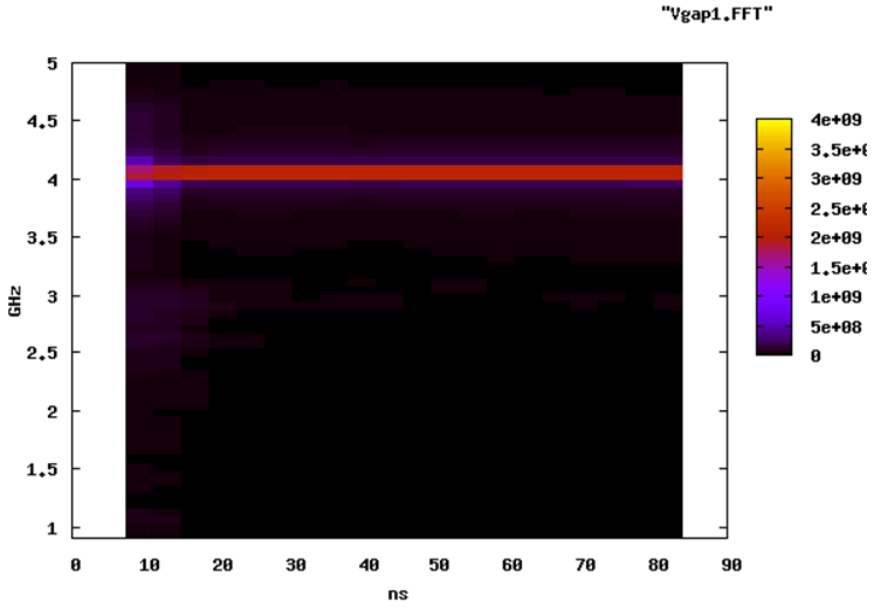

Figure 3.2.61. Time-frequency analysis (TFA) showing time variation of frequencies generated for a transparent cathode.

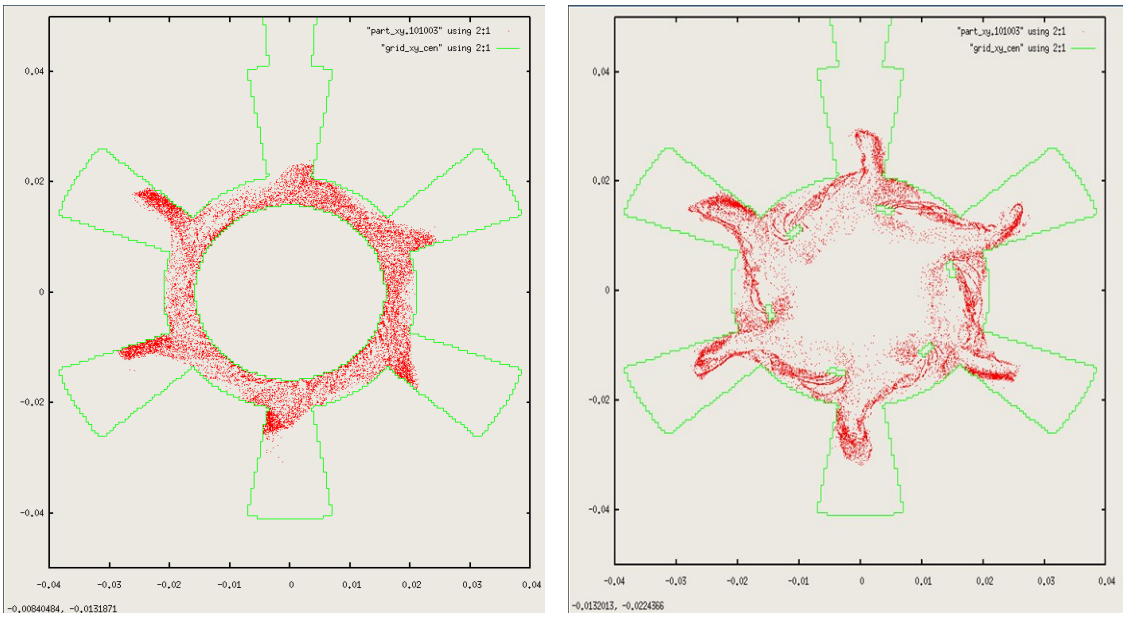

Figure 3.2.62. 2π-mode, 6-spoke electron cloud operation solid cathode (left) and transparent cathode (right).

3.2.5.3 Preliminary rodded cathode in A6 magnetron

The preliminary design for the rodded cathode that is placed in the A6 strongly resembles the rodded cathode from the work previously discussed [54] and contains the same number of rods placed in the same configuration with roughly the same ratio of individual rod diameter to total cathode diameter. In this case, the outer diameter is matched to be the same as the solid and transparent cathode, 1.58 cm. For a 350 kV voltage and 0.6 T magnetic field, this is shown in operation with electrons displayed in red, Figure 3.2.63.

The results of this run (Figure 3.2.64 through Figure 3.2.67) indicate heavy mode competition between the 2π/3-mode (2 electron spokes), the π-mode (3 spokes), and the 4π/3-mode (4 spokes), with less power than either the solid or the transparent cathode. At this moment, it became clear that the topology would have to be optimized for better

performance. It is worth mentioning that in a magnetron, the close placement of the anode's 6 20-degree slot resonators, along with other factors, means that modes that contain 2, 3, 4, 5, or 6 spokes are relatively close in frequency and phase velocity to one another. This means that electron kinetic energy can easily slip into modes surrounding the targeted dominant resonance mode, a phenomenon known as mode competition.

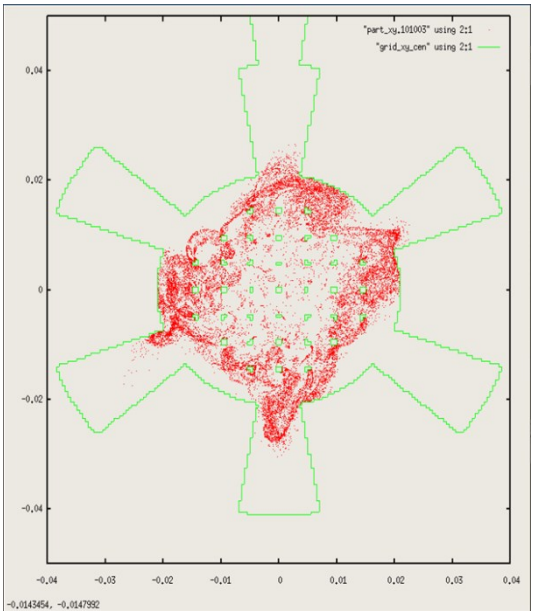

Figure 3.2.63. Preliminary rodded cathode geometry during operation. Electrons shown in red.

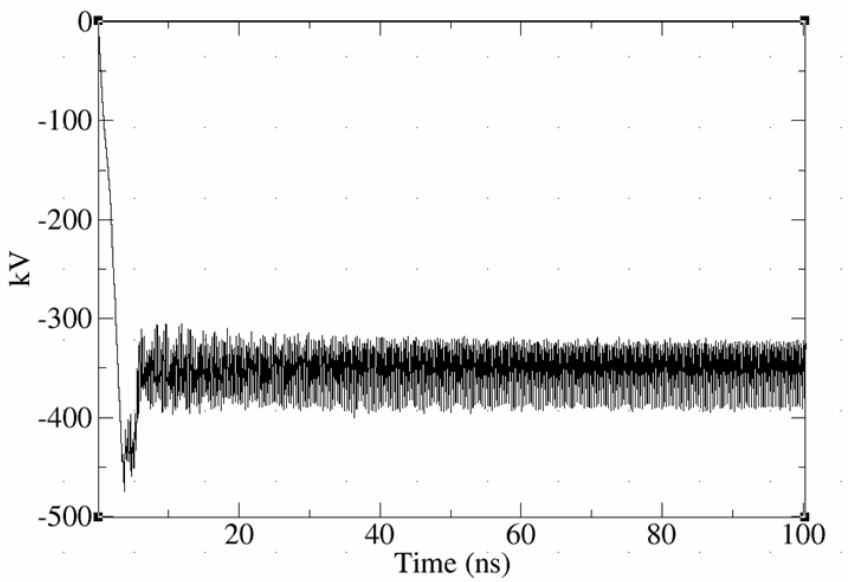

Figure 3.2.64. 350 kV applied voltage waveform for a rodded cathode.

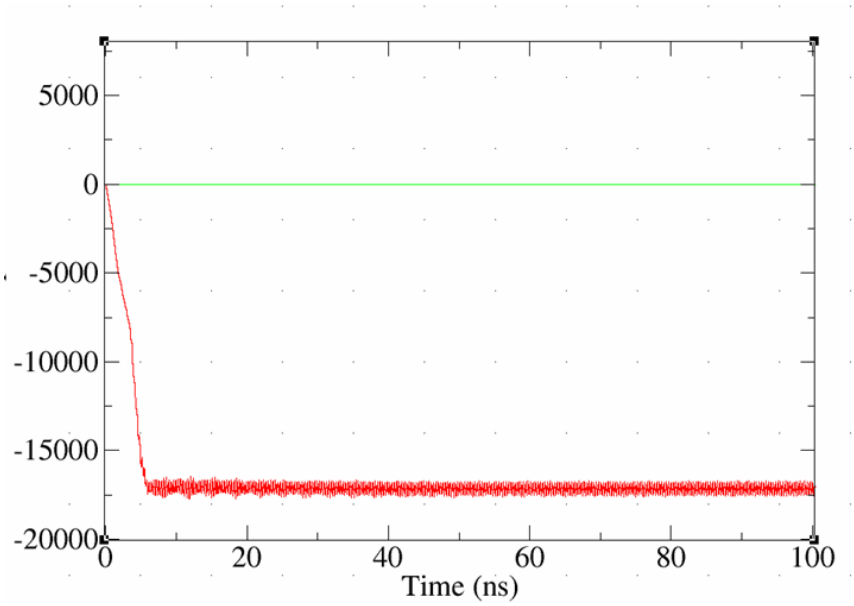

Figure 3.2.65. Anode current in kA (red) for a rodded cathode.

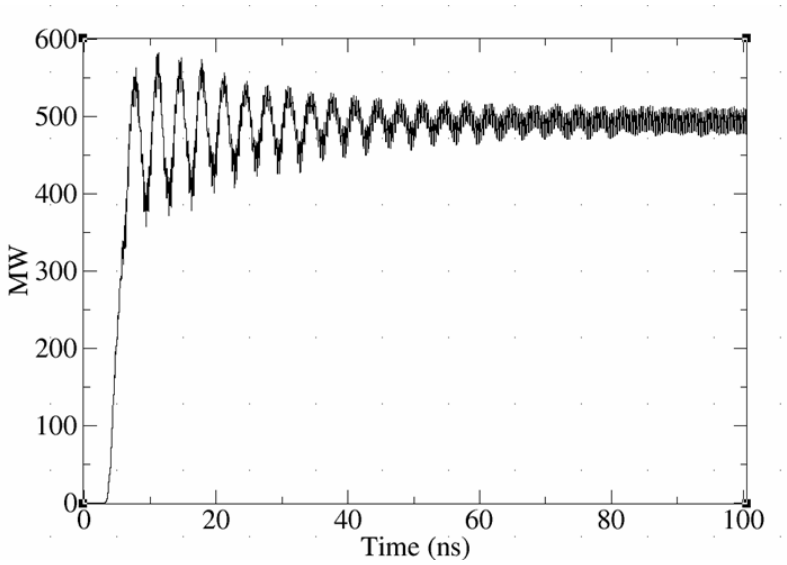

Figure 3.2.66. Microwave output power for a rodded cathode.

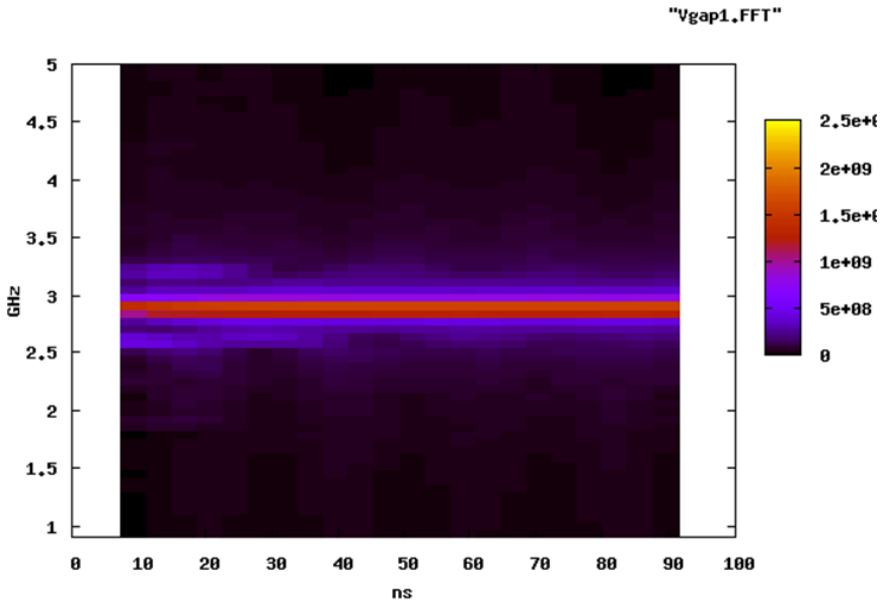

Figure 3.2.67. Time-frequency analysis (TFA) showing time variation of frequencies generated for a rodded cathode.

The remaining subsections of this chapter detail the algorithms used to populate a rodded-cathode topology and the results that followed.

3.2.5.4 Rodded cathode Algorithm #1 – Rod density variation

Description: Algorithm #1, where (i) the distance a between single rods of the rodded cathode is fixed, and (ii) the total number of rods and the topology of the rodded cathode are determined by the outer diameter of the 3D cylindrical space, within which the cathode is confined. The population of the rodded cathode interior is performed by linear translation in two orthogonal Cartesian X- and Y-directions of an initial "seeded" rod located in the geometrical center of the magnetron, where X=0 and Y=0. It turned out, however, that Algorithm #1 produced a rodded cathode topology with the outer diameter being less than the outer diameter of the solid and the transparent cathodes, which is used for comparison of the A6 magnetron operation with different cathodes. The smaller diameter of the rodded cathode resulted in less anode current and, hence, less output microwave power, while allowing the A6 magnetron to operate in the π-mode. There appeared to be a relation between (i) the reduced outer diameter of the rodded cathode populated using Algorithm #1, and (ii) the reduced output microwave power obtained with this construction of the rodded cathode, as compared with the output microwave power obtained by the A6 magnetron using the other two cathode designs it was compared with.

The spacing between rods for this Algorithm #1 was eventually expressed as a multiple of the rod density of the original, preliminary rodded cathode described in the previous section, *e.g.* 0.5, 0.75, 1.25, *etc.* For example, a 0.5 rod density would have fewer rods, and a 1.25 rod density would have more. Using this convention, most densities resulted in 2π/3-

or 4π/3-mode operation; however, a curious result was found. The rod densities 0.75 and 1.5 reliably outputted π-mode at most applied voltages, especially for a density of 1.5. For other rod densities the magnetron has a propensity to operate in the 4π/3 mode with 4 spokes, probably because it is patterned as an X-Y grid, which often has four corners and likely primes the electron bunches with four spokes. Two possible explanations as to why 0.75 and 1.5 output the π-mode across most voltages even though they also appear to prime in the 4π/3-mode are (i) these configurations might express most of their outer-most rods well below the solid cathode's 1.58 cm radius, where π-mode is more likely to be generated or (2) there is a metamaterial-like interaction with these spacings. The latter might be especially true since the rod spacing for the 1.5 density is exactly half that of the 0.75 density, suggesting a periodicity effect. In Figure 3.2.68 are shown the 1.0, 0.75, and 1.5 density rodded cathode geometries. Operation of the 1.5 density rodded cathode in the π-mode is illustrated in Figure 3.2.69.

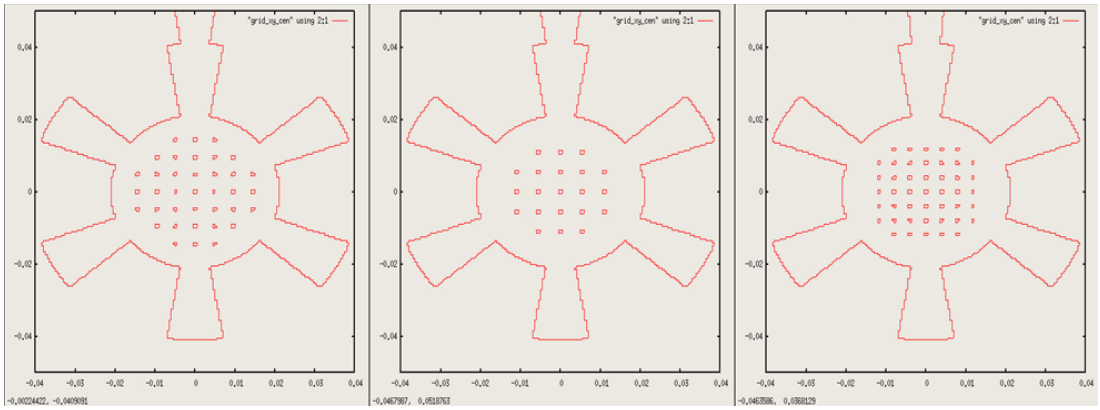

Figure 3.2.68. Algorithm #1 with (left) original rod density, (middle) 0.75 rod density, and (right) 1.5 rod density.

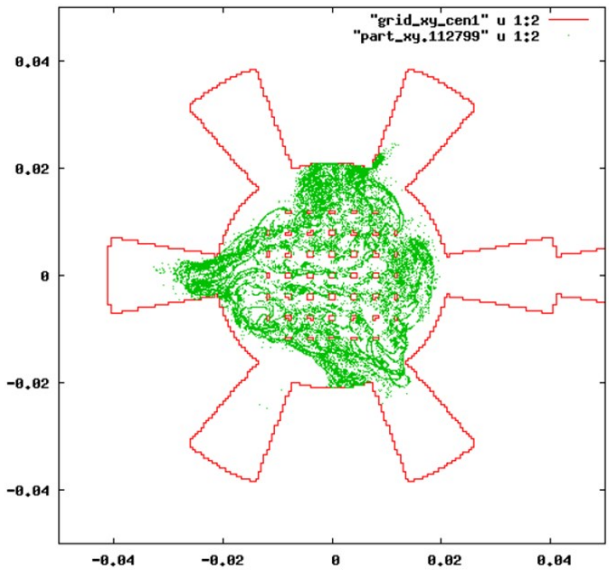

Figure 3.2.69. π-mode operation of the 1.5 density rodded cathode.

3.2.5.4.1 Algorithm #1: additional variation

In addition to variation of the rod density, the rod thickness was also increased and swept over a variety of densities. The approach of increasing the rod diameter was unsuccessful in terms of increasing output power and improving π- or 2π-mode operation, as is illustrated in Figure 3.2.70.

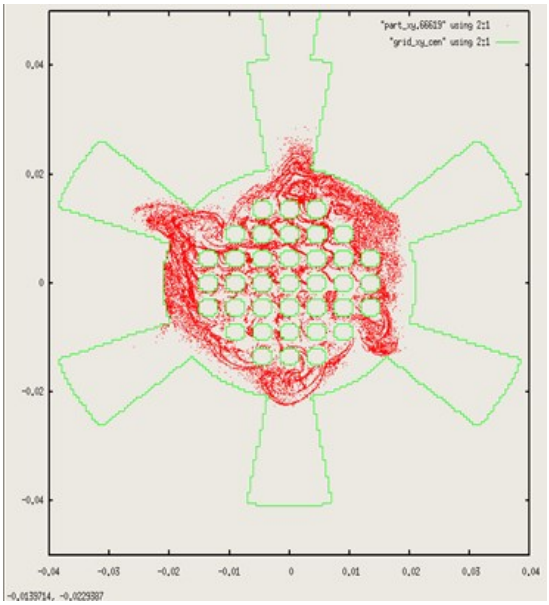

Figure 3.2.70. Thicker rods were implemented for Algorithm #1 density scan.

3.2.5.5 Rodded cathode Algorithm #2 – Integer number of rods in X- or Y-direction

Description: Algorithm #2, where (i) the outer diameter of the rodded cathode is fixed, and (ii) the distance between single rods *a*, the total number of rods, and the topology of the rodded cathode are determined by the number of linear translations in two orthogonal Cartesian X- and Y-directions of an initial "seeded" rod located in the geometrical center of the magnetron, where X=0 and Y=0. What happens in this case is artificial construction of a four-fold symmetry of the rodded cathode having, however, the required outer diameter. The resultant four-fold symmetry was created by virtue of the fact that the linear translation in two orthogonal X- and Y-directions is used for the rodded cathode construction. This results in the so-called "cathode priming" of the magnetron operation by a four-fold symmetric $2\pi/3$ mode, which is characterized by two or four magnetron

spokes in the 6-resonator magnetron. This regime of A6 magnetron operation is not appropriate for the radial scheme of microwave output power extraction that was studied. It took some time to understand how the artificial four-fold symmetry of the rodded cathode affects the A6 magnetron operation in a negative manner.

The convention used to differentiate between different topologies of Algorithm #2 are the integer numbers N = 2, 3, 4, 5, *etc.* These integer numbers state the number of rods that exist after the center rod in either the X- or Y-direction. Figure 3.2.71 presents the geometry for N = 3, 4, and 5. In general, Algorithm #2 also produces poor results with typical operation modes that are undesirable.

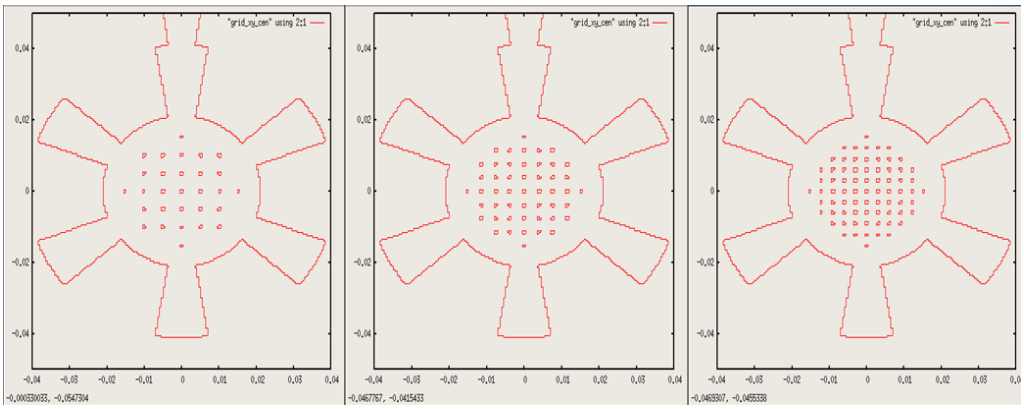

Figure 3.2.71. Algorithm #2 with (left) N = 3, (middle) N = 4, and (right) N = 5.

3.2.5.6 Rodded cathode Algorithm #3 – Transparent/rodded hybrid

As was mentioned earlier, it took some time to recognize that Algorithms #1 and #2 suffered from four-fold symmetry priming which often results in $2\pi/3$- or $4\pi/3$-mode operation, which is not desired. At this point, it was decided to employ an algorithm that is

point-symmetric about the center rod, *i.e.* the X-Y plane origin. A simple solution to this is to place a X-Y-gridded rodded cathode inside a transparent cathode that was clocked to various angles, Figure 3.2.72. This approach would retain the favorable priming characteristics of the transparent cathode, yet also include the microwave field penetration effects of a grid of rods.

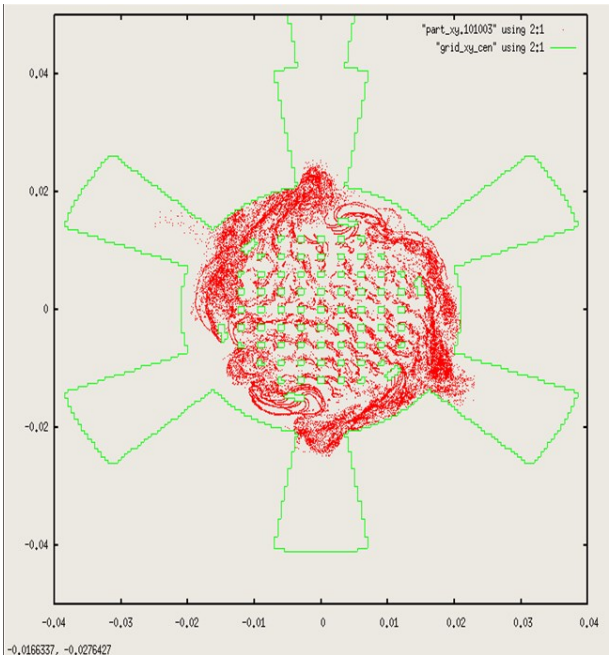

Figure 3.2.72. Algorithm #3: transparent cathode with X-Y-gridded rods inside.

Let it be noted that Algorithm #3 was later reworked due to low-performance to Algorithm #4, which has the characteristic of the inner-most rods abandoning the X-Y-gridding and adopting a true point-symmetry configuration.

3.2.5.7 Rodded cathode Algorithm #4 – Point-symmetry about center rod

Description: Algorithm #3, where (i) the outer diameter of the rodded cathode is fixed, and (ii) the distance between single rods, the total number of rods, and the topology of the rodded cathode is determined by the azimuthal, θ-, and radial, R-, translations of an initial "seeded" rod located at an arbitrary position within the 3D cylindrical space determined by the outer cathode diameter, where θ=0 and $R \leq R_{out}$. In this case, the total number and the spatial position of single rods were determined by the initial "clocking angle" of the "seeded" rod, the number of azimuthal translations, and the number of layers distributed along the radius of the rodded cathode. An illustration of Algorithm #4 with 2, 4, and 6 layers is given in Figure 3.2.73.

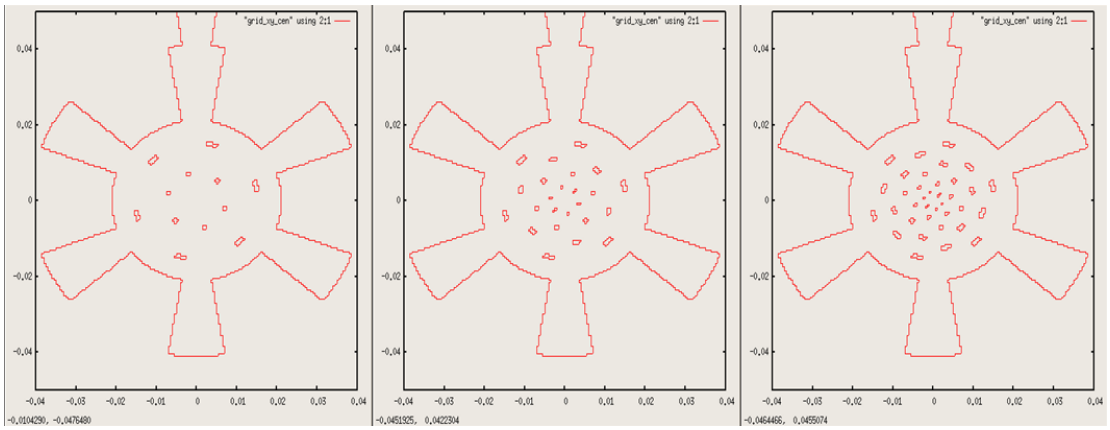

Figure 3.2.73. Algorithm #4: Full point-symmetry with (left) 2, (middle) 4, and (right) 6 layers.

ICEPIC simulations of A6 magnetron operation with this design of the rodded cathode (6 azimuthal translations) shows a great dependence of all magnetron operating parameters on the initial clocking angle and the number of layers of the rodded cathode.

This was very consistent with results obtained in simulations of the A6 magnetron with the transparent cathode, which also showed the dependence of magnetron operation on the transparent cathode clocking angle. Influence of the lower layers on the top-most "transparent cathode" is still not understood. A clear trend was that performance drops with the greater number of layers that are added. Retention of the 2π-mode is still possible with 2 layers, however, as can be seen in Figure 3.2.74. However, as additional layers are added, the propensity to operate in the 2π/3 mode increases.

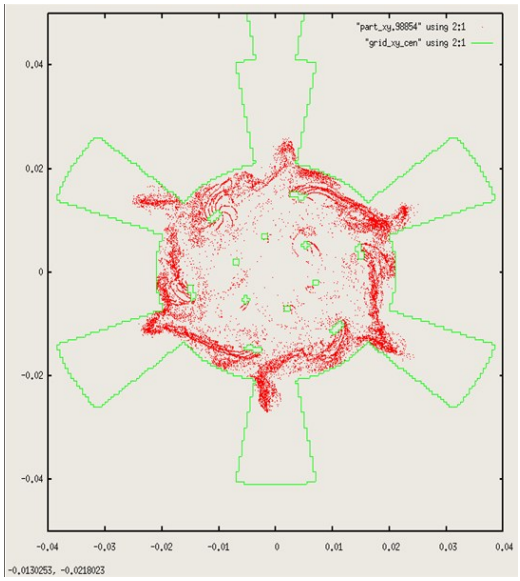

Figure 3.2.74. Algorithm #4: number of layers, N = 2, operating in 2π-mode.

3.2.5.8 Note of propensity of π-mode of operation

Successful operation of the rodded cathode in the π-mode across a large range of applied voltages using Algorithm #1's 0.75 and 1.5 rod density could be an improvement in output power in the π-mode generated by smaller-radius solid cathodes. Since π-mode operation

is useful for the recent hot topic of axial extraction in relativistic magnetrons [18, 38], the rodded cathode merits further study. Below are results of an Algorithm #1 rod density of 1.5 operating at a voltage of 350 kV and 0.6 T magnetic field.

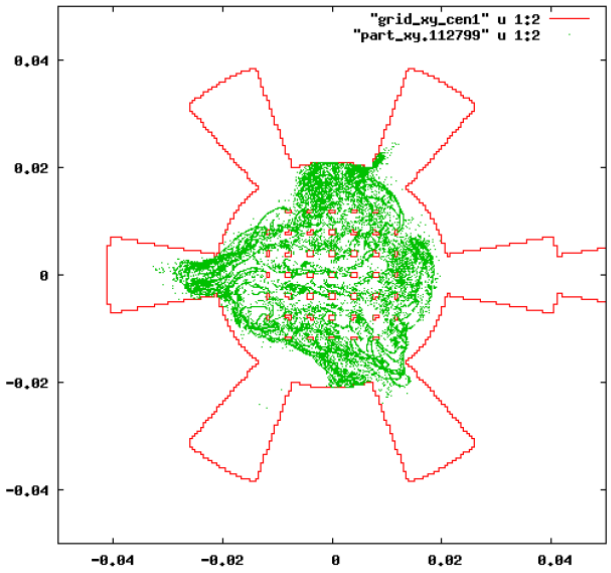

Figure 3.2.75. Algorithm #1: π-mode of operation at DC voltage 350 kV.

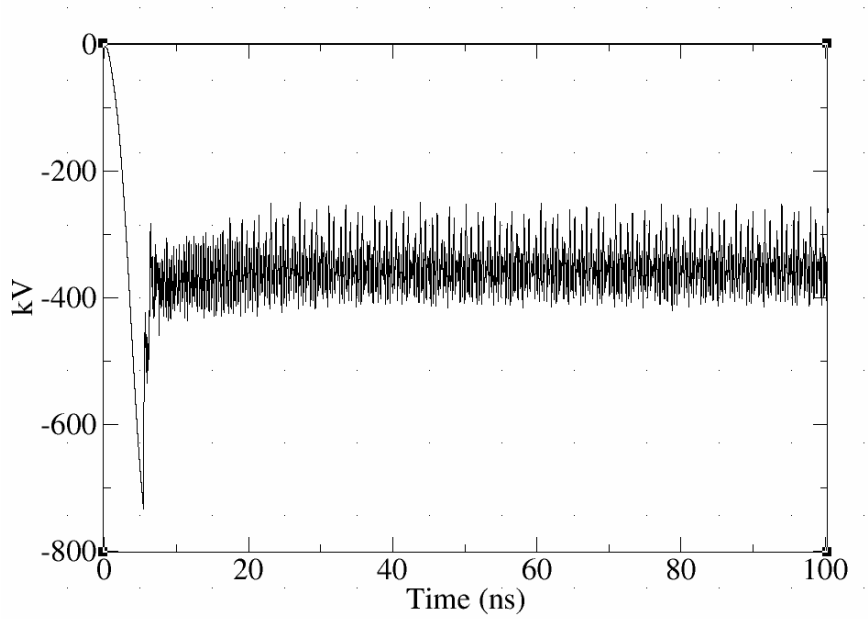

Figure 3.2.76. Applied DC voltage of 350 kV.

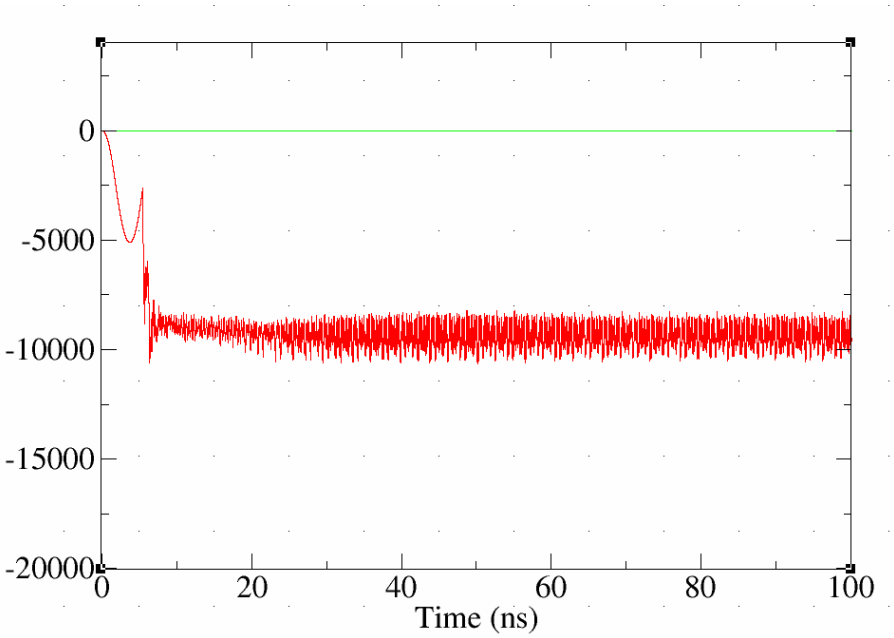

Figure 3.2.77. Anode current in kA (red).

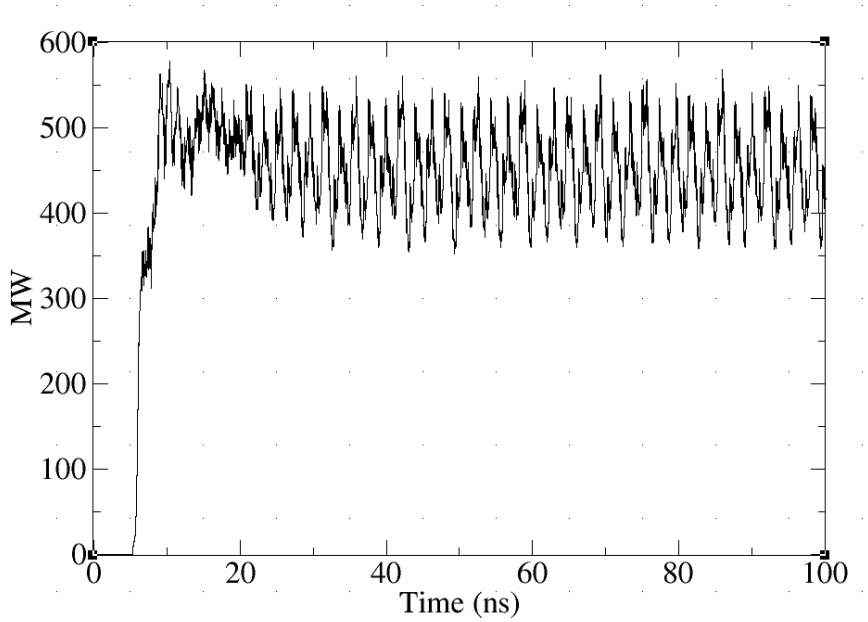

Figure 3.2.78. Microwave output power.

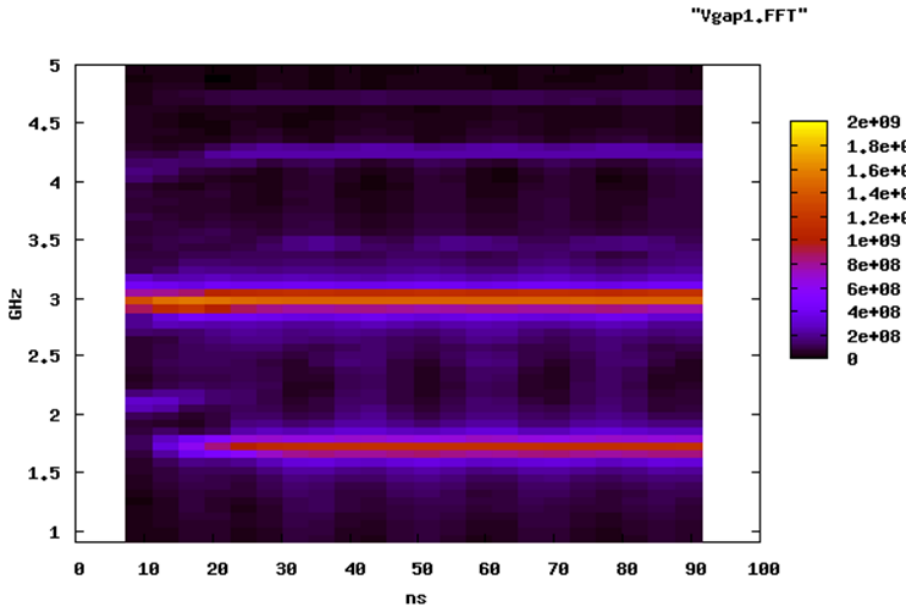

Figure 3.2.79. Time-frequency analysis (TFA) showing time variation of frequencies generated.

The microwave power output of the Algorithm #1 0.75-density rodded cathode at 0.6 T across a range of operating voltages is compared to that of the solid and transparent cathode, Figure 3.2.80.

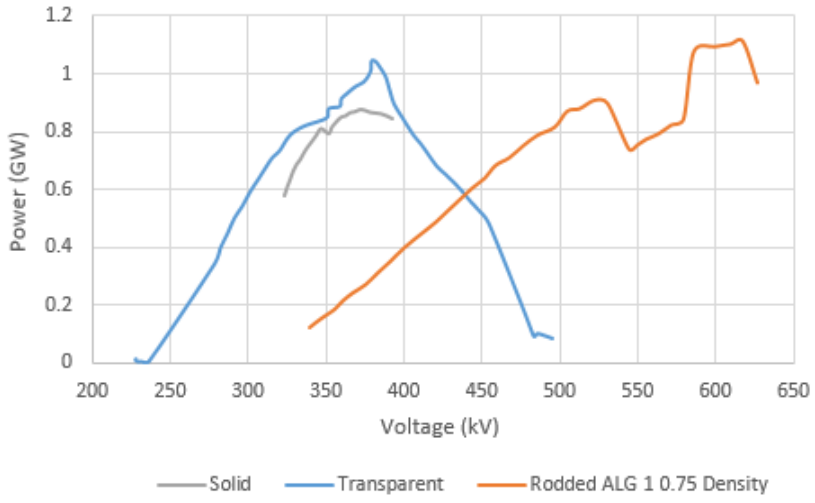

Figure 3.2.80. Simulated power vs. operation voltage (at 0.6 T) for the solid, transparent, and Algorithm #1 0.75 density rodded cathode.

3.2.5.9 Conclusions for the rodded cathode

After validation of the A6 magnetron ICEPIC model, a variety of Algorithms was employed to generate a rodded-cathode topology with high performance in terms of microwave output power and fast-rate of mode rise-time. To this end, it has been demonstrated that a rodded cathode exhibits two favorable characteristics: (i) equal-to or faster establishment of operating mode when compared to the transparent cathode and (ii) operation in the π-mode over a wide range of DC input voltages for Algorithm #1's 0.75 and 1.5 rod density.

There was a general trend for Algorithm #1, #2, and #3 to operate in either the $2\pi/3$- or $4\pi/3$ mode, and the tendency for Algorithm #4 to operate in the $2\pi/3$-mode. This is interesting since the former group is of four-fold symmetry and the last group is based upon point symmetry. Although the ability of the rodded cathode to influence the operating mode has no mature explanation, the four-fold symmetry of some Algorithms used to populate a topology quite likely primes for the $4\pi/3$ mode due to single or groups of outer-most rods occurring in fours.

There is also evidence that the microwave mode electric field penetrates far into the rodded cathode structure, as can be seen in Figure 3.2.63, Figure 3.2.69, Figure 3.2.70, Figure 3.2.72, and Figure 3.2.75. This field is strong enough to cause emission from even the center rod of each array. Figure 3.2.75 illustrates not only this, but that the emission from these deep rods occurs in a pattern that can be traced in orderly curves in the shape of a π-mode. This is reminiscent of the transparent cathode, where the strips allow the penetration of the E_θ component of the microwave mode to penetrate to the axis of the device, where it enhances the radial **E x B** drift of electrons that is responsible for spoke formation over a wider range of radii when compared to the solid cathode.

The penetration of microwaves mode down to the axis was the primary inspiration for the transparent cathode, aside from cathode priming. However in the case of the rodded cathode, there exist bodies that both absorb and emit electrons that either give to or take energy away from the deeply-penetrating operating mode. Clearly, this is a more complicated interaction than the case where the mode interacts with a non-emitting matrix of rods in a metamaterial-like fashion.

Perhaps the behavior of the penetrating mode can be tuned to better match the fields in the A-K gap. For example, as this was just a straight-forward comparison of the rodded cathode of radius 1.58 cm to solid and transparent cathodes with the same radius, it might be advantageous to reduce the radius of the rodded cathode to (i) attenuate or balance the wave-cathode interaction with the rest of the mode located in the A-K gap and to (ii) increase the A-K gap in the spirit of increasing efficiency and reducing the ill-effects of gap closure and resulting pulse shortening. For the first point (i), decreasing the radius might also increase the propensity for π-mode operation in the A-K gap, a trend that was seen with the solid cathode. Additionally, a rodded cathode seen in Figure 3.2.75 that might harbor π-mode fields in its interior might easily mesh with π-mode fields in the A-K gap encouraged by the smaller radius for a more favorable interaction.

Overall, the rodded cathode's propensity to operate in the π-mode in certain topologies is of particular interest for axial extraction in relativistic magnetrons for ultra-compact HPM sources, which rely upon π-mode fields to selectively construct a Gaussian-like microwave output radiation pattern (TE_{11}) that has its main lobe maximum in the direction normal to the antenna's aperture surface.

3.2.6 PULSERAD firing into an MDO load – PSPICE (TopSPICE)

The Marx-bank-powered PULSERAD with MDO load was simulated in the TopSPICE demo version, Figure A1, to provide a meaningful comparison to experimental data, to approximate parasitics in the system, and to provide a guide for future changes to the system, such as alteration of the 7 Ω $CuSO_4$ resistor or addition of parallel or series resistance onto the 20 Ω transmission line. In particular, the simulated voltage waveforms

on the PFL and 20 Ω transmission line D-dot probe locations were able to greatly inform the interpretation the experimental data, Figure 3.2.81 and Figure 3.2.82. The experimental data trace for the PFL D-dot was compensated by -80 kV so that it was at the same potential as the transmission line D-dot probe. The 2:1 ratio of starting voltage between simulation and experiment PFL voltage is likely due to the way the Marx bank is charged in 6 parallel sections, while the simulation represents a charged capacitor bank that is fully erected. Another substantial difference between the simulated curves lack the decay seen in the measured curves; this is probably attributed to signal droop in the sensor.

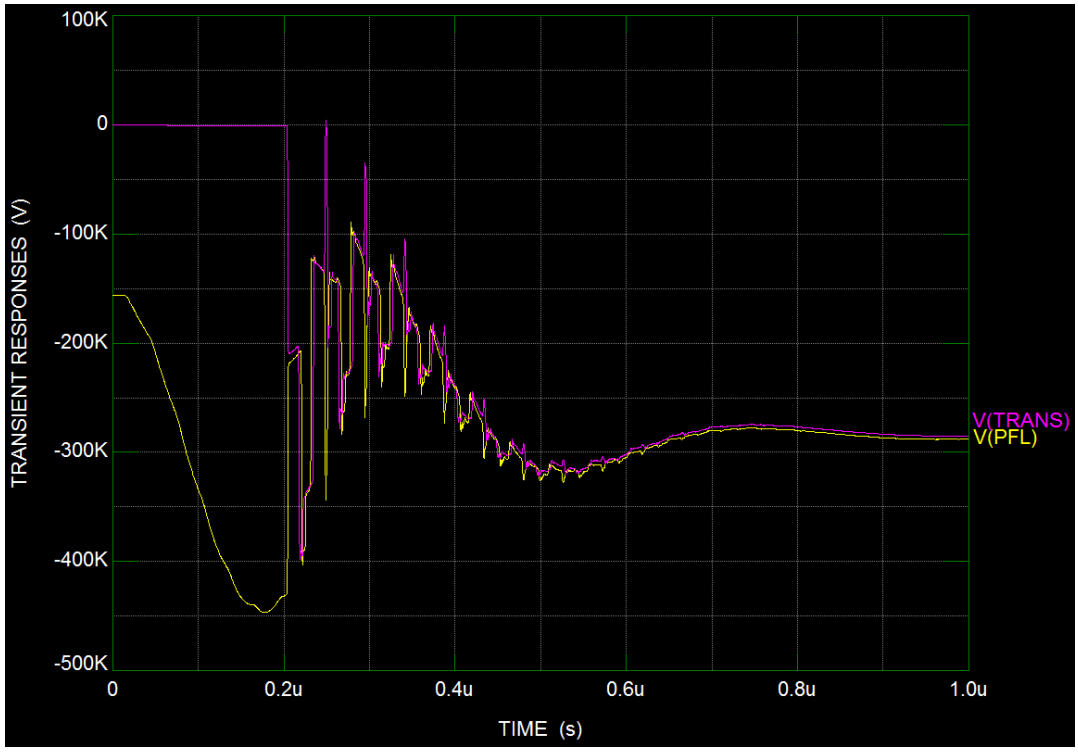

Figure 3.2.81. Simulated voltage waveforms for the D-dot probes located on the PFL and transmission line.

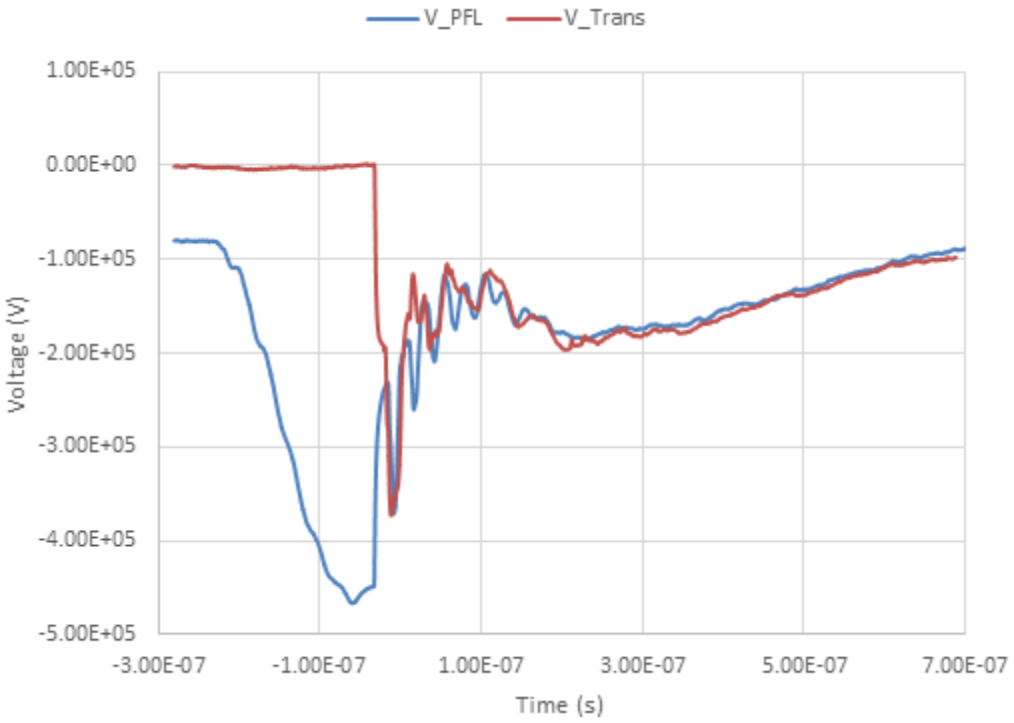

Figure 3.2.82. Experimental data for the D-dot probes located on the PFL and transmission line.

TopSPICE simulations also confirmed the expected voltage pulse and informed the experimental current waveform seen in experiment, Figure 3.2.83 and Figure 3.2.84. To match simulation to experiment, the MDO load was modeled as a dynamically-changing resistive load. In the first few nanoseconds that the voltage pulse arrives, it is modeled as a 500 Ω load, and then it is switched in parallel to a 135 Ω load. Plasma gap closure is emulated by switching both of these resistors in parallel to another 500 Ω resistor, for a total load impedance of 88 Ω. However, experimental data suggests that the shorted impedance of the MDO is 50 Ω. A moment after gap closure the line is at 184 kV and the

current is 3.23 kA. Taking into account the 7 Ω CuSO4 resistor that is in series, R_{total} = 184 kV/3.23 kA = 57 Ω. This makes for a 50 Ω shorted impedance for the MDO.

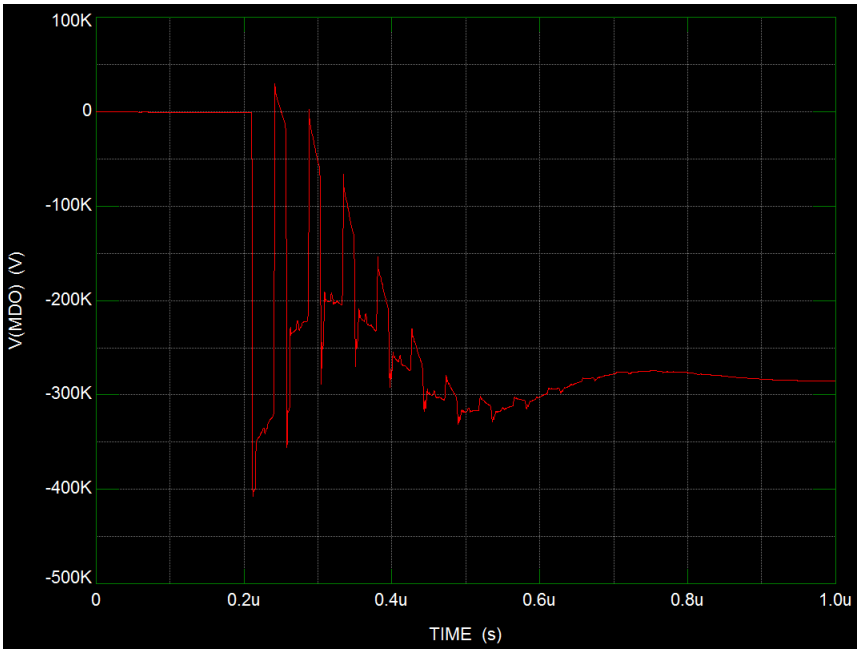

Figure 3.2.83. 30 ns voltage pulse(s) delivered to the MDO.

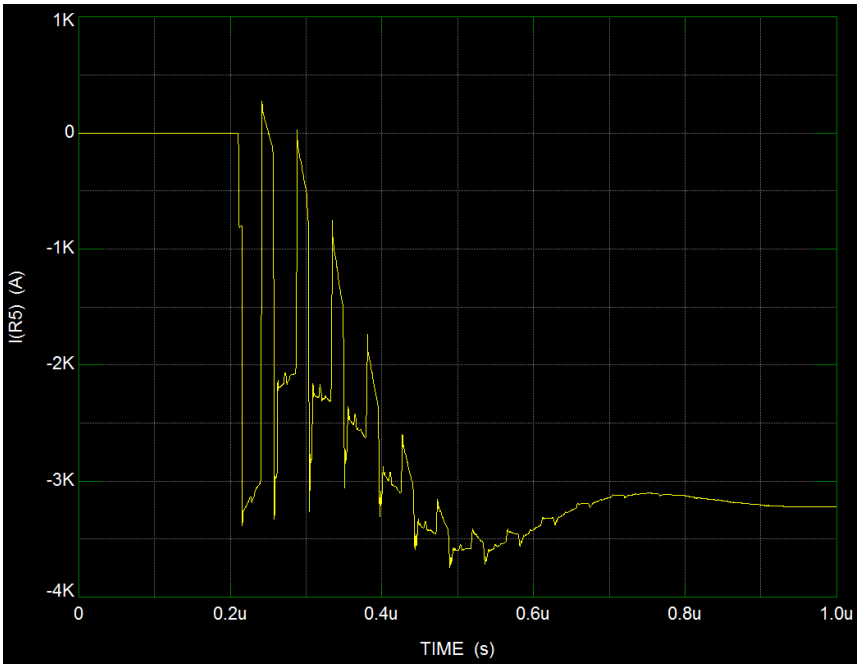

Figure 3.2.84. Current delivered to the MDO.

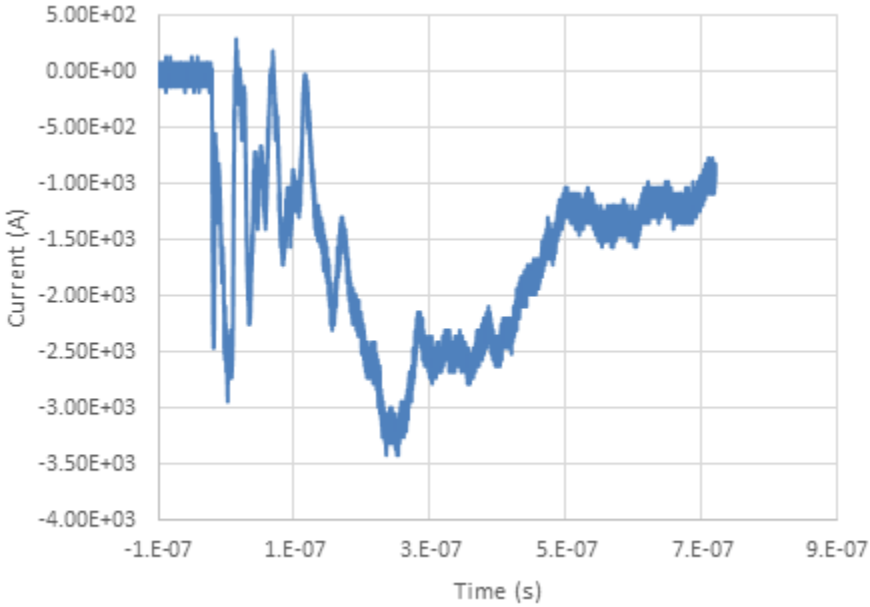

Figure 3.2.85. Experimental data of current delivered to the MDO.

Lastly, the TopSPICE simulations allowed the estimation of parasitics in the system. For a PFL voltage risetime of 160 ns, this was accomplished by adding 4 μH of parasitic inductance in series with the Marx. In addition, though it was not known what the SPICE switch model parasitic capacitance was, adding 2 pF in parallel seemed to match the measured pre-pulse signal on the transmission line D-dot probe.

3.2.7 PULSERAD's pulsed electromagnet circuit – PSPICE (TopSPICE)

The recently reconfigured PULSERAD accelerator/pulser that would power the MDO in experiment required a pulsed electromagnet circuit capable of producing up to 0.8 T of insulating magnetic field. One of the central challenges of building such a circuit was the computer modeling of the circuit's thyristor switch. An accurate computer model of the thyristor was needed to select critical snubber resistor and capacitor values to prevent system failure. The Naval Research Lab's (NRL) methodology for custom creating spec-sheet-matched thyristor components in simulation was used [58]. In lieu of the Microcap circuit simulator used by NRL, the TopSPICE trial version (a PSPICE variant) was used. Due to the logical and computational constraints of PSPICE, the simulated circuit had to be adapted to capture important dynamics and to intelligently alter the real-time behavior of the thyristor switch. To do this, the circuit employed two sample-and-hold circuits to save critical voltage states, described in Figure A2, to measure dI/dt through the switch and the voltage drop across the crowbar diode at specific instances in; these values were used to determine the thyristor's behavior.

NRL's method modelled a thyristor as a time-varying resistor that exponentially ramps up its resistance after the reverse current through the thyristor reaches a threshold. This threshold reverse current varies across thyristor type and is a function of the value of dI/dt of the current through the thyristor as it approaches zero Amps: dI/dt was measured in the circuit via the sample-and-hold circuit placed across the parasitic inductance that is in series with the time-varying "thyristor" resistor. Due to the complex time behavior of the thyristor's resistance, the NETLIST feature of TopSPICE had to be used, see Figure A3. The TopSPICE model was compared against an NRL example, Figure 3.2.86 and Figure 3.2.87, and thyristor spec sheet data after insertion of a multiplicative correction factor was added to the front of the thyristor's exponential-ramp resistive function. This correction factor changed the simulated 0.321 Coulomb Q_{rr} reverse-recovery charge to the spec-sheet intended 0.176 C for the given dI/dt experienced by the thyristor just prior to switch opening. Due to the limitations of TopSPICE, only one of the TopSPICE curves is shown in comparison to the NRL data.

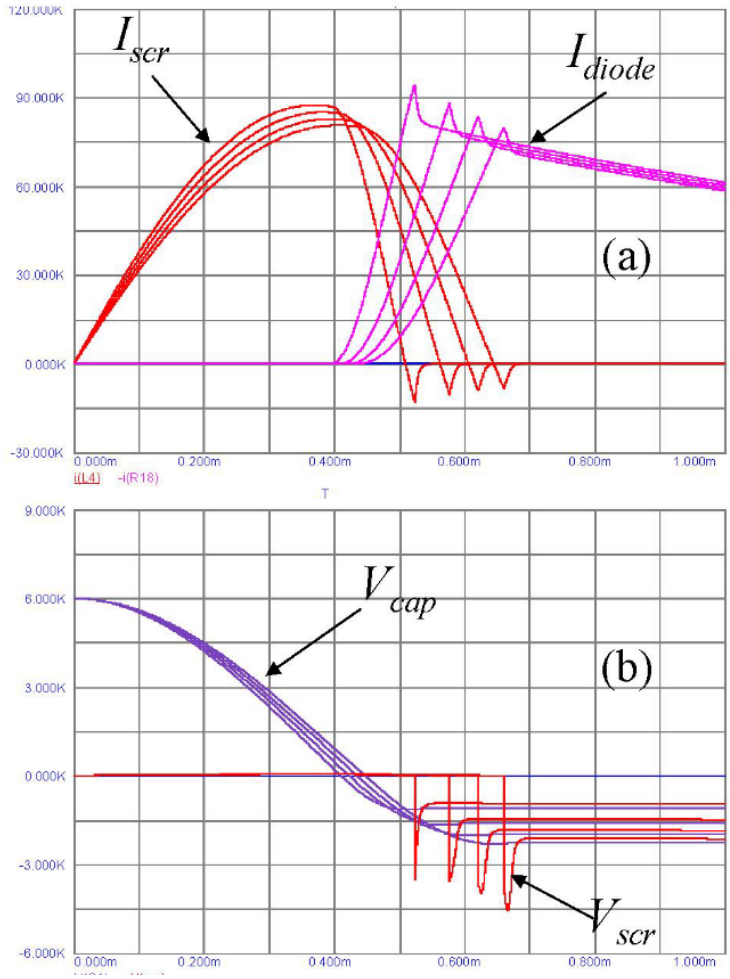

Figure 3.2.86. NPGS Microcap simulation of railgun circuit using a variety of parasitic inductances [58].

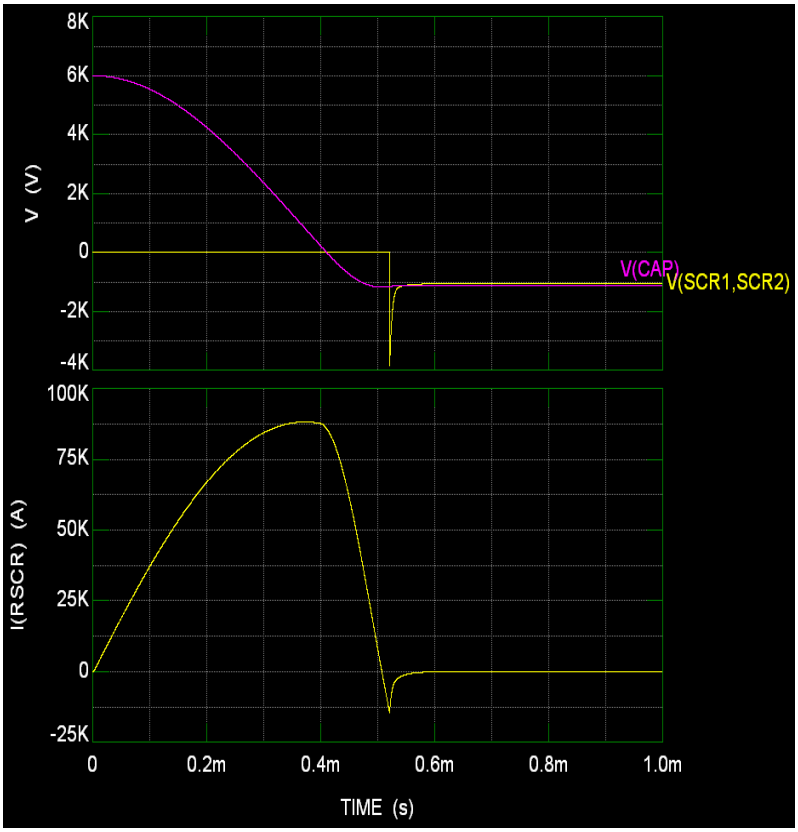

Figure 3.2.87. UNM PSPICE simulation of NPGS railgun circuit at one value of parasitic inductance.

After comparison of the TopSPICE model, the PULSERAD's pulse electromagnet was simulated with the intent of properly selecting the capacitor and resistor elements of the snubber circuit needed to protect the operation of the thyristor switch. Results for the system with no snubber attached are shown below in Figure 3.2.88. The integrated Qrr reverse-recovery charge in this figure is 10.3 mC, which compares to the spec sheet calculated value of 9.6 mC. At this point the TopSPICE computer model developed was considered to be validated.

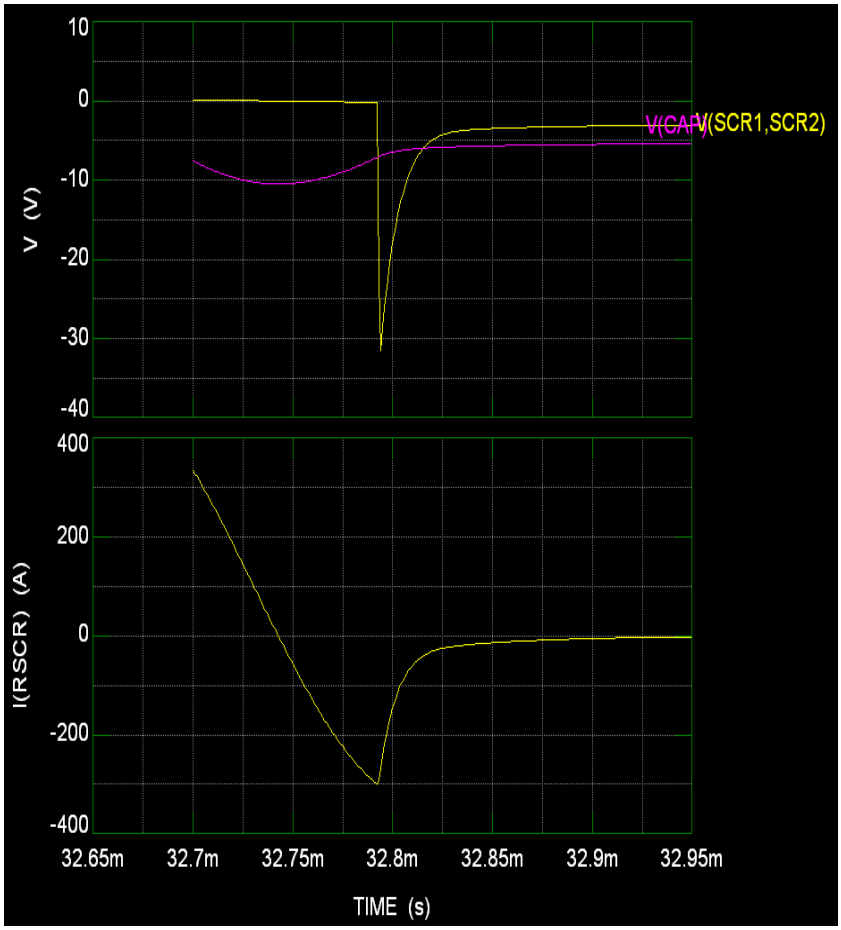

Figure 3.2.88. PSPICE results of UNM pulsed electromagnet circuit with no snubber.

The snubber must be tuned to provide quite a few protective roles at once. These roles include: (1) dV/dt damping across the thyristor to prevent latching, (2) overvoltage protection during thyristor reverse recovery, and (3) yet still keep dI/dt below a specified value during switch closure, as the conductive cross-sectional area of the thyristor starts small and spreads at a finite rate. Snubbers also protect the thyristors against over voltage in the case that several thyristors are used in series, but this need was eliminated with the choice to go with only one thyristor. Should this circuit be amended in the future to include

another series thyristor (the trigger circuit allows for use of an additional thyristor), the TopSPICE NETLIST is included in Figure A3 for snubber considerations. The switch breakdown and closing times for separate thyristors should be simulated with a delay between them to test voltage response across each switch to determine ill effects, and snubber values must be chosen to address these. Even in this case, it might be wholly appropriate to equip both thyristors with separate snubbers that have half the resistive value and double the capacitive value of the snubber installed for the single thyristor.

The snubber worksheets provided by ABB Semiconductors [59] proved to be of little help to pulsed power applications, as it applies to 60 Hz HVAC applications. To show an example, for the pulsed electromagnet circuit, their analytical method recommended a 0.115 Ω, 150 μF snubber. This snubber did result in a reduction in the maximum reverse recovery voltage from 32 V to 17 V (Figure 3.2.89). Unfortunately, this snubber would cause a 42 kA surge (Figure 3.2.89) in the first μs of switch closure that would exceed the 1 kA/μs dI/dt limit and damage the thyristor. It was obvious that a higher resistance and lower capacitance was needed. By trial and error, a snubber of 50 Ω and 2.5 μF was chosen.

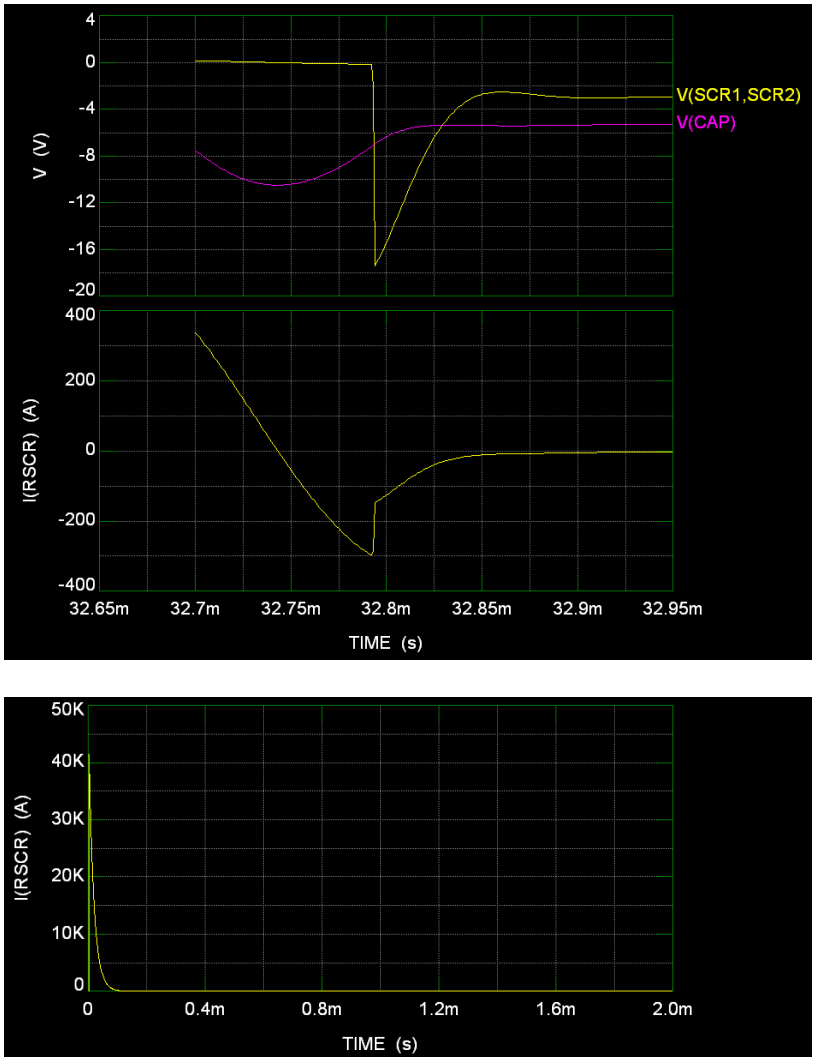

Figure 3.2.89. PSPICE result of UNM pulsed electromagnet circuit with 0.115 Ω, 150 μF snubber recommended by ABB Semiconductors. The large current spike during thyristor closure (bottom) would destroy the switch.

Because of the large capacitance of the chosen thyristor, the low reverse recovery voltage on the thyristor of 32 V, which is much less than the 4.6 kV reverse voltage holdoff threshold, and the lack of rapidly fluctuating voltage across the thyristor when it is open, a

snubber might not be needed at all. However, a properly-valued snubber was applied as a good measure of safety for the system.

CHAPTER 4 EXPERIMENT OVERVIEW

4.1 Systems

This chapter section details the systems used for experimental verification of the MDO, specifically the Marx-bank PULSERAD pulser, which was recently reconfigured at UNM, and its UNM-developed pulsed electromagnet circuit subcomponent.

4.1.1 PULSERAD PI-110A electron accelerator/pulser

The Physics International PULSERAD PI-110A is a Marx bank pulser acquired by UNM in the 1990's. Although it was originally outfitted with a 12-stage Marx bank and Blumlein, it was recently reconfigured via guidance by Kenneth R. Prestwich [60] into a 6-stage Marx system, charging a 20 Ω coaxial PFL that switches into a matched coaxial transmission line through an oil-gap switch to provide a 350+ kV pulse with 2-4 ns rise-time and 30 ns flat top into a matched 20 Ω resistive load [61]. The purpose of this reconstruction was to erect the required electric field for resonance of the desired microwave mode in less time than the cavity fill time for that mode, for example 4-5 ns for the π-mode and 2π-mode [11, 62]. MAGIC simulations show that this results in a faster rise time of the microwave mode and higher saturated power level. This effect is especially pronounced with the use of a transparent cathode, which amplifies early priming to the desired mode. In addition, the 30 ns flat top offers better study of steady-state HPM source behavior and is an improvement over UNM's other pulser, the SINUS-6, which provides a 16 ns half-sinusoid pulse. Below is a diagram of the PULSERAD with an MDO load, Figure 4.1.1 [41]. Also shown below

are images of the oil-breakdown peaking switch with viewport window removed and during firing, Figure 4.1.2.

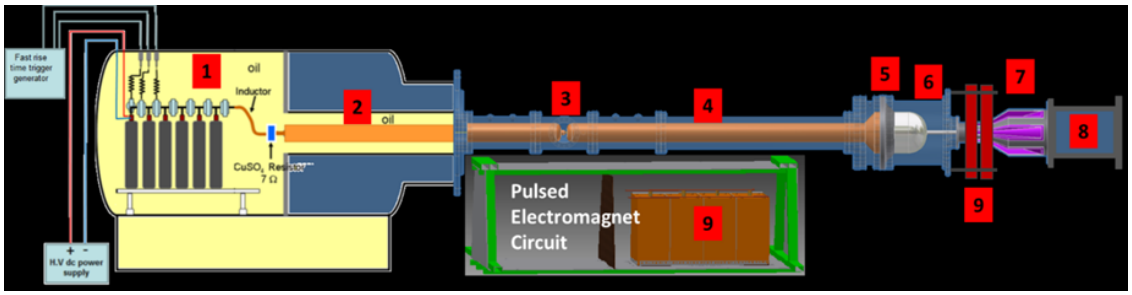

Figure 4.1.1. PULSERAD diagram: (1) 6-stage Marx generator, (2) 30 ns, 20 Ω PFL, (3) low-inductance 2-4 ns breakdown oil switch, (4) 20 Ω transmission line, (5) low-inductance oil-vacuum interface, (6) low-inductance vacuum chamber, (7) MDO, (8) leakage electron beam dump, and (9) pulsed electromagnet and associated circuit [41].

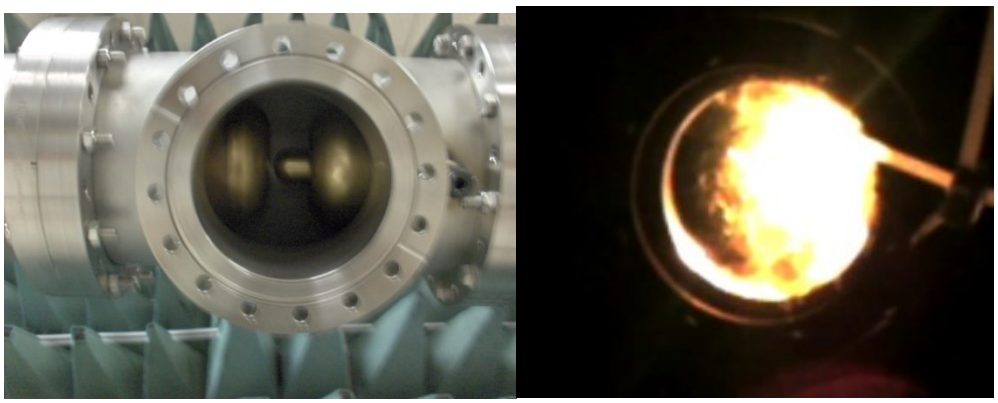

Figure 4.1.2. Low-inductance 2-4 ns oil breakdown switch.

The Marx bank consists of 6 0.050 mF case-center-grounded capacitors which are charged in parallel to ~±20-35 kV and discharged in series via 7 SF_6 switches that are

pressurized to 12 PSI. The trigger electrodes of three of these switches that are nearest to ground see a 50 kV pulse delivered by a 60 PSI SF_6 trigger switch. The negative voltage output of the Marx feeds directly into a curved-rod "inductor," then through a 7 Ω $CuSO_4$ (copper sulfate) resistor that is inline with the PFL. In series, the bank is equivalent to 8.33 μF that is charged to a voltage of ~360 kV. The erected Marx capacitance is much greater than the capacitive PFL load, meaning that the Marx will deliver nearly twice its voltage to it, or ~720 kV. When the 2-4 ns oil switch breaks, half of this voltage is transmitted from the 20 Ω PFL to the 20 Ω transmission line.

The ns-regime oil breakdown switch gap is adjustable with an o-ring-sealed, telescoping Allen wrench that has an attached 0-100 marks/revolution rotation dial gauge. Each turn of the Allen wrench rotates the PFL electrode in a 1:1 ratio. As the PFL electrode rotates, it moves in or out at a rate of 14 threads per inch; this translates to 1.814 mm/turn (0.0714 inches) or 0.5514 turns/mm (14 turns/inch). The electrode is fully protruded out at 25.40 mm (1 inch) and can retreat to a length of 15.60 mm (0.614 inches), Figure 4.1.3. It requires 5.404 turns to be repositioned fully in to fully out. A chart detailing what combinations of oil-switch gap and Marx charging voltage that are needed to achieve a given transmission line (and matched 20 Ω load) voltage is given in Figure A4. Experiments with the MDO indicate that for a 4 mm oil switch gap and a ±25 kV Marx charging voltage, the PFL will transmit between 180-200 kV down the transmission line.

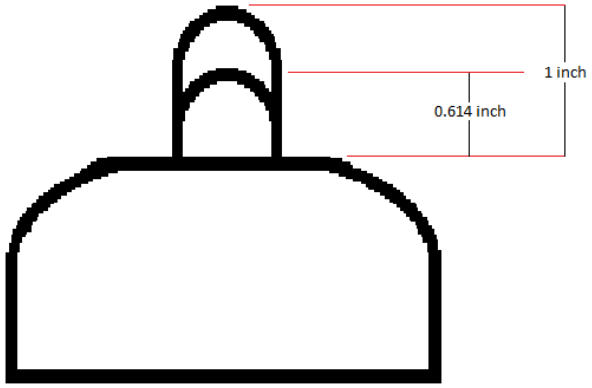

Figure 4.1.3. Adjustment range of the low-inductance oil switch.

4.1.1.1 PULSERAD's pulsed electromagnet circuit

A new pulsed electromagnet circuit was built to provide magnetic insulation for HPM sources run on the PULSERAD, Figure 4.1.4. This system provides power to a Helmholtz coil pair that provides a magnetic field for the MDO at a capacitor charging value of 3.572 kV/T. Due to the LC-circuit sinusoidal ramp up of current in the electromagnetic coils and the 1 ms magnetic diffusion time of the pulsed field into the stainless steel MDO structure, this system is fired 24 ms prior to the PULSERAD. It was required to hold off 5 kV for a 1.6 mF capacitor bank, to switch this stored energy via a semiconductor thyristor switch into a 2.5 mH, 7 Ω electromagnet load, with design flexibility for more powerful future electromagnet coil designs, and to do this with a robust set of safety features such as bay-door interlocks and a capacitive energy resistive dump capable of absorbing 50 kJ. It also needed to feature an optically-isolated thyristor trigger switch and to output system current and voltage diagnostics with signals between 0-10 V for easy integration with a LabView

control system. A PSPICE cartoon of the circuit is seen in Figure A5, and a CAD representation of the system is shown in Figure A6.

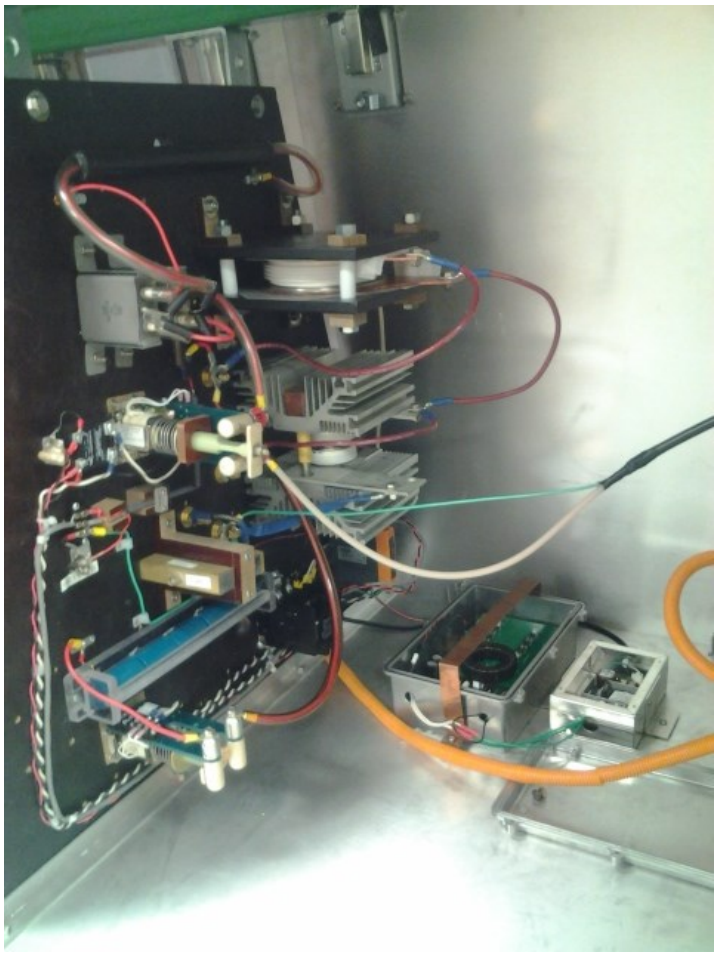

Figure 4.1.4. PULSERAD's pulsed electromagnet circuit.

Triggering of the thyristor was accomplished with an optically-isolated transmitter and receiver. It was necessary to provide a large-magnitude short pulse followed by a small-magnitude longer pulse to satisfy the thyristor's triggering requirements, Figure 4.1.5. To accomplish this, a compact toroid tape-wound current transformer was used with

two primary coils and one secondary coil. Two monostables converted the incoming optical pulse into two pulses of different lengths, which activated two separate MOSFET drivers to dump a hold-up capacitor enforced 15 V into each primary coil. The secondary coil, with the aid of voltage-clamped and reverse-current-protection Shotkey diodes, fed the thyristor gate. To accommodate for the expansion of the pulsed electromagnet circuit to include two thyristors, the trigger circuit PCB was modified to include a second trigger circuit, which borrows the design from the Naval Postgraduate School (NPGS) [63], Figure A7 and Figure A8. Seen in Figure A9 and Figure 4.1.6 are UNM's PCB board design and final trigger circuit.

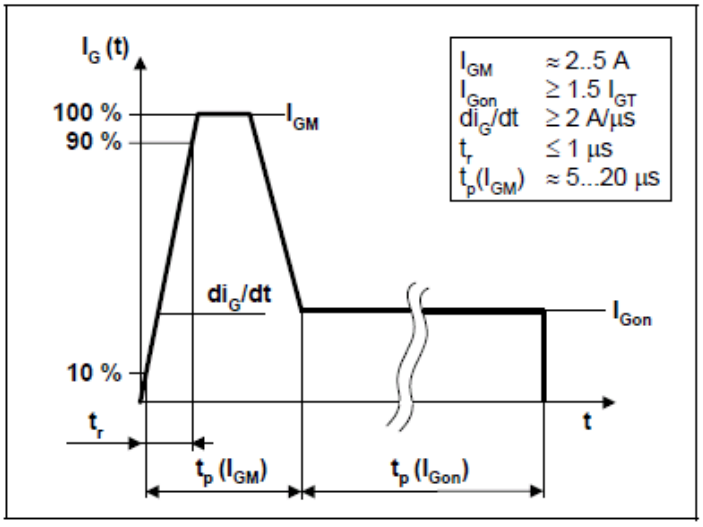

Figure 4.1.5. Required thyristor current waveform [64].

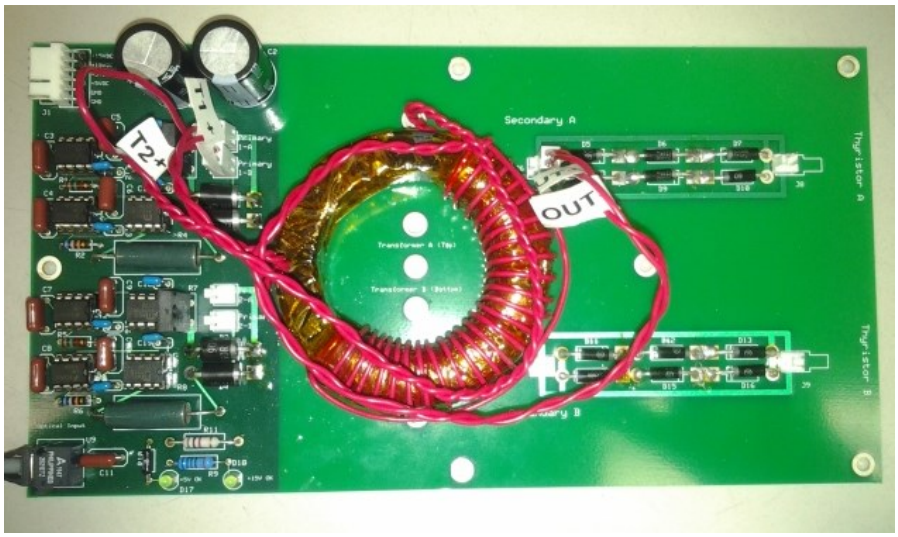

Figure 4.1.6. UNM's thyristor trigger circuit.

A low-current coil encapsulating both the primary and secondary coils provided a constant reverse current to eliminate core saturation and domain memory between shots. This constant-current reverse coil was a fix that allowed the trigger circuit to continue to feed sharp-corners and long pulses to the thyristor gate, without drooping or signal rounding. A representative waveform is shown below, Figure 4.1.7.

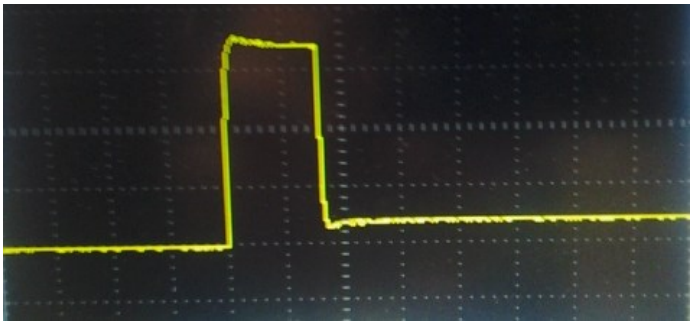

Figure 4.1.7. Current waveform for the UNM thyristor trigger circuit.

4.2 Diagnostics

The diagnostics needed for experimental verification of these microwave sources relate to the PULSERAD PI-110 pulser, its associated pulsed electromagnet circuit, the output microwave energy, and RF pulse shape. They are responsible for monitoring the system from initial charge-up until final microwave production.

4.2.1 PULSERAD PI-110A diagnostics

For the PULSERAD PI-110A pulser, Marx-bank charging voltage, current, and SF_6 gas switch pressure are monitored via its analog control panel. Microwave diode current is monitored by a Rogowski coil [65-69] just upstream from the magnetron; it has a L/R time of ~1 μs, allowing for effective self-integration of the current signal and easy output directly to a fast oscilloscope. The Rogowski was calibrated by previous students using a custom pulser that consists of a short coaxial line that is charged, then switched into a resistive, matched load [70]. This produces a very flat voltage pulse and, hence, flat current pulse. Current dumped by the coaxial line into the load was then recorded via voltage on a scope. At the same time, the Rogowski signal was recorded. Comparison between these two signals yielded the calibration constant of 26.5 V/kA.

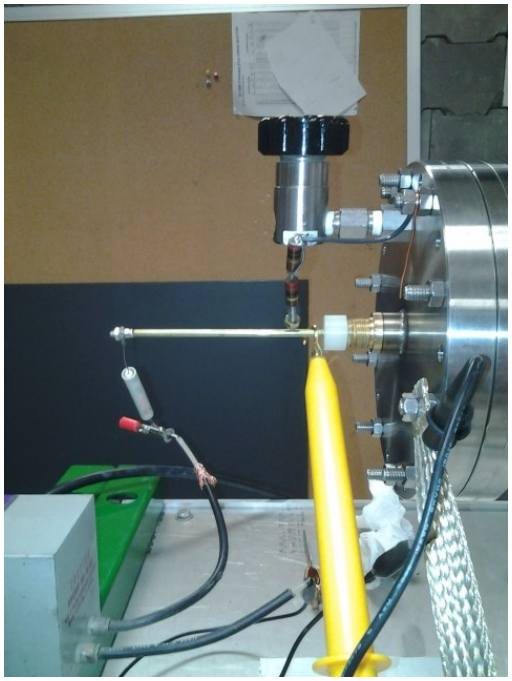

Figure 4.2.1. D-dot probe calibration setup.

Two D-dot probes monitor the voltage of the PFL and of the transmission line connected to the MDO. These probes are modified N-type connectors, with the center conductor extending to a position equal to the outer wall of the transmission line. These probes were calibrated by removing the downstream 20 Ω transmission line's inner conductor and replacing it with the 10 foot inner conductor of the PFL; this provided a clean, continuous section of transmission line that could propagate voltage waves. A flange was installed on the end of the transmission line, with an N-type connector at its center that connected to a 45° tapered copper conductor sleeve that fit over the end of the transmission line's inner conductor, shown in Figure 4.2.1. The choice of 45° minimizes excitation of harmonics down the line. The line was then filled with oil. On the outside face of the N-type connector, a thin conductive rod was attached that was used to charge the inner

conductor to 2-5 kV, attach a high-voltage probe, and to serve as an electrode on which a matched 20 Ω resistor was pressed to discharge the transmission line and excite the two D-dot probes. A variac-controlled 10 kV power supply was used to charge the line. The D-dot probe signals were captured using a fast oscilloscope and numerically integrated to obtain the temporal profile of the voltage on the line. The pre-discharge voltage on the line was captured by a high voltage probe connected to a multimeter; to provide the high voltage probe with the required 1 MΩ input impedance, a 1.1 MΩ resistor was placed in parallel with 12 MΩ input impedance of the multimeter. By comparing the magnitude of the multimeter voltage with the integrated voltage, the calibration constants of the two D-dot probes were calculated: $3.4\text{x}10^{-13}\ V^{-1}$ for the PFL and $3.74\text{x}10^{-13}\ V^{-1}$ for the downstream transmission line that connects to the MDO. A numerically-integrated calibration signal is shown in Figure 4.2.2. An RC integrator was also built and tested, but suffered from noise problems, which is often a problem for high-impedance systems and sensors. As a result, it was necessary to integrate the signals between shots or after experiments were concluded. An example of the attenuated raw and numerically-integrated D-dot signal on the 20 Ω transmission line for a voltage launched into a matched 20 Ω load is given in Figure 4.2.3 and Figure 4.2.4 [41].

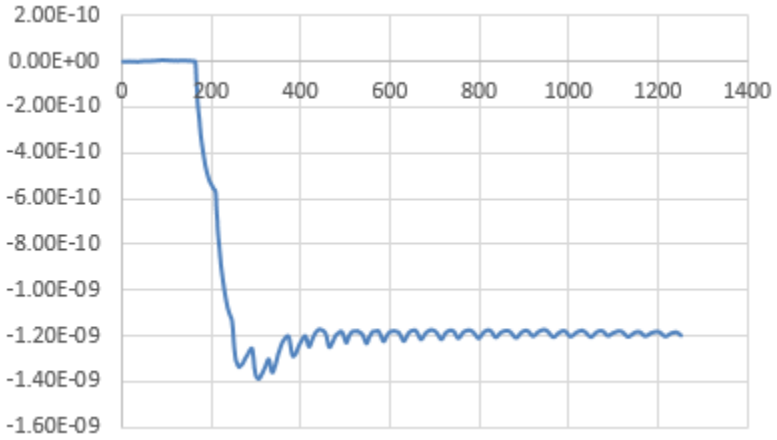

Figure 4.2.2. Numerically-integrated D-dot calibration signal showing a voltage difference of 3.5 kV.

.

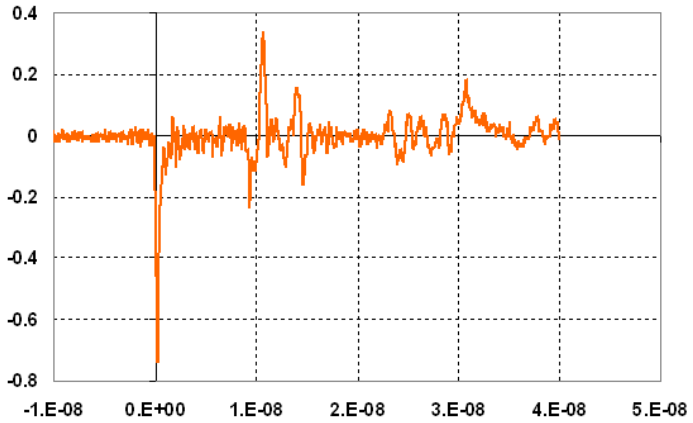

Figure 4.2.3. Attenuated D-dot signal in downstream transmission line while PULSERAD fired into a matches 20 Ω load.

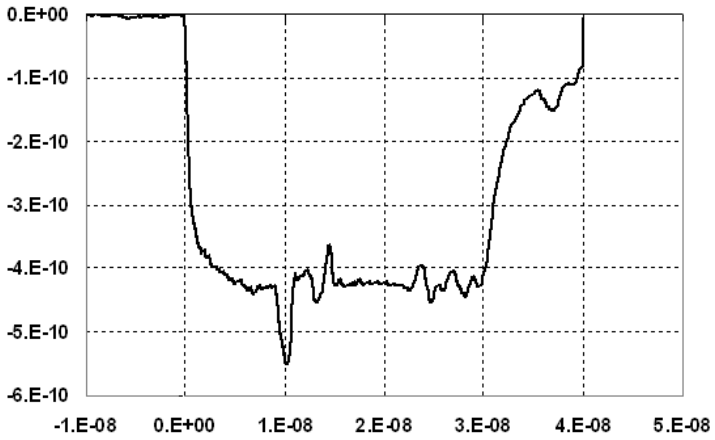

Figure 4.2.4. Numerically-integrated D-dot signal of the signal in Figure 4.2.3 showing a ~2 ns rise-time, 30 ns flat top voltage pulse.

The pulsed electromagnet circuit on the PULSERAD employs a variety of operational diagnostics. A precision current viewing resistor (CVR) measures current through the coils and a 1000:1 resistive divider measures voltage on its capacitors. These diagnostic signals were designed to output 0-10 V from a BNC connector for input along an RG232 cable into an oscilloscope or a LabView control system. Capacitor charging was accomplished with an 8 kV, 250 mA Glassman power supply that was voltage and current controlled and monitored via a USB2.0-boosted cable by software provided by Glassman High Voltage Inc. The pulsed electromagnet circuit's housing enclosure also mounts an LCD 1000-to-1 voltage meter to facilitate safety.

4.2.2 Microwave power and frequency diagnostics

As described below, the MDO experiments relied on use of a variety of waveguides and an alcohol calorimeter to determine frequency content, power envelope, and total power and efficiency.

4.2.2.1 L-band detector and S-band – power and frequency characteristics

Microwave power, frequency, and pulse shape was measured with an open L-band rectangular waveguide that is coupled into a RG-214 cable via a waveguide-to-coax adapter, which leads to a fast oscilloscope. Use of the fast oscilloscope not only provided RF voltage and power, but the ability to run a fast Fourier transform (FFT) and time frequency analysis (TFA) on the microwave pulse to more precisely track magnetron output mode behavior. Due to the large aperture of the L-band detector and its close proximity to the ~1 GW MDO source, four 20 dB attenuators (total of 80 dB) were used to decrease the signal amplitude before it arrived at the oscilloscope. Because large signals can to some degree bypass more than 40 dB of attenuation through their ground terminals, two 20 dB attenuators were placed between the detector and the cable, and another two 20 dB attenuators were placed between the cable and the scope. The L-band rectangular waveguide was originally mounted on a stand to measure radiated field distribution profile as a function of angle; however. the large power led to breakdown, probably at the waveguide-to-coax adaptor structure which contains many sharp metal edges and corners. This was evidenced by microwave pulse shapes that lasted a small fraction of the MDO's anticipated 30 ns microwave pulse, Figure 4.2.5.

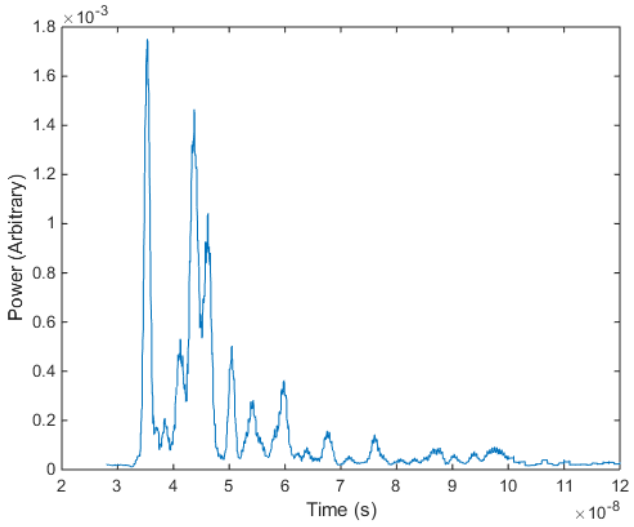

Figure 4.2.5. RF pulse from MDO is truncated due to breakdown in the L-band waveguide detector.

The L-band detector was then filled and sealed with SF_6 gas, and thin slices of carbon-impregnated Eccosorb foam were placed over the waveguide aperture to achieve reasonable pulse shapes. An S-band -20 dB directional coupler waveguide detector was eventually substituted in the experiment. The ~2.5 GHz signal is just outside of the waveguide's band of 2.60-3.95 GHz, so some small degree of evanescent attenuation could be expected. However, there seemed to be no evidence that the coupling holes experienced breakdown, as the RF envelope profile appeared to be superior to that obtained using the L-band detector. Ignoring breakdown issues, it would have been possible with the L-band detector to approximate an effective aperture size of the detector (~80% of the size of the aperture) and use the measured attenuation of the RG214 cables, Figure A10 and Figure A11, to calculate a field-mapping integration to approximate the microwave power. However, both the placing of thin slices of Eccosorb over the L-band detector and use of

an S-band or X-band detector predicated the loss of attenuation knowledge and impossibility of calculating radiated power. A properly-measured RF pulse shape was, however, useful in conjunction with an energy measurement from the calorimeter to quickly calculate radiated power.

If a field-mapping integration is desired in the future, it is recommended that two identical higher frequency band waveguide detectors with pyramidal horn antennas be used. These detectors would attach to Port 1 and Port 2 of a network analyzer and their horn antennas would face each other at a measured distance. Because it is straightforward to calculate the gain between two pyramidal horn antennas of equal size, the gain value can be subtracted from the attenuation value measured by the network analyzer to arrive at the total attenuation value of the detector as a function of frequency. Using an appropriate effective aperture size for the antenna, this detector could then be used to calculate a field-map integral of the total power radiated, provided the detector is placed in the far-field region of the antenna by using sufficient separation.

4.2.2.2 Calorimeter - power

The microwave calorimeter diagnostic was constructed because of its ability to measure any radiated mode without complication, even if some of them exist simultaneously. This cannot be said for the open rectangular waveguide method described above or for direct field couplers, which are sensitive to mode and polarization. Unfortunately, axial extraction schemes in magnetrons can preserve the symmetry of degenerate modes in the interaction space, so any mode can be effectively used to excite a unique circular-waveguide mode. This is what forced the need for a mode-flexible microwave power diagnostic. While it

would have been possible to purchase or design/manufacture a field diagnostic such as a directional coupler on the wall of a circular waveguide fitted to the downstream end of the MDO or compact magnetron, it was more straightforward to manufacture a calorimeter instead. The UNM calorimeter has proven useful in other experiments, such as with backward wave oscillator (BWO) with double-helix Bragg reflector that simultaneously output a circular TE_{11} and TM_{01} modes, Figure 4.2.6.

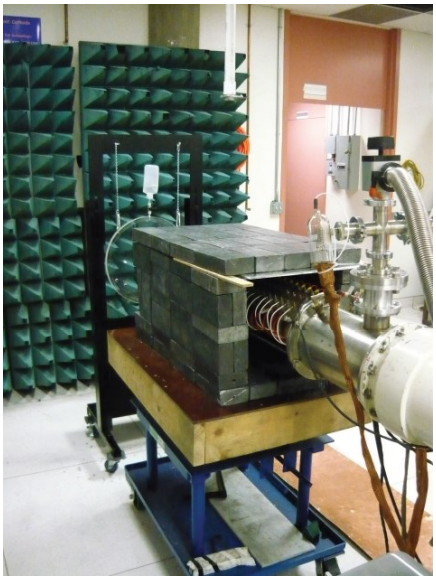

Figure 4.2.6. Calorimeter in use for a UNM BWO experiment that outputs a simultaneous TE_{11} and TM_{01} mode.

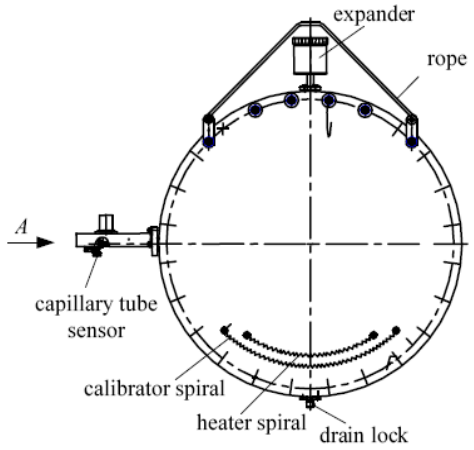

Figure 4.2.7. UNM's calorimeter construction is similar to that used in Tomsk, Russia (above) [71].

Design of the calorimeter was inspired by those used in Tomsk, Russia and at the University of Maryland, [71] and [72]. Its structure consists of two round sections of clear acrylic (polystyrene) glass of 45 cm diameter and thickness 0.9525 cm (3/8 inch), which sandwich a 40 cm diameter, 0.9525 cm thick layer of pure ethanol and several rigidity struts. HPM impinging on the surface of the calorimeter are of course reflected, absorbed, and transmitted to varying degree depending on frequency, as measured by two horn antennas and a network analyzer, Figure 4.2.8. A typical power absorption coefficient for the MDO and compact magnetron experiments producing 2.4 GHz was ~61%. This absorption coefficient spectrum closely matches that measured by the University of Maryland, Figure 4.2.9.

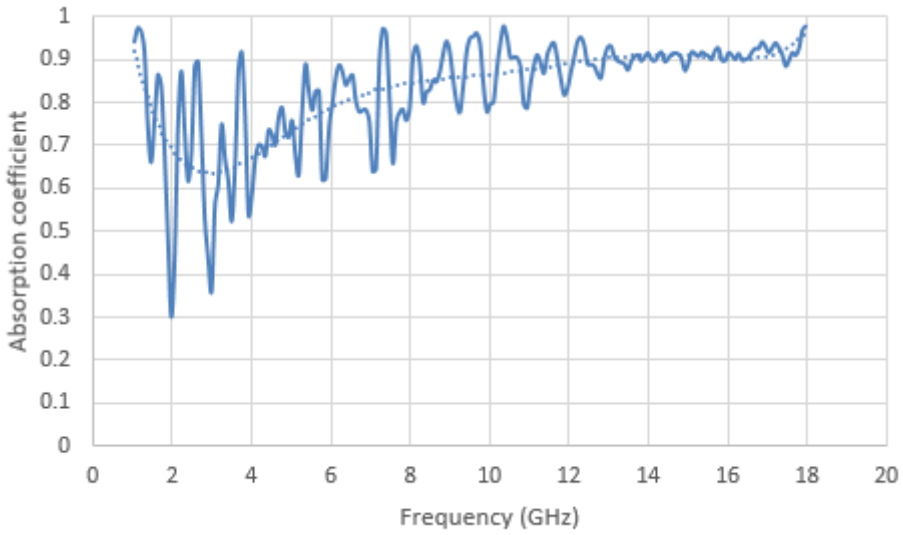

Figure 4.2.8. Absorption coefficient for the UNM calorimeter.

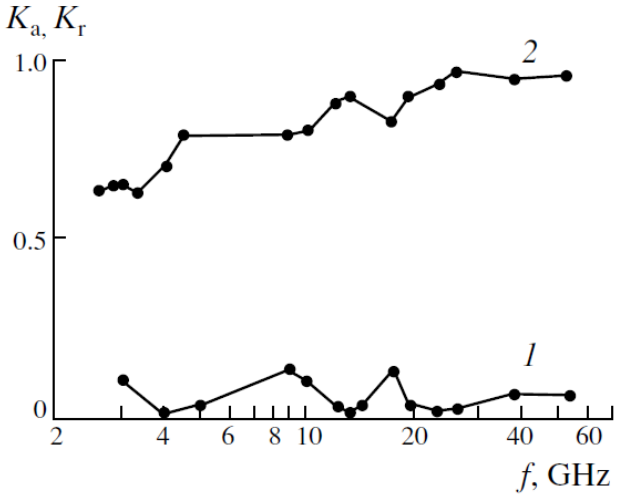

Figure 4.2.9. University of Maryland calorimeter reflection coefficient K_r (1) and absorption coefficient K_a (2) [72]. This is comparable to K_a for the UNM calorimeter.

Once microwave energy is absorbed, it causes expansion of the alcohol volume into a glass capillary tube of inner diameter 1 mm. The volume of expansion is not dependent on the spatial distribution of the thermal energy gained by the HPM absorption, nor upon the diffusion or convection of this energy in the body of alcohol; it is this principle that allows the calorimeter to be used in the first place. However, thermal energy of the system is slowly lost to the environment, and the alcohol temperature returns to room temperature with a characteristic $1/e$ decay time of less than 30 s.

Measurement of the expansion of this volume was accomplished with a resistive bridge, where one leg of the bridge contains a 1 MΩ resistor and the variable-resistance capillary tube, which is a glass 1 mm inner-diameter tube with two parallel, separated stainless-steel filaments. The moving column of ethanol between the two parallel filaments provides a changing voltage. The other leg of the resistive bridge is located in the calorimeter control panel, Figure 4.2.10, and contains a fixed-value resistor and a two-stage (fine and course) potentiometer that is adjusted for voltage comparison to the first bridge leg containing the capillary tube sensor. This bridge is powered via a PWM voltage signal that minimizes Ohmic heating in the capillary expansion tube. An Arduino UNO microcontroller provided this PWM signal, which was buffered immediately to the potentiometer leg of the resistor bridge and also transmitted to a control box located at the calorimeter that would apply an appropriate signal to the capillary tube leg of the resistor bridge, Figure A12. Two low-noise, low-input-offset instrumentation amplifiers were then used, one to subtract the differential signals of the capillary tube sensor and another to compare that subtraction with the voltage from the potentiometer leg of the bridge. This final signal is transmitted to the microcontroller, which measures the resistance via a 10-

bit analog-to-digital converter and outputs the value to the LCD screen and to a PC's USB COM-port, where it is displayed in a Arduino software scrolling data screen. The calorimeter control panel also sends voltages to two nichrome wires in the alcohol body that (1) keep a convex alcohol meniscus in the capillary tube prior to HPM firing (potentiometer-controlled 9 V power supply) and (2) that also provide precise depositions of energy into the calorimeter for calibration purposes (TTL-controlled 20 V power supply). The custom Arduino UNO PCB "shield" and its functional schematic are seen in Figure A13.

Figure 4.2.10. Calorimeter control panel.

Calibration of the calorimeter was straightforward: TTL+ switch a well regulated 20 V DC power supply into the 6 Ω nichrome wire calibration coil that is immersed into the body of alcohol. Measurement of the voltage across the calibration wire and integrating the square pulse over time yielded the ohmic-heating energy deposition. An example of the capillary tube sensor response to a deposition of 8 J is in Figure 4.2.11, and a calibration

curve yielded after averaging several shots at a series of energies is in Figure 4.2.12. It is important to note that calibration data must be obtained immediately prior to or after taking data, as small changes in the alcohol resistivity due to impurities can alter the readings. Great care must be given to properly shield the calorimeter's capillary tube with well-sealed aluminum foil prior to use with a HPM source; its twin wires connect directly to the input of sensitive IC amplifiers and behave exactly as antennas.

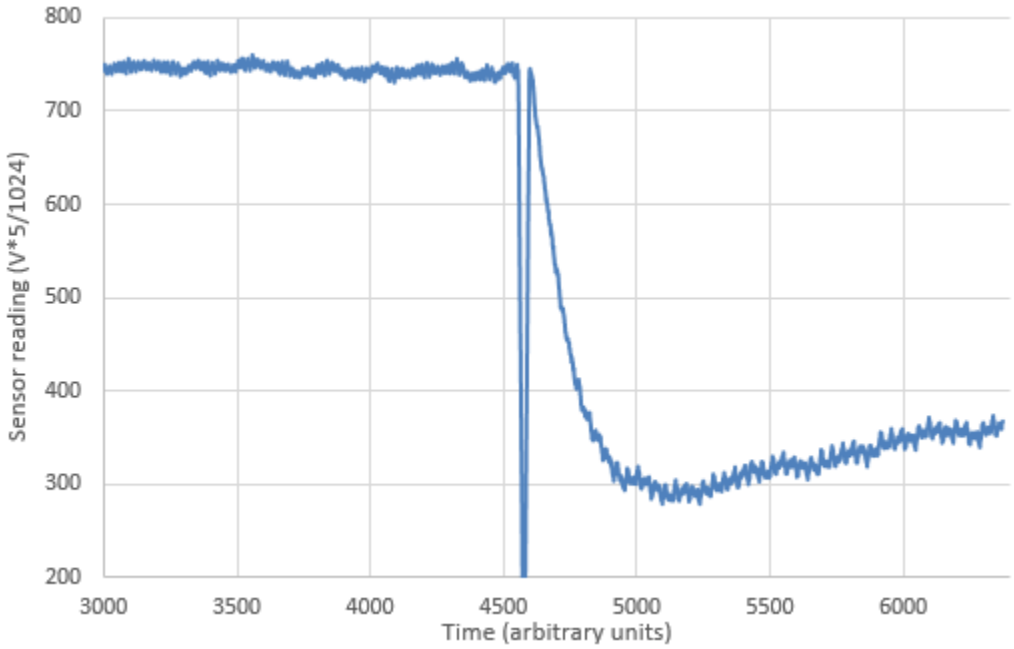

Figure 4.2.11. Calorimeter calibration response to 8 J.

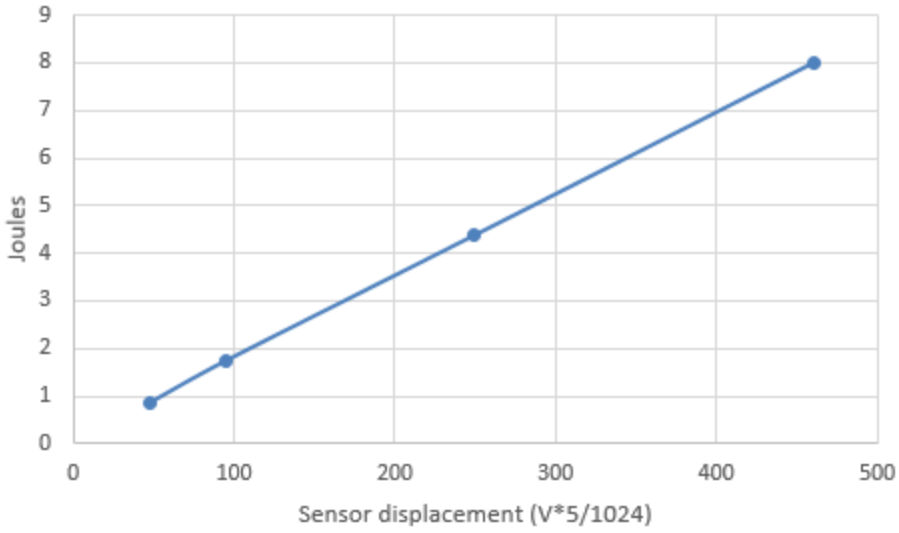

Figure 4.2.12. Calorimeter calibration curve.

CHAPTER 5 EXPERIMENTAL RESULTS

Using the above experimental setup, experiments were performed to test the efficacy of a variety of cathode endcaps, as well as to ascertain the power and efficiency of the full-size MDO. Due to time constraints, a B-field scan, field map, and verification of the MDO's ability to output a TE_{11} mode by insertion of metal vane fillers was not performed.

5.1 Endcap

Experiments were performed using the UNM in-house manufactured S-band radial-extraction relativistic A6 magnetron powered by the SINUS-6 accelerator modified for magnetron operation because the MDO was not yet manufactured at the time [26, 52]. The magnetron and the vacuum region where the leakage current flows were immersed in a uniform axial magnetic field created by a Helmholtz coil pair.

A solid graphite cathode of a radius of 1.58 cm and an annular profile with an inner radius of 0.895 cm was employed. In experiments, a combination of variable cathode lengths, endcap designs on the cathode edges, and dielectric coating thicknesses on the endcaps were used (Figure 5.1.2). The cylindrical channel for the leakage electrons has length ~9 cm (from anode block to the metal flange, Figure 5.1.2) and radius 4.11 cm.

A capacitive-divider probe mounted in the accelerator's coaxial transmission line just upstream of the magnetron's vacuum-oil interface monitored the accelerator voltage. Total current and leakage current were monitored using self-integrating Rogowski coils located upstream and downstream of the magnetron vanes. A thin Lexan target on the downstream end flange was used to confirm the presence and nature of leakage current by

surface damage. Output microwave power flowing radially out of one of the cavities was detected using a directional coupler and registered using a fast oscilloscope.

In experiments the cathode was extended beyond the anode block. We intentionally added disc-shaped graphite endcaps that extended radially beyond the inner radius of the magnetron vanes at the cathode edge to provide a barrier to electrons drifting downstream and to provide an axial field that would decelerate electrons drifting axially downsream.

It is pertinent to note that the large diameter of tested endcaps would be a source of electrons moving upstream along parallel electric and magnetic fields to the vanes should electron emission from the discs occur. Upstream leakage current was not measured, as diagnostics were limited to measuring only the total diode current and downstream leakage current via two Rogowski coils. As such, only downstream current losses could be measured and used to identify endcap designs that reduce these losses. However, proposed later in this section is an endcap design that might eliminate both upstream and downstream leakage currents from the endcap.

A thin dielectric coating on the endcap reduces the surface fields on the conductive surface by a factor of about the dielectric constant ε_r. Solid Rexolite and curable liquid Rexolite adhesives were the dielectrics of choice due to their arc-damage resistance and ease of machinability. The baked liquid adhesive has the same characteristics as solid Rexolite (its dielectric constant is 2.53). The endcaps were dipped into the adhesive liquid and were baked to easily form the thin films as necessary. It was important in experiments to ensure that no air was trapped between the cathode and the dielectric layer so that the surface fields on the cathode are appropriately reduced and air bubbles are avoided when

baking the adhesive. Bubbles can be sites of electron cascade through the bulk dielectric [73].

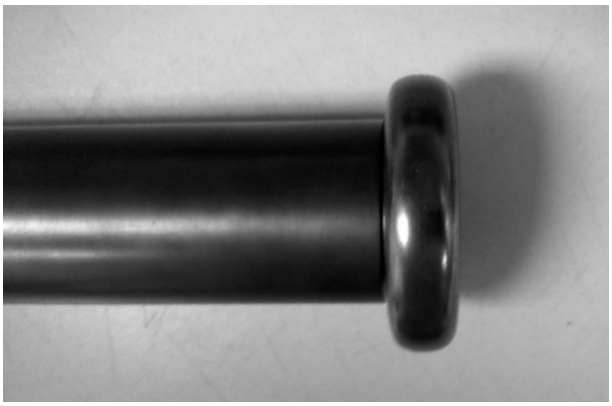

Figure 5.1.1. Photograph of a short, bare endcap (Design A in Figure 5.1.2).

The polished endcaps (one of them is shown in Figure 5.1.1) were tested with and without dielectric coating. The dielectric coatings covered a variety of surface areas and had different thicknesses for each test, *e.g.* 0.02 cm, 0.25 cm, and 1.0 cm. The smaller endcap had a diameter of 4.75 cm and a width of 1.2 cm, and the large endcap had a diameter of 5.6 cm and width of 1.5 cm. They were mounted on solid cathodes that extended either 2.5 cm or 5.9 cm from the end of the magnetron vanes.

When the larger endcap is mounted 5.9 cm from the end of the magnetron vanes, a planar diode of gap 1.25 cm is formed between the endcap and the end flange, Figure 5.1.2 D. The aim was to increase the downstream leakage current from an uncoated endcap by increasing the electric fields on downstream endcap surface. This served to better demonstrate the suppressive characteristics of dielectric coating. All endcaps can be seen in Figure 5.1.2.

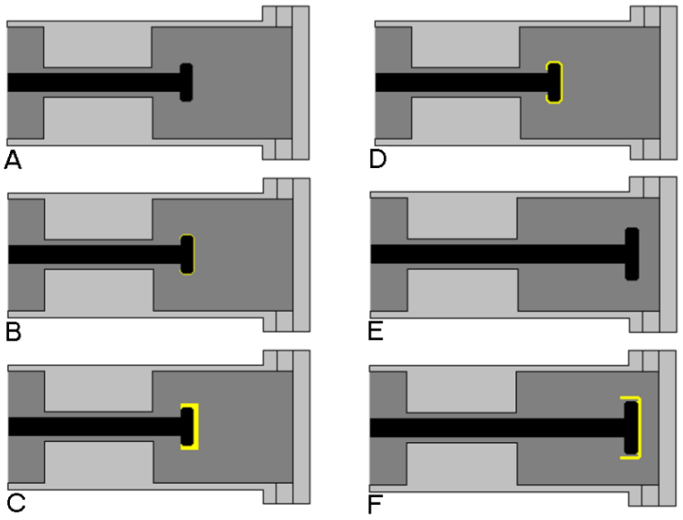

Figure 5.1.2. Magnetron cathode endcap designs that were tested. The yellow indicates the dielectric coating.

The endcaps were machined from graphite, and their surfaces were fine sanded and polished to a metallic finish to decrease the threshold electric field for explosive electron emission. There were no other special preparations taken to prevent explosive emission, such as reducing ion contaminant desorption through bakeout or use of ultrahigh vacuum. Experiments were conducted at low 10^{-5} Torr.

The measured maximum leakage currents from the various graphite endcaps using the same 260 kV voltage pulse at 0.53 T are summarized in Table 2. With no endcap, downstream leakage current from the solid cathode was about 1.18 kA. Show the

Table 2. Summary of graphite endcap results for 260 kV and 0.53 T.

Design	No endcap	A	B	C	D	E	F
$I_{leakage}$, A	1180	50	15	240	1700	145	1100

Thinner dielectric coatings were more effective at suppressing downstream emission than thicker dielectric coatings. There was no indication that an optimal thickness exists; experiments suggest that it is best to form as thin a dielectric film as possible. For example, the large endcap (D) emitted 1.7 kA of leakage current with no coating in the planar diode with a 1.25 cm gap between electrodes with 5.6 cm diameter. A thick dielectric (1 cm) coating on this endcap produced 1.1 kA (design F), and a 0.25 cm coating produced only 145 A (design E). However, for endcap design E (Figure 5.1.2) using the dielectric coating in the presence of high fields on the downstream surface of the endcap, an annular pattern was visible on the thin Lexan film that covered the downstream metal flange. The radius of the pattern corresponds to the maximal radius of the coating. This result can be explained by a surface breakdown on the dielectric initiated by the electric field on the triple point - that is the region where there is a contact of graphite, dielectric, and vacuum. The breakdown develops along the circumferential surface of the coating surface. For the thin coating the potential difference between the coating surface and the cathode is very small. Therefore, development of the avalanche process proceeds along a weak tangential electric field resulting in the small leakage current. This is unlike the case for a thicker coating, where a much larger electric field develops, leading to a surface breakdown. The main conclusion we draw from this is that the dielectric coating allows for the elimination

of leakage current (no sign of electron bombardment in the central area of Lexan film) when no surface breakdown occurs from emission along the surface of the triple point.

In the design of high current electron accelerators, triple points are typically hidden in a region where electron emission is nearly impossible, as for example, in the SINUS-6 accelerator, Figure 5.1.3. This accelerator is capable of producing electrons with energy up to 0.7 MeV.

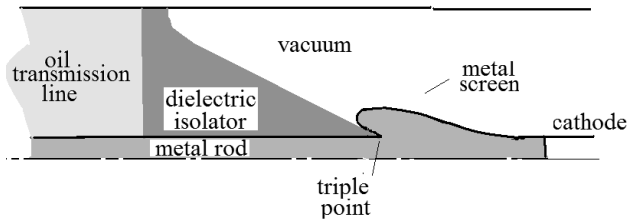

Figure 5.1.3. The triple point in the UNM SINUS-6 electron accelerator is hidden under the metal screen so that electric field in this place is lower than the threshold for explosive electron emission. Emission from the metal screen is absent and/or lines of the applied magnetic field along which electrons are moving do not cross the dielectric surface.

This nesting of the triple point is a good design example for cathode endcaps that use a dielectric coating, so as to prevent emission from the triple point. In Figure 5.1.4 such a cathode design is shown. Here note that the thickness of the electron hub in the extended cathode is small. In addition, the dielectric coating of the total surface of the endcap and the triple point are hidden in a region where the electric field is nearly absent. Thus, electrons that are born on the metal part of the cathode do not deposit onto the dielectric surface, which could initiate surface breakdown. Furthermore, the triple point

cannot initiate the development of an avalanche along dielectric coating. Moreover, the coating (as we show in this work) is a reliable barrier for electrons that are born on the metal surface of the graphite endcap.

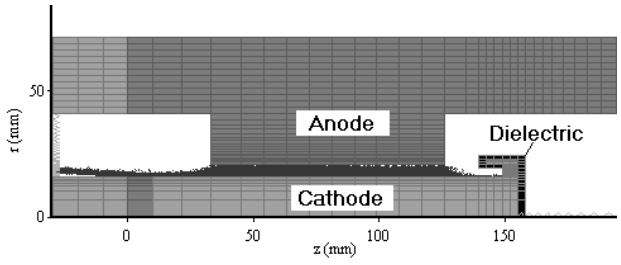

Figure 5.1.4. Design of an endcap with hidden triple point. Electron leakage current is nearly entirely suppressed.

It is planned to use the design of Figure 5.1.4 for a transparent cathode to minimize leakage current in experiments with a compact magnetron, should the insulating magnetic field be provided by a Helmholtz pair instead of a solenoid or permanent magnet. Simulations show that bombardment of electrons on the dielectric of this endcap is not likely. Electrons drifting downstream from the magnetron interaction space are tapered down due to the physics introduced by extending the cathode past the vanes. It is noteworthy that even though electrons do not appear to bombard the dielectric in simulation, they flow on trajectories that pass close by it. Optimization of dimensions of this proposed cathode might lessen the risk of secondary electron bombardment.

There is also the issue of applicability of a dielectric-coated endcap to longer-pulse magnetrons with higher pulse voltages. MAGIC simulations show that electric fields on

the surface of the dielectric coating reach a maximum of 200 kV/cm due to field enhancement for a 260 kV accelerator pulse. The maximum field on the graphite underneath the dielectric is ~80 kV/cm, which is near to or at the explosive emission threshold for graphite for a 16 ns pulse. The experiment with the larger endcap in the planar diode configuration suggests that the dielectric coating might be a good barrier to emission in situations where emission from the graphite might normally occur, *e.g.* in higher fields or longer pulses.

Finally, it was noted that endcap design affected total microwave efficiency and power. In our experiment, the solid cathode used extended ~2.5 cm beyond the anode block, both with and without an endcap. We have no results for the case where the cathode does not extend past the anode block. For no dielectric coating on the small endcap (Design A in Figure 5.1.2), microwave power was increased by 44% and total system current was reduced by 1.8 kA, or about 30%. The thinnest dielectric coating on the small endap produced almost as much microwave power increase. For all other small endcap designs, where medium to thick dielectric coatings were used, and for all large endcap designs, microwave power was severely diminished, most likely due to the introduction of excessive upstream leakage current from the endcap dielectric surface breakdown entering the magnetron interaction space at unfavorable phases between the electron spokes. Results for impact of output microwave power are shown in Figure 5.1.5 through Figure 5.1.9.

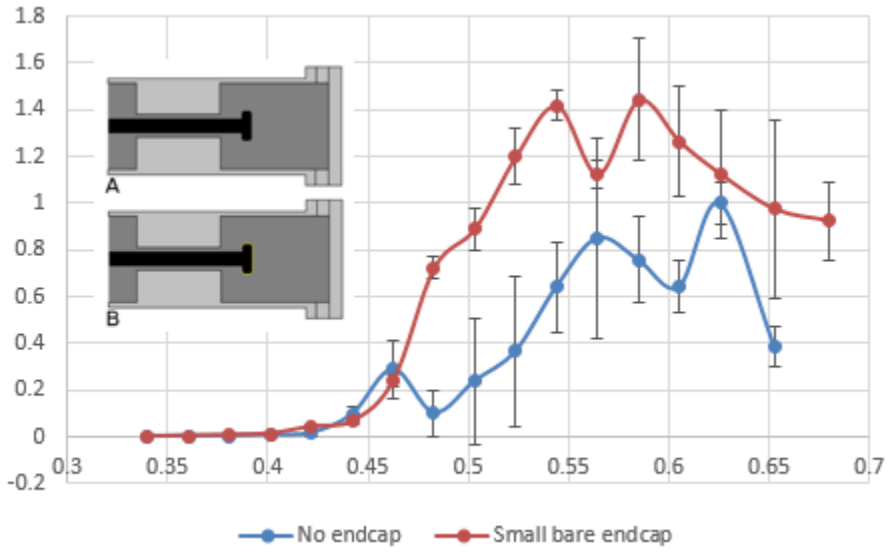

Figure 5.1.5. Normalized power for endcap designs A & B (red) vs. no endcap (blue).

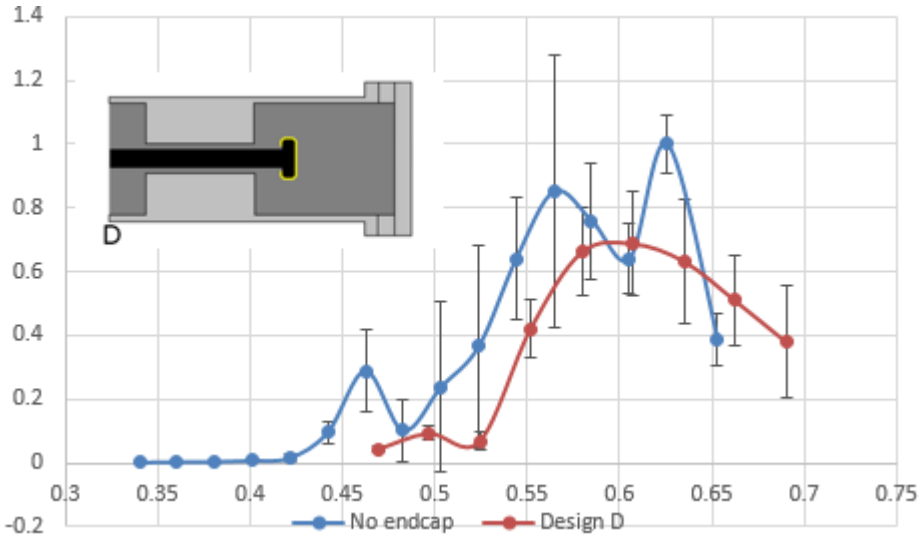

Figure 5.1.6. Normalized power for endcap design D (red) vs. no endcap (blue).

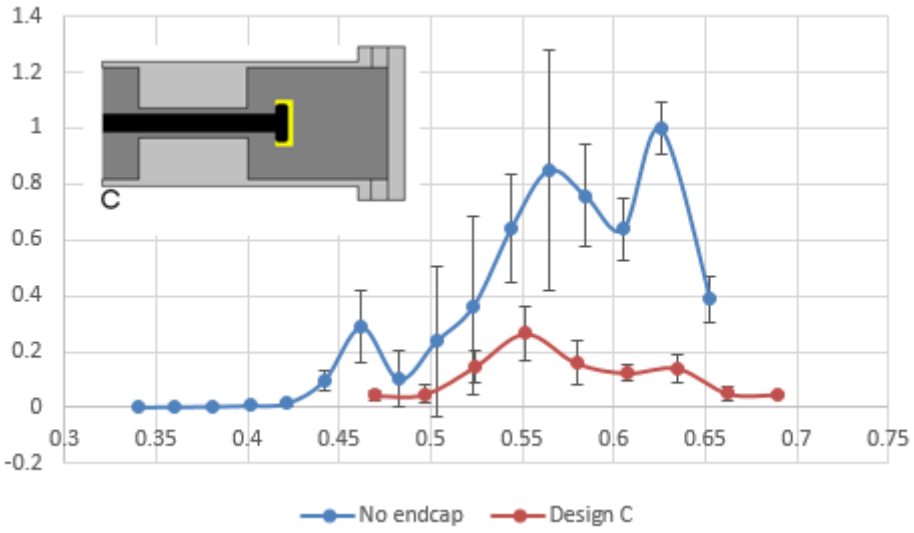

Figure 5.1.7. Normalized power for endcap design C (red) vs. no endcap (blue).

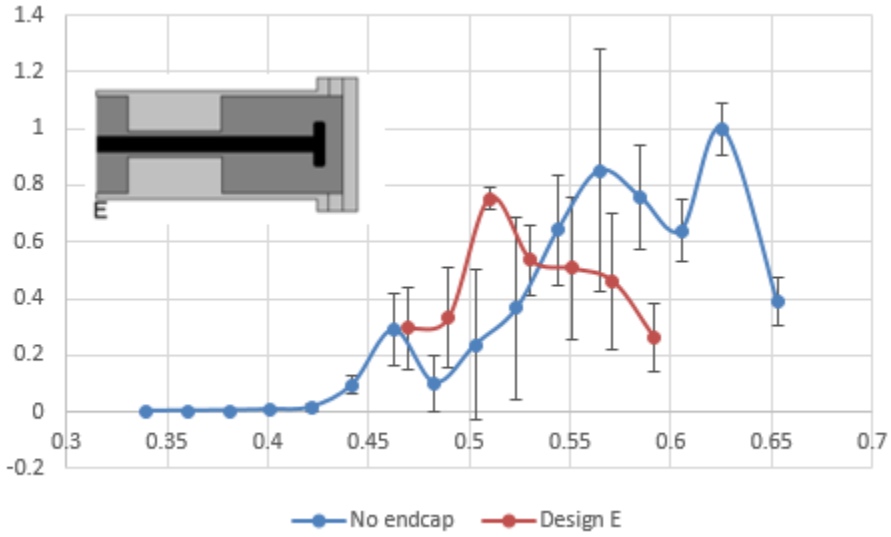

Figure 5.1.8. Normalized power for endcap design E (red) vs. no endcap (blue).

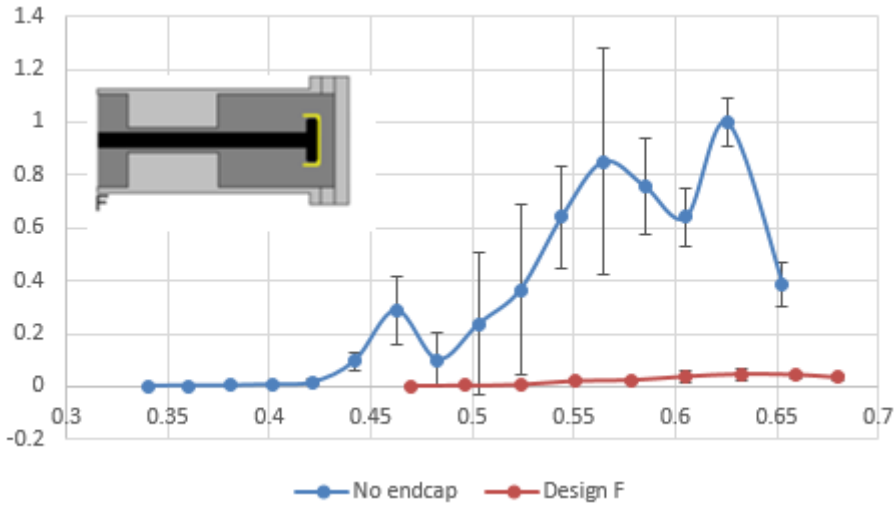

Figure 5.1.9. Normalized power for endcap design F (red) vs. no endcap (blue).

In conclusion, a reduction in electron leakage current from over 1 kA to on the order of 10 A was achieved. This was accomplished using polished graphite endcaps with thin dielectric coatings on an extended cathode. Thin coatings were more effective than thicker coatings because the development of a surface breakdown in weaker tangential electric fields (for the case of thin coatings) compared with stronger tangential electric fields (for the case of thicker coatings) is less likely, even though the same triple point exists for both cases. One final point to take from the experiment is that the use of polished graphite as the endcap material is a rather poor choice for a material with a desired high explosive emission threshold. This indicates that better results would be achieved by using a better material that is polished, cleaned, and conditioned. One example is polished stainless steel, which has been demonstrated to hold off 350-400 kV/cm at voltage pulses as long as 200 ns [74]. While clean vacuum system and conditioning etiquette at UNM is not advanced, the use of 16 ns or 30 ns pulses should contribute for better results in future experiments.

5.2 MDO

As mentioned previously, due to time constraints only MDO power and efficiency (via calorimetry), radiated field pattern with 6-cavity axial extraction (via neon light grid), and images of air and diode plasma breakdown were measured. There were no tests done with 4- or 2-cavity extraction, nor was an integrated field mapping with a waveguide detector performed. However, the variety of diagnostics, such as current, voltage, and fast-scope RF pulse profile, provided rich insight into the system's operation.

Images were captured of air breakdown just outside of the circular antenna aperture using one or more mirrors and a long-exposure digital camera, Figure 5.2.1 and Figure 5.2.2. The latter image indicates that the radial component of a non-rotating circular TE_{31} output mode is breaking down the air and both images suggest that the breakdown is enhanced at the sharp edges of the output flange. The location of the maximum radial component of the TE_{31} mode is in-line with the MDO's vanes, Figure 5.2.3, which is consistent with simulations. This figure also displays the plasma gap closure in the MDO's interaction space. The distal end of the cathode's endcap is dark, which indicates little-to-no emission. However, the proximal side of the sphere is illuminated, suggesting that emission there is present for at least a portion of the gap-closure event in the A-K gap. Plasma closure is responsible for impedance collapse and eventual shorting of many HPM vacuum devices; this event limits the maximum length of a HPM pulse to between ~80-200 ns, a phenomenon known as "pulse shortening" [75]. In a magnetron the plasma is born from the cathode during the explosive emission process and travels towards the anode at 1-2 cm/μs. A closer image of the breakdown streamers on the output flange and of plasma closure in the MDO is given in Figure 5.2.4.

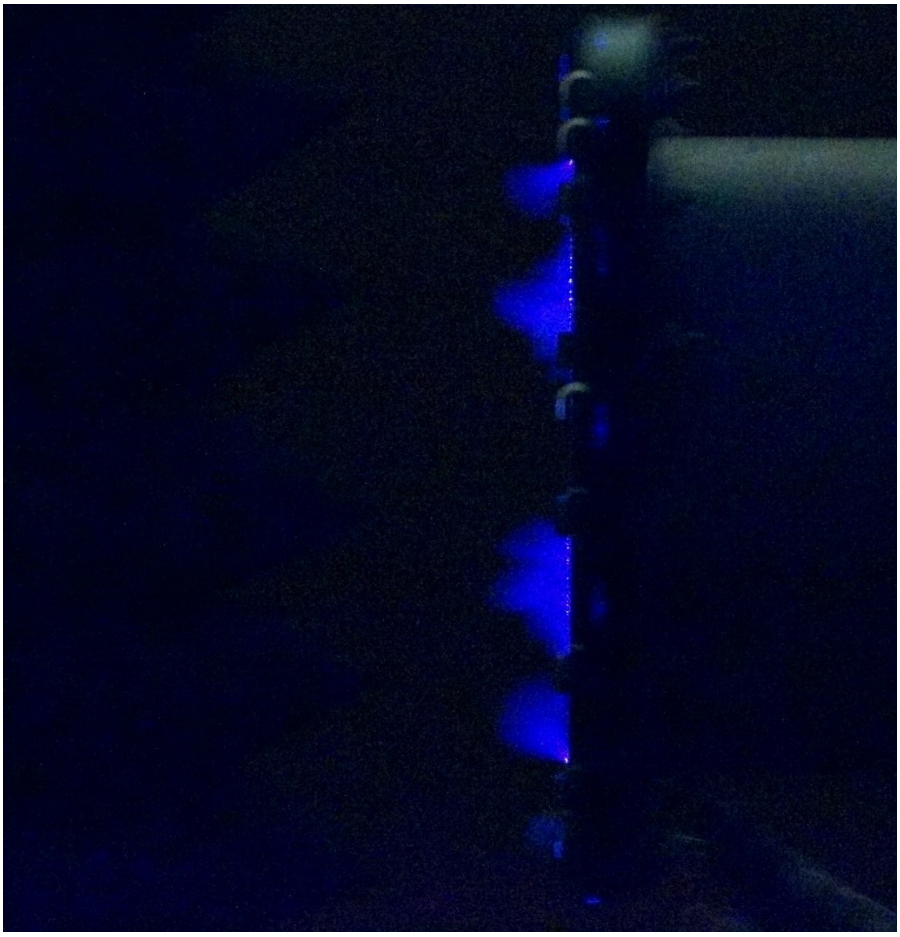

Figure 5.2.1. Air breakdown just outside the circular antenna aperture.

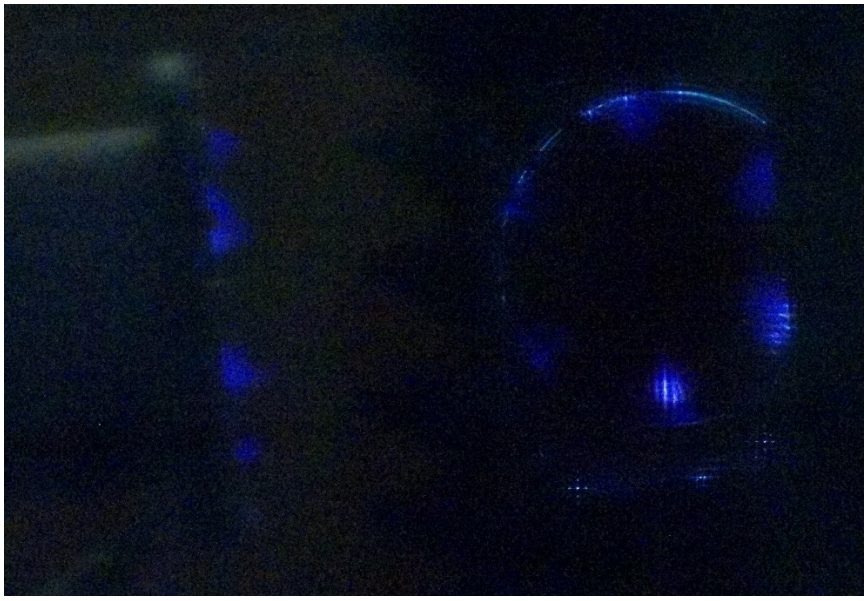

Figure 5.2.2. Thick paper used to cover the transparent antenna aperture indicates the presence of a non-rotating TE_{31} mode.

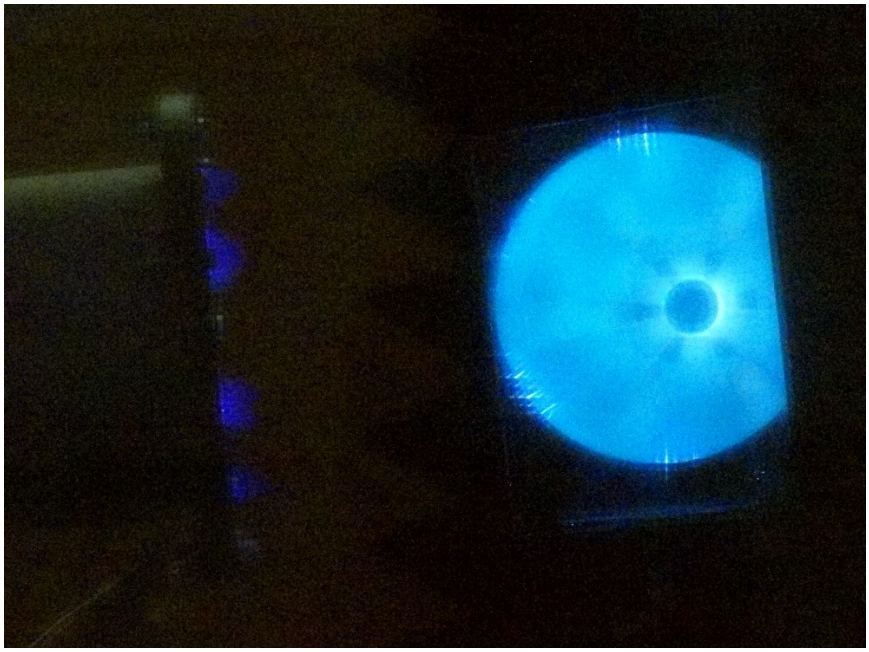

Figure 5.2.3. The thick paper is removed to also reveal gap-closure in the MDO.

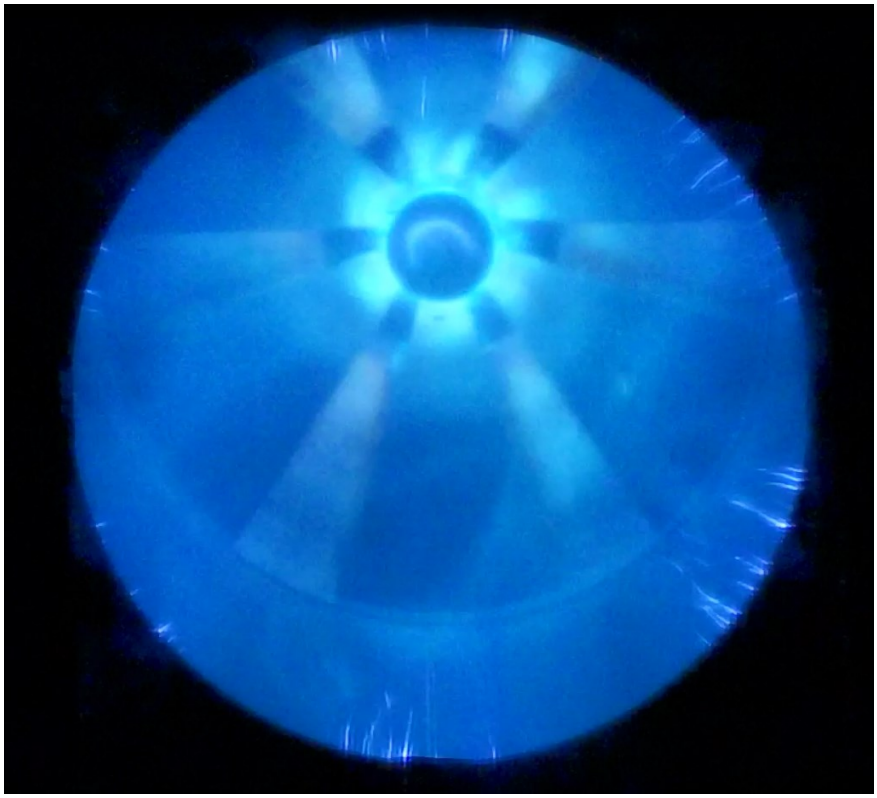

Figure 5.2.4. A closer image of breakdown streamers on the output flange and of plasma closure in the MDO.

In addition, images were captured of the output mode pattern using a neon bulb array, which consisted of a foam panel with small, unconnected neon lights arranged in a Cartesian grid. Figure 5.2.5 shows a pattern that has a null in the center, which is again consistent with a TE_{31} mode. The pronounced blue glow and dimmer neon lights seen on the image to the right suggest that greater window breakdown suppresses microwave power output. The brighter "square" seen in the bottom right of both shot patterns results from the use of longer neon lights embedded in those locations, not from greater microwave power flux.

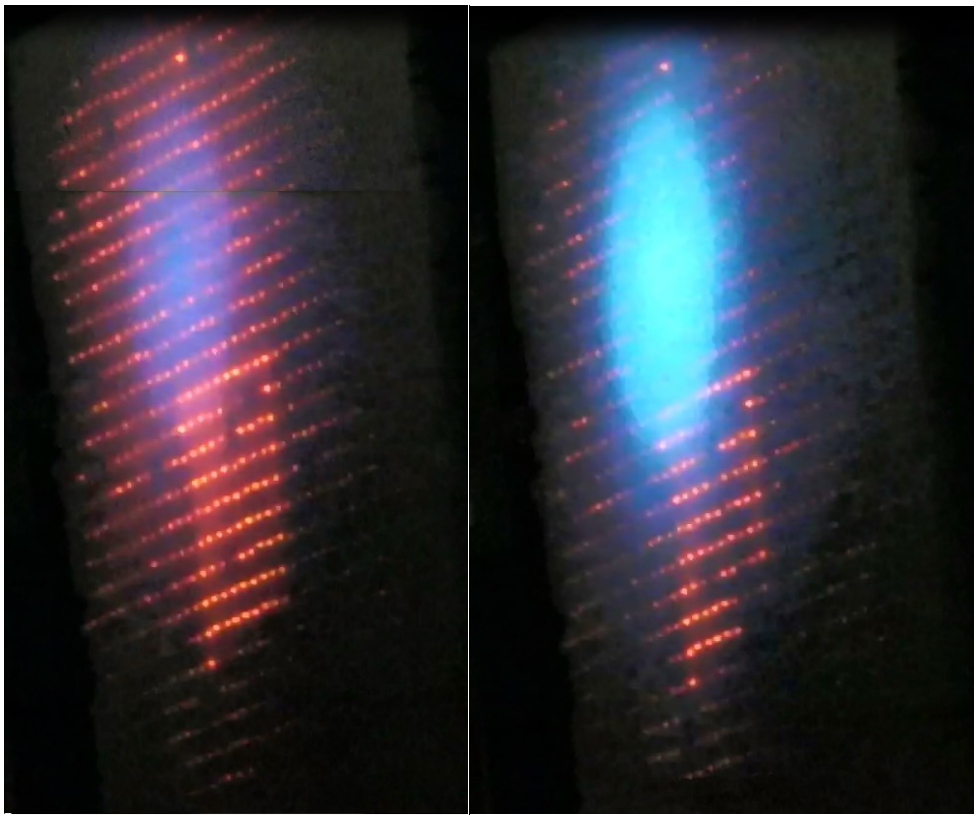

Figure 5.2.5. Neon-grid field pattern test. The left image shows the null in the center, and the right image suffers from pronounced window breakdown.

The PULSERAD's D-dot and Rogowski probes, as well as the waveguide detector, returned a wealth of information. Figure 5.2.6 shows the numerically-integrated D-dot probe signals positioned on the 20 Ω PFL and 20 Ω transmission line that was loaded with the MDO. The blue trace shows the charging of the PFL in ~162 ns, indicating that the 6 0.050 mF series capacitors (8.33 μF combined) see a total parasitic inductance of 3-4 μH when charging the PFL. It also shows the 4 ns oil switch breakdown and the depletion of the PFL into the matched transmission line. After depletion of the PFL, the Marx continually tries to recharge the PFL and transmission line, but at a lower voltage. At

approximately 140 ns after the oil switch breaks and the MDO turns on, it appears that plasma gap closure and impedance collapse begins to short out the MDO. At this point in time, the remaining energy in the Marx bank is slowly lost and the Marx voltage can be seen on both D-dot traces.

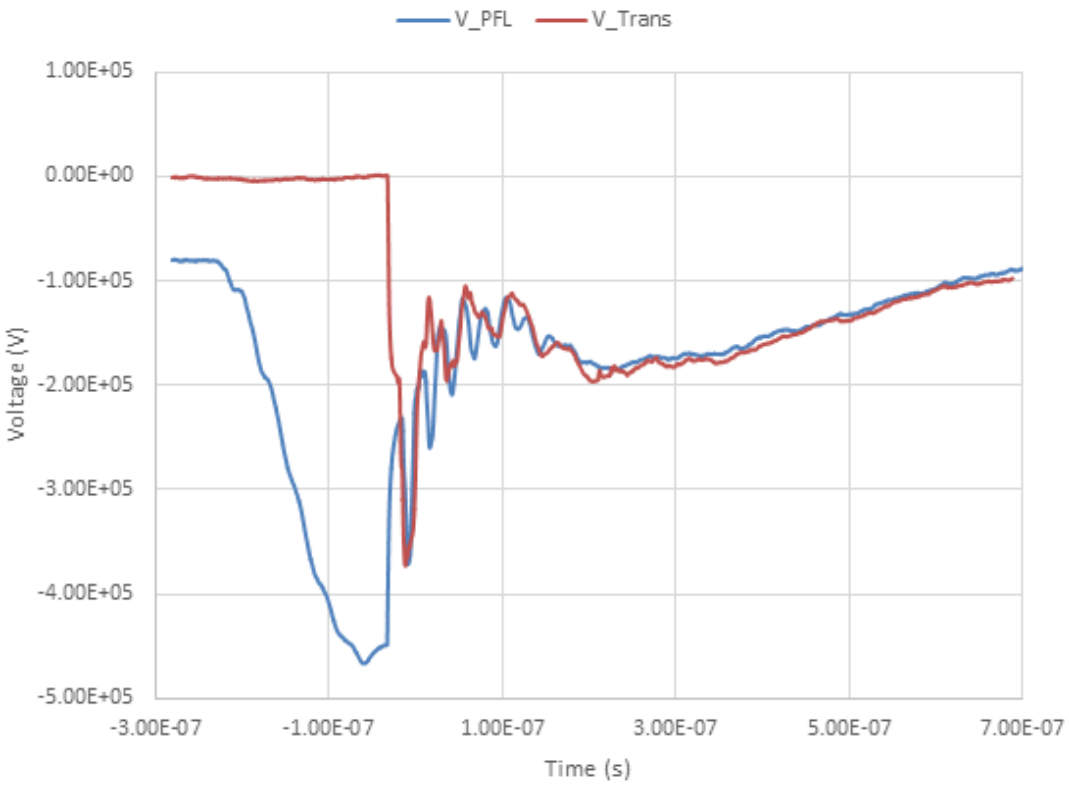

Figure 5.2.6. Numerically-integrated D-dot probe signals of the voltage on the PFL and transmission line that feeds the MDO.

In this shot, the nearly half-voltage rising edge of the 20 Ω transmission line's D-dot probe (red curve) indicates that 200 kV is delivered to the MDO. This 200 kV is the saturated transmission line voltage, which lasts on the D-dot probe until 12 ns after the

switch firing; Figure 4.2.4 shows that this signal only requires 5 ns to achieve full saturation. When the 200 kV first sees the MDO, it very briefly appears as a near-infinite-impedance open circuit because current has not yet begun to emit from the cathode. This causes a reflected wave of amplitude 372 kV to appear at the D-dot probe 16 ns later, but this quickly decays to 354 kV. It is this reflected wave bouncing up and down the PFL and transmission line that causes the signal on both D-dot probes to suffer periodic voltage spikes. The behavior of both D-dot probes is consistent with MAGIC 2D and TopSPICE simulations done in Chapter 3.

However, the MDO voltage does not settle at the indicated 354 kV. There are two reasons to support this conclusion. First, Figure 5.2.6 shows that the voltage drops off from 354 kV to below 200 kV at exactly 30 ns after the oil switch closes. This is the depletion of energy in the PFL, and it occurs only 16 ns after the reflected voltage wave reaches the D-dot probe, which is before the MDO current reaches saturation 23-26 ns after the voltage wave hits the MDO, if 3-6 ns delay in current turn on is assumed, Figure 5.2.8. In other words, the details of the dynamic MDO impedance changes are masked by the depletion of the PFL. Second, the voltage wave reflected from the MDO load along the 20 Ω transmission line must be consistent with the MDO's impedance. In this particular shot, the MDO saturates at a current of 2.5 kA. If 354 kV is assumed, then the impedance is 142 Ω, from $Z_0 = V_0/I$. However, if this voltage is assumed in $V_L = V_0 (1 + (Z_L - Z_0)/(Z_L + Z_0)$, the resultant impedance is 154 Ω. Solving these two equations simultaneously yields a more reasonable operating voltage and impedance: 350 kV and 140 Ω. While this difference is not so pronounced, in other shots, it can represent as much as ~20 kV difference.

Current was measured in the Rogowski coil, Figure 5.2.7, and also closely matches TopSPICE simulation data. The first 30 ns of the current pulse represents the proper discharge of the PFL energy into the MDO where microwaves are produced, Figure 5.2.8. The initial sharp current peak in the latter figure is the result of voltage pulse reshaping after experiencing sharp, but short, impedance changes in the oil-vacuum interface and the result of voltage wave amplification that results from a delay in current start time, and thus high impedance of the MDO load, when the voltage wave arrives from its 20 Ω transmission line. The subsequent 12 ns current "ramp-up" to saturation is likely the result of upstream leakage current from the cathode and endcap that subtracts from the current signal and the result of higher-radius upstream leakage current from the endcap providing enough space charge to limit emission from the cathode. Two cathodes, one stainless steel and the other POCO graphite, were employed in experiment, and both exhibited the same current waveforms. The current in the region ~140 ns after the primary 30 ns pulse begins is likely a regime where the A-K gap in the MDO is filled with plasma. Taking into account the in-line 7 Ω CuSO4 resistor, the voltage, and the current, this suggests that the impedance of the MDO collapses to ~50 Ω.

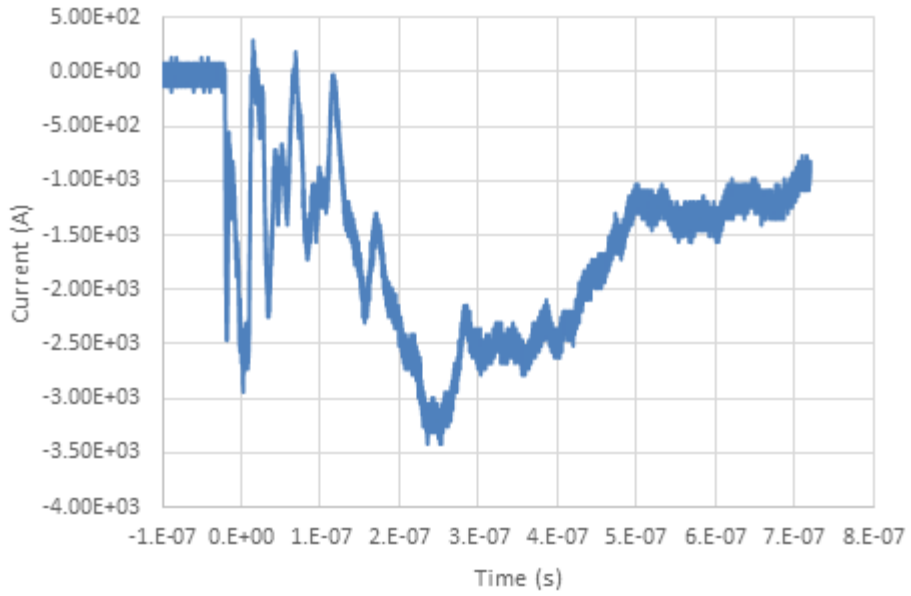

Figure 5.2.7. MDO current, as measured by the self-integrating Rogowski coil.

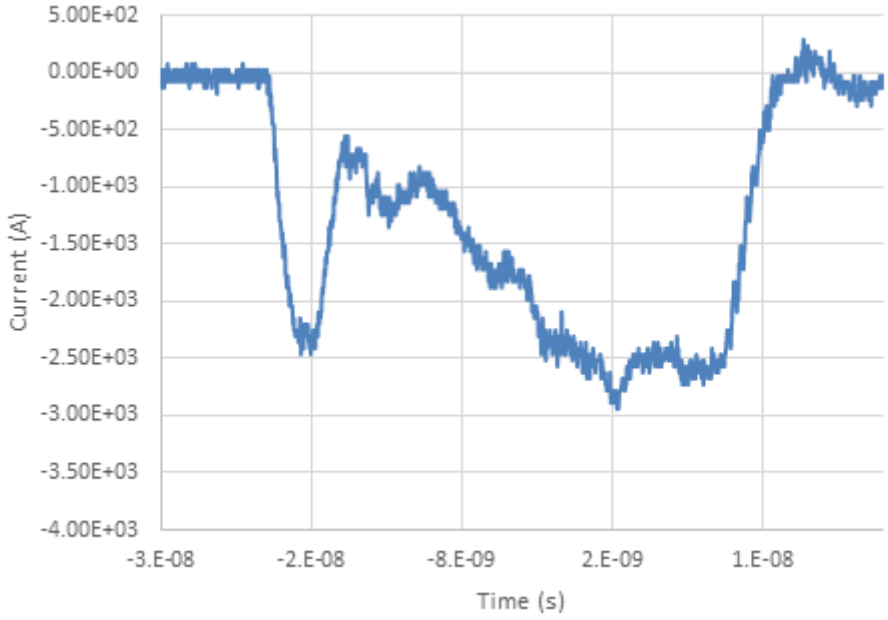

Figure 5.2.8. Primary 30 ns current pulse.

Calorimetry data was taken under a variety of voltage and magnetic field settings. The total energy of the pulse was calculated by dividing the measured Joule deposition in the calorimeter by the absorption coefficient from Figure 4.2.8, 61%. The RF pulse envelope was obtained by applying a moving window averaging filter with window width of 4 to 6 RF cycles (a 30 ns pulse is 75 cycles at 2.5 GHz) on the waveguide detector signal. An effective window width is greater than the period, 1/f, but less than the pulse length. This envelope was integrated and divided into the total energy to obtain a scaling factor. Finally, this scaling factor is multiplied by the measured RF pulse envelope to properly display the power of the RF pulse. The peak or average peak of this scaled RF pulse is then compared to the peak current and the steady-state MDO voltage to obtain the efficiency.

The goal of the first set of calorimetry data was to demonstrate ~70% efficiency at ~1 GW, and it used the original MAGIC simulation data, Figure 3.2.12, of the MDO with spherical endcap and with the CIRCUIT command enabled. This data informed the Marx charging voltage and insulating field to be used: 0.45 T and 26 kV on the Marx bank for a projected 844 MW at 69% efficiency, and 0.43 T and 27.5 kV for a projected 1.15 GW at 64% efficiency. Using these settings, the above-shown air breakdown occurred outside of the MDO window. To compensate, a plastic bag was secured around the window and filled with SF_6 gas. Despite multiple attempts to re-seal the bag, it continued to deflate, no doubt aided by the pressure differential at small holes caused by the high density of the gas and due to static charging of the plastic that pulled it to the output window. The 4 cm proximity of the calorimeter to the output window also limited the design of the bag. As such, window breakdown was not prevented for these shots. These shots also employed a D-band waveguide, which was prone to breakdown at higher powers that resulted in truncated and

misshapen RF pulse profiles. At the time, an RF profile that was between 25-35 ns and had a non-erratic shape was considered as useful.

Using the accelerator setting for a projected 1.15 GW and observing window breakdown, the captured RF waveforms were erratic and suggested breakdown in the L-band waveguide detector. As such, power and efficiency calorimetry calculations were not reliable. For example, the RF pulse in Figure 5.2.9 was truncated to 10 ns, resulting in erroneous post-processing power and efficiency values of 2.5 GHz and 136%. There was no confidence that firing the system at a projected 844 MW would be reliable, as well, Figure 5.2.10 and Figure 5.2.11, and though it returned reasonable power and efficiencies, the waveforms were erratic.

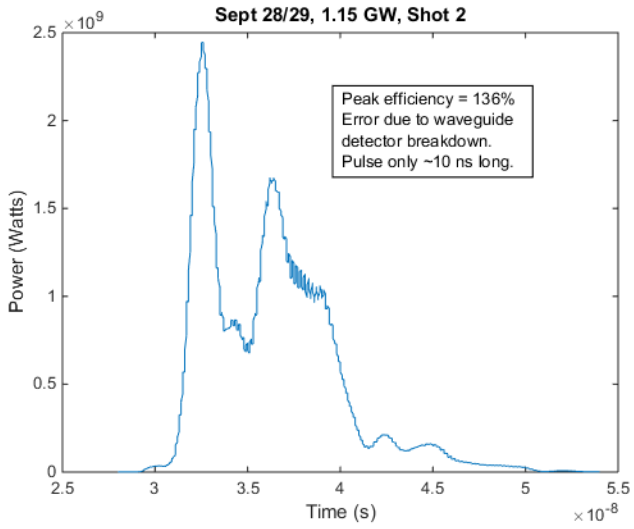

Figure 5.2.9. Erroneous calorimetry data of the RF profile and efficiency at an anticipated value of 1.15 GW at 64% efficiency. Breakdown in the L-band waveguide detector truncated this ~30 ns RF pulse to only 10 ns.

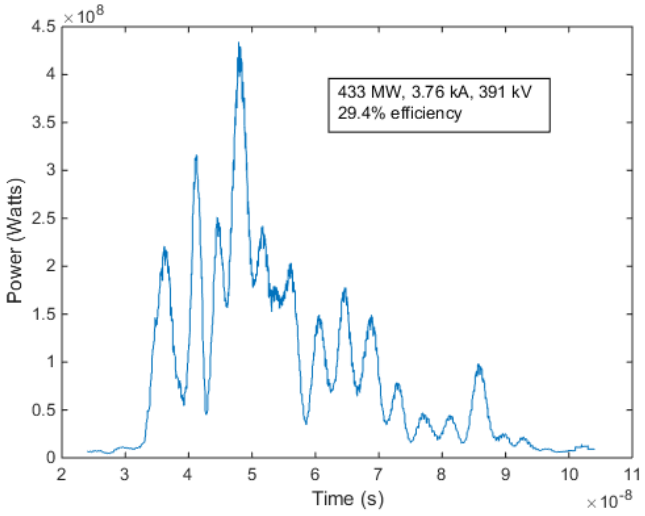

Figure 5.2.10. Calorimetry data of the RF profile and efficiency at an anticipated value of 844 MW at 69% efficiency.

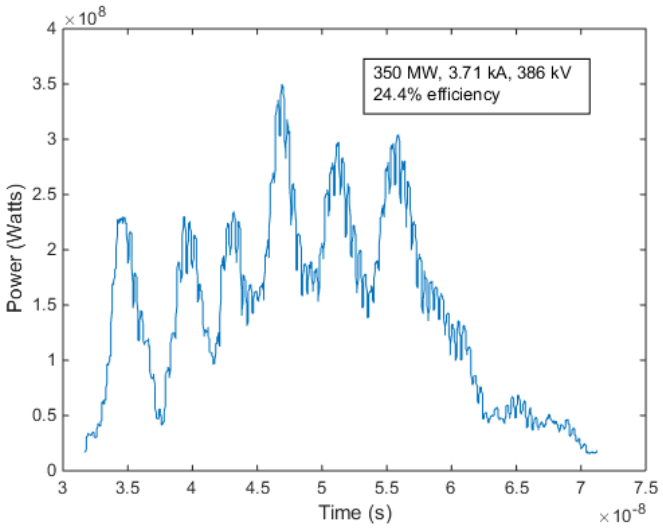

Figure 5.2.11. Calorimetry data of the RF profile and efficiency at an anticipated value of 844 MW at 69% efficiency.

The fast Fourier transforms (FFT) of the RF pulse indicated that the operating frequency for both the "844 MW" and "1.15 GW" settings was ~2.38 GHz, Figure 5.2.12. This is the π-mode frequency predicted by MAGIC. The presence of the π-mode was also supported by the air breakdown patterns in Figure 5.2.1 through Figure 5.2.4. However, the 4π/3-mode was expected at these settings, which suggested that not only were the actual powers and efficiencies (without breakdown distortion) likely incorrect, but that the MAGIC simulation model was also suspect.

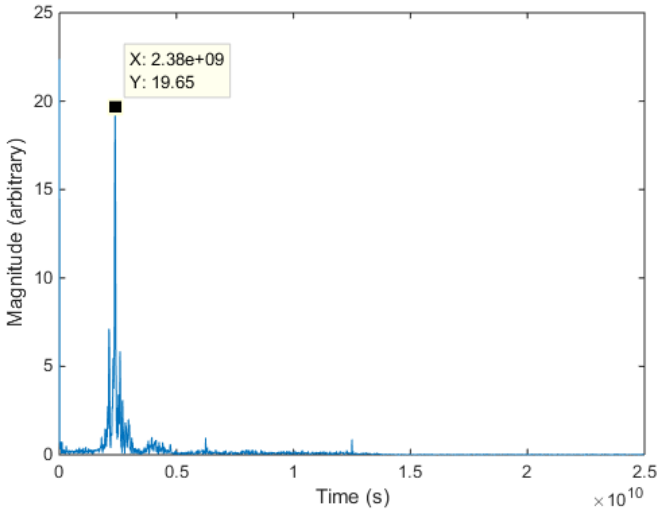

Figure 5.2.12. Typical FFT of the MDO operated with settings that were anticipated to produce 844 MW and 1.15 GW.

This inspired the changes to the MAGIC MDO model that are detailed in Chapter 3.2. Instead of forcing the incoming voltage wave to 350 kV via a feedback system using the CIRCUIT command, an approach was used that replicated the natural voltage reflections of a wave moving from a 20 Ω transmission line into a dynamic MDO load impedance.

This was accomplished by launching a 200 kV voltage wave into the MDO using a short 20 Ω geometry section at the input port. The results, Table 1, were then used to inform the experiment to sidestep the inaccuracies caused by window breakdown. The aim was to de-tune the MDO by firing at a high magnetic field to produce a power low enough not to cause window breakdown. A Marx bank charging voltage of 25 kV was selected to launch the 200 kV wave, and a magnetic field of 0.51 T was chosen to provide an anticipated

power and efficiency of 520 MW and 72%. Changes to the L-band waveguide detector were also made to prevent breakdown in its interior; it was filled with SF_6 gas and 4 cm-thick carbon-impregnated foam from donor Eccosorb material was placed in front of its aperture.

Using these settings, window breakdown was not observed, and so calorimetry data would be more accurate, as microwave energy would not in part go to ionization of the air. There was a large degree of shot-to-shot variability: 179-205 kV (14% variability) at the 20 Ω transmission line, 346-393 kV (13% variability) on the MDO, and currents ranging from 2.401-3.328 kA (32% variability). A typical shot is shown in Figure 5.2.13 and Figure 5.2.14. The FFT of these shots indicated that the magnetron was operating predominantly in the 4π/3-mode (f = 2.55 GHz), with some presence of the π-mode (f = 2.38 GHz) and another unidentified mode, Figure 5.2.13. This mix of frequencies caused amplitude modulation of the RF envelope due to the beat frequency and it suggested that the MDO was operating at the boundary of the π-mode and 4π/3-mode. This effect was especially pronounced in Figure 5.2.15 and Figure 5.2.16.

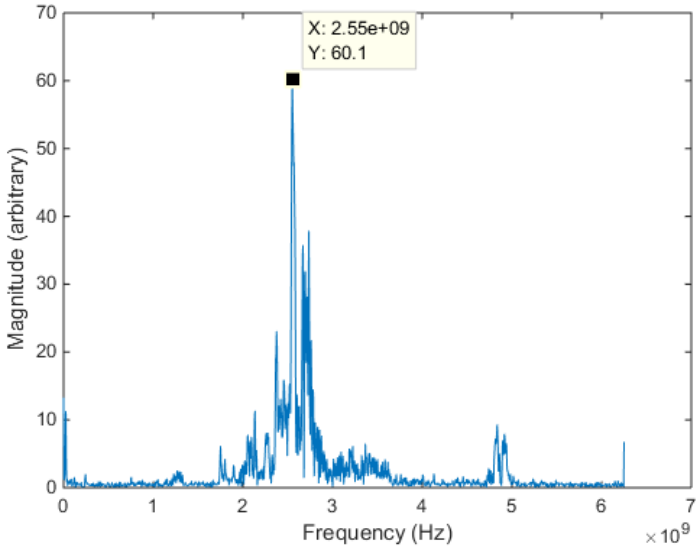

Figure 5.2.13. Typical FFT at 0.51 T and 355 kV.

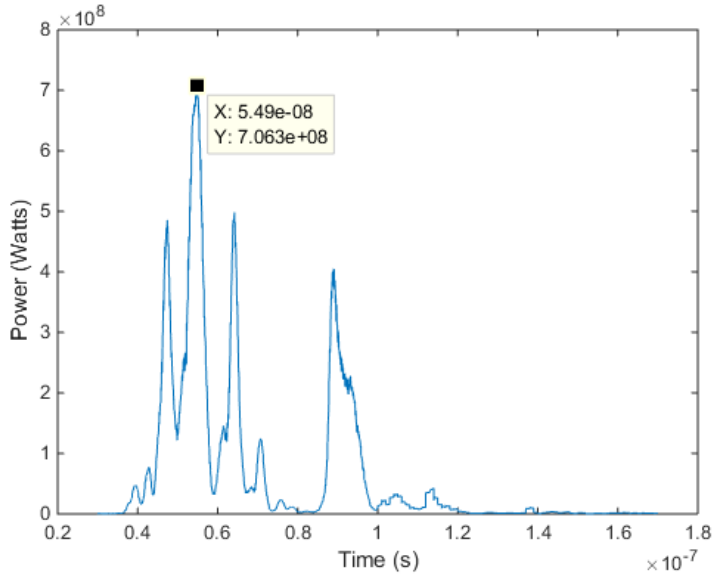

Figure 5.2.14. Typical RF power envelope at 0.51 T and ~360 kV, indicating a beat frequency between multiple modes and possible breakdown in the L-band detector.

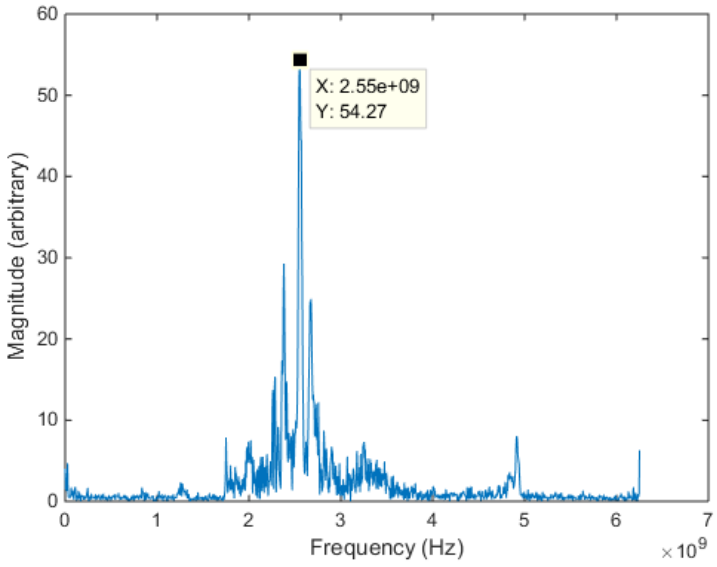

Figure 5.2.15. Heavy mode competition at 0.51 T and ~350 kV.

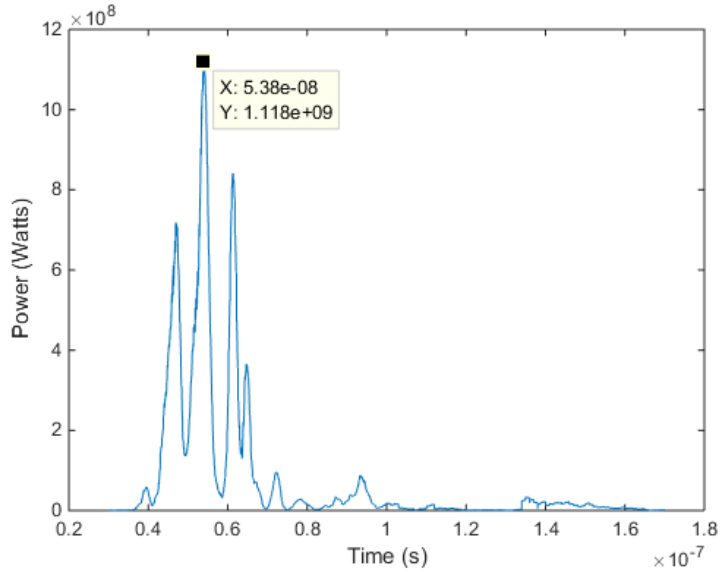

Figure 5.2.16. Heavy mode competition at large beat frequency amplitude at 0.51 T and 350 kV leading to artificially-high peak power.

Due to the transient nature of and the beating of competing modes in the RF pulses, it was difficult to quantify an average power that could be used to calculate accurate power and efficiency values. As such, using the peak of each RF envelope resulted in an average peak efficiency of 66.7% for MDO voltages of 349-350 kV and typical currents of ~3.05 kA and an average peak efficiency of 51.4% for 353-364 kV and typical currents of 3.24 kA. However, the average efficiencies are likely 2/3rds the value, 45% and 35% respectively.

One clean 4π/3-mode shot was obtained in this data run, however, with a smooth RF profile and clean FFT that indicated 63.5% efficiency at 853 MW for 362 kV and 3.71 kA, Figure 5.2.17 and Figure 5.2.18.

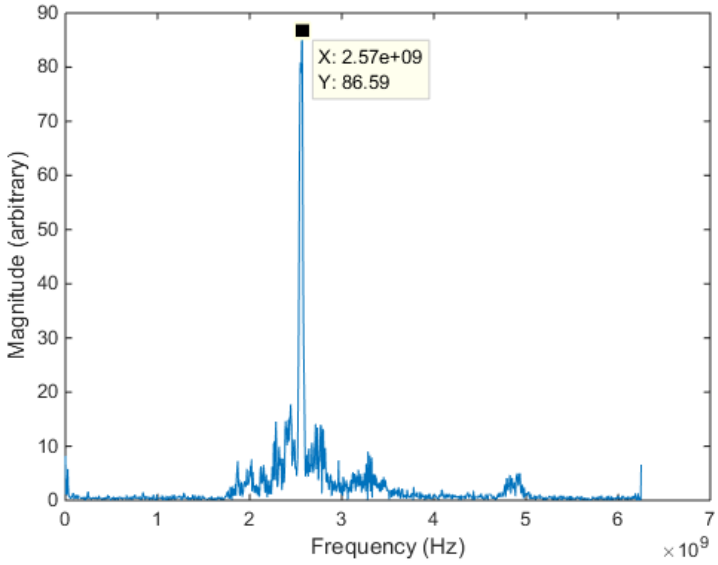

Figure 5.2.17. Clean 4π/3-mode operation at 63.5% efficiency.

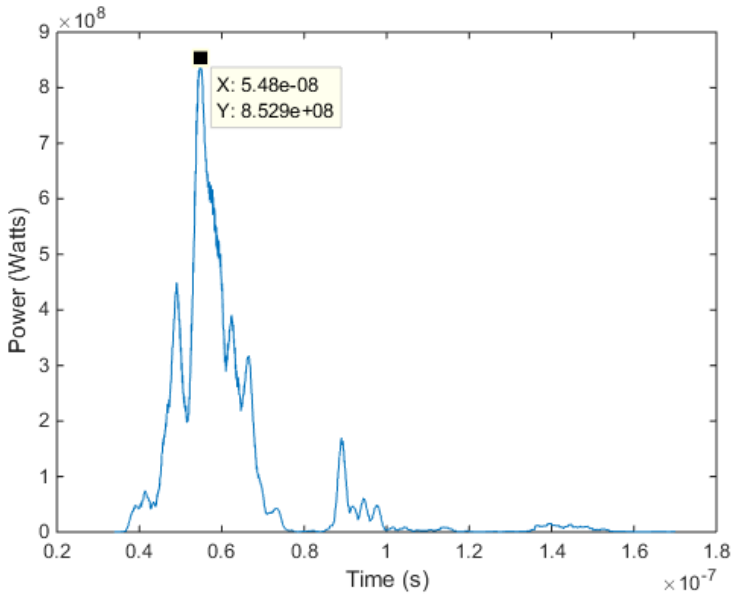

Figure 5.2.18. RF power envelope indicating 853 MW at 63.5% efficiency for the 4π/3-mode operating mode.

Subsequent experiments were aimed to capture more data points for the 4π/3-mode, but were unsuccessful. These experiments utilized an S-band -20 dB directional coupler waveguide detector to provide a more accurate RF profile than the breakdown-prone L-band detector. Using the same magnetic field and Marx voltage settings, a dominant 2.13 GHz, 2.58 (4π/3-mode), and 4.93 GHz signal were expressed in the FFT's, Figure 5.2.19 and Figure 5.2.20. Average power and efficiency was lower as expected, 194 MW at η = 16% for 357-364 kV and 2.60-3.22 kA. The presence of the 2.13 GHz and 4.93 GHz signal is not explained by simulation and could be the result of emission from the endcap at a radius between 1-2 cm. Recall that the standard A6 magnetron has a cathode radius of 1.58 cm and excites the 2π-mode at a frequency of ~4.6 GHz; the 4.93 GHz mode could be the

result of a 2π-mode excited by electrons emitted at larger radius from the spherical endcap. The 2.13 GHz could be the 2π/3-mode excited in a similar way. A brief set of experiments at 0.57 T and ~345 kV indicated that the 4π/3-mode amplitude was reduced as expected, but that the 2.13 GHz mode continued to dominate it, Figure 5.2.21. This suggested that the 4π/3-mode operates in a very low range of magnetic field, as the π-mode interferes at lower magnetic field values, and a host of other modes interfere at higher values.

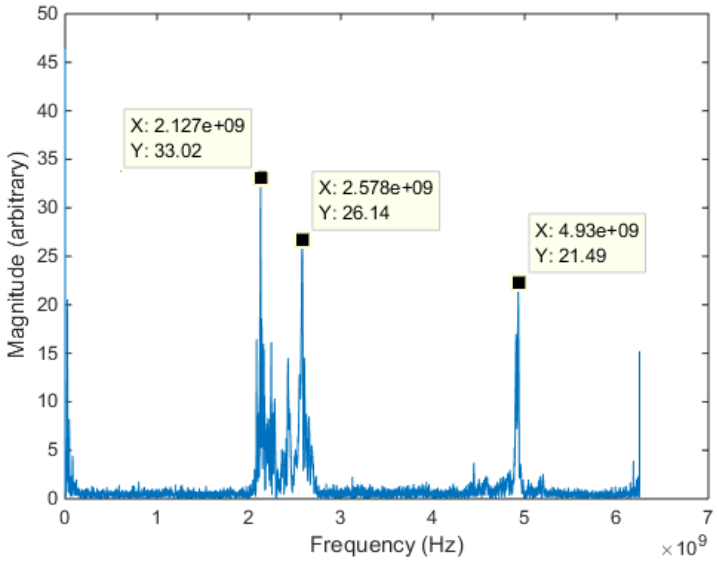

Figure 5.2.19. Subsequent experiments seeking to generate the 4π/3-mode also generated additional modes.

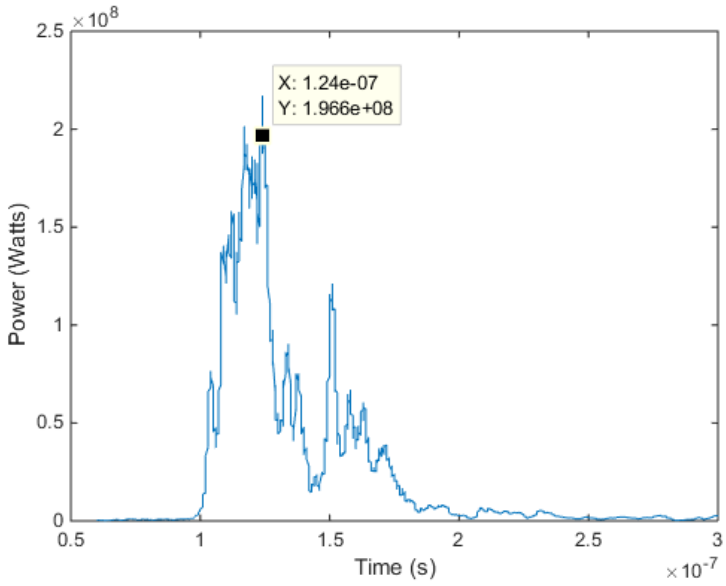

Figure 5.2.20. RF power envelope for 0.51 T and 360 kV.

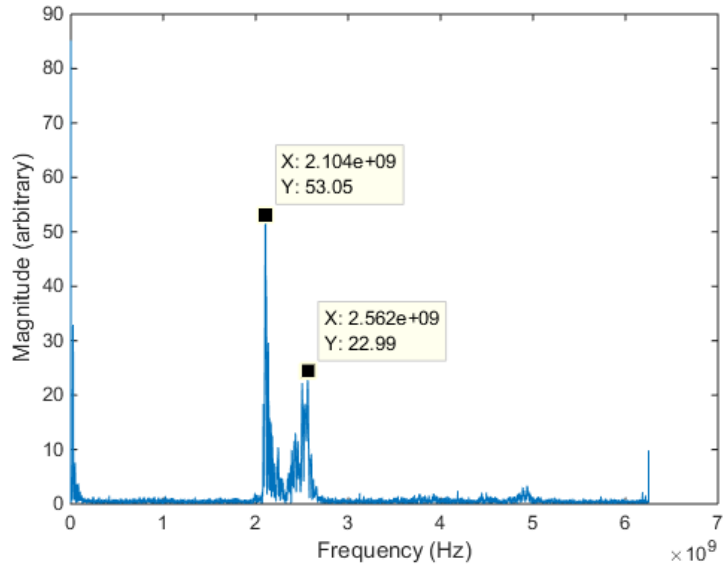

Figure 5.2.21. At 0.57 T and 345 kV, the 4π/3-mode was less present.

As a result of the 4π/3-mode being difficult to excite, calorimetry data was taken of the π-mode using the S-band waveguide detector and an improved SF_6 bag over the MDO antenna aperture. Mature RF power envelopes for a clean π-mode were captured at 0.45 T, 345-360 kV, and 3.52-4.16 kA, Figure 5.2.22 through Figure 5.2.24. For voltages and currents of 350-356 kV and 3.52-3.65 kA the average efficiency was 40.4%, and for 359-364 kV and 3.71-4.16 kA the average efficiency was 36.5%.

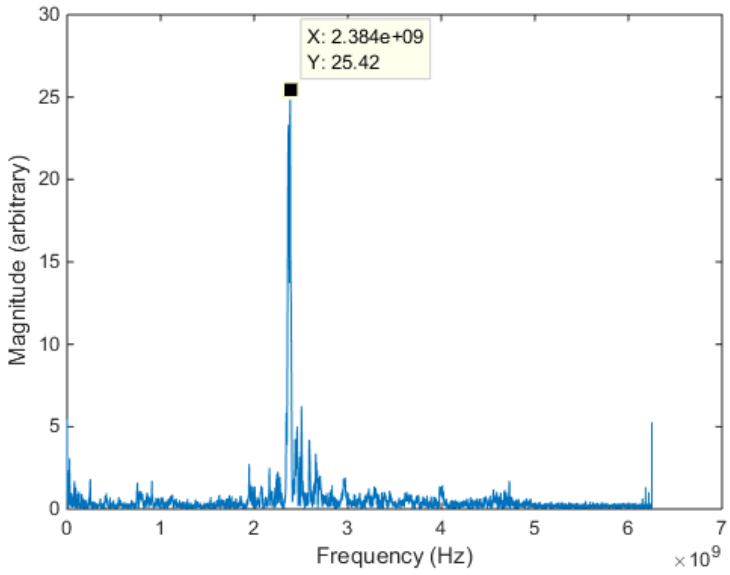

Figure 5.2.22. FFT of π-mode at 0.45 T and 345-360 kV on the MDO.

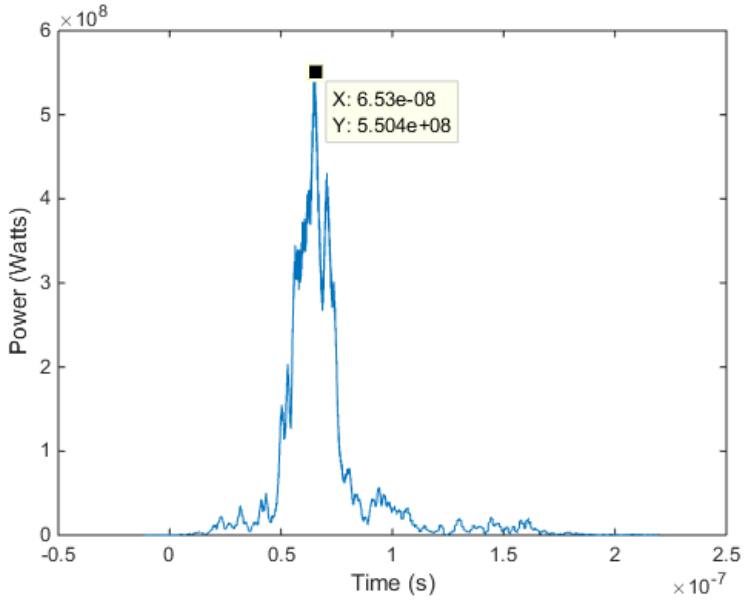

Figure 5.2.23. RF power envelope at 0.45 T, 350 kV, and 3.52 kA.

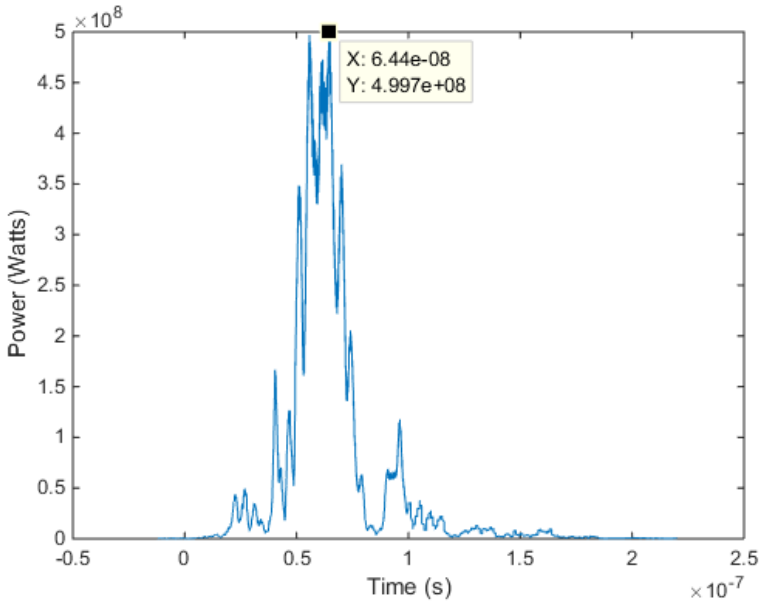

Figure 5.2.24. RF power envelope at 0.45 T, 351 kV, and 3.56 kA.

CHAPTER 6 CONCLUSION

This dissertation represents a highly-diversified investigation into high efficiency axial diffraction output schemes for relativistic magnetrons and into technologies made to support them. A combination of simulation and experiment was used to test the MDO and to bring a number of diagnostics and accelerator systems online as well. What follows is commentary regarding specific sources and technologies.

Regarding the compact magnetron, simulations have shown it to produce greater than 500 MW in a Gaussian-like TE_{11} output mode at 14% efficiency. With improvements that reduce the dynamic polarization rotation of this TE_{11} mode for better applicability to use in radar, it can output 250 MW at $\eta = 11\%$. Even though these efficiencies are low for a relativistic magnetron, the designs are very compact and accommodate the use of a permanent magnet, which appreciably increases the total HPM system efficiency and eases implementation in the field. Future experiments at UNM are planned.

Regarding the rodded metamaterial-like cathode in an A6 magnetron, it was shown to produce π-mode operation over a wide range of applied **E** and **B** fields, which is advantageous for use in axial-extraction schemes for production of a TE_{11} mode. A comprehensive rod topology scan was performed for cathodes with radius ~1.58 cm. Most topologies produced poor performance in the $2\pi/3$ or $4\pi/3$ modes, probably a result of the 4-fold symmetry of their Cartesian arrangement and the priming effects that it provides. There was evidence of RF penetration into the cathode down the axis of the device. This suggests that the cathode might provide an ambiguous A-K electric field for modulating electrons, making it more difficult to achieve synchronism.

Regarding the experimental verification of the MDO with spherical endcap, the goal of these experiments was to show ~1 GW operation at $\eta = 70\%$. To this end, 40.4% efficient operation in the π-mode was achieved and the results hint that 63.5% efficient operation in the $4\pi/3$-mode is possible. Only one data point of the MDO operating in a clean $4\pi/3$-mode was captured because it appeared to occur for only a very narrow electric and magnetic field range. This is surprising because in simulation, the $4\pi/3$-mode is excited over a very wide range of magnetic fields and at very high powers and efficiencies. This undesired behavior is most likely caused by electron emission from the endcap at a radius greater than the 1 cm cathode radius. At >0.51 T applied field, current reaching the anode from a 1 cm cathode via the $4\pi/3$-mode is greatly reduced. Current emitted up to a radius of 2 cm from the spherical endcap has two effects on this current. The first is that space charge created by emission from larger radii has a large effect on electron mobility to the anode for electrons emitted from the 1 cm cathode. Second, electrons emitted from cathodes larger than 1 cm and up to 1.58 cm in the presence of higher magnetic fields will produce the 2π-mode (and possibly $2\pi/3$-mode). Presence of multiple modes encourages loss from any mode into others, thereby reducing power and efficiency. Elimination of the endcap might result in effective $4\pi/3$-mode generation.

As such, these experiments suggest that it is perhaps more advantageous to use a bucking magnetic field than to use an endcap. However, not using an endcap in a Helmholtz coil field might be better than both and should be tested at UNM. Use of an endcap in experiment was more successful on a standard A6 magnetron compared to an MDO due to the low fields present on the endcap surface in the former case.

This section will briefly list recommendations for improvements to the experimental setup:

1. In the continuing MDO experiments, consider removing the spherical endcap. This will likely result in full expression of a 70% efficient $4\pi/3$-mode. Although this risks electron impact on the window, the cylindrical waveguide section might serve as an effective beam dump.
2. Due to the close proximity of the calorimeter to the MDO antenna, RF breakdown of the air in that region, and the need for installation of a breakdown-resistant SF_6 bag, constructing a larger-diameter (>30 cm) to handle 1 GW of output power is recommended. If this section continues the use of a 17.5° taper, then it will preserve the inherent directivity of the MDO's horn antenna and result in a more-narrow main lobe. The 40 cm cylindrical waveguide that is now attached degrades the directivity of the antenna's aperture. Should the surface area of the calorimeter not be sufficient for future measurements, reconstructing its alcohol container to a larger diameter will not distort the measured energy, so long as sufficient supporting struts are installed in its interior. The energy measured by this diagnostic is independent of alcohol volume.
3. The PULSERAD's shot-to-shot delivery voltage had some variation. For example, the voltages delivered to the 20 Ω transmission line by the PFL were between 179-205 kV at a specific Marx charging voltage and oil-switch gap (4 mm). This variation becomes amplified to a small degree once it reaches the higher impedance of the MDO load. As per recommendations of Ken Prestwich, this might be slightly

improved by installing an annular $CuSO_4$ resistor near the downstream end of the 20 Ω transmission line to better match the load to the line. This parallel resistance would also reduce pre-pulse charging of the MDO load and shot-to-shot variability. In addition, because the Marx bank has significantly more energy than needed to power the MDO load, the impedance collapse of the MDO will lead to significant energy deposition in it, causing damage. This might be mitigated by placing a 20 Ω CuSO4 resistor in series with the 20 Ω transmission line somewhere near its downstream end.

4. Finally, due to the presence of small-amplitude 60 Hz (possibly ground) noise in the lab's shielded screen room, the signals of the PULSERAD's pulsed electromagnet coil current viewing resistor (CVR) and the calorimeter detector are plagued with noise. In particular, the calorimeter is very sensitive and requires large amplifier gains to detect very small changes in high impedance sensors. This noise required quicker sampling (and later signal averaging) at ~80% duty cycle on the (low noise) batteries. This heaving taxing on the battery leads to signal droop, requiring a calibration curve be constructed both before and after experiments. If this 60 Hz noise is eliminated, the system can return to a 10% or less duty cycle.

APPENDIX

This appendix contains additional figures that are relevant to the topics referenced by them in the main chapters, but are not necessary for the understanding of them.

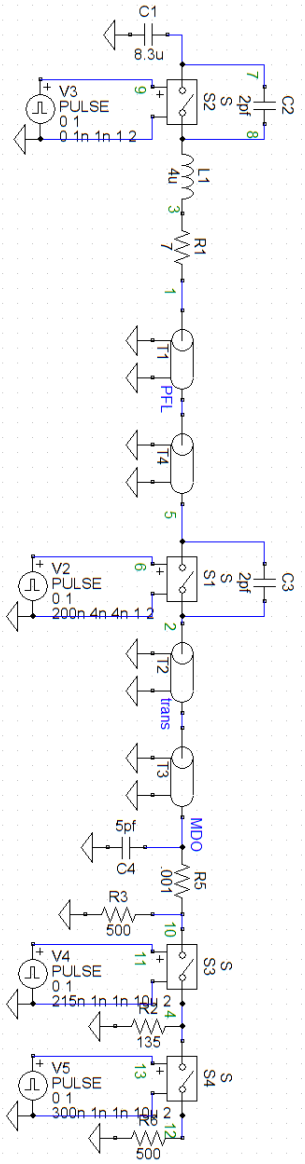

Figure A1. TopSPICE model of the PULSERAD firing into an MDO load.

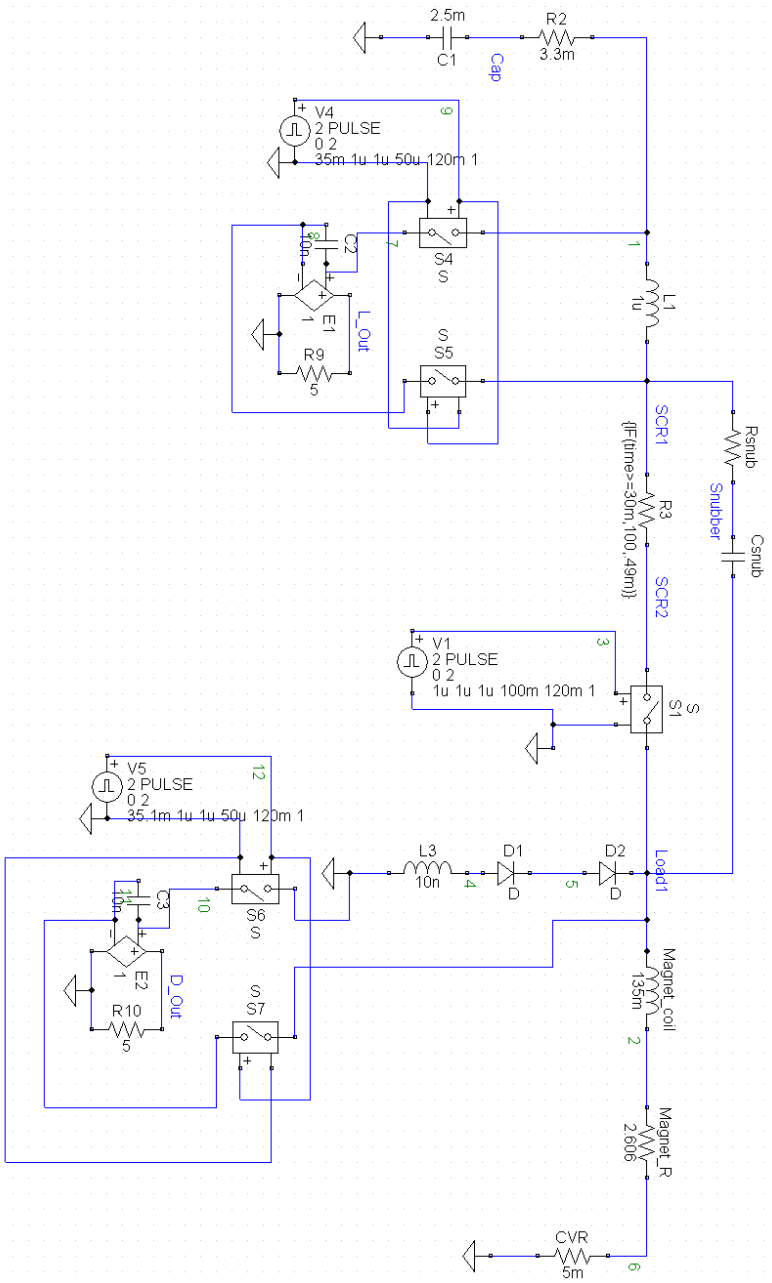

Figure A2. TopSPICE model of pulsed electromagnet circuit, complete with two sample-and-hold subcircuits used to control thyristor behavior.

```
#REVISION: Rev: 121
#.PARAM Lparasitic=1u Cbank=4.08m Rcap=3.3m TimeDvDt=506.73u TimeIrr=520.4u Lload=14u Charge=6000 Rstray=6m
.PARAM Lparasitic=1u Cbank=2.5m Rcap=3.3m TimeDvDt=33.114001m TimeIrr=32.793m Lload=135m Charge=5000 Rstray=2.606
.MODEL Smod VSWITCH (Ron=1u Roff=1MEG Von=1V Voff=0V)
.MODEL Smod2 VSWITCH (Ron=1 Roff=1e12 Von=1V Voff=0V)
.MODEL Dmod D (RS=0.407m BV=6000)
Lstray1 1 SCR1  Lparasitic
Lind Load2 0 Lload
S1 SCR2 Load1 2 0  Smod
D1 Diode2 Load1  Dmod
D2 Diode3 Diode2 Dmod
Rstray1 Load1 Load2 Rstray
V1 2 0  2 PULSE  0 2 1u 1u 1u 100m 120m 1
C1 Cap 0  Cbank IC=Charge
Rc Cap 1  Rcap
RSCR SCR1 SCR2  {IF(time>=TimeIrr, ((-V(Cap)+V(D_Out))/( 0.0011*(V(L_Out)/Lparasitic)^0.7873 ))*
+ exp( (time-TimeIrr) / ((8e-7*(V(L_Out)/Lparasitic)^0.591)/(0.0011*(V(L_Out)/Lparasitic)^0.7873) -
+ (0.0011*(V(L_Out)/Lparasitic)^0.7873)/(2*(V(L_Out)/Lparasitic))) ) +
+ ((8e-7*(V(L_Out)/Lparasitic)^0.591)/(0.0011*(V(L_Out)/Lparasitic)^0.7873) -
+ (0.0011*(V(L_Out)/Lparasitic)^0.7873)/(2*(V(L_Out)/Lparasitic)))/Cbank - Rcap + Lparasitic/
+ ((8e-7*(V(L_Out)/Lparasitic)^0.591)/(0.0011*(V(L_Out)/Lparasitic)^0.7873) -
+ (0.0011*(V(L_Out)/Lparasitic)^0.7873)/(2*(V(L_Out)/Lparasitic))),0.49m)}
E1 L_Out 0 4 5  1
R9 0 L_Out  5
S4 1 4 6 0   Smod2
S5 5 SCR1 6 0  Smod2
C2 5 4 0.1n
#V4 6 0 2 PULSE  0 2 506.73u 0.01u 0.01u 0.1u 120m 1
#V4 6 0 2 PULSE  0 2 506.73u 0.01u 0.01u 0.1u 120m 1
V4 6 0 2 PULSE  0 2 32.743m 0.01u 0.01u 0.1u 120m 1
E2 D_Out 0 7 8  1
R10 0 D_Out  5
S6 0 7 9 0   Smod2
S7 8 Load1 9 0   Smod2
C3 8 7  0.1n
#V5 9 0  2 PULSE  0 2 520.3u 0.01u 0.01u 0.1u 120m 1
#V5 9 0  2 PULSE  0 2 520.1u 0.01u 0.01u 0.1u 120m 1
V5 9 0  2 PULSE  0 2 32.791m 0.01u 0.01u 0.1u 120m 1
R11 SCR1 SCR2  100k
Lstray2 0 damp 10n
Rdamp damp Diode3 500n
#Rstray2 0 Load3  5m

Rsnubber SCR1 Snubber 1
Csnubber Snubber Load1 5u IC=Charge
#Rsnubber SCR1 Snubber 47
#Csnubber Snubber Load1 0.1u IC=Charge
#Rsnubber SCR1 Snubber 2
#Csnubber Snubber SCR2 42.4u IC=Charge
#Csnubber Snubber Load1 42.4u IC=Charge


#.TRAN 0.1u 1m 0m 0.05u UIC
.TRAN 1u 32.95m 32.7m 1u UIC
.PRINT TRAN I(RSCR) V(SCR1,SCR2) V(Cap) V(L_out) V(1,SCR1)
#V(L_Out) V(1,SCR1)
.PROBE
.END
```

Figure A3. PSPICE netlist of the PULSERAD pulsed electromagnet circuit. “RSCR” details the time-varying resistance of the thyristor switch.

Oil Switch Gap (mm)	V_{charge} (kV)	V_{trans} (kV)	PSI (SF_6)
3.623	25	432	10
1.814	25	251	10
4	20	DNF	10
	22.5	DNF	12.5
	25	201	12
	27.5	218	12
	30	225	14
	32.5	233	16
	35	251	18
5	27.5	223	18
	30	240	22
	32.5	260	22
	35	280?	24

Figure A4. Oil-switch gap and Marx charging voltages used to achieve various V_{trans}.

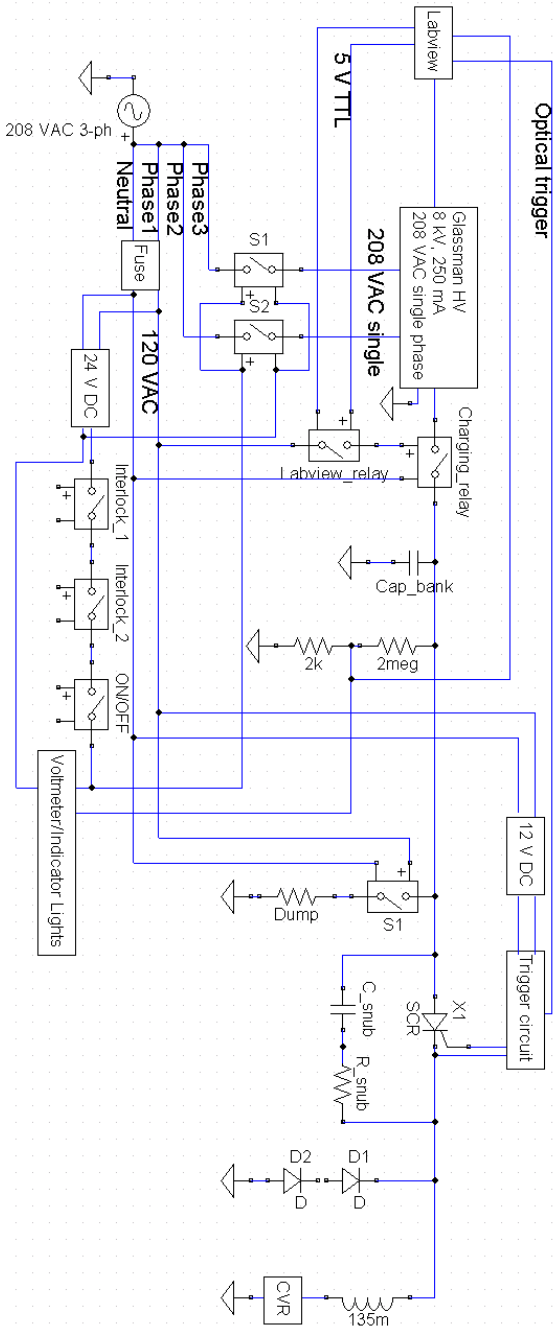

Figure A5. PSPICE model of pulsed electromagnet circuit.

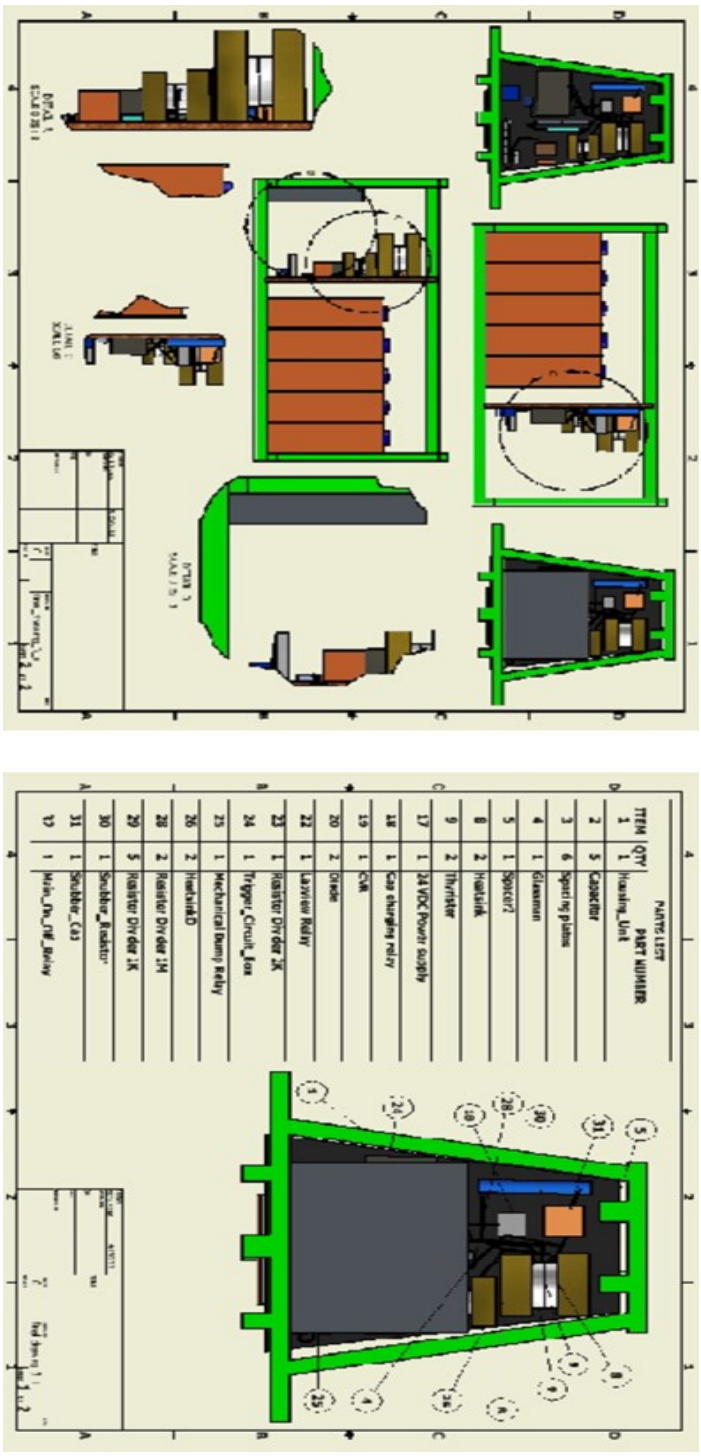

Figure A6. CAD representation of pulsed electromagnet system.

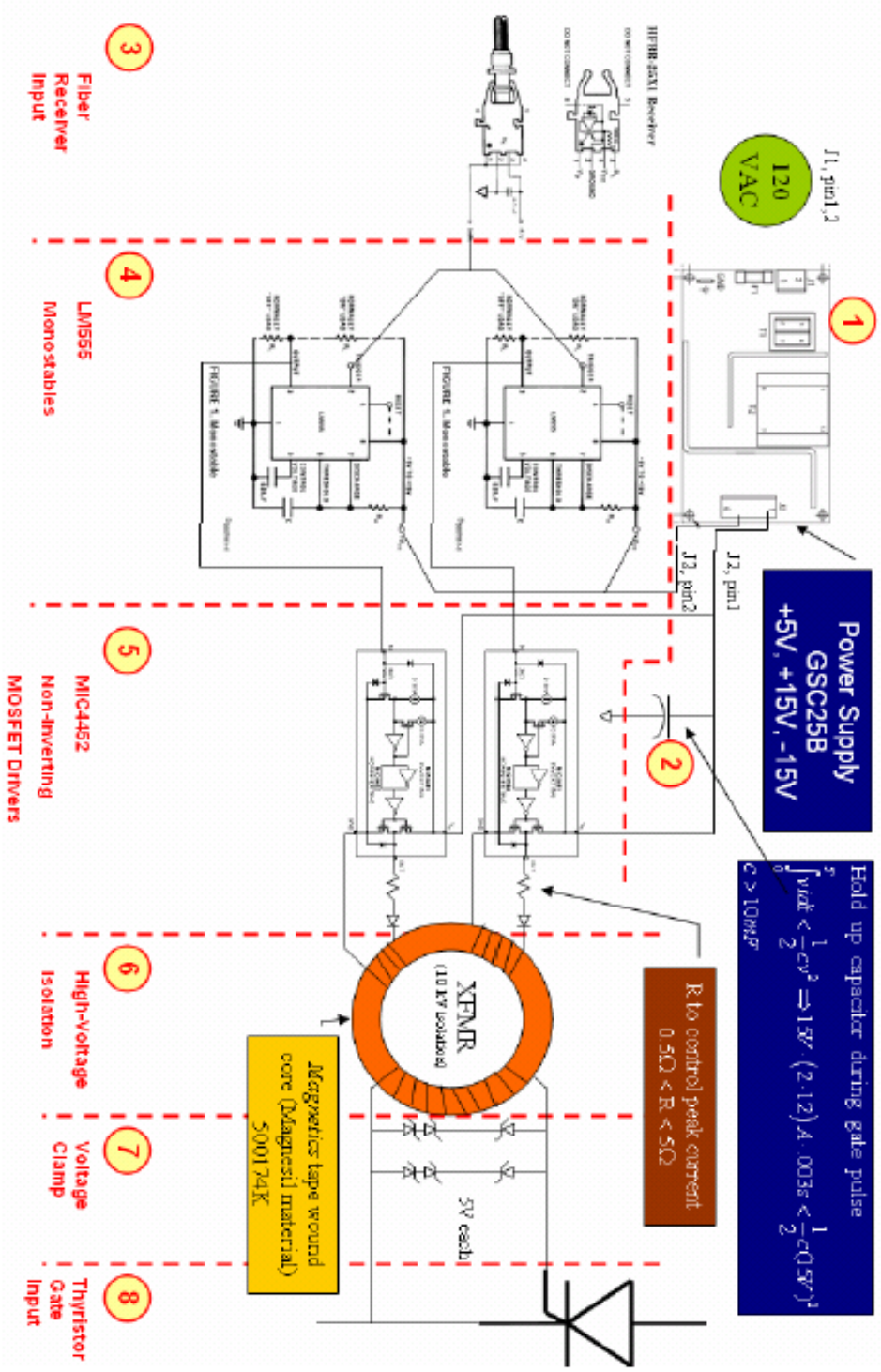

Figure A7. NPGS thyristor trigger design closely informs UNM design [63].

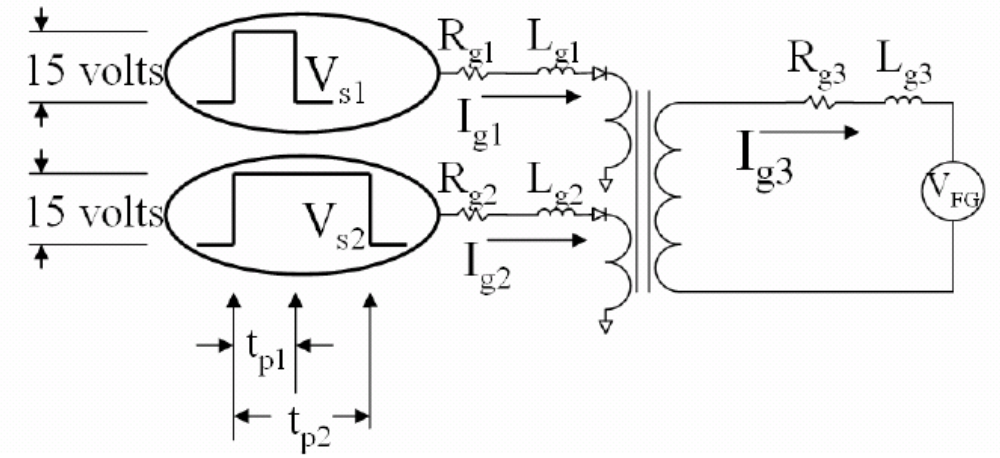

Figure A8. Use of one transformer core to produce required thyristor gate signal [63].

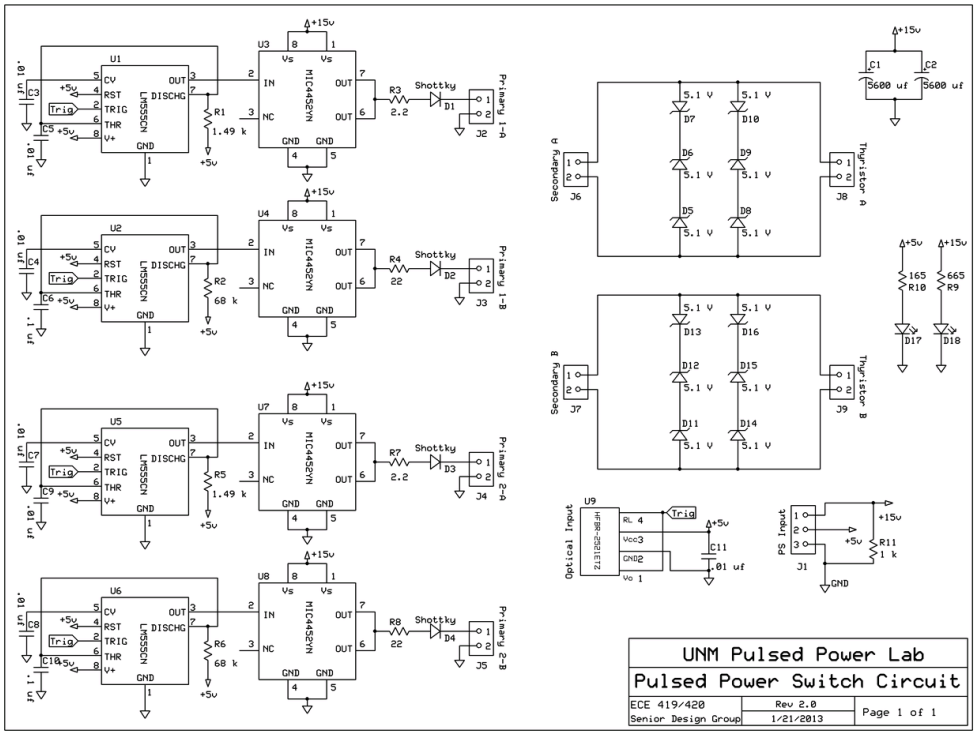

Figure A9. UNM's PCB board thyristor trigger circuit layout.

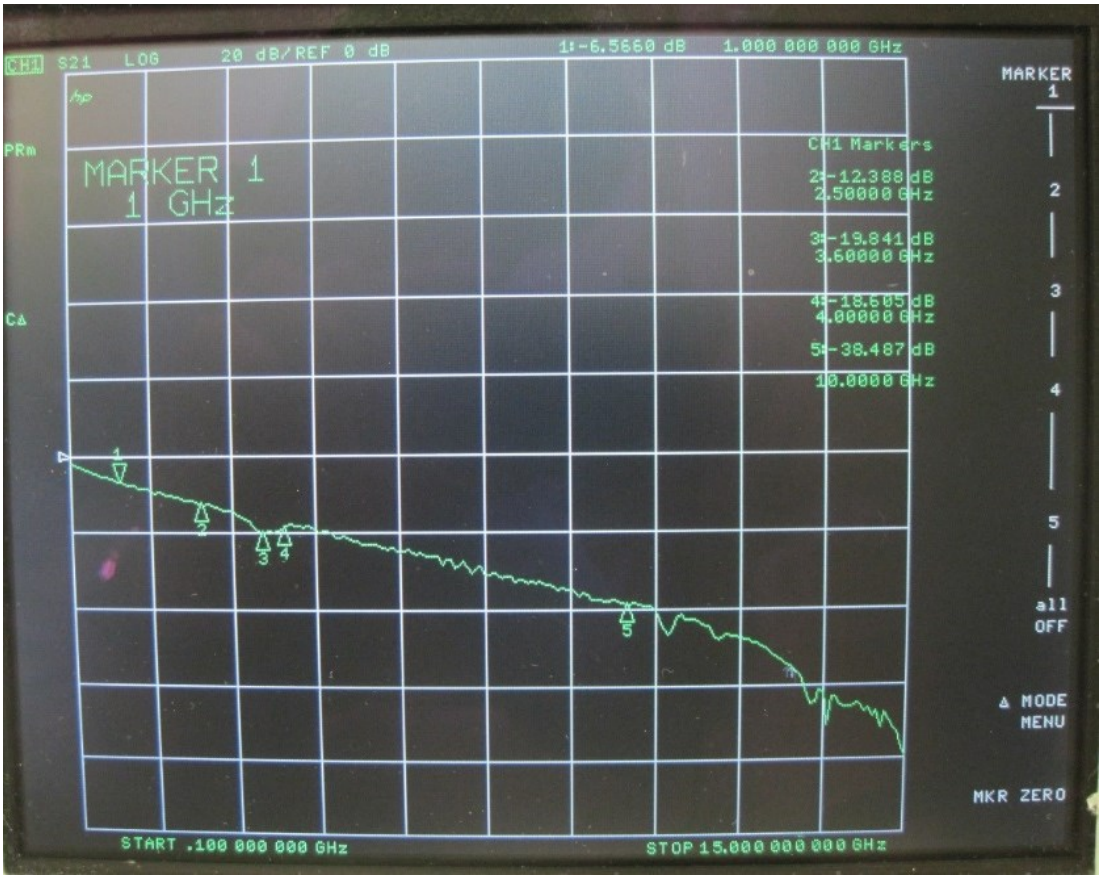

Figure A10. “Purple” cable set RG-214 attenuation vs. frequency.

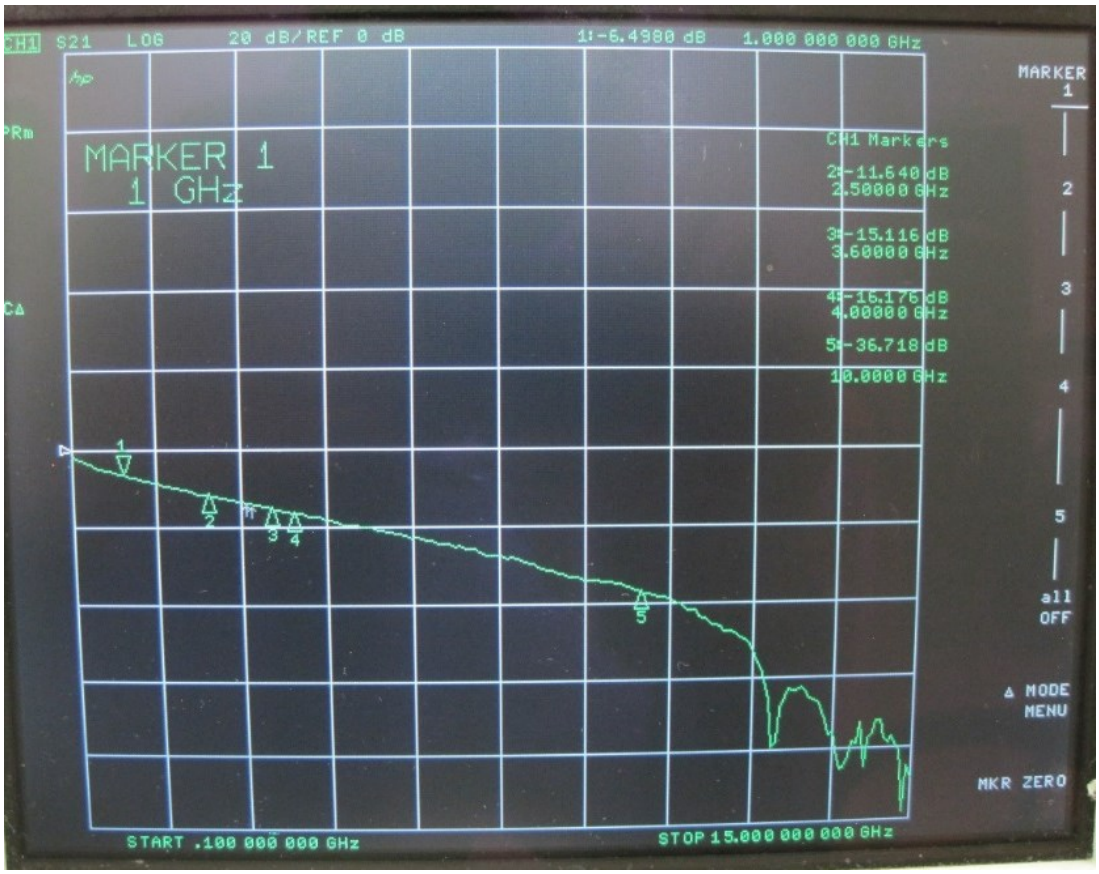

Figure A11. “Blue” cable set RG-214 attenuation vs. frequency.

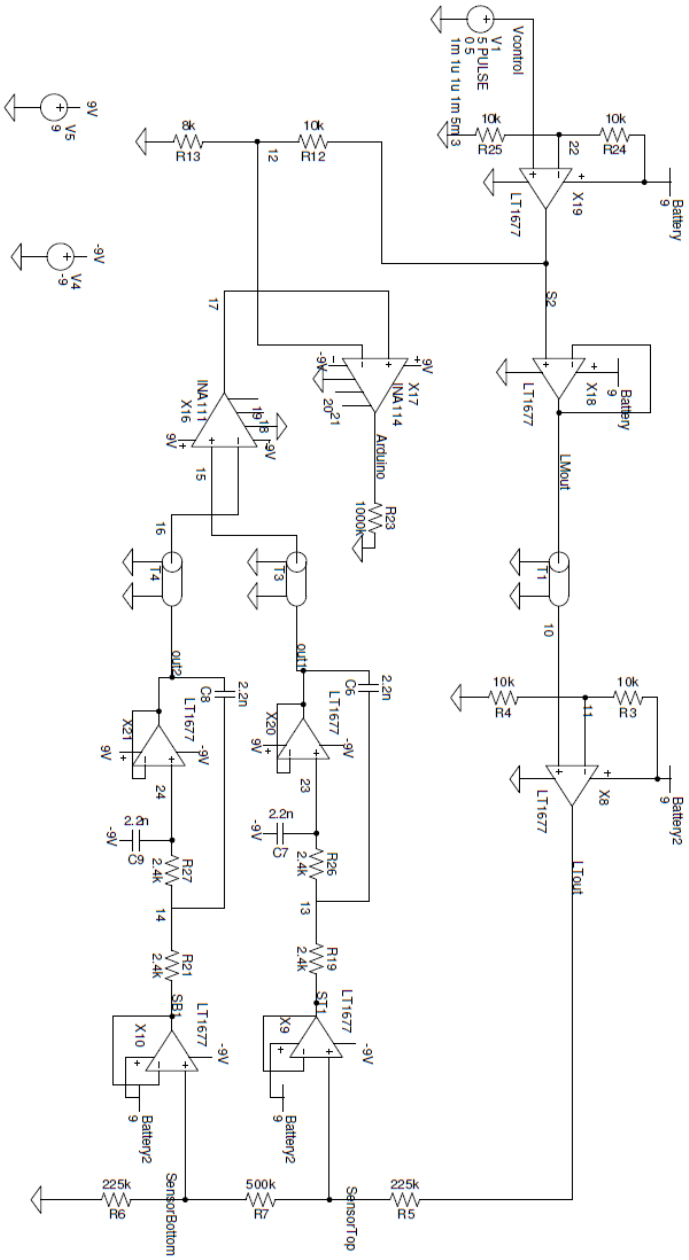

Figure A12. Analog electronics used to measure movement in the capillary tube sensor. Amplifiers to the left of the transmission lines are in the calorimeter control panel, and amplifiers to the right are remotely located in a box on the calorimeter.

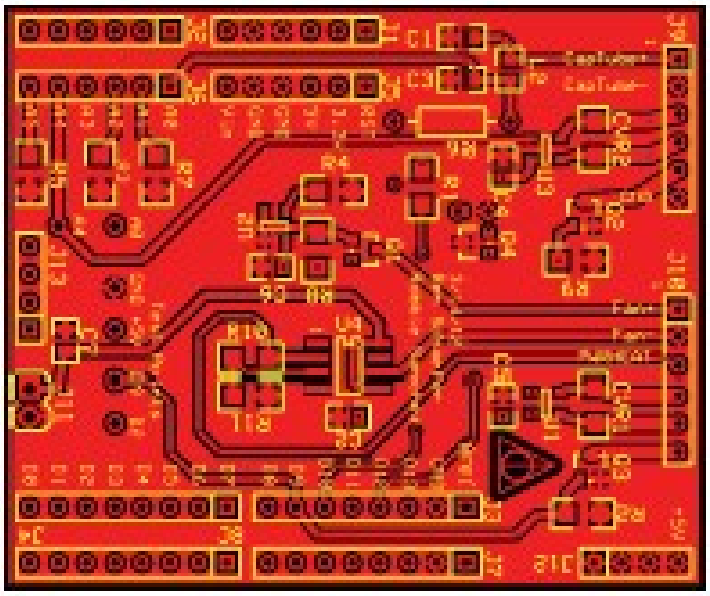

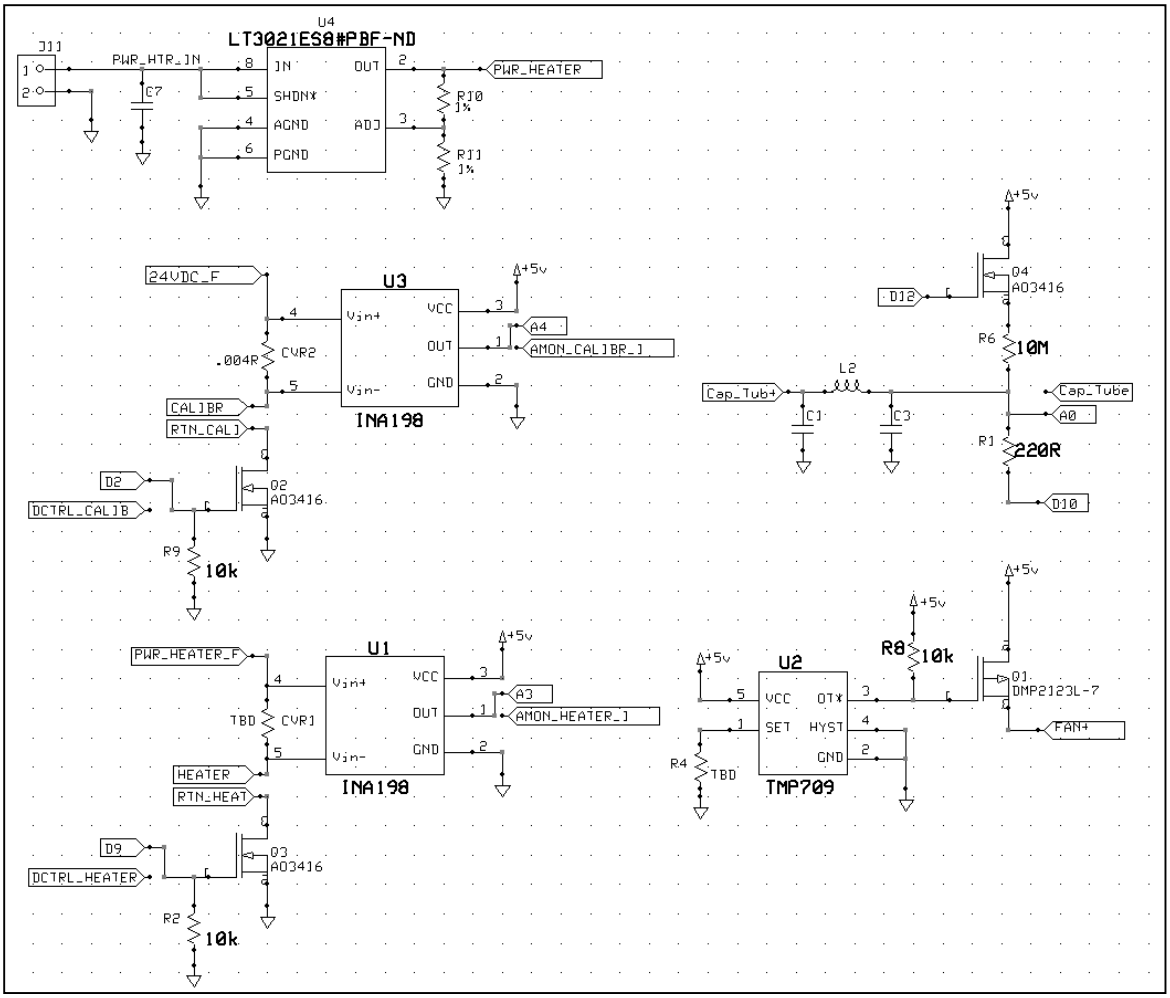

Figure A13. Arduino UNO shield used to house one leg of the sensor's resistor bridge, to measure the signal voltage, and to interface with switches and displays.

REFERENCES

[1] H. A. H. Boot, and J. T. Randall, "The cavity magnetron," *IEEE Proc. Radiolocation Conv.*, vol. 93, pp. 928-938, 1946.

[2] H. A. H. Boot, and J. T. Randall, "Historical notes on the cavity magnetron," *IEEE T. Electron. Dev.,* vol. 23, pp. 724-729, 1976.

[3] J. Benford, J. A. Swegle, and E. Schamiloglu, *High power microwaves*, 2nd ed., New York: Taylor & Francis, 2007.

[4] G. B. Collins, *Microwave Magnetrons*, New York: McGraw-Hill Book Co., 1948.

[5] T. H. Martin, *J. C. Martin on Pulsed Power*: Springer US, 1996.

[6] A. Palevsky, and G. Bekefi, "Microwave Emission from Pulsed, Relativistic E-Beam Diodes .2. Multiresonator Magnetron," *Phys. Fluids,* vol. 22, pp. 986-996, 1979.

[7] D. J. Kaup, "Modeling of an A6 relativistic magnetron with analytics and numerics," *Phys. Scr.,* vol. T107, pp. 39-48, 2004.

[8] D. J. Kaup, "Theoretical modeling of an A6 relativistic magnetron," *Phys. Plasmas,* vol. 11, pp. 3151-3164, 2004.

[9] H. W. Chan, C. P. Chen, and R. C. Davidson, "Numerical Study of Relativistic Magnetrons," *J. Appl. Phys.,* vol. 73, pp. 7053-7060, 1993.

[10] H. W. Chan, C. Chen, and R. C. Davidson, "Computer simulation of relativistic multiresonator cylindrical magnetrons," *Appl. Phys. Lett.,* vol. 57, pp. 1271, 1990.

[11] H. L. Bosman, M. I. Fuks, S. Prasad, and E. Schamiloglu, "Improvement of the output characteristics of magnetrons using the transparent cathode," *IEEE Trans. Plasma Sci.,* vol. 34, pp. 606-619, 2006.

[12] M. Fuks, and E. Schamiloglu, "Rapid start of oscillations in a magnetron with a "transparent" cathode," *Phys. Rev. Lett.,* vol. 95, pp. 205101-205101-4, 2005.

[13] R. V. Lovelace, and T. F. T. Young, "Relativistic Hartree Condition for Magnetrons - Theory and Comparison with Experiments," *Phys. Fluids,* vol. 28, pp. 2450-2452, 1985.

[14] N. F. Kovalev, B. D. Kol'chugin, V. E. Nechaev, M. M. Ofitserov, E. I. Soluyanov, and M. I. Fuks, "Relativistic magnetron with diffraction output," *Sov. Tech. Phys. Lett.,* vol. 3, 1977.

[15] N. F. Kovalev, A. A. Kolomenski, E. G. Krastelev, M. I. Kuznetsov, M. I. Petelin, M. I. Fuks, and L. N. Chekanova, "High-power relativistic magnetron with wavelength 3 cm," *Sov. Tech. Phys. Lett.,* vol. 6, 1980.

[16] M. Daimon, and W. Jiang, "Modified configuration of relativistic magnetron with diffraction output for efficiency improvement," *Appl. Phys. Lett.,* vol. 91, pp. 191503-191503-3, 2007.

[17] M. Daimon, K. Itoh, G. Imada, and W. Jiang, "Experimental demonstration of relativistic magnetron with modified output configuration," *Appl. Phys. Lett.,* vol. 92, pp. 191504-191504-3, 2008.

[18] M. I. Fuks, and E. Schamiloglu, "70% Efficient Relativistic Magnetron With Axial Extraction of Radiation Through a Horn Antenna," *IEEE Trans. Plasma Sci.,* vol. 38, pp. 1302-1312, 2010.

[19] B. W. Hoff, A. D. Greenwood, P. J. Mardahl, and M. D. Haworth, "All Cavity-Magnetron Axial Extraction Technique," *IEEE Trans. Plasma Sci.,* vol. 40, pp. 3046-3051, 2012.

[20] M. Franzi, R. M. Gilgenbach, B. Hoff, G. Greening, Y. Y. Lau, N. M. Jordan, D. Simon, D. French, and J. Luginsland, "Coaxial all cavity extraction in the Recirculating Planar Magnetron," *Proc. IEEE 15th IVEC (Monterey, CA, 2014)*, pp. 89-90.

[21] S. N. Vlasov, G. M. Zhislin, I. M. Orlova, M. I. Petelin, and G. G. Rogacheva, "Irregular waveguides as open resonators," *Radiophys. Quantum El.,* vol. 12, pp. 972-978, 1969.

[22] H. Wood, P. Mardahl, D. French, B. Hoff, and K. Hendricks, "Controllable Axial Overmoding in an MDO," *IEEE Trans. Plasma Sci.,* vol. 40, pp. 2094-2098, 2012.

[23] M. I. Fuks, N. F. Kovalev, A. D. Andreev, and E. Schamiloglu, "Mode conversion in a magnetron with axial extraction of radiation," *IEEE Trans. Plasma Sci.,* vol. 34, pp. 620-626, 2006.

[24] R. W. Lemke, T. C. Genoni, and T. A. Spencer, "Three-dimensional particle-in-cell simulation study of a relativistic magnetron," *Phys. Plasmas,* vol. 6, pp. 603-613, 1999.

[25] R. B. Anderson, W. D. Getty, M. L. Brake, Y. Y. Lau, R. M. Gilgenbach, and A. Valfells, "Multipactor experiment on a dielectric surface," *Rev. Sci. Instrum.,* vol. 72, pp. 3095-3099, 2001.

[26] C. Leach, S. Prasad, M. I. Fuks, and E. Schamiloglu, "Suppression of Leakage Current in a Relativistic Magnetron Using a Novel Design Cathode Endcap," *IEEE Trans. Plasma Sci.,* vol. 40, pp. 2089-2093, 2012.

[27] W. Li, and Y. G. Liu, "Modified magnetic field distribution in relativistic magnetron with diffraction output for compact operation," *Phys. Plasmas,* vol. 18, pp. 023103, Feb, 2011.

[28] M. R. Lopez, R. M. Gilgenbach, D. W. Jordan, S. A. Anderson, M. D. Johnston, M. W. Keyser, H. Miyake, C. W. Peters, M. C. Jones, V. B. Neculaes, Y. Y. Lau, T. A. Spencer, J. W. Luginsland, M. D. Haworth, R. W. Lemke, and D. Price, "Cathode effects on a relativistic magnetron driven by a microsecond E-beam accelerator," *IEEE Trans. Plasma Sci.,* vol. 30, pp. 947-955, 2002.

[29] Y. M. Saveliev, S. N. Spark, B. A. Kerr, M. I. Harbour, S. C. Douglas, and W. Sibbett, "Effect of cathode end caps and a cathode emissive surface on relativistic magnetron operation," *IEEE Trans. Plasma Sci.,* vol. 28, pp. 478-484, 2000.

[30] D. J. Johnson, M. E. Savage, R. A. Sharpe, A. V. Batrakov, and D. I. Proskurovsky, "Pulsed HV vacuum breakdown of polished, powder coated, and E-beam treated large area stainless steel electrodes with 0.5 to 7 mm gaps," *IEEE T. Dielect. El. In.,* vol. 13, pp. 52-64, 2006.

[31] S. Humphries, *Principles of charged particle acceleration*, New York: J. Wiley, 1986.

[32] Y. Gao, J. H. Yin, J. F. Sun, Z. Zhang, P. F. Zhang, and Z. F. Su, “Electron Emission Suppression from Cathode Surfaces of a Rod-Pinch Diode,” *Chin. Phys. Lett.,* vol. 27, pp. 055201, 2010.
[33] G. B. Frazier, "Electron field emission from coated and uncoated conductors," Physics International Company, 1975.
[34] N. M. Jordan, Y. Y. Lau, D. M. French, R. M. Gilgenbach, and P. Pengvanich, “Electric field and electron orbits near a triple point,” *J. Appl. Phys.,* vol. 102, pp. 033301-033301-10, 2007.
[35] V. A. Nevrovsky, "Analysis of elementary processes leading to surface flashover in vacuum," *Proc. IEEE 18th ISDEIV (Eindhoven, Netherlands, 1998),* pp. 159-161.
[36] K. D. Bergeron, “Theory of Secondary-Electron Avalanche in Vacuum Flashover of Insulators,” *Bull. Am. Phys. Soc.,* vol. 21, pp. 1146-1146, 1976.
[37] V. Belyaev, “Model of surface flashover of insulator in vacuum,” *Proc. IEEE 18th ISDEIV (Eindhoven, Netherlands, 1998),* pp. 4.
[38] C. Leach, S. Prasad, M. Fuks, and E. Schamiloglu, “Compact Relativistic Magnetron with Gaussian Radiation Pattern,” *IEEE Trans. Plasma Sci.*, vol. 40, pp. 3116-3120, 2012.
[39] Y. T. Lo, and S. W. Lee, *Antenna handbook*, New York: Van Nostrand Reinhold, 1993.
[40] C. Leach, S. Prasad, M. Fuks, and E. Schamiloglu, "Compact A6 magnetron with permanent magnet," *Proc. IEEE 13th IVEC (Monterey, CA, 2012)*, pp. 491-492.
[41] S. Prasad, “Office of Naval Research UNM research review presentation (MDO and BWO TE11 Bragg reflector),” *UNM Pulsed Power, Beams, and High Power Microwaves Lab*, 2014.
[42] H. Zou, J.-U. Li, T.-M. Li, H. Li, T.-W. Zhang, H.-Y. Wang, and X.-Y. Yu, “Primary Research of Mode-Converter in MDO,” *(reprint, 2011)*.
[43] B. Goplen, L. Ludeking, D. Smithe, and G. Warren, “USER-CONFIGURABLE MAGIC FOR ELECTROMAGNETIC PIC CALCULATIONS,” *Comput. Phys. Commun.,* vol. 87, pp. 54-86, 1995.
[44] R. E. Peterkin, and J. W. Luginsland, “A virtual prototyping environment for directed-energy concepts,” *Comput. Sci. Eng.,* vol. 4, pp. 42-49, 2002.
[45] D. Meeker, “Finite Element Method Magnetics,” *http://www.femm.info/wiki/HomePage*, 2008.
[46] A. Corporation, “High Frequency Structure Simulator (HFSS),” *http://www.ansoft.com/products/hf/hfss/*, 2010.
[47] P. Development, “TopSpice 8 Demo Version,” *http://penzar.com/topspice/topspice.htm*, 2012.
[48] Y. Kane, “Numerical solution of initial boundary value problems involving maxwell's equations in isotropic media,” *IEEE Trans. Antennas Propag.,* vol. 14, pp. 302-307, 1966.
[49] A. Taflove, and S. C. Hagness, *Computational Electrodynamics: The Finite-difference Time-domain Method*: Artech House, 2005.
[50] G. Gray, and T. Kolda, “Algorithm 8xx: APPSPACK 4.0: Asynchronous parallel pattern search for derivative-free optimization,” *ACM T. Math. Software*, to appear (accepted Nov. 2005).

[51] T. Kolda, “Revisiting asynchronous parallel pattern search for nonlinear optimization,” *SIOPT,* vol. 16, pp. 563-586, 2005.

[52] S. Prasad, M. Roybal, K. Prestwich, M. Fuks, C. J. Buchenauer, and E. Schamiloglu, "Magnetron experiments on the short-pulse "SINUS-6" accelerator," *Proc. IEEE 9th IVEC with 9th IVESC (Monterey, CA, 2008),* pp. 441-442.

[53] M. T. Bettencourt, K. L. Cartwright, A. D. Greenwood, P. J. Mardahl, and S. E. Olson, “Virtual Prototyping of Directed Energy Weapons,” *DoD HPCMP-UGC (2010)*, pp. 7.

[54] A. D. Andreev, and K. J. Hendricks, “Multicavity Magnetron "Rodded" Quasi-Metamaterial Cathode,” *IEEE Trans. Plasma Sci.,* vol. 41, pp. 620-627, 2013.

[55] C. Leach, A. Andreev, and E. Schamiloglu, “UNM Final Report – Rodded Cathode ICEPIC, 30 April 20,” *UNM Pulsed Power, Beams, and High Power Microwaves Laboratory*, 2013.

[56] R. A. Richardson, J. Denavit, M. S. Di Capua, and P. W. Rambo, “Transport of relativistic electron beams along wire arrays,” *J. Appl. Phys.,* vol. 69, pp. 6261, 1991.

[57] C. Leach, S. Prasad, M. Fuks, and E. Schamiloglu, “Suppression of Leakage Current in a Relativistic Magnetron using a Novel Design Cathode Endcap,” *IEEE Trans. Plasma Sci.*, vol. 40, pp.2089-2093, 2012.

[58] J. Bernardes, and S. Swindler, "Modeling and Analysis of Thyristor and Diode Reverse Recovery in Railgun Pulsed Power Circuits," *Proc. IEEE Pulsed Power Conf. (Monterey, CA, 2005),* pp. 79-82.

[59] ABB Switzerland Ltd., Semiconductors, "Application Note 5SYA 2020-02 - Design of RC Snubbers for Phase Control Applications," Oct. 11, 2014.

[60] K. R. Prestwich, “Design considerations for 300 kV, 20 Ohm, 50 ns, 3ns risetime pulse generator,” *Design notes for UNM Pulsed Power, Beams, and High Power Microwaves Laboratory,* pp. 1-4, Nov. 2, 2005.

[61] S. Prasad, C. Leach, K. Prestwich, C. J. Buchenauer, M. Fuks, and E. Schamiloglu, "Experimental demonstration of the output characteristics of the A6 magnetron on Pulserad 110a, a very short rise-time accelerator at UNM," *Proc. IEEE 13th IVEC (Monterey, CA, 2012),* pp. 495-496.

[62] Y. P. Bliokh, G. S. Nusinovich, A. G. Shkvarunets, and Y. Carmel, “Self-excitation of microwave oscillations in plasma-assisted slow-wave oscillators by an electron beam with a movable focus,” *Phys. Rev. E,* vol. 70, pp. 046501, 2004.

[63] J. H. Black, “Solid state capacitor discharge pulsed power supply design for railguns,” Thesis, Naval Postgraduate School, Monterey, CA, 2007.

[64] ABB Switzerland Ltd., Semiconductors, "Phase Control Thyristor 5STP 26N6500 " Oct. 11, 2014.

[65] J. P. Dupraz, A. Fanget, W. Grieshaber, and G. F. Montillet, "Rogowski coil: Exceptional current measurement tool for almost any application," *Proc. IEEE Power Eng. Soc. Gen. Meeting, PES (Tampa, FL, 2007)*, pp. 1-8.

[66] C. D. M. Oates, A. J. Burnett, and C. James, "The design of high performance Rogowski coils," *Proc. IEEE Int. Conf. Power Electron. (2002),* pp. 568-573.

[67] J. D. Ramboz, “Machinable Rogowski coil, design, and calibration,” *IEEE Trans. Instrum. Meas.,* vol. 45, pp. 511-515, 1996.

[68] D. G. Pellinen, M. S. Dicapua, S. E. Sampayan, H. Gerbracht, and M. Wang, "Rogowski Coil for Measuring Fast, High-Level Pulsed Currents," *Rev. Sci. Instrum.,* vol. 51, pp. 1535-1540, 1980.

[69] D. A. Ward, and J. L. T. Exon, "Using Rogowski coils for transient current measurements," *Eng. Sci. Educ. J.*, pp. 105-113, 1993.

[70] L. Rui, W. Xinxin, Z. Xiaobing, Y. Jianqiang, N. Zou, and H. Luya, "Method for calibrating a Rogowski coil of fast time response," *Rev. Sci. Instrum.,* vol. 78, pp. 084702-084702-2, 2007.

[71] A. I. Klimov, P. V. Vykhodtsev, A. A. Elchaniniov, O. B. Kovalchuk, I. K. Kurkan, S. D. Polevin, E. M. Tomeninov, and V. V. Rostov, "A calorimeter for high power microwave pulse measurement," *Proc. 15th Int. Symp. High Current Electron. (2008)*, pp. 422-424.

[72] A. G. Shkvarunets, "A broadband microwave calorimeter of large cross section," *Instrum. Exp. Tech.,* vol. 39, pp. 535-538, 1996.

[73] S. S. L. Testa, and G. C. Montanari, "Advanced modeling of electron avalanche process in polymeric dielectric voids: Simulations and experimental validation," *J. Appl. Phys.,* vol. 108, pp. 10, 2010.

[74] D. J. Johnson, W. E. Fowler, M. E. Savage, and W. A. Stygar, "Suppression of electron emission from large surface area stainless steel electrodes." *IEEE 20th Proc. Symp. Disch. El. (2002),* pp. 131-134.

[75] J. M. Gahl, C. Grabowski, D. Young, and O. Ishihara, "Pulse shortening in a high power backward wave oscillator," *Proc. IEEE Int. Conf. Plasma Sci. (Boston, MA, 1996),* pp. 230.